

Ministry of Education and Science of the Russian Federation
Saint Petersburg National Research University of Information
Technologies, Mechanics, and Optics

NANOSYSTEMS:
PHYSICS, CHEMISTRY, MATHEMATICS

2017, volume 8(1)

Наносистемы: физика, химия, математика

2017, том 8, № 1



NANOSYSTEMS:

PHYSICS, CHEMISTRY, MATHEMATICS

ADVISORY BOARD MEMBERS

Chairman: V.N. Vasiliev (*St. Petersburg, Russia*),
V.M. Buznik (*Moscow, Russia*); V.M. Ievlev (*Voronezh, Russia*), P.S. Kop'ev (*St. Petersburg, Russia*), N.F. Morozov (*St. Petersburg, Russia*), V.N. Parmon (*Novosibirsk, Russia*),
A.I. Rusanov (*St. Petersburg, Russia*),

EDITORIAL BOARD

Editor-in-Chief: I.Yu. Popov (*St. Petersburg, Russia*)

Section Co-Editors:

Physics – V.M. Uzdin (*St. Petersburg, Russia*),
Chemistry, material science – V.V. Gusarov (*St. Petersburg, Russia*),
Mathematics – I.Yu. Popov (*St. Petersburg, Russia*).

Editorial Board Members:

V.M. Adamyan (*Odessa, Ukraine*); O.V. Al'myasheva (*St. Petersburg, Russia*);
A.P. Alodjants (*Vladimir, Russia*); S. Bechta (*Stockholm, Sweden*); J. Behrndt (*Graz, Austria*);
M.B. Belonenko (*Volgograd, Russia*); V.G. Bepalov (*St. Petersburg, Russia*); J. Brasche (*Clausthal, Germany*);
A. Chatterjee (*Hyderabad, India*); S.A. Chivilikhin (*St. Petersburg, Russia*); A.V. Chizhov (*Dubna, Russia*);
A.N. Enyashin (*Ekaterinburg, Russia*), P.P. Fedorov (*Moscow, Russia*); E.A. Gudilin (*Moscow, Russia*);
V.K. Ivanov (*Moscow, Russia*), H. Jónsson (*Reykjavik, Iceland*); A.A. Kiselev (*Houston, USA*); Yu.S. Kivshar (*Canberra, Australia*);
S.A. Kozlov (*St. Petersburg, Russia*); P.A. Kurasov (*Stockholm, Sweden*); A.V. Lukashin (*Moscow, Russia*);
V.A. Margulis (*Saransk, Russia*); I.V. Melikhov (*Moscow, Russia*); G.P. Miroshnichenko (*St. Petersburg, Russia*);
I.Ya. Mittova (*Voronezh, Russia*); H. Neidhardt (*Berlin, Germany*); K. Pankrashkin (*Orsay, France*);
A.V. Ragulya (*Kiev, Ukraine*); V. Rajendran (*Tamil Nadu, India*); A.A. Rempel (*Ekaterinburg, Russia*);
V.Ya. Rudyak (*Novosibirsk, Russia*); D Shoikhet (*Karmiel, Israel*); P Stovicek (*Prague, Czech Republic*);
V.M. Talanov (*Novocherkassk, Russia*); A.Ya. Vul' (*St. Petersburg, Russia*); A.V. Yakimansky (*St. Petersburg, Russia*),
V.A. Zagrebnov (*Marseille, France*).

Editors:

I.V. Blinova; A.I. Popov; A.I. Trifanov; E.S. Trifanova (*St. Petersburg, Russia*),
R. Simoneaux (*Philadelphia, Pennsylvania, USA*).

Address: University ITMO, Kronverkskiy pr., 49, St. Petersburg 197101, Russia.

Phone: +7(812)232-67-65, **Journal site:** <http://nanojournal.ifmo.ru/>,

E-mail: popov1955@gmail.com

AIM AND SCOPE

The scope of the journal includes all areas of nano-sciences. Papers devoted to basic problems of physics, chemistry, material science and mathematics inspired by nanosystems investigations are welcomed. Both theoretical and experimental works concerning the properties and behavior of nanosystems, problems of its creation and application, mathematical methods of nanosystem studies are considered.

The journal publishes scientific reviews (up to 30 journal pages), research papers (up to 15 pages) and letters (up to 5 pages). All manuscripts are peer-reviewed. Authors are informed about the referee opinion and the Editorial decision.

CONTENT

MATHEMATICS

- M.M. Aripov, A.S. Matyakubov
Self-similar solutions of a cross-diffusion parabolic system with variable density: explicit estimates and asymptotic behaviour 5
- O. Karpova, K. Sabirov, D. Otajanov, A. Ruzmetov, A. A. Saidov
Absorbing boundary conditions for Schrödinger equation in a time-dependent interval 13
- J. Kerner, T. Mühlenbruch
On a non-separable quantum many-particle system on the half-line 20
- K.K. Sabirov, M. Aripov, D.B. Sagdullayev
Stationary nonlinear Schrödinger equation on the graph for the triangle with outgoing bonds 24
- Z. Sobirov, D. Babajanov, D. Matrasulov
Nonlinear standing waves on planar branched systems: shrinking into metric graph 29
- Y. Yamazaki, S. Ohmori
Ultradiscretization of reaction-diffusion type partial differential equations exhibiting pulse propagation 38
- J. Yusupov
Tunable wave packet transport in branched periodic lattices with time-dependent external field 42

PHYSICS

- B. Abdullaev, C.-H. Park, K.-S. Park, I.-J. Kang
Metal-insulator (fermion-boson)-crossover origin of pseudogap phase of cuprates I: anomalous heat conductivity, insulator resistivity boundary, nonlinear entropy 48
- B. Abdullaev, D.B. Abdullaev, C.-H. Park, M.M. Musakhanov
Normal state pair nematicity and hidden magnetic order and metal-insulator (fermion-boson)- crossover origin of pseudogap phase of cuprates II 59
- A.E. Atamuratov, A. Abdikarimov, M. Khalilloev, Z.A. Atamuratova, R. Rahmanov, A. Garcia-Loureiro, A. Yusupov
Simulation of DIBL effect in 25 nm SOI-FinFET with the different body shapes 71

| | |
|--|------------|
| A.E. Atamuratov, M. Khalilloev, A. Abdikarimov, Z.A. Atamuratova, M. Kittler, R. Granzner, F. Schwierz Simulation of DIBL effect in junctionless SOI MOSFETS with extended gate | 75 |
| Z.T. Azamatov, N.A. Akbarova, I.A. Kulagin, V.E. Gaponov, V.I. Redkorechev, A.M. Isayev Digital holographic interferometry in physical nanomeasurements | 79 |
| G. Babajanova, K. Nakamura Fast-forward of standard dynamics with use of electromagnetic field | 85 |
| B.L. Oksengendler, N.R. Ashurov, S.E. Maksimov, I.Z. Uralov, O.V. Karpova Fractal structures in perovskite-based solar cells | 92 |
| I. Setiawan, B.E. Gunara, J.S. Kosasih, K. Nakamura Accelerated dynamics in adiabatically-tunable asymmetric double-well potential | 99 |
| I.A. Silanteva, A.A. Yurchenko, P.N. Vorontsov-Velyaminov, A.P. Lyubartsev Equilibrium properties of 3-arm star-shaped polyions: an entropic sampling Monte Carlo study | 108 |
| A. Tanaka, T. Cheon Adiabatic cycles in quantum systems with contact interactions | 121 |
| <u>CHEMISTRY AND MATERIAL SCIENCE</u> | |
| E.A. Belenkov, M.M. Brzhezinskaya, V.A. Greshnyakov Crystalline structure and properties of diamond-like materials | 127 |
| S.A. Drozdov, V.G. Nazarov, S.A. Nozdrachev, Yu.V. Rudyak, G.O. Rytikov The polymer composites' morphological structure simulation | 137 |
| Information for authors | 146 |

Self-similar solutions of a cross-diffusion parabolic system with variable density: explicit estimates and asymptotic behaviour

M. M. Aripov, A. S. Matyakubov

National University of Uzbekistan, Applied Mathematics and Computer Analysis,
Universitet, 4, Tashkent, 100174, Uzbekistan
mirsaidaripov@mail.ru, almasa@list.ru

PACS 02.30.Jr, 02.30.Mv, 11.10.Jj, 11.10.Lm

DOI 10.17586/2220-8054-2017-8-1-5-12

In this paper, we study the properties of self-similar solutions of a cross-diffusion parabolic system. In particular, we find the Zeldovich–Barenblatt type solution to the cross diffusive system. The asymptotic behavior of self-similar solutions are analyzed for both the slow and fast diffusive regimes. It is shown that coefficients of the main term of the asymptotic of solution satisfy some system of nonlinear algebraic equations.

Keywords: cross-diffusive system, non-divergence form, finite speed, perturbation, global solutions, asymptotic behavior, numerical analysis.

Received: 25 July 2016

Revised: 28 August 2016

1. Introduction

Consider in $Q = \{(t, x) : t > 0, x \in \mathbb{R}^N\}$ the cross-diffusive system of equations in non-divergence form with Cauchy conditions:

$$|x|^n \frac{\partial u}{\partial t} = v^{\alpha_1} \nabla \left(|x|^k u^{m_1-1} \nabla u \right) + |x|^n u^{\beta_1}, \quad (1)$$

$$|x|^n \frac{\partial v}{\partial t} = u^{\alpha_2} \nabla \left(|x|^k v^{m_1-1} \nabla v \right) + |x|^n v^{\beta_2},$$

$$u(0, x) = u_0(x), \quad v(0, x) = v_0(x), \quad x \in \mathbb{R}^N. \quad (2)$$

where $n, k, m_1, m_2, \alpha_1, \alpha_2, \beta_1, \beta_2$ are the numerical parameters, $\nabla(\cdot) = \text{grad}_x(\cdot)$, are the functions $u = u(t, x) \geq 0, v = v(t, x) \geq 0$ are the solutions.

It is clear that the system (1) is degenerate. Therefore, it does not have classical solutions on the domain defined by equations $u(t, x) = 0, v(t, x) = 0, \nabla u = 0, \nabla v = 0$, meaning system (1) may not have a classical solution. Therefore, in this case we consider a weak solution having the property $u(t, x) \geq 0, v(t, x) \geq 0; v^{\alpha_1} \nabla \left(|x|^k u^{m_1-1} \nabla u \right), u^{\alpha_2} \nabla \left(|x|^k v^{m_1-1} \nabla v \right) \in C(Q)$ and obeying to the system (1) in sense of a distribution [1].

Non-divergent form equations and system of equations (1) are often used to describe various physical phenomena, such as the diffusive process for biological species, the resistive diffusion phenomena in force-free magnetic fields, curve shortening flow, spreading of infectious disease and so on, see for [2–8].

In [2] for the system (1) (for $n = 0, k = 0$, and $m_1 = 1, m_2 = 1$) the authors proved that: (i) when $\min\{a, b\} \leq \lambda_1$, then there exists global positive classical solution, and all positive classical solutions cannot blow up in finite time in the meaning of maximum norm; (ii) when $\min\{a, b\} > \lambda_1$, there is no global positive classical solution.

Previous studies [3] with positive solutions of some degenerate and quasilinear parabolic systems are given by:

$$\begin{aligned} u_{it} &= f_i(u_{i+1}) (\Delta u_i + a_i u_i) \\ u_{nt} &= f_n(u_1) (\Delta u_n + a_n u_n), \quad x \in \Omega, \quad t > 0, \quad i = 1, 2, \dots, n-1. \end{aligned}$$

The local existence and uniqueness of classical solution also proven in [3]. It is also shown that: (i) when $\min\{a_1, \dots, a_n\} \leq \lambda_1$ then there exists global positive classical solution, and all positive classical solutions cannot blow up in finite time in the meaning of maximum norm; (ii) when $\min\{a_1, \dots, a_n\} > \lambda_1$, and the initial datum (u_{10}, \dots, u_{n0}) satisfies some assumptions, then the positive classical solution is unique and blows up in finite time, where λ_1 is the first eigenvalue of Δ in Ω with homogeneous Dirichlet boundary conditions.

Some properties of solutions for the non-divergence form in single equation, such as the existence, non-uniqueness, the blow-up properties etc. have been discussed by many authors [4–6]. Finite speed properties of a

perturbation of distribution (FSPD) and the asymptotic behavior of self-similar solutions for another systems are considered in [9–12].

In [13, 14], the Cauchy problem for the following two equations with variable coefficients is studied:

$$\rho(x) \frac{\partial u}{\partial t} = \operatorname{div} \left(u^{m-1} |\nabla u|^{p-2} \nabla u \right) + \rho(x) u^\beta,$$

and

$$\rho(x) \frac{\partial u}{\partial t} = \operatorname{div} \left(u^{m-1} |\nabla u|^{p-2} \nabla u \right) + u^\beta, \quad x \in \mathbb{R}^N, \quad t > 0,$$

where $p > 1$, $m + p - 3 > 0$, $\beta > m + p - 2$, $\rho(x) = |x|^{-n}$ or $\rho(x) = (1 + |x|)^{-n}$. The authors showed that under some constraints for the parameters and for the initial data, any nontrivial solution of the Cauchy problem blows up in finite time. Moreover, the authors established a sharp universal estimate of the solution near the blow-up point.

Ref. [7] considers the degenerate and quasilinear parabolic systems having non divergent form given by:

$$\begin{cases} u_{it} = u_i^{p_i} (\Delta u_i + a_i u_{i+1}), \quad i = 1, 2, \dots, m, \quad u_{m+1} = u_1, \\ u_i(x, 0) = u_{i0}(x), \quad i = 1, 2, \dots, m, \quad x \in \Omega, \\ u_i(x, t) = 0, \quad i = 1, 2, \dots, m, \quad x \in \partial\Omega, \quad t > 0, \end{cases}$$

where a_i, p_i are the positive constants, $\Omega \in \mathbb{R}^N$ is a bounded domain with smooth boundary $\partial\Omega$. The local existence and uniqueness of classical solution are proved. Moreover, it proved that all solutions exist globally with homogeneous Dirichlet boundary conditions.

Ref. [8], investigates positive solutions of the degenerate parabolic equation not in divergence form: $u_t = u^p \Delta u + u^q |\nabla u|^2 - u^r$, subject to null Dirichlet boundary conditions. The existence of global solutions and the large time behavior for them is studied. The main effort is paid to obtain uniform asymptotic profiles for decay solutions, under various dominations of the nonlinear diffusion or absorption. It is shown that the large time property of the solution u behaves just like $(1 + (r - 1)t)^{-1/(r - 1)}$ if the decay is governed by the nonlinear absorption with $1 < r < p + 1$.

In this paper we consider the problem of constructing Zeldovich–Barenblatt type solution for the cross system equation (1). Using comparison methods, the property of FSPD of the Cauchy problem for a cross-diffusion parabolic system not in divergence form is established. The asymptotic behavior is discussed for a solution of the cross-diffusion parabolic system equations in non-divergence form for slow and fast diffusion cases depending on the value of the numerical parameters. On the basis of the asymptotic of solutions, suitable initial approximations are offered for the iterative process in the cases of the slow and fast diffusions, depending on the numerical parameter values.

2. The self-similar system of equations

Here, we provide a method of nonlinear splitting [15] for construction of self-similar equation for the system given by Eqs. (1). We look for the solutions $u(t, x), v(t, x)$ in the form:

$$\begin{aligned} u(t, x) &= \bar{u}(t) w(\tau(t), r), \\ v(t, x) &= \bar{v}(t) \psi(\tau(t), r). \end{aligned} \tag{3}$$

Then, we obtain $\bar{u}(t), \bar{v}(t)$ as $\bar{u}(t) = (T + t)^{1/(1-\beta_1)}, \bar{v}(t) = (T + t)^{1/(1-\beta_2)}$.

From Eqs. (3) and (1), we obtain the following system of equations:

$$\begin{aligned} r^n \frac{\partial w}{\partial \tau} &= \psi^{\alpha_1} r^{1-N} \frac{\partial}{\partial r} \left(r^{N-1+k} w^{m_1-1} \frac{\partial w}{\partial r} \right) + b_1 r^n \tau^{-1} \left(w^{\beta_1} - \frac{1}{1-\beta_1} w \right), \\ r^n \frac{\partial \psi}{\partial \tau} &= w^{\alpha_2} r^{1-N} \frac{\partial}{\partial r} \left(r^{N-1+k} \psi^{m_2-1} \frac{\partial \psi}{\partial r} \right) + b_2 r^n \tau^{-1} \left(\psi^{\beta_2} - \frac{1}{1-\beta_2} \psi \right), \end{aligned} \tag{4}$$

where:

$$\begin{aligned}\tau(t) &= \int (T+t)^{\frac{\alpha_1}{1-\beta_2} + \frac{m_1-1}{1-\beta_1}} dt = \int (T+t)^{\frac{\alpha_2}{1-\beta_1} + \frac{m_2-1}{1-\beta_2}} dt \quad \text{at} \quad \frac{\alpha_1}{1-\beta_2} + \frac{m_1-1}{1-\beta_1} + 1 \neq 0, \\ \tau(t) &= \ln(T+t) \quad \text{at} \quad \frac{\alpha_1}{1-\beta_2} + \frac{m_1-1}{1-\beta_1} + 1 = 0, \\ b_i &= \left(\frac{\alpha_i}{1-\beta_{3-i}} + \frac{m_i-1}{1-\beta_i} + 1 \right)^{-1}, \quad i = 1, 2, \quad r = |x|, \\ \frac{\alpha_1}{1-\beta_2} + \frac{m_1-1}{1-\beta_1} &= \frac{\alpha_2}{1-\beta_1} + \frac{m_2-1}{1-\beta_2}.\end{aligned}$$

It is easy to show that the system (4) has approximately self-similar solution given by:

$$u(\tau, r) = f(\xi), \quad \psi(\tau, r) = \phi(\xi), \quad \xi = r^{\frac{2-k}{2}} / \tau^{\frac{2-k}{4-2k+2n}}, \quad (5)$$

where ξ is self-similar variable and the functions $f(\xi)$, $\phi(\xi)$ fulfill the following approximately self-similar system of equations:

$$\begin{aligned}\phi^{\alpha_1} \xi^{1-\frac{2N}{2-k}} \frac{d}{d\xi} \left(\xi^{\frac{2N}{2-k}-1} f^{m_1-1} \frac{df}{d\xi} \right) + \frac{2}{(2-k)(n+2-k)} \xi^{\frac{2N}{2-k}+1} \frac{df}{d\xi} + \frac{4b_1}{(2-k)^2} \xi^{\frac{2N}{2-k}} \left(f^{\beta_1} - \frac{1}{1-\beta_1} f \right) &= 0, \\ f^{\alpha_2} \xi^{1-\frac{2N}{2-k}} \frac{d}{d\xi} \left(\xi^{\frac{2N}{2-k}-1} \phi^{m_2-1} \frac{d\phi}{d\xi} \right) + \frac{2}{(2-k)(n+2-k)} \xi^{\frac{2N}{2-k}+1} \frac{d\phi}{d\xi} + \frac{4b_2}{(2-k)^2} \xi^{\frac{2N}{2-k}} \left(\phi^{\beta_2} - \frac{1}{1-\beta_2} \phi \right) &= 0.\end{aligned} \quad (6)$$

In the following, we will consider nontrivial, nonnegative solutions of the system (6) satisfying the following conditions:

$$\begin{aligned}f(0) &= M_1, \quad \phi(0) = M_2, \quad M_1 \in \mathbb{R}^+, \quad M_2 \in \mathbb{R}^+, \\ f(d_1) &= \phi(d_2) = 0, \quad 0 < d_1 < \infty, \quad 0 < d_2 < \infty.\end{aligned} \quad (7)$$

3. The slow diffusion case ($m_{3-i} > 1 + \alpha_i$, $i = 1, 2$). Explicit estimates of the solution of problem (1)–(2)

Using the solution comparison method of [1] and the standard equations method of [15] for solving the problem (6)–(7), we can obtain the estimates for the solution of the problem (1)–(2).

We note that the functions:

$$\bar{f}(\xi) = A \left(a - \xi^{\frac{2n}{2-k}+2} \right)_+^{p_1}, \quad \bar{\phi}(\xi) = B \left(a - \xi^{\frac{2n}{2-k}+2} \right)_+^{p_2}, \quad (8)$$

where $p_i = \frac{m_{3-i} - \alpha_i - 1}{(m_1 - 1)(m_2 - 1) - \alpha_1 \alpha_2}$, $i = 1, 2$, $(b)_+ = \max(0, b)$, $a^{p_1} A = M_1$, $a^{p_2} B = M_2$ at $\xi < a^{\left(\frac{2n}{2-k}+2\right)^{-1}}$ satisfy Eq. (7).

Theorem 1. Let $m_{3-i} > 1 + \alpha_i$, $p_i m_i - 1 > 0$, $i = 1, 2$,

$$\begin{aligned}M_i^{\beta_i-1} &\leq \frac{1}{1-\beta_i} + \frac{N+n}{n+2-k} \frac{p_i}{b_i(p_i m_i - 1)}, \quad i = 1, 2, \\ M_i^{m_i-1} M_{3-i}^{\alpha_i} &= \frac{a}{(p_i m_i - 1)(n+2-k)^2}, \quad i = 1, 2, \\ u_+(0, x) &\geq u_0(x), \quad v_+(0, x) \geq v_0(x), \quad x \in \mathbb{R}^N.\end{aligned}$$

Then, in Q the problem (1)–(2) has a global solution with the estimate:

$$\begin{aligned}u(t, x) &\leq u_+(t, x) = \bar{u}(t) \bar{f}(\xi), \\ v(t, x) &\leq v_+(t, x) = \bar{v}(t) \bar{\phi}(\xi).\end{aligned} \quad (9)$$

Proof. Theorem 1 is proved by the method of comparison of solutions. As comparable functions, we take the functions $u_+(t, x)$, $v_+(t, x)$, defined by Eq. (9). Then, according to (3), (5) and $M_i^{m_i-1} M_{3-i}^{\alpha_i} = \frac{a}{(p_i m_i - 1)(n+2-k)^2}$, $i = 1, 2$, we get:

$$\begin{aligned}Lu_+(t, x) &= \left(-\frac{4p_1(N+n)}{(2-k)^2(n+2-k)(p_1 m_1 - 1)} - \frac{4b_1}{(1-\beta_1)(2-k)^2} \right) \xi^{\frac{2n}{2-k}} \bar{f}(\xi) + \frac{4b_1}{(2-k)^2} \xi^{\frac{2n}{2-k}} \bar{f}^{\beta_1}(\xi), \\ Lv_+(t, x) &= \left(-\frac{4p_2(N+n)}{(2-k)^2(n+2-k)(p_2 m_2 - 1)} - \frac{4b_2}{(1-\beta_2)(2-k)^2} \right) \xi^{\frac{2n}{2-k}} \bar{\phi}(\xi) + \frac{4b_2}{(2-k)^2} \xi^{\frac{2n}{2-k}} \bar{\phi}^{\beta_2}(\xi).\end{aligned}$$

From these expressions and $\bar{f}(\xi) \leq Aa^{p_1} = M_1$, $\bar{\phi}(\xi) \leq Ba^{p_2} = M_2$, we find, that for execution, the inequalities $Lu_+ \leq 0$, $Lv_+ \leq 0$ are enough to fulfill the conditions

$$M_i^{\beta_i-1} \leq \frac{1}{1-\beta_i} + \frac{N+n}{n+2-k} \frac{p_i}{b_i(p_i m_i - 1)}, \quad i = 1, 2.$$

By the conditions of the theorem, the last inequalities are satisfied. Then, according to the theorem, for comparison of problem (1)–(2) solutions, there is a global solution in Q and the following estimation $u_+(t, x) \geq u(t, x)$, $v_+(t, x) \geq v(t, x)$, $x \in \mathbb{R}^N$ holds.

We note for the solutions of Cauchy problem (1)–(2), we have FSPD properties.

4. The asymptotic behavior of self-similar solutions of the problem (6)–(7)

Let us introduce the following notations:

$$b_{i1} = p_i(p_i m_i - 1), \quad b_{i2} = -\frac{p_i}{(n+2-k)^2}, \quad b_{i3} = \frac{b_i}{(n+2-k)^2 a}, \quad i = 1, 2.$$

Assume $\frac{\alpha_1}{1-\beta_2} + \frac{m_1-1}{1-\beta_1} = \frac{\alpha_2}{1-\beta_1} + \frac{m_2-1}{1-\beta_2}$. Then the following theorem is valid:

Theorem 2. *Let $\frac{\alpha_1}{1-\beta_2} + \frac{m_1-1}{1-\beta_1} + 1 > 0$. Then compactly supported solution of the problem (6), (7) as $\xi \rightarrow a^{(\frac{2n}{2-k}+2)^{-1}}$ has the following asymptotic behavior:*

$$\begin{aligned} f(\xi) &= c_1 \left(a - \xi^{\frac{2n}{2-k}+2} \right)^{p_1} (1 + o(1)), \\ \phi(\xi) &= c_2 \left(a - \xi^{\frac{2n}{2-k}+2} \right)^{p_2} (1 + o(1)), \end{aligned} \quad (10)$$

if one of the the following conditions are fulfilled:

(1) $p_1 = \frac{1}{1-\beta_1}$, $p_2 = \frac{1}{1-\beta_2}$ and the coefficients c_i ($i = 1, 2$) are the roots of the systems of nonlinear algebraic equations:

$$b_{i1} c_i^{m_i-1} c_{3-i}^{\alpha_i} + b_{i2} + b_{i3} c_i^{\beta_i-1} = 0, \quad i = 1, 2.$$

(2) $p_i < \frac{1}{1-\beta_i}$, $p_i m_i > 1$, $i = 1, 2$ and the coefficients c_i ($i = 1, 2$) are the roots of the systems of nonlinear algebraic equations:

$$b_{i1} c_i^{m_i-1} c_{3-i}^{\alpha_i} + b_{i2} = 0, \quad i = 1, 2.$$

(3) $p_1 = \frac{1}{1-\beta_1}$, $p_2 < \frac{1}{1-\beta_2}$, $p_2 m_2 > 1$ and the coefficients c_i ($i = 1, 2$) are the roots of the systems of nonlinear algebraic equations:

$$\begin{cases} b_{11} c_1^{m_1-1} c_2^{\alpha_1} + b_{12} + b_{13} c_1^{\beta_1-1} = 0, \\ b_{21} c_2^{m_2-1} c_1^{\alpha_2} + b_{22} = 0. \end{cases}$$

(4) $p_1 < \frac{1}{1-\beta_1}$, $p_2 = \frac{1}{1-\beta_2}$, $p_1 m_1 > 1$ and the coefficients c_i ($i = 1, 2$) are the roots of the systems of nonlinear algebraic equations:

$$\begin{cases} b_{11} c_1^{m_1-1} c_2^{\alpha_1} + b_{12} = 0, \\ b_{21} c_2^{m_2-1} c_1^{\alpha_2} + b_{22} + b_{23} c_2^{\beta_2-1} = 0. \end{cases}$$

Proof. To simplify such auxiliary systems of equations, one can use the following transformations:

$$f(\xi) = \bar{f}(\xi) y_1(\eta), \quad \phi(\xi) = \bar{\phi}(\xi) y_2(\eta), \quad \eta = -\ln \left(a - \xi^{\frac{2n}{2-k}+2} \right), \quad (11)$$

where $\bar{f}(\xi) = \left(a - \xi^{\frac{2n}{2-k}+2} \right)^{p_1}$, $\bar{\phi}(\xi) = \left(a - \xi^{\frac{2n}{2-k}+2} \right)^{p_2}$ and $y_1(\eta)$, $y_2(\eta)$ – the new functions.

Now, let us study the asymptotic behavior of solutions of Eqs. (6) and (7) at $\xi \rightarrow a^{(\frac{2n}{2-k}+2)^{-1}}$.

After transformation (11), Eqs. (6) and (7) will take the following form:

$$y_{3-i}^{\alpha_i} \frac{d}{d\eta} (Ly_i) + a_{i1}(\eta) y_{3-i}^{\alpha_i} Ly_i + a_{i2}(\eta) \left(\frac{dy_i}{d\eta} + a_{i0}(\eta) y_i \right) + a_{i3}(\eta) y_i + a_{i4}(\eta) y_i^{\beta_i} = 0, \quad (i = 1, 2). \quad (12)$$

Here,

$$Ly_i = y_i^{m_i-1} \left(\frac{dy_i}{d\eta} + a_{i0}(\eta) y_i \right), \quad a_{i0}(\eta) = -p_i, \quad a_{i1}(\eta) = \frac{n+N}{n+2-k} \frac{e^{-\eta}}{a-e^{-\eta}} - p_i m_i + 1,$$

$$a_{i2}(\eta) = \frac{1}{(n+2-k)^2}, \quad a_{i3}(\eta) = -\frac{b_i}{(n+2-k)^2(1-\beta_i)} \frac{e^{-\eta}}{a-e^{-\eta}}, \quad a_{i4}(\eta) = \frac{b_i}{(n+2-k)^2} \frac{e^{-(1+p_i(\beta_i-1))\eta}}{a-e^{-\eta}},$$

$$i = 1, 2.$$

We assumed that $\xi \in [\xi_0, \xi_1]$, $0 < \xi_0 < \xi_1$, $\xi_1 = a^{\left(\frac{2n}{2-k}+2\right)^{-1}}$. Therefore, the function $\eta(\xi)$ has the following properties:

$$\eta'(\xi) > 0 \text{ at } \xi \in [\xi_0, \xi_1], \quad \eta_0 = \eta(\xi_0) > 0, \quad \lim_{\xi \rightarrow \xi_1} \eta(\xi) = +\infty.$$

The auxiliary system of equations (12) studied under the following limitations:

$$\lim_{\eta \rightarrow +\infty} a_{ij}(\eta) = a_{ij}^0 \quad (i = 1, 2; j = 0, 1, 2, 3, 4),$$

exist and are finite and nonzero, that is $0 < |a_{ij}^0| < +\infty$.

The solutions of the system (12), in a certain vicinity of $+\infty$ satisfy the inequalities:

$$y_i(\eta) > 0, \quad y_i' + a_{i0}(\eta)y_i \neq 0 \quad (i = 1, 2).$$

Assuming in Eqs. (12):

$$v_i(\eta) = y_i^{m_i-1} \left(\frac{dy_i}{d\eta} + a_{i0}(\eta) y_i \right), \quad i = 1, 2, \quad (13)$$

we obtain the identity:

$$v_i'(\eta) \equiv -a_{i1}(\eta)v_i(\eta) - a_{i2}(\eta)v_i(\eta)y_i^{1-m_i}y_{3-i}^{-\alpha_i} - a_{i3}(\eta)y_iy_{3-i}^{-\alpha_i} - a_{i4}(\eta)y_i^{\beta_i}y_{3-i}^{-\alpha_i}, \quad (i = 1, 2). \quad (14)$$

Furthermore, consider the functions:

$$g_i(\lambda_i, \eta) \equiv -a_{i1}(\eta)\lambda_i - a_{i2}(\eta)\lambda_iy_i^{1-m_i}y_{3-i}^{-\alpha_i} - a_{i3}(\eta)y_iy_{3-i}^{-\alpha_i} - a_{i4}(\eta)y_i^{\beta_i}y_{3-i}^{-\alpha_i}, \quad (15)$$

where $\lambda_i \in \mathbb{R}$, $(i = 1, 2)$.

Let us suppose $\frac{\alpha_1}{1-\beta_2} + \frac{m_1-1}{1-\beta_1} + 1 > 0$. Then,

$$\lim_{\eta \rightarrow +\infty} a_{i1}(\eta) = -p_i m_i + 1, \quad \lim_{\eta \rightarrow +\infty} a_{i3}(\eta) = 0, \quad \lim_{\eta \rightarrow +\infty} a_{i2}(\eta) = \frac{1}{(n+2-k)^2},$$

$$\lim_{\eta \rightarrow +\infty} a_{i4}(\eta) = \begin{cases} \frac{b_i}{a(n+2-k)^2}, & \text{at } 1 + p_i(\beta_i - 1) = 0, \\ 0, & \text{at } 1 + p_i(\beta_i - 1) > 0, \quad i = 1, 2. \end{cases}$$

and the functions $g_i(\lambda_i, \eta)$ ($i = 1, 2$) preserve sign on some interval $[\eta_1, +\infty) \subset [\eta_0, +\infty)$ for every fixed value λ_i ($i = 1, 2$).

Therefore, the functions $g_i(\lambda_i, \eta)$ ($i = 1, 2$) for all $\eta \in [\eta_1, +\infty)$ satisfies one of the inequalities:

$$g_i(\lambda_i, \eta) > 0 \quad \text{or} \quad g_i(\lambda_i, \eta) < 0 \quad (i = 1, 2). \quad (16)$$

Let us assume that for the functions $v_i(\eta)$ ($i = 1, 2$) the limit at $\eta \rightarrow +\infty$ does not exist. Consider the case, where one of the inequalities (16) are fulfilled. By force of the function's $v_i(\eta)$ ($i = 1, 2$) oscillation, the straight line $\bar{v}_i = \lambda_i$ ($i = 1, 2$) and its graph intersects an infinite number of times in the interval $[\eta_i, +\infty)$ ($i = 1, 2$). However, this is impossible, since the interval $[\eta_i, +\infty)$ ($i = 1, 2$) is justly one of the inequalities (16) and therefore, it follows from Eq. (15), that graph of the functions $v_i(\eta)$ ($i = 1, 2$) intersects the straight line $\bar{v}_i = \lambda_i$ ($i = 1, 2$) only once in the interval $[\eta_i, +\infty)$ ($i = 1, 2$). Therefore, for the functions $v_i(\eta)$ ($i = 1, 2$) the limit at $\eta \rightarrow +\infty$ exists.

Assuming the functions $v_i(\eta)$ ($i = 1, 2$) are defined in accordance with Eq. (13) and have a limit at $\eta \rightarrow +\infty$, one can show that $y_i'(\eta)$ ($i = 1, 2$) has a limit at $\eta \rightarrow +\infty$, which is equal to zero. Then,

$$v_i(\eta) = y_i^{m_i-1} \left(\frac{dy_i}{d\eta} + a_{i0}(\eta) y_i \right) = a_{i0}^0 (y_i^0)^{m_i} + o(1), \quad i = 1, 2 \text{ at } \eta \rightarrow +\infty$$

and by (14) derivative of functions $v_i(\eta)$ ($i = 1, 2$) has a limit at $\eta \rightarrow +\infty$, which obviously equals zero.

Consequently,

$$\lim_{\eta \rightarrow +\infty} \left(a_{i1}(\eta)v_i(\eta) + a_{i2}(\eta)v_i(\eta)y_i^{1-m_i}y_{3-i}^{-\alpha_i} + a_{i3}(\eta)y_iy_{3-i}^{-\alpha_i} + a_{i4}(\eta)y_i^{\beta_i}y_{3-i}^{-\alpha_i} \right) = 0 \quad (i = 1, 2).$$

It is easy to see that the system (12) has a solution $(y_1(\eta), y_2(\eta))$ with a finite non-zero limit at $\eta \rightarrow +\infty$ necessary to comply with the conditions of Theorem 2. Then the compactly supported solution of the problem (6)–(7) has an asymptotic of the form (10) as $\xi \rightarrow a\left(\frac{2n}{2-k}+2\right)^{-1}$.

Thus, the theorem is proved.

Corollary 1. *A weak solution of the problem (1)–(2) has the following asymptotic form:*

$$u_A(t, x) \approx c_1(T+t)^{\frac{1}{1-\beta_1}} \left(a - \left(\frac{|x|^{\frac{2-k}{2}}}{\tau\left(\frac{2n}{2-k}+2\right)^{-1}} \right)^{\frac{2n}{2-k}+2} \right)^{p_1},$$

$$v_A(t, x) \approx c_2(T+t)^{\frac{1}{1-\beta_2}} \left(a - \left(\frac{|x|^{\frac{2-k}{2}}}{\tau\left(\frac{2n}{2-k}+2\right)^{-1}} \right)^{\frac{2n}{2-k}+2} \right)^{p_2},$$

at $|x| \rightarrow a^{\frac{1}{2-k+n}} \tau^{\frac{1}{n+2-k}}$, where constants c_1, c_2, p_1, p_2 are defined above.

5. Fast diffusion case ($p_i < 0, i = 1, 2$). Explicit estimates of the solution of problem (1)–(2)

Suppose that for system of equations (6) the following conditions are fulfilled:

$$f'(0) = 0, \phi'(0) = 0, f(\infty) = 0, \phi(\infty) = 0. \quad (17)$$

Then, the functions

$$\bar{f}(\xi) = A_1 \left(a + \xi^{\frac{2n}{2-k}+2} \right)^{p_1}, \quad \bar{\phi}(\xi) = A_2 \left(a + \xi^{\frac{2n}{2-k}+2} \right)^{p_2}, \quad p_i = \frac{m_{3-i} - 1 - \alpha_i}{(m_1 - 1)(m_2 - 1) - \alpha_1 \alpha_2}, \quad i = 1, 2,$$

satisfy Eq. (17), where $a > 0$.

Theorem 3. *Let $p_i < 0, \beta_i < 1, \frac{p_i}{1-p_i m_i} \frac{n+N}{n+2-k} - \frac{b_i}{1-\beta_i} + b_i a^{p_i(\beta_i-1)} \geq 0,$*

$$A_i^{m_i-1} A_{3-i}^{\alpha_i} = \frac{1}{(1-p_i m_i)(n+2-k)^2}, \quad i = 1, 2, \quad u_0(x) \geq u_-(0, x), \quad v_0(x) \geq v_-(0, x), \quad x \in \mathbb{R}^N.$$

Then, for problem (1)–(2), there is a global solution in Q and for it, the following estimation is correct: $u(t, x) \geq u_-(t, x), v(t, x) \geq v_-(t, x), x \in \mathbb{R},$ where

$$u_-(t, x) = \bar{u}(t) \bar{f}(\xi), \quad v_-(t, x) = \bar{v}(t) \bar{\phi}(\xi). \quad (18)$$

Theorem 3 is proved by the solution comparison method similar to the proof of Theorem 1.

Furthermore, we introduce the following notations:

$$b_{i4} = p_i \left(\frac{n+N}{n+2-k} + p_i m_i - 1 \right), \quad b_{i5} = \frac{p_i}{(n+2-k)^2} - \frac{b_i}{1-\beta_i(n+2-k)^2}, \quad i = 1, 2.$$

Also, we assume $\frac{\alpha_1}{1-\beta_2} + \frac{m_1-1}{1-\beta_1} = \frac{\alpha_2}{1-\beta_1} + \frac{m_2-1}{1-\beta_2}$. Then the following theorem is valid:

Theorem 4. *Let $\frac{\alpha_1}{1-\beta_2} + \frac{m_1-1}{1-\beta_1} + 1 > 0, \beta_i > 1, p_i < 0, i = 1, 2.$ Then, vanishing at infinity, the solution of the problem (6), (17) at $\xi \rightarrow \infty$ has an asymptotic:*

$$f(\xi) = c_3 \left(a + \xi^{\frac{2n}{2-k}+2} \right)^{p_1}, \quad \phi(\xi) = c_4 \left(a + \xi^{\frac{2n}{2-k}+2} \right)^{p_2},$$

where the coefficients c_i ($i = 3, 4$) are the roots of systems of the nonlinear algebraic equations:

$$b_{i4} c_{i+2}^{m_i-1} c_{5-i}^{\alpha_i} + b_{i5} = 0, \quad i = 1, 2.$$

The proof of the Theorem 4 is similar to that of the Theorem 2.

Corollary 2. *A weak solution of the problem (1)–(2) has the following asymptotic:*

$$u_A(t, x) \approx c_3(T+t)^{\frac{1}{1-\beta_1}} \left(a + \left(\frac{|x|^{\frac{2-k}{2}}}{\tau\left(\frac{2n}{2-k}+2\right)^{-1}} \right)^{\frac{2n}{2-k}+2} \right)^{p_1},$$

$$v_A(t, x) \approx c_4(T+t)^{\frac{1}{1-\beta_2}} \left(a + \left(\frac{|x|^{\frac{2-k}{2}}}{\tau\left(\frac{2n}{2-k}+2\right)^{-1}} \right)^{\frac{2n}{2-k}+2} \right)^{p_2},$$

at $|x| \tau^{-\frac{1}{n+2-k}} \rightarrow +\infty$, where the constants c_3, c_4, p_1, p_2 are defined above.

6. Numerical analysis of solutions

We note that due to the non-uniqueness of solutions, many different cases arise in the numerical study of problem (1)–(2). It is important to choose a proper initial approximation that preserves its nonlinearity properties. On the basis of the above qualitative studies, we produced numerical calculations. The numerical results show quick convergence of the iterative process to the solution of the Cauchy problem (1)–(2), due to the successful choice of the initial approximation. Below, some numerical experiment results for different numerical parameter values are presented.

Results of the numerical experiments and graphs show that the self-similar solutions are very appropriate approximations. Fig. 1 shows a compactly supported solution of the problem (1)–(2). Figs. 2 and 3 show the properties of the solution for problem (1)–(2), vanishing at infinity.

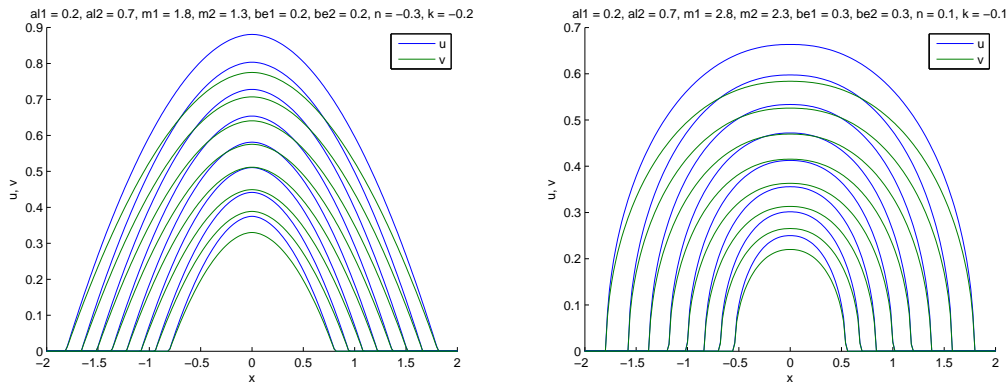


FIG. 1. Slow diffusion case $p_i > 0, i = 1, 2: n < 0, k < 0$ and $n > 0, k < 0$

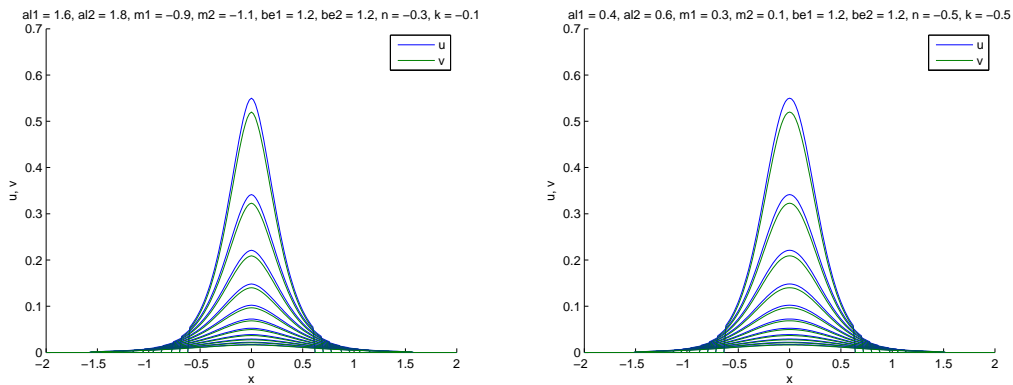


FIG. 2. Fast diffusion case $p_i < 0, i = 1, 2: n - k < 0$ and $n - k = 0$

7. Conclusions

The Zeldovich–Barenblatt type solution for the cross diffusive system is obtained. The finite speed properties of the Cauchy problem for a cross-diffusion parabolic system with a source are studied using comparison method. The asymptotic behavior of self-similar solutions both for slow and fast diffusion cases are analyzed. It is shown that the coefficients in the main term of the asymptotic of the solution satisfy a system of nonlinear algebraic equations.

Results of the computational experiments show, that the self-similar solutions are very appropriate approximations and the iterative method based on the Picard method is effective for the numerical solution of nonlinear problems and leads to nonlinear effects if we use as initial approximation the solutions of self similar equations constructed by the nonlinear splitting and by the standard equation methods [9, 10, 15].

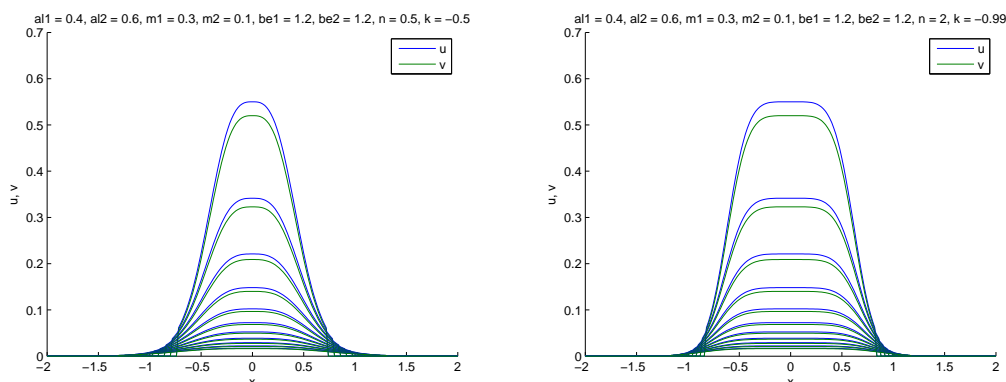


FIG. 3. Fast diffusion case $p_i < 0, i = 1, 2: n - k = 1$ and $n - k > 1$

References

- [1] Samarskii A.A., Galaktionov V.A., Kurdyumov S.P., Mikhailov A.P. *Blow-up in Quasilinear Parabolic Equations*. Walter de Grueter, Berlin, 1995, 4, 535 p.
- [2] Wang M.X., Xie C.H. A degenerate strongly coupled quasilinear parabolic system not in divergence form. *Z. Angew. Math. Phys.*, 2004, **55**, P. 741–755.
- [3] Haihua Lu. Global existence and blow-up analysis for some degenerate and quasilinear parabolic systems. *Electronic Journal of Qualitative Theory of Differential Equations*, 2009, **49**, P. 1–14.
- [4] Zhou W., Yao Z. Cauchy problem for a degenerate parabolic equation with non-divergence form. *Acta Mathematica Scientia*, 2010, **30** (5), P. 1679–1686.
- [5] Chunhua J., Jingxue Y. Self-similar solutions for a class of non-divergence form equations. *Nonlinear Differ. Equ. Appl. Nooda*, 2013, **20** (3), P. 873–893.
- [6] Raimbekov J.R. The Properties of the Solutions for Cauchy Problem of Nonlinear Parabolic Equations in Non-Divergent Form with Density. *Journal of Siberian Federal University. Mathematics and Physics*, 2015, **8** (2), P. 192–200.
- [7] Gao Y., Meng Q., Guo Y. Study of properties of solutions for quasilinear parabolic systems. *MATEC Web of Conferences*, 2016, **61** (1), P. 1–4.
- [8] Zhou Sh., Zheng S. Asymptotic behavior of solutions to a degenerate parabolic equation with a gradient source term. *Asymptotic Analysis*, 2015, **91** (2), P. 91–102.
- [9] Aripov M., Sadullaeva Sh.A. Qualitative Properties of Solutions of a Doubly Nonlinear Reaction-Diffusion System with a Source. *Journal of Applied Mathematics and Physics*, 2015, **3**, P. 1090–1099.
- [10] Aripov M., Sadullaeva Sh.A. An asymptotic analysis of a self-similar solution for the double nonlinear reaction-diffusion system. *Nanosystems: physics, chemistry, mathematics*, 2015, **6** (6), P. 1–10.
- [11] Aripov M., Rakhmonov Z. Estimates and Asymptotic of Self-similar Solutions to a Nonlinear Filtration Problem with Variable Density and Nonlocal Boundary Conditions. *Universal Journal of Computational Mathematics*, 2016, **4** (1), P. 1–5.
- [12] Sadullaeva Sh.A. Numerical Investigation of Solutions to A Reaction-Diffusion System with Variable Density. *Journal of Siberian Federal University. Mathematics and Physics*, 2016, **9** (1), P. 90–101.
- [13] Martynenko A.V., Tedeev A.F. The Cauchy Problem for a Quasilinear Parabolic Equation with a Source and Inhomogeneous Density. *Computational Mathematics and Mathematical Physics*, 2007, **47**, P. 238–248.
- [14] Martynenko A.V., Shramenko V.N. Estimate of solutions of the Cauchy Problem near the Time of Exacerbation for a Quasilinear Parabolic Equation with a Source and a Variable Density. *Nonlinear Boundary Value Problems*, 2010, **20**, P. 104–115.
- [15] Aripov M. *Standard Equation's Methods for Solutions to Nonlinear problems*. Fan, Tashkent, 1988, 138 p.

Absorbing boundary conditions for Schrödinger equation in a time-dependent interval

O. Karpova^{1,2}, K. Sabirov^{1,3}, D. Otajanov¹, A. Ruzmetov¹, A. A. Saidov¹

¹Turin Polytechnic University in Tashkent,
17 Kichik Halka Yuli, Tashkent, 100095, Uzbekistan

²National University of Uzbekistan, Tashkent, Uzbekistan

³Tashkent University of Information Technologies, Tashkent, Uzbekistan
ola_july@mail.ru

PACS 02.60.Lj; 02.70.Bf

DOI 10.17586/2220-8054-2017-8-1-13-19

We consider the reflection-transmission of the Gaussian wave packet through the moving wall with absorbing boundary conditions based on the time dependent one-dimensional Schrödinger equation. The reflection coefficient is calculated for the case when the walls are fixed, and probability density is calculated for the case when the wall is moving linearly.

Keywords: absorbing boundary conditions, Gaussian wave packet, one-dimensional Schrödinger equation.

Received: 10 August 2016

Revised: 5 September 2016

1. Introduction

Absorbing boundary conditions (ABC) for different wave equations have attracted much attention in different practically important contexts (see, e.g., papers [1–10] for review). Such boundary conditions describe absorption of particles and waves in their transition from one domain to another one. From the physical viewpoint particle absorption can occur in dissipative media. In addition, such type of boundary condition appears in reflectionless transmission of particles (waves) through the boundary of a given domain. Therefore one uses similar terminology for the boundary conditions of both types of processes, calling them absorbing or transparent boundary conditions. Strict mathematical treatment of ABC for different wave equations, including quantum mechanical Schrödinger equation can be found in the Refs. [11–16]. For both processes the boundary conditions can be derived by factorization of the differential operator corresponding to a wave equation which in general lead to complicated equations for the boundary conditions. The explicit form of such boundary conditions is much more complicated than those of Dirichlet, Neumann and Robin conditions.

For absorbing boundary conditions the wave equation cannot be solved analytically and always requires using numerical methods. Depending on the type of the wave equation, they require different discretization schemes, which vary also for the process types. Finding an effective numerical scheme is a complicated task, especially, for quantum mechanical wave equations. Therefore, in some cases it is reasonable to use approximate methods enabling simplification of the numerical solution. One such method, based on the use of dispersion relation was introduced in the Ref. [11] for solving time-dependent Schrödinger equation with ABC on a finite interval. Later, it was improved by Kuska [11] with the use of alternative approximation for dispersion relation. In this paper we extended the results of Kuska to the case of moving boundaries. In particular, using the approach developed in the Ref. [12], we reduce time-dependent Schrödinger equation with moving boundary conditions into that of fixed ones. Imposing the ABC for the problem with moving boundaries, we derive the corresponding boundary conditions for the Schrödinger equation on a finite interval with unit length which is then solved numerically.

2. Absorbing boundary conditions for fixed interval

Here, following the Refs. [10, 11] we briefly recall derivation of the approximate ABC for one dimensional Schrödinger equation on a finite interval. Consider the one-dimensional time-dependent Schrödinger equation:

$$i\hbar \frac{\partial \psi}{\partial t}(x, t) = -\frac{\hbar^2}{2m} \frac{\partial^2 \psi}{\partial x^2}(x, t) + V(x) \psi(x, t), \quad (1)$$

describing the motion of a quantum particle with the mass m in the interval $x \in (-\infty, +\infty)$ under the influence of the potential V . Taking a plane wave of the form:

$$\psi(x, t) = \exp[-i(\omega t - kx)], \quad (2)$$

from Eqs. (1) and (2) one gets the dispersion relation for the wave vector k [11]:

$$\hbar^2 k^2 = 2m [\hbar\omega - V]. \quad (3)$$

This relation can be solved for k and yields (in the units $m = \hbar = 1$):

$$k = \pm \sqrt{2[\omega - V]}, \quad (4)$$

where the plus sign describes waves moving to $x = +\infty$ and the minus sign means waves moving to $x = -\infty$. The left boundary has to be transparent for waves travelling to the left and the right boundary must be transparent for those heading right.

The square root function can be approximated using the rational function approximation method following [11]:

$$\sqrt{z - z_0} \approx \sqrt{z_0} \frac{1 + 3z/z_0}{3 + z/z_0}. \quad (5)$$

With the approximation (5) for the square root in the dispersion relation (4) one gets:

$$k = \pm k_0 \sqrt{\frac{2(\omega - V)}{k_0^2}} \approx \pm k_0 \frac{1 + 3z}{3 + z}, \quad (6)$$

with

$$z = \frac{2(\omega - V)}{k_0^2}.$$

We write (6) as:

$$k(3 + z) \approx \pm k_0(1 + 3z).$$

Putting expression for z into the above equation, one gets:

$$k \left(3 \frac{k_0^2}{2} + \omega - V \right) \approx \pm k_0 \left(\frac{k_0^2}{2} + 3\omega - 3V \right).$$

By using the correspondence between quantities k and ω with their operator definitions:

$$k \Leftrightarrow -i \frac{\partial}{\partial x} \quad \text{and} \quad \omega \Leftrightarrow i \frac{\partial}{\partial t},$$

we obtain the following partial differential equation for the ABC:

$$-i \left(3 \frac{k_0^2}{2} - V \right) \frac{\partial \psi}{\partial x}(x, t) + \frac{\partial^2 \psi}{\partial t \partial x}(x, t) = \pm k_0 \left(\frac{k_0^2}{2} - 3V \right) \psi(x, t) \pm 3ik_0 \frac{\partial \psi}{\partial t}(x, t). \quad (7)$$

The plus sign in (7) corresponds to the boundary conditions for the right side wall of the interval, while the minus sign in (7) corresponds to the boundary conditions for the left wall of the interval.

2.1. Numerical results

For the numerical experiments, we consider the transport of Gaussian wave packet:

$$\psi(x, 0) = \sqrt{\pi\sigma} \exp\left(-\frac{(x - \xi)^2}{2\sigma}\right) \exp(ik_0 x), \quad (8)$$

through the wall located at the right side. We consider that the particle is initially located near the right wall ($\xi = 3L/4$) in order to minimize the calculation time of the reflection-transmission process through this wall. The discrete one dimensional space is chosen between $-2L < x < 4L$, which is large enough to satisfy the normalization condition:

$$\int_{-\infty}^{+\infty} \psi^*(x, t) \psi(x, t) dx = 1, \quad (9)$$

during numerical computation.

In Fig. 1, the evolution of the Gaussian wave packet described by the time-dependent Schrödinger equation with ABC given by Eq. (7) is presented. As it can be seen from this plot, for given initial conditions of the Gaussian wave packet, the reflectionless transmission through the boundary of the domain occurs.

In Fig. 2, we plot the dependence of the reflection coefficient on the initial mean wave vector of the wave packet. As it can be seen from the plot, there is an energy range for which the reflection coefficient becomes minimal. For these energies the wall becomes almost transparent. In order to calculate the reflection coefficient, R , we follow the evolution of the initially normalized probability of the quantum particle (wave packet) inside the interval ($x \in [0, L]$) and continue this until that moment when the scattering starts through the domain wall

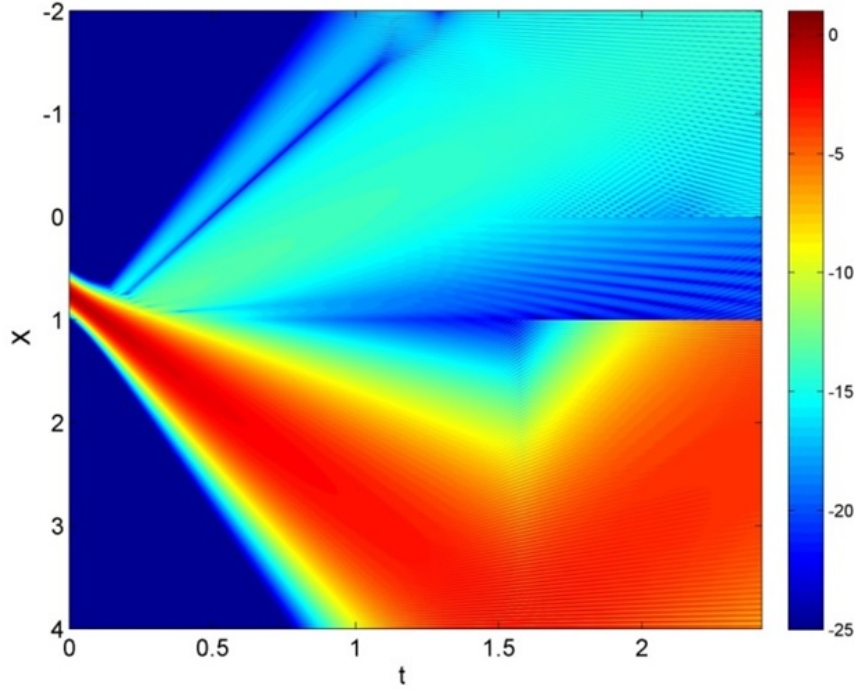


FIG. 1. (Color online) The spatiotemporal evolution of the probability density in logarithmic scale for the Gaussian wave packet described by Eq. (1), for which absorbing boundary conditions (7) are imposed. Initial wave packet width $\sigma = 0.05L$, the length of the interval $L = 1$, and the initial position of quantum particle (wave packet) is $\xi = 3L/4$. Numerical calculations are carried out with the discretization parameters: one dimensional space grid size $\Delta x = 10^{-3}$ and time step size $\Delta t = 10^{-4}$. The mean value of the wave vector of the initial wave packet is $k_0 = 25$.

(at $x = L$) with ABC, and to the time when the scattering (reflection and transmission) processes are totally completed. Normalization condition implies that the summation of the reflection and transmission coefficient must be equal to 1, until the domain (discretized 1D space) is taken long enough ($-2L < x < 4L$) where the tail of probability density of the wave packet will not reach to the edge of the domain (at $x = 4L$) due to dispersion during simulation.

For the normalized wave function by Eq. (9), one can easily track of the transmitted quantum particle (wave packet) position by computing the following integral:

$$\int_L^{4L} \psi^*(x, t)x\psi(x, t)dx, \quad (10)$$

which is necessary to verify that the transmission was completed totally.

Easy quantification of the wave packet reflection through the ABC can be done by checking the probability of the wave packet inside the domain $-2L < x < 4L$. During the transmission process, the integral (10) will be increasing and when it reaches to some value and stabilizes at this value, one can be sure that the process is completed.

3. Absorbing boundary conditions for time-dependent interval

Here, we extend the treatment of the previous section to the case of moving boundaries, by considering time-dependent interval with one moving end which is given as:

$$x = 0 \quad \text{and} \quad x = L(t) . \quad (11)$$

Earlier, the Schrödinger equation with time-dependent boundary conditions given in a one-dimensional box has been studied by many authors (see, e.g., [12, 17] and references therein) The Schrödinger equation with time-dependent boundary conditions is an ill posed problem unless the moving boundaries are not mapped onto fixed ones [12, 17]. This can be done by introducing a new coordinate as [12, 17]:

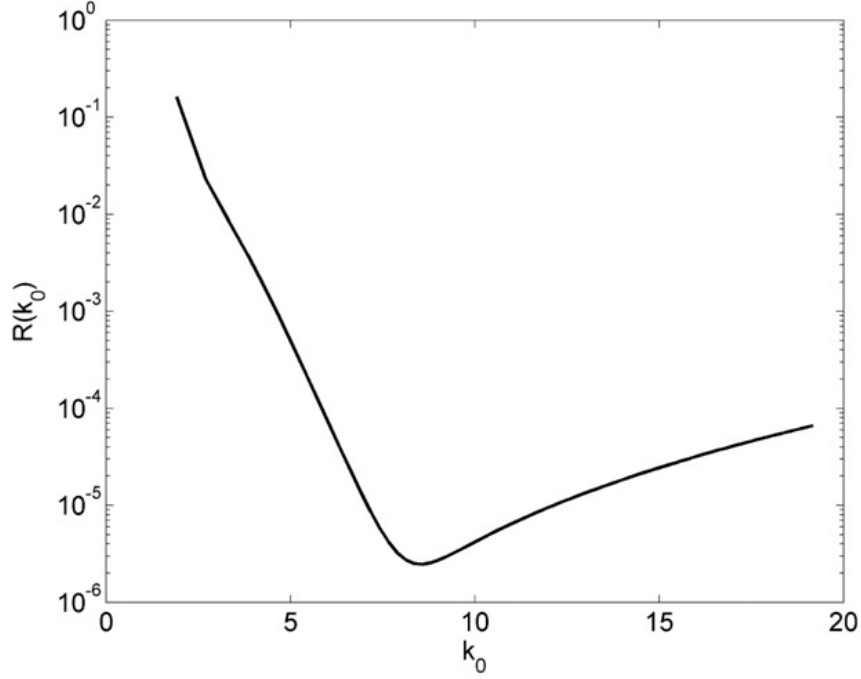


FIG. 2. Dependence of the reflection coefficient on the initial wave vector of wave packet is computed. Initial wave packet width $\sigma = 0.05L$, the length of the interval $L = 1$ and the initial position of quantum particle (wave packet) $\xi = 3L/4$. Numerical calculations are carried out with the discretization parameters: one dimensional space grid size $\Delta x = 10^{-3}$ and time step size $\Delta t = 10^{-4}$.

$$y = \frac{x}{L(t)}, \quad (12)$$

which leads to Eq. (1) in the following form ($V = 0$):

$$i \frac{\partial \psi(y, t)}{\partial t} = -\frac{1}{2L^2} \frac{\partial^2 \psi(y, t)}{\partial y^2} + i \frac{\dot{L}}{L} y \frac{\partial \psi(y, t)}{\partial t}, \quad (13)$$

with

$$\dot{L} = \frac{dL}{dt}.$$

And for the partial differential equation (13), one can apply the new boundary conditions at $y = 0$ and $y = 1$. The normalization condition for the wave function $\psi(y, t)$ is given by:

$$\int_{-\infty}^{+\infty} \psi^*(y, t) \psi(y, t) dy = \text{const.} \quad (14)$$

To construct ABC, the boundary should be almost transparent for a plane wave of the form:

$$\psi(y, t) = \exp(-i\omega t + ikLy). \quad (15)$$

Then, from Eqs. (15) and (13), one gets the dispersion relation for the wave vector k :

$$\omega = \frac{k^2}{2}.$$

This relation can be solved for k and yields:

$$k^2 - 2\omega = 0,$$

with the solution:

$$k_{1,2} = \pm \sqrt{2\omega}.$$

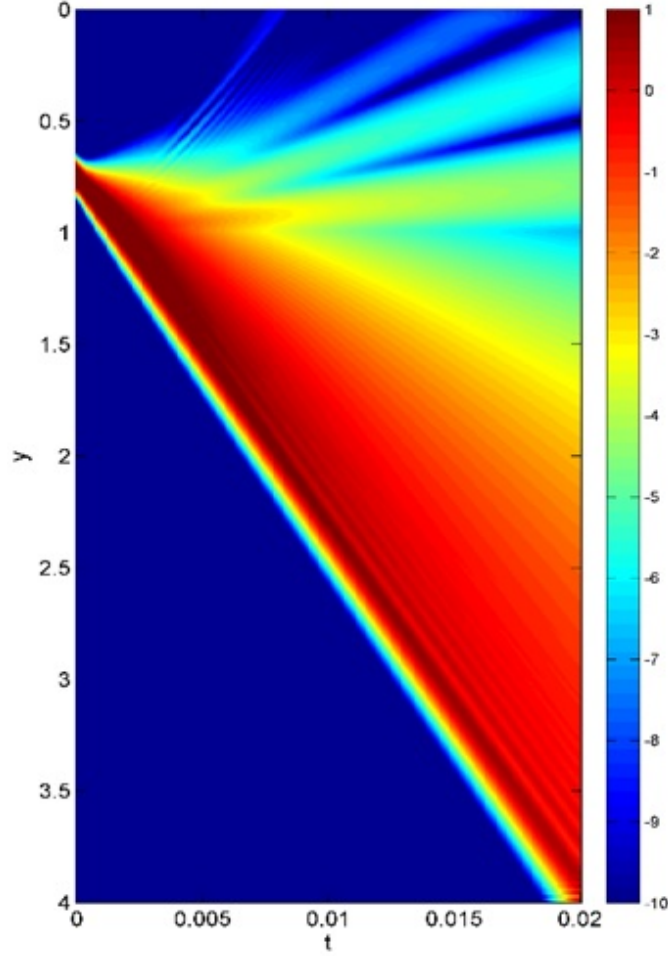


FIG. 3. The spatiotemporal evolution of the probability density in logarithmic scale for the Gaussian wave packet described by Eq. (13) for linearly moving (with velocity $b = 10^{-6}$) boundary given by Eq. (17). The mean value of wave vector of the initial wave packet $k_0 = 70$. Initial value of the wave packet width $\sigma = 0.001L_0$, the initial length of the interval $L_0 = 1$ and the initial position of quantum particle (wave packet) at $\xi = 3L_0/4$. Numerical calculations are carried out with the discretization parameters: one dimensional fixed space grid size $\Delta y = 10^{-3}$, and time step size $\Delta t = 10^{-4}$.

Using the rational function approximation as in the above equation (5) we write:

$$k = \pm k_0 \sqrt{\frac{2\omega}{k_0^2}} \approx \pm k_0 \frac{1 + 3z}{3 + z},$$

with

$$z = \frac{2\omega}{k_0^2}.$$

Replacing k and ω by corresponding differential operators as:

$$k \Leftrightarrow -i \frac{\partial}{\partial y}, \quad \omega \Leftrightarrow i \frac{\partial}{\partial t},$$

we obtain adsorbing boundary conditions the same as in the case of a fixed interval Eq. (7):

$$-\frac{3ik_0^2}{2} \frac{\partial}{\partial y} \psi(y, t) + \frac{\partial^2}{\partial t \partial y} \psi(y, t) = \pm \frac{k_0^3}{2} \psi(y, t) \pm 3ik_0 \frac{\partial}{\partial t} \psi(y, t). \quad (16)$$

Here, the equation with the positive sign corresponds to the ABC at the right boundary, while the negative sign corresponds to the ABC at the left boundary.

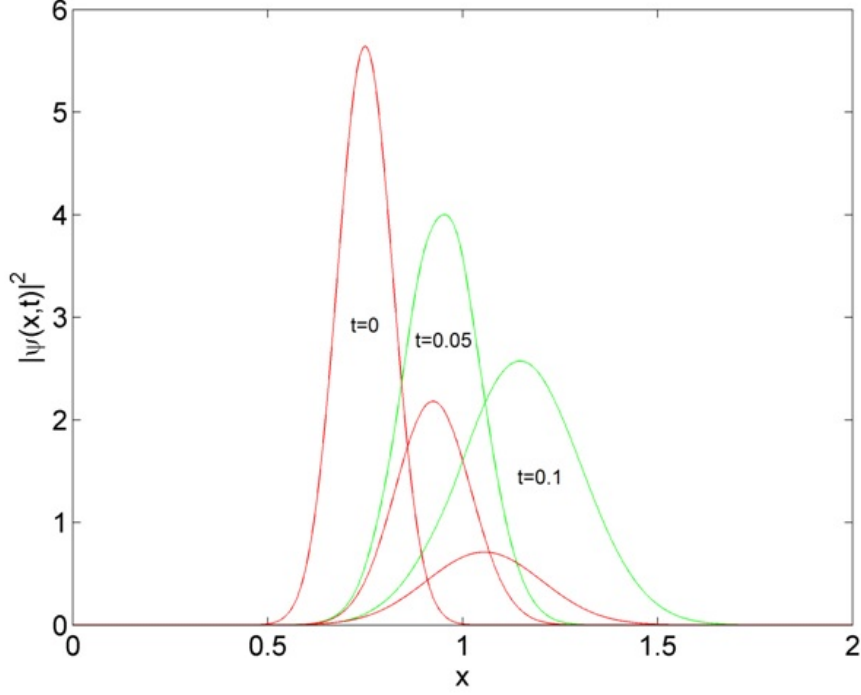


FIG. 4. (Color online) Profile of the Gaussian WP at different time moments for fixed (green) and for time-dependent (red) intervals. The parameters of the packet are chosen as $\xi = 3/4$; $\sigma = 0.001$; $k_0 = 20$.

Furthermore, using the following discretization scheme [11]:

$$\begin{aligned}\psi(y, t) &\approx \frac{1}{4} (\psi_{j+1}^{n+1} + \psi_j^{n+1} + \psi_{j+1}^n + \psi_j^n), \\ \frac{\partial \psi}{\partial y}(y, t) &\approx \frac{1}{2\Delta y} (\psi_{j+1}^{n+1} - \psi_j^{n+1} + \psi_{j+1}^n - \psi_j^n), \\ \frac{\partial \psi}{\partial t}(y, t) &\approx \frac{1}{2\Delta t} (\psi_{j+1}^{n+1} + \psi_j^{n+1} - \psi_{j+1}^n - \psi_j^n), \\ \frac{\partial^2 \psi}{\partial t \partial y}(y, t) &\approx \frac{1}{\Delta y \Delta t} (\psi_{j+1}^{n+1} - \psi_j^{n+1} - \psi_{j+1}^n + \psi_j^n).\end{aligned}$$

with

$$\psi_j^n = \psi(y_j, t_n).$$

We have the following discretization for the boundary condition:

$$\begin{aligned}&-3ik_0^2 \frac{1}{2\Delta y} (\psi_{j+1}^{n+1} - \psi_j^{n+1} + \psi_{j+1}^n - \psi_j^n) + \frac{1}{\Delta y \Delta t} (\psi_{j+1}^{n+1} - \psi_j^{n+1} - \psi_{j+1}^n + \psi_j^n) \\ &= \pm k_0^3 \frac{1}{4} (\psi_{j+1}^{n+1} + \psi_j^{n+1} + \psi_{j+1}^n + \psi_j^n) \pm 3ik_0 \frac{1}{2\Delta t} (\psi_{j+1}^{n+1} + \psi_j^{n+1} - \psi_{j+1}^n - \psi_j^n)\end{aligned}$$

or

$$\begin{cases} b_2 \psi_j^{n+1} + b_1 \psi_{j+1}^{n+1} = b_4 \psi_j^n + b_3 \psi_{j+1}^n, & \text{for } y = 0, (j = 1), \\ b_1 \psi_j^{n+1} + b_2 \psi_{j+1}^{n+1} = b_3 \psi_j^n + b_4 \psi_{j+1}^n, & \text{for } y = 1, (j = y\Delta y), \end{cases}$$

where the coefficients are given:

$$\begin{aligned}b_1 &= -\frac{3ik_0^2}{2\Delta y} + \frac{1}{\Delta y \Delta t} + \frac{k_0^3}{4} + \frac{3ik_0}{2\Delta t}, & b_2 &= \frac{3ik_0^2}{2\Delta y} - \frac{1}{\Delta y \Delta t} + \frac{k_0^3}{4} + \frac{3ik_0}{2\Delta t}, \\ b_3 &= -\frac{3ik_0^2}{2\Delta y} - \frac{1}{\Delta y \Delta t} + \frac{k_0^3}{4} - \frac{3ik_0}{2\Delta t}, & b_4 &= \frac{3ik_0^2}{2\Delta y} + \frac{1}{\Delta y \Delta t} + \frac{k_0^3}{4} - \frac{3ik_0}{2\Delta t}.\end{aligned}$$

In Fig. 3, the evolution of the Gaussian wave packet described by Eq. (13) is presented for the linearly moving boundary given by:

$$L(t) = L_0 + bt. \quad (17)$$

The plot shows reflectionless transmission of the packet through the boundary of the interval.

Figure 4 presents the profile at the GWP at different time moments both for constant and time-dependent intervals. The initial position of the packet is chosen as $\xi = 3/4$. As is shown in the plot, in case of time-dependent BCs dispersion of the packet occurs more quickly than that for the fixed interval.

4. Conclusions

Thus, we have formulated and solved the problem of absorbing boundary conditions for the time-dependent interval by considering time-dependent Schrödinger equation. The time-dependence of the boundary is taken as linear. We found that unlike the case of fixed boundaries, for time-dependent absorbing boundary conditions provide more extensive (reflectionless) transmission of the particle through the domain boundaries and during considerably shorter time. The results of this work can be useful for modeling of quantum systems touching to absorbing or transparent media.

References

- [1] Goldberg A., Schey H.M. and Schwartz J.I. Computer-generated motion pictures of one-dimensional quantum-mechanical transmission and reflection phenomena. *Am. J. Phys.*, 1967, **35**(3), P. 177.
- [2] Galbraith I., Ching Y.S. and Abraham E. Two dimensional time dependent quantum mechanical scattering event. *Am. J. Phys.*, 1984, **52**(1), P.60–68.
- [3] Frenslley W. Boundary conditions for open quantum systems driven far from equilibrium. *Rev. Mod. Phys.*, 1990, **62**(3), P. 745.
- [4] Engquist B. and Majda A. Absorbing boundary conditions for numerical simulation of waves. *Math. Comput.*, 1977, **31**(139), P. 629–651.
- [5] Givoli D. Non-reflecting boundary conditions. *J. Comp. Phys.*, 1991, **94**(1), P. 1–29.
- [6] Kosloff R. and Kosloff D. Absorbing boundaries for wave propagation problems. *J. Comp. Phys.*, 1986, **63**(2), P. 363–376.
- [7] Antoine X. et al. Absorbing boundary conditions for relativistic quantum mechanics equations. *J. Comput. Phys.*, 2014, **277**, P. 268–304.
- [8] Antoine X. et al. Absorbing boundary conditions for the one-dimensional Schrödinger equation with an exterior repulsive potential. *J. Comput. Phys.*, 2009, **228**(2), P. 312–335.
- [9] Arnold A. Numerically absorbing boundary conditions for quantum evolution equations. *VLSI design*, 1998, **6**(1-4), P. 313–319.
- [10] Shibata T. Absorbing boundary conditions for the finite-difference time-domain calculation of the one-dimensional Schrödinger equation. *Phys. Rev. B*, 1991, **43**(11), P. 6760.
- [11] Kuska J.-P. Absorbing boundary conditions for the Schrödinger equation on finite intervals. *Phys. Rev. B*, 1992, **46**(11), P. 5000.
- [12] Makowski A.J. and Dembiński S.T. Exactly solvable models with time-dependent boundary conditions. *Phys. Lett. A*, 1991, **154**(5), P. 217–220.
- [13] Crank J. and Nicolson P. A practical method for numerical evaluation of solutions of partial differential equations of the heat-conduction type. *Advances in Comput. Math.*, 1996, **6**(1), P. 207–226.
- [14] Dubeibe F.L. Solving the time-dependent Schrödinger equation with absorbing boundary conditions and source terms in Mathematica 6.0. *Int. J. Mod. Phys. C*, 2010, **21**(14), P. 1391–1406.
- [15] Jiang Sh. and Greengard L. Fast evaluation of nonreflecting boundary conditions for the Schrödinger equation in one dimension. *Computers & Mathematics with Applications*, 2004, **47**(6), P. 955–966.
- [16] Neuhauer D. and Baer M. The time-dependent Schrödinger equation: Application of absorbing boundary conditions. *J. Chem. Phys.*, 1989, **90**(11), P. 4351–4355.
- [17] Nakamura K. et al. Ideal quantum gas in an expanding cavity: Nature of nonadiabatic force. *Phys. Rev. E*, 2011, **83**(4), P. 041133.

On a non-separable quantum many-particle system on the half-line

J. Kerner, T. Mühlenbruch

Department of Mathematics and Computer Science, FernUniversität in Hagen, 58084 Hagen, Germany

Joachim.Kerner@fernuni-hagen.de, Tobias.Muehlenbruch@fernuni-hagen.de

PACS 03.65.Db, 73.21.Hb, 05.45.Ac

DOI 10.17586/2220-8054-2017-8-1-20-23

In this paper we will report on a one-dimensional, non-separable quantum many-particle system. It consists of two (distinguishable) particles moving on the half-line \mathbb{R}_+ being subjected to two different kinds of two-particle interactions: singular many-particle interactions localized at the origin and a binding-potential leading to a molecular-like state. We will formulate the model precisely, obtaining a well-defined self-adjoint operator (the Hamiltonian for our system) and elaborate on its spectral properties. In addition, we will present possible directions for future research.

Keywords: singular many-particle interactions, molecule, spectral analysis, quantum graph.

Received: 6 June 2016

Revised: 5 August 2016

1. Introduction

The origin of the model presented in this paper is found in an investigation of many-particle quantum chaos using (compact) quantum graphs [1, 2]. Since the motion of a single particle on a quantum graph with complex topology becomes chaotic through the scattering of the particle in the vertices of the graph [3], the idea was to introduce many-particle interactions which are present only whenever at least one particle hits a vertex. In this way the scattering properties and hence the dynamics of the system are affected in a way to encode many-particle correlations which then enables one to study many-particle quantum chaos.

The one-particle configuration space of the model presented in this paper is the half-line $\mathbb{R}_+ = [0, \infty)$ and hence a simple, non-compact quantum graph (as we will see later, it is the non-compactness of the graph which generates a rich spectral theory). Furthermore, the Hamiltonian can be formally written as:

$$H = -\frac{\partial^2}{\partial x^2} - \frac{\partial^2}{\partial y^2} + v(x, y) [\delta(x) + \delta(y)] + v_b(|x - y|), \quad (1.1)$$

$v : \mathbb{R}^2 \rightarrow \mathbb{R}$ being symmetric and $v_b : \mathbb{R}_+ \rightarrow [0, \infty]$ being the binding-potential leading to a molecular-like state. We note that the original model as presented in [4] was formulated without binding-potential. It was later added in [5], connecting the model to the one discussed in [6].

The nature of the singular two-particle interactions considered can be directly understood from the formal expression (1.1) and the properties of the δ -distribution. Indeed, since the δ -distribution is supported on the origin only, these two-particle interactions are present only whenever at least one of the particles is situated at the origin. Quite surprisingly, although one is tempted to regard such singular interactions as a small perturbation only, we will see that this is not always the case. Indeed, as a main result, it was shown in [5] that the singular interactions (given they are repulsive and strong enough) lead to a destruction of the ground state of the molecule and hence destabilize the system.

Finally, we would like to mention that the model presented in this paper has various possible applications in different areas of theoretical and applied physics. On the one hand, it might serve as a toy-model to describe electrons moving in composite wires [7] while, on the other hand, it is of theoretical interest by being an approachable many-particle model. In addition, it provides an example of a non-separable quantum many-particle model which are, despite their importance, otherwise only rarely discussed [8, 9].

2. The model

As in [5] the binding-potential v_b is chosen to be:

$$v_b(|x - y|) := \begin{cases} 0 & \text{if } |x - y| \leq d, \\ +\infty & \text{else,} \end{cases} \quad (2.1)$$

$0 < d \leq \infty$ characterising the ‘size’ of the molecule. Due to the presence of the binding-potential, the two-particle configuration space is reduced from \mathbb{R}_+^2 to Ω which is given by:

$$\Omega := \{(x, y) \in \mathbb{R}_+^2 \mid |x - y| \leq d\}. \quad (2.2)$$

For later purposes, we also define:

$$\partial\Omega_\sigma := \{(x, y) \in \Omega \mid x = 0 \vee y = 0\}, \quad (2.3)$$

and

$$\partial\Omega_D := \{(x, y) \in \Omega \mid |x - y| = d\}, \quad (2.4)$$

so that the boundary $\partial\Omega$ decomposes into $\partial\Omega_\sigma$ and $\partial\Omega_D$. Now, in order to arrive at a rigorous realization of (1.1), we construct a suitable quadratic form on the Hilbert space $L^2(\Omega)$. We set:

$$q_d[\varphi] := \int_{\Omega} |\nabla\varphi|^2 dx - \int_{\partial\Omega_\sigma} \sigma(y) |\varphi_{bv}|^2 dy, \quad (2.5)$$

being defined on the domain $\mathcal{D}_q := \{\varphi \in H^1(\Omega) : \varphi|_{\partial\Omega_D} = 0\}$. We note that the Dirichlet boundary conditions along $\partial\Omega_D$ are induced by (2.1). Furthermore, we set $\sigma(y) := -v(0, y)$ and $\varphi_{bv} := \varphi|_{\partial\Omega_\sigma}$ which are well defined according to the trace theorem for Sobolev functions [10].

Remark 2.1. *The quadratic form (2.5) corresponds to a variational formulation of a boundary-value problem for the two-dimensional Laplacian $-\Delta$ on Ω with coordinate dependent Robin boundary conditions along $\partial\Omega_\sigma$ and Dirichlet boundary conditions along $\partial\Omega_D$. Indeed, the boundary conditions along $\partial\Omega_\sigma$ read:*

$$\begin{aligned} \frac{\partial\varphi}{\partial n}(0, y) + \sigma(y)\varphi(0, y) &= 0, \quad \text{and} \\ \frac{\partial\varphi}{\partial n}(y, 0) + \sigma(y)\varphi(y, 0) &= 0, \end{aligned} \quad (2.6)$$

for a.e. $y \in [0, d]$. Here, $\frac{\partial}{\partial n}$ denotes the inward normal derivative along $\partial\Omega_\sigma$.

The following was proved in [4, 5].

Theorem 2.2. *Let $\sigma \in L^\infty(0, d)$ with $0 < d \leq \infty$ be given. Then, $q_d[\cdot]$ is densely defined, closed and semi-bounded from below.*

Hence, according to the representation theorem for quadratic forms [11], there exists a unique self-adjoint operator being associated with $q_d[\cdot]$. This operator, being the Hamiltonian of our systems, shall be denoted by $-\Delta_\sigma^d$ and his domain by $\mathcal{D}(-\Delta_\sigma^d) \subset \mathcal{D}_q$.

Remark 2.3. *We note that the case $d = \infty$ corresponds to the model where no binding potential is considered in (1.1). In other words, the operator $-\Delta_\sigma^\infty$ is the self-adjoint Hamiltonian of the model discussed in [4].*

3. Spectral properties of the operator $-\Delta_\sigma^d$

As mentioned above, due to the non-compactness of the half-line, the spectrum $\sigma(-\Delta_\sigma^d)$ cannot be expected to be purely discrete. Indeed, using the method of Weyl sequences for forms [12], the following was established in [4, 5].

Theorem 3.1. *Let $\sigma \in L^\infty(0, d)$ with $0 < d < \infty$ be given. Then:*

$$\sigma_{ess}(-\Delta_\sigma^d) = [\pi^2/2d^2, \infty). \quad (3.1)$$

Furthermore, if $d = \infty$ and $\sigma \in L^\infty(\mathbb{R}_+)$ is such that $\lim_{y \rightarrow \infty} |\sigma(y)| = 0$, then:

$$\sigma_{ess}(-\Delta_\sigma^d) = [0, \infty). \quad (3.2)$$

In the case of vanishing binding-potential, i.e., $d = \infty$, Theorem 3.1 shows that the essential spectrum starts at zero given the modulus of the boundary potential σ decays to zero as $y \rightarrow \infty$. In particular, this holds independently of the sign of σ , i.e., the singular interactions could be attractive ($\sigma > 0$) or repulsive ($\sigma < 0$) or anything in between. A natural question is then the following: Given the singular interactions are ‘attractive enough’, can eigenvalues below the bottom of the essential spectrum be expected? And what about the ground state energy of the system?

Theorem 3.2. [4] For $d = \infty$ let $\sigma \in L^1(\mathbb{R}_+)$ be such that $\inf \sigma_{ess}(-\Delta_\sigma^\infty) = 0$ and

$$\int_0^\infty \sigma(y) \, dy > 0. \quad (3.3)$$

Then there exists an eigenvalue at negative energy.

Furthermore, let $E_\sigma := \inf \sigma(-\Delta_\sigma^\infty)$ denote the ground state energy. Then:

$$-2\|\sigma\|_\infty^2 \leq E_\sigma \leq -2\|\sigma\|_\infty^2 + 8\|\sigma\|_\infty^2 \int_0^\infty [|\sigma|_\infty - \sigma(y)] e^{-2\|\sigma\|_\infty y} \, dy. \quad (3.4)$$

We now turn to the case of non-vanishing binding-potential, i.e., $0 < d < \infty$. In the case of vanishing singular interactions ($\sigma \equiv 0$), $-\Delta_\sigma^d$ is a positive operator and therefore cannot possess negative spectral values. However, according to Theorem 3.1, the essential spectrum starts only at $\pi^2/2d^2$ and for this reason one might ask the following question: do there exist non-negative eigenvalues with value smaller than $\pi^2/2d^2$? Using the results of [13], the following could be established in [5].

Theorem 3.3. Assume that $0 < d < \infty$ and $\sigma \equiv 0$. Then:

$$\sigma_d(-\Delta_\sigma^d) \neq \emptyset. \quad (3.5)$$

In other words, there exists a non-negative eigenvalue below the bottom of the essential spectrum.

Remark 3.4. Theorem 3.3 is quite remarkable from a physical point of view since the molecule can remain localized around the origin without any attractive interactions present. In other words, the existence of such a bound states is a purely quantum mechanical effect which is induced by the geometry of the one-particle configuration space. If the one-particle configuration space was the whole line instead of the half-line, no such bound state would exist.

We now investigate the stability of the discrete part of the spectrum in the presence of singular two-particle interactions. From a physical point of view, one expects the discrete spectrum to remain non-empty given the singular two-particle interactions are purely attractive or at least not too strong if repulsive.

Proposition 3.5. [5] For given $\sigma \in L^\infty(0, d)$ and $0 < d < \infty$ the following holds:

1. If $\sigma(y) \geq 0$ for almost every $y \in [0, d]$, then $\sigma_d(-\Delta_\sigma^d) \neq \emptyset$.
2. There exists a constant $c > 0$ such that $\sigma_d(-\Delta_\sigma^d) \neq \emptyset$ for all σ with $\|\sigma\|_\infty < c$.

Finally, as a main result, the following was proved in [5].

Theorem 3.6. Let $0 < d < \infty$ be given. Then there exists a constant $\gamma < 0$ such that $\sigma_d(-\Delta_\sigma^d) = \emptyset$ for all $\sigma \in L^\infty(0, d)$ for which $\sigma(y) \leq \gamma$ holds for almost every $y \in [0, d]$.

As already referred to in the introduction, Theorem 3.6 shows that the discrete part of the spectrum becomes trivial given the singular two-particle interactions are repulsive and strong enough. In this case, the singular two-particle interactions destabilize the system by leading to a destruction of the (isolated) ground state of the molecule and hence cannot be treated as a small perturbation only.

4. Outlook

As mentioned earlier, the model presented is interesting from a theoretical point of view since it provides an example of an approachable many-particle system. For example, in an upcoming paper, we will construct the resolvent of the Hamiltonian (1.1) without binding-potential explicitly. This then enables one to study scattering properties of the system in detail.

It would be also interesting to investigate the Cauchy problem for the Schrödinger equation corresponding to a family of Hamiltonians $-\Delta_{\sigma(t)}^d$ (see, e.g., [14]). What regularity of the map $t \mapsto \sigma(t)$ is needed in order to prove existence of a strong solution? How does the time-dependence of σ affect the stability of the system?

Finally, it would be interesting to investigate the mean-field behavior of the N -particle (mean-field) Hamiltonian corresponding to (1.1) (see, e.g., [15]). Is it possible to approximate the exact time-evolution of an N -particle state $\varphi_0 \otimes \dots \otimes \varphi_0$ with $\varphi_0 \in L^2(\mathbb{R}_+)$ by a tensor product $\varphi_t \otimes \dots \otimes \varphi_t$, φ_t being the solution to some non-linear Schrödinger equation? Due to the singular nature of the two-particle interactions, is it possible to derive better convergence estimates?

Acknowledgements

JK would like to thank S. Egger for helpful discussions. We would also like to thank M.L. Glasser for his interest in our model and for providing stimulating references.

References

- [1] Bolte J., Kerner J. Quantum graphs with singular two-particle interactions. *Journal of Physics A: Mathematical and Theoretical*, 2013, **46** (4), P. 045206.
- [2] Bolte J., Kerner J. Quantum graphs with two-particle contact interactions. *Journal of Physics A: Mathematical and Theoretical*, 2013, **46** (4), P. 045207.
- [3] Kottos T., Smilansky U. Quantum Chaos on Graphs. *Physical Review Letters*, 1997, **79**, P. 4794–4797.
- [4] Kerner J., Mühlenbruch T. Two interacting particles on the half-line. *Journal of Mathematical Physics*, 2016, **57**, P. 023509.
- [5] Kerner J., Mühlenbruch T. On a two-particle bound system on the half-line. ArXiv:1604.06693.2016, 2016 (to appear in *Reports on Mathematical Physics*).
- [6] Queisser F., Unruh W.G. Long-lived resonances at mirrors. ArXiv:1503.08814, 2015.
- [7] Fossheim K., Sudboe A. *Superconductivity: Physics and applications*. Wiley, 2004.
- [8] Glasser M.L. A solvable non-separable quantum two-body problem. *Journal of Physics A: Mathematical and Theoretical*, 1993, **26** (17), P. L825.
- [9] Glasser M.L., Nieto L.M. Solvable quantum two-body problem: entanglement. *Journal of Physics A: Mathematical and Theoretical*, 2005, **38** (24), P. L455.
- [10] Dobrowolski M. *Angewandte Funktionalanalysis: Funktionalanalysis, Sobolev-Räume und Elliptische Differentialgleichungen*. Springer-Verlag, 2005.
- [11] Blank J., Havlíček M., Exner P. *Hilbert space operators in quantum physics*. Springer Verlag, 2008.
- [12] Stollmann P. *Caught by Disorder: Bound States in Random Media*. Springer Science & Business Media, 2012, 166 p.
- [13] Exner P., Šeba P., Št'oviček P. On Existence of a bound state in an L-shaped waveguide, *Czechoslovak Journal of Physics B*, 1989, **39** (11), P. 1181–1191.
- [14] Hmidi T., Mantile A., Nier F. Time-dependent Delta-interactions for 1D Schrödinger Hamiltonians. *Mathematical Physics, Analysis and Geometry*, 2010, **13**, P. 83–103.
- [15] Pickl P. A Simple Derivation of Mean Field Limits for Quantum Systems. *Letters in Mathematical Physics*, 2011, **97**, P. 151–164.

Stationary nonlinear Schrödinger equation on the graph for the triangle with outgoing bonds

K. K. Sabirov^{1,2}, M. Aripov³, D. B. Sagdullayev⁴

¹Turin Polytechnic University in Tashkent, 17 Niyazov Str. 100095 Tashkent, Uzbekistan

²Tashkent University of Information Technologies, Amir Temur Str. 108, Tashkent, Uzbekistan

³Department of Mathematics, National University of Uzbekistan,
University Str. 1, 100174, Tashkent, Uzbekistan

⁴Department of High Mathematics, Tashkent State University of Economy,
Uzbekistan Str., 49, 100003, Tashkent, Uzbekistan

karimjonsabirov80@gmail.com

PACS 05.45.Yv

DOI 10.17586/2220-8054-2017-8-1-24-28

We consider the stationary (cubic) nonlinear Schrödinger equation (NLSE) on a simple metric graph in the form of a triangle with three infinite outgoing bonds. Exact solutions are obtained for primary star graph with the boundary vertex conditions providing the wave function weights continuity and flux conservation for the case of repulsive nonlinearity.

Keywords: Nonlinear Schrödinger equation, a metric graph, repulsive nonlinearity.

Received: 10 July 2016

Revised: 25 August 2016

1. Introduction

The nonlinear evolution equation on metric graphs have attracted much attention over the last decade [1–10]. Such interest is caused by the possibility of modeling nonlinear waves and soliton transport in networks and branched structures by nonlinear wave equations on metric graphs. The latter is of practical importance for the problem of engineering network architectures providing tunable transport of heat, spin, charge, light and information transport in networks. In addition, such equations can be used for to model soliton transport in DNA double helix, conducting polymers, branched optical waveguides, Josephson junction networks and Bose-Einstein condensation in branched traps.

Earlier, the problem of soliton transport in branched structures and networks was mainly studied within the tight-binding approach [11]. However, such an approach doesn't provide comprehensive treatment of the problem, thus one needs to use continuous NLSE on graphs.

Considerable progress has been made so far in the obtaining of soliton solutions of different nonlinear wave equations on metric graphs. The integrability of nonlinear Schrödinger equation on simple metric graphs was shown and soliton solutions providing reflectionless transmission of solitons through the graph vertex have been obtained in [1]. Exact solutions for the stationary NLSE and their stability were studied in the Refs. [3–7]. Dispersion relations for the linear and NLSE on networks are discussed in [12]. Sine-Gordon equation on metric graphs has been studied in [8,9]. The NLSE and soliton transport in planar graphs were studied in [10].

In this paper, we treat the stationary NLSE on the graph for a triangle with outgoing bonds shown in Fig. 1. Graphs are the systems consisting of bonds which are connected at the vertices [13]. The bonds are connected according to a rule that is called the topology of a graph. The topology of a graph is given in terms of so-called adjacency matrix (or connectivity matrix) which can be written as [14, 15]:

$$C_{ij} = C_{ji} = \begin{cases} 1 & \text{if } i \text{ and } j \text{ are connected,} \\ 0 & \text{otherwise,} \end{cases} \quad i, j = 1, 2, \dots, V.$$

This paper is organized as follows. In the next section we will present formulation of the problem for the graph shown in Fig. 1. Section III presents derivation of the solution for the stationary NLSE on this graph by considering the repulsive nonlinearity. In section IV, we discuss the extension of these results to the case of the attractive nonlinearity. Finally, section V presents some concluding remarks.

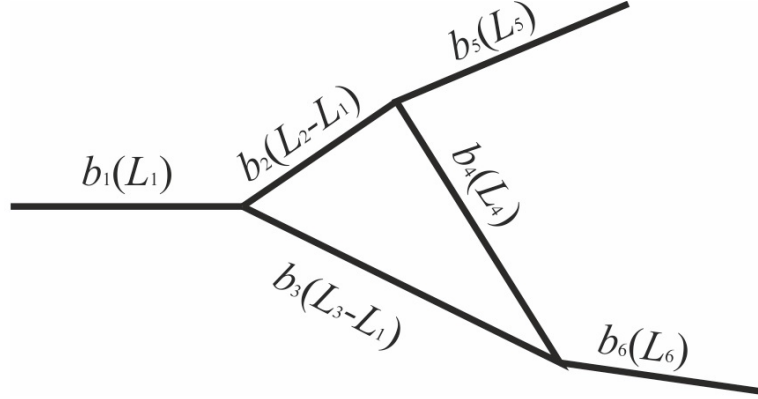


FIG. 1. The graph for the triangle with outgoing bonds

2. Stationary Schrödinger equation on the graph for the triangle with outgoing infinite bonds

Consider a metric graph presented in Fig. 1 which consists of a triangle with finite sides connected to outgoing infinite leads ($b_{1,4,5,6} \sim (0; L_{1,4,5,6})$, $b_{2,3} \sim (L_1; L_{2,3})$).

Then, the time-independent (stationary) NLSE on each bond of b of such graph can be written as:

$$-\psi_b'' + \beta_b |\psi_b|^2 \psi_b = \lambda^2 \psi_b, \quad \beta_b > 0. \quad (1)$$

Eq. (1) is a multi-component equation in which the components are connected to each other through the vertex boundary conditions providing the “glue” for the bonds at the branching of points of a graph. For the graph in Fig. 1, such boundary conditions can be written as:

$$\psi_1(x)|_{x=0} = 0, \quad \psi_5(x)|_{x=L_5} = 0, \quad \psi_6(x)|_{x=L_6} = 0, \quad (2)$$

$$\sqrt{\beta_1} \psi_1(x)|_{x=L_1} = \sqrt{\beta_2} \psi_2(x)|_{x=L_1} = \sqrt{\beta_3} \psi_3(x)|_{x=L_1}, \quad (3)$$

$$\left[\frac{1}{\sqrt{\beta_1}} \frac{\partial \psi_1(x)}{\partial x} - \frac{1}{\sqrt{\beta_2}} \frac{\partial \psi_2(x)}{\partial x} - \frac{1}{\sqrt{\beta_3}} \frac{\partial \psi_3(x)}{\partial x} \right] \Big|_{x=L_1} = 0, \quad (4)$$

$$\sqrt{\beta_2} \psi_2(x)|_{x=L_2} = \sqrt{\beta_4} \psi_4(x)|_{x=0} = \sqrt{\beta_5} \psi_5(x)|_{x=0}, \quad (5)$$

$$\frac{1}{\sqrt{\beta_2}} \frac{\partial \psi_2(x)}{\partial x} \Big|_{x=L_2} - \frac{1}{\sqrt{\beta_4}} \frac{\partial \psi_4(x)}{\partial x} \Big|_{x=0} - \frac{1}{\sqrt{\beta_5}} \frac{\partial \psi_5(x)}{\partial x} \Big|_{x=0} = 0, \quad (6)$$

$$\sqrt{\beta_3} \psi_3(x)|_{x=L_3} = \sqrt{\beta_4} \psi_4(x)|_{x=L_4} = \sqrt{\beta_6} \psi_6(x)|_{x=0}, \quad (7)$$

$$\frac{1}{\sqrt{\beta_3}} \frac{\partial \psi_3(x)}{\partial x} \Big|_{x=L_3} - \frac{1}{\sqrt{\beta_4}} \frac{\partial \psi_4(x)}{\partial x} \Big|_{x=L_4} - \frac{1}{\sqrt{\beta_6}} \frac{\partial \psi_6(x)}{\partial x} \Big|_{x=0} = 0 \quad (8)$$

and the wave function is normalized as:

$$\sum_{j=1}^6 \int_{b_j} |\psi_j(x)|^2 dx = 1. \quad (9)$$

Dirichlet boundary conditions are imposed at the bond edges.

3. Solution of the time-independent NLSE on the graph for the triangle with outgoing bonds

The solution of Eq. (1) can be written in the form:

$$\psi_b(x) = f_b(x) e^{i\gamma_b}, \quad (10)$$

where b is bond index, $\gamma_b = \text{const}$, $f_b(x)$ is a real function obeying the equation:

$$-f_b'' + \beta_b f_b^3 = \lambda^2 f_b. \quad (11)$$

From the boundary conditions we have $\gamma_b = \gamma$ and it is clear that the functions f_b should fulfill Eqs. (2) – (9).

Exact solutions for Eq. (11) for finite interval and periodic boundary conditions can be found in the Refs. [18, 19]. Here, we consider this problem for the metric graph boundary conditions given by Eq. (2). The solution of Eq. (11) fulfilling these boundary conditions can be written as:

$$f_b(x) = B_b \operatorname{sn}(\alpha_b x + \delta_b | k_b),$$

where $\operatorname{sn}(ax|k)$ are the Jacobian elliptic functions [20], $\delta_1 = 0$, $\delta_{5,6} = -\alpha_{5,6} L_{5,6}$.

Inserting the last equation into Eq. (10) and comparing the coefficients of similar terms we have:

$$B_b = \sigma_b \sqrt{\frac{2}{\beta_b}} \alpha_b k_b, \quad \lambda^2 = \alpha_b^2 (1 + k_b^2), \quad (12)$$

where $\sigma_b = \pm 1$.

Using Eqs. (2)–(9) and the relations [20]:

$$\begin{aligned} \int_a^b \operatorname{sn}^2(\alpha(x-c)|k) dx &= \frac{1}{k^2} \int_a^b [1 - \operatorname{dn}^2(\alpha(x-c)|k)] dx \\ &= \frac{1}{k^2}(b-a) - \frac{1}{\alpha k^2} E[\operatorname{am}(\alpha(b-c)|k)] + \frac{1}{\alpha k^2} E[\operatorname{am}(\alpha(a-c)|k)], \end{aligned}$$

we obtain the following system of transcendental equations with respect to α_b , δ_b and k_b :

$$\sqrt{\beta_1} B_1 \operatorname{sn}(\alpha_1 L_1 | k_1) = \sqrt{\beta_2} B_2 \operatorname{sn}(\alpha_2 L_1 + \delta_2 | k_2) = \sqrt{\beta_3} B_3 \operatorname{sn}(\alpha_3 L_1 + \delta_3 | k_3), \quad (13)$$

$$\frac{B_1 \alpha_1}{\sqrt{\beta_1}} \operatorname{cn}(\alpha_1 L_1 | k_1) \operatorname{dn}(\alpha_1 L_1 | k_1) - \frac{B_2 \alpha_2}{\sqrt{\beta_2}} \operatorname{cn}(\alpha_2 L_1 + \delta_2 | k_2) \operatorname{dn}(\alpha_2 L_1 + \delta_2 | k_2)$$

$$- \frac{B_3 \alpha_3}{\sqrt{\beta_3}} \operatorname{cn}(\alpha_3 L_1 + \delta_3 | k_3) \operatorname{dn}(\alpha_3 L_1 + \delta_3 | k_3) = 0, \quad (14)$$

$$\sqrt{\beta_2} B_2 \operatorname{sn}(\alpha_2 L_2 + \delta_2 | k_2) = \sqrt{\beta_4} B_4 \operatorname{sn}(\delta_4 | k_4) = \sqrt{\beta_5} B_5 \operatorname{sn}(\delta_5 | k_5), \quad (15)$$

$$\frac{B_2 \alpha_2}{\sqrt{\beta_2}} \operatorname{cn}(\alpha_2 L_2 + \delta_2 | k_2) \operatorname{dn}(\alpha_2 L_2 + \delta_2 | k_2) - \frac{B_4 \alpha_4}{\sqrt{\beta_4}} \operatorname{cn}(\delta_4 | k_4) \operatorname{dn}(\delta_4 | k_4)$$

$$- \frac{B_5 \alpha_5}{\sqrt{\beta_5}} \operatorname{cn}(\delta_5 | k_5) \operatorname{dn}(\delta_5 | k_5) = 0, \quad (16)$$

$$\sqrt{\beta_3} B_3 \operatorname{sn}(\alpha_3 L_3 + \delta_3 | k_3) = \sqrt{\beta_4} B_4 \operatorname{sn}(\alpha_4 L_4 + \delta_4 | k_4) = \sqrt{\beta_6} B_6 \operatorname{sn}(\delta_6 | k_6), \quad (17)$$

$$\frac{B_3 \alpha_3}{\sqrt{\beta_3}} \operatorname{cn}(\alpha_3 L_3 + \delta_3 | k_3) \operatorname{dn}(\alpha_3 L_3 + \delta_3 | k_3) - \frac{B_4 \alpha_4}{\sqrt{\beta_4}} \operatorname{cn}(\alpha_4 L_4 + \delta_4 | k_4) \operatorname{dn}(\alpha_4 L_4 + \delta_4 | k_4)$$

$$- \frac{B_6 \alpha_6}{\sqrt{\beta_6}} \operatorname{cn}(\delta_6 | k_6) \operatorname{dn}(\delta_6 | k_6) = 0, \quad (18)$$

$$\frac{B_1^2}{k_1^2} L_1 + \frac{B_2^2}{k_2^2} (L_2 - L_1) + \frac{B_3^2}{k_3^2} (L_3 - L_1) + \frac{B_4^2}{k_4^2} L_4 + \frac{B_5^2}{k_5^2} L_5 + \frac{B_6^2}{k_6^2} L_6$$

$$+ \frac{B_2^2}{k_2^2 \alpha_2} E[\operatorname{am}(\alpha_2 L_1 + \delta_2 | k_2) | k_2] + \frac{B_3^2}{k_3^2 \alpha_3} E[\operatorname{am}(\alpha_3 L_1 + \delta_3 | k_3) | k_3] + \sum_{j=4}^6 \frac{B_j^2}{k_j^2 \alpha_j} E[\operatorname{am}(\delta_j | k_j) | k_j]$$

$$= 1 + \sum_{j=1}^6 \frac{B_j^2}{k_j^2 \alpha_j} E[\operatorname{am}(\alpha_j L_j + \delta_j | k_j) | k_j], \quad (19)$$

where $\delta_1 = 0$, $\delta_{5,6} = -\alpha_{5,6} L_{5,6}$, $E(\varphi|k)$ and $\operatorname{am}(u|k)$ are the incomplete elliptic integral of the second kind and the Jacobi amplitude, respectively. In the general case, this system can be solved using the different (e.g., Newton's or Krylov's method) iteration schemes. However, below, we will show the solvability of this system for two special cases.

First case. Let:

$$\frac{4n_1 + 1}{L_1} = \frac{4(n_{2,3}^{(2)} - n_{2,3}^{(1)})}{L_{2,3} - L_1} = \frac{4n_4}{L_1} = \frac{4n_{5,6} + 1}{L_{5,6}},$$

where $n_j \in \mathbf{N} \cup \{0\}$, $j = 1, 2, 3, 4, 5, 6$, $n_{2,3}^{(2)} > n_{2,3}^{(1)}$. Choosing:

$$\alpha_{1,5,6} = \frac{4n_{1,5,6} + 1}{L_{1,5,6}} K(k_{1,5,6}), \quad \alpha_{2,3} = \frac{4(n_{2,3}^{(2)} - n_{2,3}^{(1)})}{L_{2,3} - L_1} K(k_{2,3}), \quad \alpha_4 = \frac{4n_4}{L_4} K(k_4),$$

$$\delta_{2,3} = \left(\frac{4(n_{2,3}^{(2)} - n_{2,3}^{(1)})}{L_{2,3} - L_1} + 1 \right) K(k_{2,3}), \quad \delta_4 = K(k_4) \quad (20)$$

we have:

$$\alpha_j = \alpha, \quad k_j = k, \quad j = 1, 2, 3, 4, 5, 6, \quad \sigma_{1,2,3,4} = -\sigma_{5,6}.$$

Here, $K(k)$ is the complete elliptic integrals of the first kind.

Using Eq. (19) and the relations:

$$\text{am}(u + 2K(k)|k) = \pi + \text{am}(u|k),$$

$$E(n\pi \pm \varphi|k) = 2nE(k) \pm E(\varphi|k),$$

we have:

$$g(k) \equiv 2 \frac{(4n_1 + 1)^2}{L_1^2} \left(\frac{L_1}{\beta_1} + \frac{L_2 - L_1}{\beta_2} + \frac{L_3 - L_1}{\beta_3} + \frac{L_4}{\beta_4} + \frac{L_5}{\beta_5} + \frac{L_6}{\beta_6} \right) K(k) (K(k) - E(k)) - 1 = 0. \quad (21)$$

The solvability of Eq. (21) is equivalent to that of NLSE on a primary star graph. Therefore we will prove the solvability of this equation. Since the following relations are valid:

$$\lim_{k \rightarrow 0} g(k) = -1, \quad \lim_{k \rightarrow 1} g(k) = +\infty,$$

and $g(k)$ is a continuous function of k on the interval $(0; 1)$ it follows that Eq. (21) has a root.

Second case. Now we consider another special case given by the relations:

$$\alpha_1 = \frac{(-1)^{n_1} p_1 + 2n_1 K(k_1)}{L_1}, \quad \alpha_{2,3} = \frac{(-1)^{n_{2,3}^{(2)}} p_{2,3} - (-1)^{n_{2,3}^{(1)}} p_1 + 2(n_{2,3}^{(2)} - n_{2,3}^{(1)}) K(k_{2,3})}{L_{2,3} - L_1},$$

$$\alpha_4 = \frac{(-1)^{n_4} p_3 - (-1)^{n_4} p_2 + 2n_4 K(k_4)}{L_4},$$

$$\delta_{2,3} = \frac{(-1)^{n_{2,3}^{(1)}} p_1 L_{2,3} - (-1)^{n_{2,3}^{(2)}} p_{2,3} L_1 + 2(n_{2,3}^{(1)} L_{2,3} - n_{2,3}^{(2)} L_1) K(k_{2,3})}{L_{2,3} - L_1}, \quad \delta_4 = (-1)^{n_4} p_2 + 2n_4 K(k_4),$$

where $-K(k_j) \leq p_m \leq K(k_j)$, $m = 1, 2, 3$, $j = 1, 2, 3, 4, 5, 6$, $n_{1,4,5,6}, n_{2,3}^{(1),(2)} \in \mathbf{N}$, $n_1, n_2^{(1)}, n_3^{(1)}$ or $n_2^{(2)}, n_4^{(2)}$, n_5 or $n_3^{(2)}, n_4^{(1)}, n_6$ cannot be odd or even at the same time and show existence of the solution of the system given by Eqs. (13)–(19). From Eqs. (13), (15) and (17) we obtain

$$\alpha_b = \alpha, \quad k_b = k, \quad \sigma_{1,2,3,4} = -\sigma_{5,6}.$$

From Eqs. (14), (16) and (18) we have:

$$\frac{(-1)^{n_1}}{\beta_1} = \frac{(-1)^{n_2^{(1)}}}{\beta_2} + \frac{(-1)^{n_3^{(1)}}}{\beta_3}, \quad \frac{(-1)^{n_2^{(2)}}}{\beta_2} = \frac{(-1)^{n_4^{(1)}}}{\beta_4} + \frac{(-1)^{n_5}}{\beta_5}, \quad \frac{(-1)^{n_3^{(2)}}}{\beta_3} = \frac{(-1)^{n_4^{(2)}}}{\beta_4} + \frac{(-1)^{n_6}}{\beta_6}.$$

Furthermore, it follows from the last equation and Eq. (19) that:

$$g(k) \equiv 4 \left(\frac{(-1)^{n_1} p + 2n_1 K(k_1)}{L_1} \right) \left(\frac{n_1}{\beta_1} + \frac{n_2^{(2)} - n_2^{(1)}}{\beta_2} + \frac{n_3^{(2)} - n_3^{(1)}}{\beta_3} + \frac{n_4^{(1)}}{\beta_4} + \frac{n_5}{\beta_5} + \frac{n_6}{\beta_6} \right) \times$$

$$\times (K(k) - E(k)) - 1 = 0. \quad (22)$$

We have:

$$\lim_{k \rightarrow 0} g(k) = -1, \quad \lim_{k \rightarrow 1} g(k) = +\infty.$$

Since $g(k)$ is a continuous function of k on the interval $(0; 1)$, it follows from the last relations that Eq. (22) has a root.

Thus, the stationary NLSE on a metric graph presented in Fig. 1 can be solved with the same success as that for finite interval, considered in the Refs. [18, 19, 21].

4. Conclusion

In this paper, we have studied the stationary nonlinear Schrödinger equation with cubic nonlinearity on the graph having the form of a triangle connected to finite outgoing leads considering the case of attractive nonlinearity. Explicit analytic solutions were obtained by imposing vertex boundary conditions providing continuity of the wave function weights and flux conservation. The method can also be extended for the case of repulsive nonlinearity, too.

The above results can be useful for modeling of different branched systems, where the static solitons appear, e.g. for Bose-Einstein condensate in networks [24–27] charge and energy modeling in DNA double helix [28–30] and branched optical waveguides [31,32], on In principle, the method developed in this work can be extended for more complicated topologies having multiple junctions.

Acknowledgements

This work is partially supported by the grant of the Committee for the Coordination Science and Technology Development.

References

- [1] Sobirov Z., Matrasulov D., Sabirov K., Sawada S., and Nakamura K. Integrable nonlinear Schrödinger equation on simple networks: Connection formula at vertices, *Phys. Rev. E*, 2010, **81**, P. 066602.
- [2] Nakamura K., Sobirov Z.A., Matrasulov D.U., and Sawada S. Transport in simple networks described by an integrable discrete nonlinear Schrödinger equation. *Phys. Rev. E*, 2011, **84**, P. 026609.
- [3] Adami R., Cacciapuoti C., Finco D., and Noja D. FAST SOLITONS ON STAR GRAPHS. *Rev. Math. Phys.*, 2011, **23**, P. 409.
- [4] Adami R., Cacciapuoti C., Finco D., and Noja D. Stationary states of NLS on star graphs. *Europhys. Lett.*, 2012, **100**, P. 10003.
- [5] Adami R., Noja D., and Ortoleva C. Orbital and asymptotic stability for standing waves of a nonlinear Schrödinger equation with concentrated nonlinearity in dimension three. *J. Math. Phys.*, 2013, **54**, P. 013501.
- [6] Sabirov K.K., Sobirov Z.A., Babajanov D., and Matrasulov D.U. Stationary nonlinear Schrödinger equation on simplest graphs. *Phys. Lett. A*, 2013, **377**, P. 860.
- [7] Noja D. Nonlinear Schrödinger equation on graphs: recent results and open problems. *Philos. Trans. R. Soc. A*, 2014, **372**, P. 20130002.
- [8] Susanto G.H. and van Gils S.A. Existence and stability analysis of solitary waves in a tricrystal junction. *Phys. Lett. A*, 2005, **338**, P. 239.
- [9] Caputo J.-G., Dutykh D. Nonlinear waves in networks: Model reduction for the sine-Gordon equation. *Phys. Rev. E*, 2014, **90**, P. 022912.
- [10] Uecker H., Grieser D., Sobirov Z., Babajanov D., and Matrasulov D. Soliton transport in tubular networks: transmission at vertices in the shrinking limit. *Phys. Rev. E*, 2015, **91**, P. 023209.
- [11] Burioni R., Cassi D., Sodano P., Trombettoni A. and Vezzani A. Soliton Propagation in Chains with Simple non Local Defects. *Physica D*, 2006, **216**, P. 71.
- [12] Banica V., Ignat L. Dispersion for the Schrödinger Equation on Networks, Arxiv: 1103.0429.
- [13] Harary F. *Graph Theory*. Addison-Wesley, Reading, 1969.
- [14] Tsampikos Kottos and Uzy Smilansky. Periodic orbit theory and spectral statistics for quantum graphs. *Ann. Phys.*, 1999, **76**, P. 274.
- [15] Sven Gnutzmann and Uzy Smilansky. Quantum Graphs: Applications to Quantum Chaos and Universal Spectral Statistics. *Adv. Phys.*, 2006, **55**, P. 527.
- [16] Gnutzmann S., Smilansky U., Derevyanko S. Stationary scattering from a nonlinear network. *Phys. Rev. A*, 2011, **83**, P. 033831.
- [17] Cascaval R.C., Hunter C.T. Linear and nonlinear Schrödinger equations on simplest networks. *Libertas Math.*, 2010, **30**, P. 85.
- [18] Carr L.D., Charles W. Clark and Reinhardt W.P. Stationary solutions of the one-dimensional nonlinear Schrödinger equation. I. Case of repulsive nonlinearity, *Phys. Rev. A*, 2000, **62**, P. 063610.
- [19] Carr L.D., Charles W. Clark and Reinhardt W.P. Stationary solutions of the one-dimensional nonlinear Schrödinger equation. II. Case of attractive nonlinearity, *Phys. Rev. A*, 2000, **62**, P. 063611.
- [20] Bowman F. *Introduction to Elliptic Functions, with Applications*. Dover, New York, 1961.
- [21] Carr L.D., Mahmud K.W. and Reinhardt W.P. Tunable tunneling: An application of stationary states of Bose-Einstein condensates in traps of finite depth. *Phys. Rev. A*, 2001, **64**, P. 033603.
- [22] D'Agosta R., Malomed B.A. and Presilla C. Stationary solutions of the Gross-Pitaevskii equation with linear counterpart. *Phys. Lett. A*, 2000, **275**, P. 424.
- [23] Infeld E., Zin P., Gocalek J. and Trippenbach M. Statics and dynamics of BEC in double square well potentials. *Phys. Rev. E*, 2006, **74**, P. 026610.
- [24] Bianconi G., Barabasi A.-L. Bose-Einstein Condensation in Complex Networks. *Phys. Rev. Lett. A*, 2001, **86**, P. 5632.
- [25] Vidal E.J.G.G., Lima R.P.A., and Lyra M.L. Bose-Einstein condensation in the infinitely ramified star and wheel graphs. *Phys. Rev. E*, 2011, **83**, P. 061137.
- [26] De Oliveira I.N., dos Santos T.B., de Moura F.A.B.F., Lyra M.L. and Serva M. Critical behavior of the ideal-gas Bose-Einstein condensation in the Apollonian network. *Phys. Rev. E*, 2013, **88**, P. 022139.
- [27] Castellanos E., Chacon-Acosta G. Polymer Bose-Einstein condensates. *Phys. Lett. B*, 2013, **722**, P. 119.
- [28] Yakushevich L.V. *Nonlinear Physics of DNA*. Wiley, Chichester, 2004.
- [29] Peyrard M. *Nonlinearity*, 2004, **17**, P. R1.
- [30] Zdravkovic S., Sataric M.V. Nonlinear Schrödinger equation and DNA dynamics. *Phys. Lett. A*, 2008, **373**, P. 126.
- [31] Leo G., Assanto G. Multiple branching of vectorial spatial solitary waves in quadratic media. *Opt. Commun.*, 1998, **146**, P. 356.
- [32] Santos M.C. Dynamic Y-branched structures in quadratic nonlinear media. *Opt. Commun.*, 2000, **180**, P. 167.

Nonlinear standing waves on planar branched systems: shrinking into metric graph

Z. Sobirov¹, D. Babajanov² and D. Matrasulov²

¹Tashkent Financial Institute, 60A, Amir Temur Str., 100000, Tashkent, Uzbekistan

²Turin Polytechnic University in Tashkent, 17 Niyazov Str., 100095, Tashkent, Uzbekistan

sobirovzar@gmail.com

PACS 05.45.Yv, 42.65.Wi, 42.65.Tg

DOI 10.17586/2220-8054-2017-8-1-29-37

We treat the stationary nonlinear Schrödinger equation on two-dimensional branched domains, so-called fat graphs. The shrinking limit when the domain becomes one-dimensional metric graph is studied by using analytical estimate of the convergence of fat graph boundary conditions into those for metric graph. Detailed analysis of such convergence on the basis of numerical solution of stationary nonlinear Schrödinger equation on a fat graph is provided. The possibility for reproducing different metric graph boundary conditions studied in earlier works is shown. Practical applications of the proposed model for such problems as Bose-Einstein condensation in networks, branched optical media, DNA, conducting polymers and wave dynamics in branched capillary networks are discussed.

Keywords: metric graph, Schrödinger equation.

Received: 11 August 2016

Revised: 4 September 2016

1. Introduction

Branched structures and networks appear in many physical systems and in complex systems from biology, ecology, sociology, economy and finance [1,2]. Particle and wave dynamics in such systems can be effectively modeled by nonlinear evolution equations on metric graphs. The latter are one dimensional system of bonds which are connected at one or more vertices (branching points). The connection rule is called the topology of the graph. When the bonds can be assigned a length, the graph is called a metric graph. Recently nonlinear evolution equations on metric graphs have attracted much attention in the literature (see the Refs. [3–10]). To solve nonlinear evolution equations on networks, one needs to impose boundary conditions on the graph vertices. Soliton solutions providing reflectionless transmission at the graph vertex together with integrable boundary conditions were derived in [3]. Different aspects of the nonlinear Schrödinger equation, including soliton solutions, are discussed in the Refs. [5,6]. Solutions of the stationary nonlinear Schrödinger equation on graphs for different vertex conditions were obtained in [4,5,8–10]. Despite the growing interest in nonlinear evolution equations and soliton dynamics in networks, most studies are still restricted by considering metric graphs, i.e. by one-dimensional motion wave motion in branched structures. However, in many cases, particle and wave motion in branched structures have certain transverse components, so that the system is two-dimensional. Such systems should be described using two-dimensional evolution equations on planar networks. Such systems can be modeled by so-called fat graphs. Previously, the linear Schrödinger equation on fat graphs was addressed in a number of works [11–13] by considering metric graph limit as transition to from planar to linear wave motions. Extension of such a study to the case of nonlinear Schrödinger equation based on the numerical treatment of the problem was done in recent work [14]. Fat graph treatment of the sine-Gordon equation for branched Y-junctions was numerically treated in [15]. Pioneering treatment of nonlinear evolution equations on fat graphs date back to Kosugi, who presented in Ref. [16] a strict mathematical treatment of the nonlinear elliptic differential equations on branched domains and estimates for the shrinking limit. The study of the nonlinear differential equation on branched domains is complicated due to the nonlinearity of the boundary conditions imposed at the branching area or vertex. In the case of nonlinear evolution equations related to physics, such boundary conditions should be derived from conservation laws or other physical conditions that greatly simplifies these boundary conditions [3,14].

In this work, we address the problem of the stationary (time-independent) nonlinear Schrödinger equation on fat graphs by focusing on metric graph limit in the shrinking of a fat graph. In particular, we obtain an estimate for the vertex boundary conditions in the shrinking limit and show that they reproduce those for the metric graph considered in [5,8]. Also, we present a treatment of the problem on the basis of numerical solution of stationary NLSE on fat graph. For small enough bond widths the numerical solution reproduces the metric graph solutions from Refs. [5,8].

Motivation for the study of the stationary NLSE comes from such problems as Bose-Einstein condensation on networks [17–22], standing waves in branched optical waveguides [23], branched liquid crystals and standing wave-polarons in polymers [24,25]. All these systems require taking into account of transverse component of the wave motion which can be done by considering stationary NLSE on fat graphs. Estimating of the “boundary” between the planar and linear motions is of importance for experiments on the study of wave motion in nonlinear networks, as such networks are always somehow planar or tubular.

This paper is organized as follows. In the next section, we give formulation of stationary NLSE on fat and metric graphs. Section III presents the results for numerical solution of the stationary NLSE on fat graph at different values of the graphs width by considering shrinking limit. In section IV, we present detailed discussion of potential application of fat graph problem to some physical systems having planar branched structure. Finally, section V gives some concluding remarks.

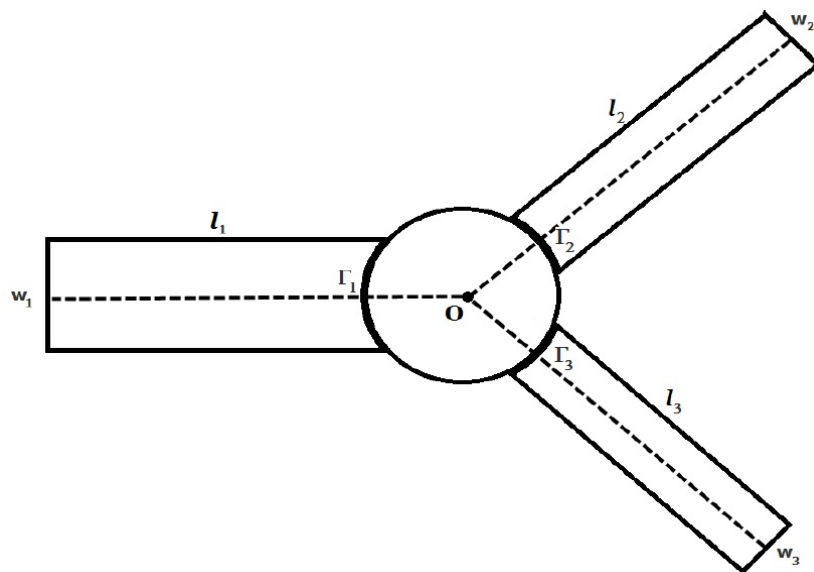


FIG. 1. Sketch of star-shaped fat and metric graphs. Dashed line presents metric graph

2. Stationary NLSE on a fat graph

Wave equations on planar branched domains, which are often called “fat graphs”, have attracted much attention in the context of wave dynamics during last decade. In particular, stationary linear wave equations on fat graphs have been studied in the Refs. [11–13, 26–28] (see [29, 30] and references therein for detailed reviews). The corresponding nonlinear problem has been mainly studied for the one-dimensional case by considering the metric graph approach. Different aspects of the nonlinear Schrödinger equation for branched one dimensional branched domains called metric graphs were previously studied earlier [4–10]. A metric graph is a set of bonds connected to each other at the vertices according to a rule which is called the topology of a graph with metrics defined in each bond. Recently, the problem of soliton transport in planar branched domains was studied based on numerical solution of NLSE on fat graph [17]. Transition from fat to metric graph problem was shown in this study.

Our purpose is to explore solutions of the stationary nonlinear Schrödinger equation over a two-dimensional branched domain in the limit when the domain shrinks to a metric graph. Therefore, we introduce two problems: “fat graph” and the “metric graph” problems. Both fat and metric graphs are presented in Fig. 1. A fat graph is a branched domain having two dimensional bonds and vertex as presented (See Fig. 1). In the following, we denote bond-lengths of such graph by l_1, l_2 and l_3 , bond-widths by w_1, w_2 and w_3 . The diameter of the vertex region $\Omega_\epsilon = \epsilon\Omega_1$ is $r\epsilon$. The stationary nonlinear Schrödinger equation (NLSE) on a “fat graph” is given as:

$$-\Delta\psi + (V_{\alpha,\epsilon} - \mu)\psi - |\psi|^2\psi = 0, \quad (1)$$

where the potential:

$$V_{\alpha,\epsilon}(x) = -\frac{\alpha}{2\pi\epsilon} \exp(-|x|^2/2\epsilon^2) \quad (2)$$

is localized at the vertex domain, $\alpha \in \mathbb{R}$ is a parameter. The potential is chosen as to reproduce delta-function in the shrinking limit, i.e.:

$$V_{\alpha,\epsilon} \sim -\alpha\epsilon\delta(x) \quad \text{for } \epsilon \rightarrow 0. \quad (3)$$

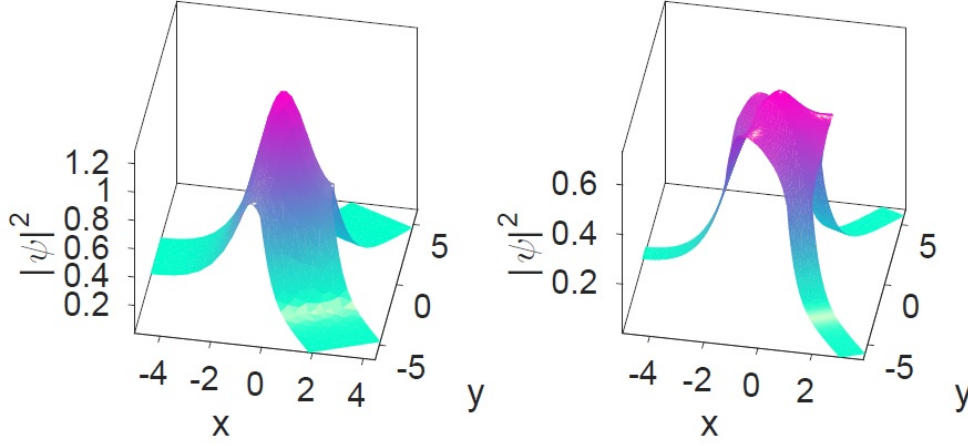


FIG. 2. Solution of NLSE on a fat graph at $\epsilon = 3$ and 1 , $\mu = -1$, $\alpha = 0.5$

In the metric graph case, we determine the coordinate for the k th bond from 0 to l_k , $k = 1, 2, 3$. The metric graph problem is determined by the stationary NLSE which is given for each bond of the graph as:

$$-\phi'' - \mu\phi - |\phi|^2\phi = 0. \quad (4)$$

These equations are related via the vertex conditions given by:

$$\phi_1 = \phi_2 = \phi_3, \quad (5)$$

$$\phi'_1 + \phi'_2 + \phi'_3 = \alpha\phi_1. \quad (6)$$

In the following, the problems given by Eqs.(4)–(6) will be called “metric graph problem”. The aim of this paper is to explore both analytically and numerically the shrinking limit of the fat graph problem given by Eqs. (1) and (2) and determining the conditions providing in the shrinking limit the transition of the fat graph problem to that of the metric graph. Such an analysis will consist of two parts: 1) an analytical estimate for the convergence of the fat graph problem to that of the metric graph and 2) numerical analysis for such convergence. The latter implies the analysis of numerical solution solution of NLSE for fat graph for different small values of the bond and vertex widths. Here, we focus on the vertex conditions considered in Refs. [5, 7, 9] which are often called “delta” type boundary conditions.

We divided the fat graph into the following parts: the first is the vertex region denoted by $\Omega_\epsilon = \epsilon\Omega_1$, where we assumed Ω_1 is a convex region with smooth enough boundary ($0 \in \Omega_1$) and tabular (rectangular) parts. In the limit $\epsilon \rightarrow 0$, the vertex region is given as a vertex point 0 , while tabular parts tends to the bonds of metric graph. The convergence problem in the case of the tabular region is well studied. Here, we refer to [16, 31]. We only focus on the vertex region and denote by $\Gamma_{k,\epsilon}$, ($k = 1, 2, 3$) the those parts(arcs) of the vertex which are connected to the bonds ($\Gamma_{k,\epsilon} = \epsilon\Gamma_k$). We impose the following boundary conditions for NLSE given by Eq. (1) in Ω_ϵ :

$$\frac{\partial\psi}{\partial n} = 0 \quad \text{on } \partial\Omega_\epsilon / (\Gamma_{1,\epsilon} \cup \Gamma_{2,\epsilon} \cup \Gamma_{3,\epsilon}). \quad (7)$$

We assume that:

$$\frac{\partial\psi}{\partial n}|_{\Gamma_{k,\epsilon}} \rightarrow \varphi'_k, \quad \psi|_{\Gamma_{k,\epsilon}} \rightarrow \varphi_k \quad \text{at } \epsilon \rightarrow 0, \quad k = 1, 2, 3,$$

where φ_k and φ'_k ($k = 1, 2, 3$) are constants.

First, we show that $\varphi_1 = \varphi_2 = \varphi_3$.

According to [16, 31] and maximum principle [32], we have $|\psi(x)| < c_1$, $|\nabla\psi(x)| \leq c_2$ for $x \in \Omega_\epsilon$

We denote $v(y) = \psi(y/\epsilon)$. The function $v(y)$ satisfies the following equation:

$$-\Delta_y v(y) - \epsilon^2 f(v(y)) + \alpha\epsilon V_{1,1} v(y) = 0, \quad (8)$$

with $f(v) = |v|^2 v + \mu v$.

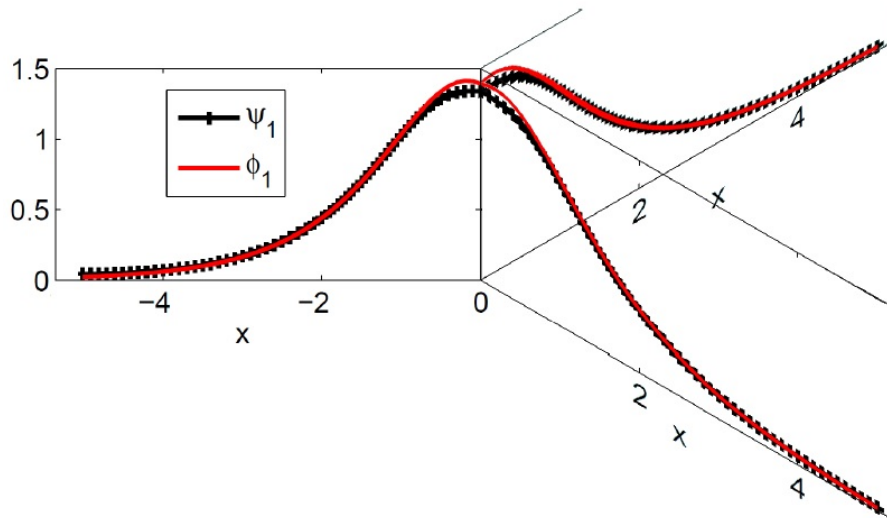


FIG. 3. Solution of NLSE on a fat graph at $\epsilon = 0.5$, $\mu = -1$, $\alpha = 0.5$

The function $v(y)$ satisfies the estimate (see, e.g. [16, 32]) $\|v\|_{C^2(\Omega_1)} \leq C_3$. From the Ascoli-Arzel theorem, there exist a sequence $\epsilon_m \rightarrow 0$ and the function $v_\infty \in C^1(\overline{\Omega_1})$, such that $\lim_{k \rightarrow \infty} \|v_m - v_\infty\|_{C^1(\overline{\Omega_1})} = 0$. Where $v_m(y)$ is the function $v(y)$ with $\epsilon = \epsilon_m$.

Then we have

$$\begin{aligned} \iint_{\Omega_1} |\nabla_y v_m(y)|^2 dy &= \int_{\partial\Omega_{\epsilon_m}} \psi_m \frac{\partial \psi_m}{\partial n} ds_x - f - \iint_{\Omega_{\epsilon_m}} [V_{\alpha, \epsilon_m}(x) \psi_m(x) + u_m(x) f(\psi_m(x))] dx \\ &\leq c_1 c_2 \epsilon_m \sum_{k=1}^3 |\Gamma_k| + c_1^4 |\Omega_1| \epsilon_m^2 + c_1 \epsilon_m \rightarrow 0. \end{aligned} \quad (9)$$

From Eq. (9) we have $v_\infty = \text{const}$, which proves $\varphi_1 = \varphi_2 = \varphi_3 = \varphi$.

Next, we verify the second vertex condition in the limiting problem. For mean values of the normal derivatives on the boundary we have ($\epsilon = \epsilon_m$):

$$\sum_{k=1}^3 \frac{1}{\epsilon} \int_{\Gamma_{k, \epsilon}} \frac{\partial \psi}{\partial n} d\Gamma_{k, \epsilon} \rightarrow \sum_k |\Gamma_k| \varphi'_k. \quad (10)$$

Conversely, integrating Eq. (10) over Ω_ϵ , we get:

$$\sum_{k=1}^3 \frac{1}{\epsilon} \int_{\Gamma_{k, \epsilon}} \frac{\partial \psi}{\partial n} d\Gamma_{k, \epsilon} + \alpha \iint_{\Omega_\epsilon} \frac{1}{\epsilon^2} V_{1,1} \left(\frac{x}{\epsilon} \right) - \frac{1}{\epsilon} \iint_{\Omega_\epsilon} |\psi|^2 \psi dx = \frac{\mu}{\epsilon} \iint_{\Omega_\epsilon} \psi dx. \quad (11)$$

According to maximum principle [32], for small ϵ , we have $\sup |u| \leq C$. Therefore, for the integrals we can write:

$$\frac{1}{\epsilon} \iint_{\Omega_\epsilon} |\psi|^2 \psi dx \sim O(\epsilon), \quad \frac{\mu}{\epsilon} \iint_{\Omega_\epsilon} \psi dx \sim O(\epsilon),$$

for small ϵ . Taking into account the above relations and properties of the potential $V_{\alpha, \epsilon}$, we obtain:

$$\lim_{\epsilon \rightarrow 0} \frac{1}{\epsilon} \int_{\Gamma_{k, \epsilon}} \frac{\partial \psi}{\partial n} d\Gamma_{j, \epsilon} = \alpha \psi(0). \quad (12)$$

Eqs. (10) and (12) lead to

$$\sum_k |\Gamma_k| \varphi'_k = \alpha \varphi. \quad (13)$$

Thus, we showed convergence of the fat graph problem given by Eqs. (1), (2) and (10) to that for metric graph with delta type boundary conditions given by Eqs. (4)–(6). In the next section, we will show such convergence on the basis of the numerical solution of stationary NLSE on fat graph.

3. Numerical treatment of the shrinking limit

Our purpose is showing convergence of the stationary NLSE on fat graph into that for metric graph in the shrinking limit using both analytically and numerical analysis of the shrinking limit. Such convergence is of practical importance for various problems dealing with wave dynamics in branched structures where one needs to neglect by transverse motion of the waves. Here, we will focus on the analysis of wave function behavior itself as well as $|\psi(x, y)|^2$. The latter has important physical meaning in the practical applications of the NLSE, e.g., density of particles in BEC, beam intensity in optics, etc.

The estimate presented by Eqs. (12) and (13) shows the convergence of the vertex boundary conditions of a fat graph with those of the metric graph. Such a convergence can be shown on the basis of numerical solution for the stationary NLSE on fat graphs by considering the shrinking limit, $\epsilon \rightarrow 0$.

Here, we will explore numerical solutions of Eq. (1) with the fat graph boundary conditions given by Eq. (10) at different fat graph bond length values of the by considering both attractive and repulsive nonlinearities. These describe bright and dark (static) solitons, respectively. Assuming $w_1 = \epsilon w_2 = \epsilon w_3$, we show that these numerical solutions reproduce the solutions of metric graph problem analytically obtained in the Refs. [5]. Solution of the metric graph problem given by Eqs. (4)–(6) was obtained in [5] and can be written as:

$$\phi_j(x, a) = \sqrt{2\mu} \operatorname{sech}(\sqrt{\mu}(x - a^j)), \quad (14)$$

where

$$a^j = \frac{1}{\mu} \operatorname{artanh} \left(\frac{\alpha}{(2j - 3)\sqrt{\mu}} \right), \quad j = 1, 2, 3.$$

In Fig. 2, solutions of the stationary NLSE on fat graph obtained by numerical solutions of two-dimensional stationary NLSE (1) with the boundary conditions (10) are for different values of the bond width $\epsilon = 3$, and 1 ($\mu = -1$, $\alpha = 0.5$). As it can be seen, the wave function is localized at the vertex in all cases.

Figure 3 compares solution of Eq. (1) for the bond width, $\epsilon = 1$ with that of for metric graph given by Eqs. (4)–(6). It can be observed the convergence of the solution of fat graph problem to that of metric graph in the shrinking limit.

In addition to the NLSE with attractive (focusing) nonlinearity given by Eq. (1), one can consider repulsive case when the wave equation is given as:

$$-\Delta\psi + (V_{\alpha, \epsilon} - \mu)\psi + |\psi|^2\psi = 0. \quad (15)$$

In Fig. 4, solutions for the fat and metric graphs are compared with the case of repulsive nonlinearity and $\epsilon = 0.3$. Unlike the attractive case, the wave function is localized on the bonds for this repulsive nonlinearity. Fig. 5 shows how the solution NLSE on fat graph depends on the chemical potential μ .

4. Standing nonlinear waves in branched planar structures

Two-dimensional branched structures, where the wave dynamics are described by the nonlinear Schrödinger equation, appear in many areas of physics. Here, we will briefly discuss physical systems where the above model can be applied.

BEC in planar networks. Bose-Einstein condensation is a remarkable phenomenon that can be described by a version of NLSE which is called Gross-Pitaevskii equation [17–21]. It can be realized in trapped cold atoms and depending on the type of a trap NLSE based model has different potentials and boundary conditions. The above model describes BEC in planar branched structures/traps which can be experimentally created in several physical systems. We note that the Bose-Einstein condensation in networks attracted much attention recently (see, e.g. Refs. [17–22]). Despite the fact that the nonlinear Schrödinger equation is a powerful tool for description of BEC dynamics, all the studies of BEC in networks used so far tight binding and statistical mechanics-based approaches [17–22]. Moreover, most of the studies of this problem do not discuss experimental realization of BEC in networks. Planar BEC can be experimentally realized in surface optical traps [33], superconductive BEC for excitons in planar systems [34] and atom chip films [35]. All these systems can be constructed in branched form, in which the BEC standing wave can be described by Eq. (1). In this case, parameter μ in Eq. (1) corresponds to the chemical potential, while $|\psi|^2$ describes number of atoms in condensate. The transition from a planar to a one-dimensional BEC dynamics corresponding to the shrinking limit of the above fat graph can then be treated similarly to that in the Ref. [36]. Other types of networks and branched systems where planar and one-dimensional

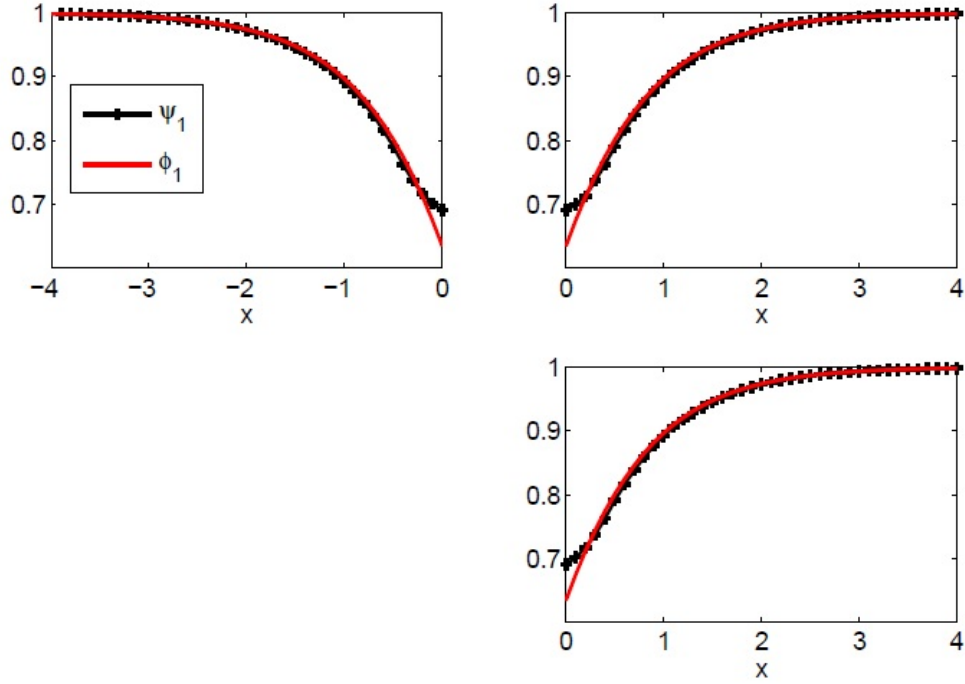


FIG. 4. Dark soliton solution of repulsive NLSE on a fat graph at $\epsilon = 0.3$, $\mu = 1$, $\alpha = 2$

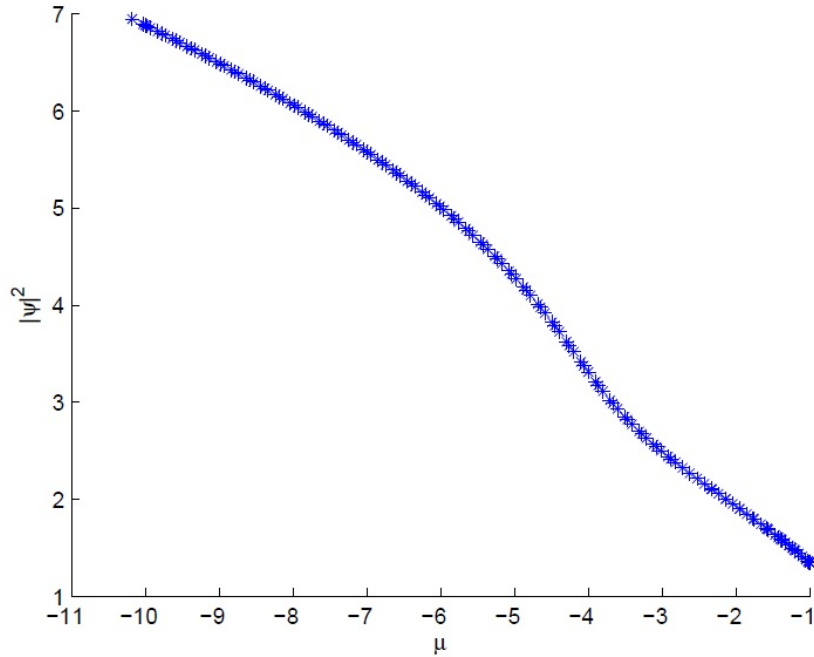


FIG. 5. Chemical potential dependence of the solution of NLSE on a fat graph at the vertex for $\epsilon = 0.5$, $\alpha = 0.5$

BEC can occur are the different types of Josephson junctions [35, 37, 38]. Networks or branched structures of Josephson junctions can be realized in different versions [39–43]. Planar Josephson junctions can be fabricated using different techniques [44, 45]. The standing wave states of the condensate in planar Josephson network can be described by our model. Conducting polymers are also branched systems where BEC can be experimentally realized [22].

Networks of planar optical waveguides and fibers. Optical waveguides are systems where the wave propagation can be described by the linear or nonlinear Schrödinger equation. The stationary nonlinear Schrödinger equation describes standing wave modes in such waveguides. Optical waveguides and fibers can be realized in linear, planar and cylindrical forms. Few papers discuss different ways for experimental realizations of planar waveguides [46,47]. Networks of such waveguides are of importance from a practical importance viewpoint. In particular, modern optical telecommunication technology requires the use of such waveguide networks rather than separate fibers. Earlier branching of nonlinear optical waves in Y-junction optical media was discussed in the Refs. [23,48]. However, these works did not use the above fat or metric graph approaches. In a branched optical system, the function ψ in Eq. (1) describes amplitude of the wave, while quantity μ corresponds to the propagation constant. By exploring the shrinking limit of NLSE on a fat graph, one can determine the minimal width of the fibers for which wave transport in such networks can be considered as one dimensional. Also, the above model can be useful for fabrication the materials and devices with tunable optical properties.

Standing waves in DNA. Remarkable branched structures where solitons and nonlinear waves can appear are DNA strands. Depending on the model and approach, such waves can be described by either the sine-Gordon equation or nonlinear Schrödinger equations [49–51]. Within the so-called Peyrard-Bishop model, the nonlinear dynamics of DNA base pairs are described by the NLSE. The base pair of DNA has a branched structure and can be considered as a star graph. Realistic wave motion in DNA is two-dimensional and the transverse component of the oscillations can play important role in DNA dynamics. Therefore, studying the shrinking limit allows one to determine the boundary between the one- and two-dimensional approaches. The two dimensional model of DNA dynamics was considered earlier in [49–51].

Conducting polymers. Polymers are molecular networks having complicated topology whose structural units can be often reduced to a star graph. One type of polymer, which are called conjugated polymers, can exhibit metallic or semiconductor properties. Conducting polymers have attracted much attention due their wide range of electronic applications [24,25]. Charge and spin excitations and their transport in conducting polymers can have solitons and standing nonlinear waves described by NLSE. The motion of such waves is usually two-dimensional but can be effectively described using a one dimensional form. Due to the finite size of its branching points, a polymer chain can be considered as a fat graph. The above NLSE on fat graph and its shrinking limit can be a powerful tool for describing charge and spin carriers dynamics in conducting polymers. This can be an especially effective method for charge transport, recombination and separation in polymer-based materials such as light-emitting diodes, organic solar cells etc.

Capillary networks. Solitons and nonlinear standing waves appear in the hydrodynamics of capillary systems, where fluid dynamics can be described by the NLSE [52]. A planar version of capillary systems as discussed in [52–57]. Nonlinear wave in branched capillary systems should be described by NLSE on a fat graph. The connection point of such network has finite size. Our model allows one to estimate the characteristic width of a capillary tube for which which wave motion in such network could be considered linear.

5. Conclusions

In this work, we studied the stationary nonlinear Schrödinger equation on fat graphs by focusing on metric graph transition in the shrinking limit. Analytical estimates for the boundary condition shrinking are obtained. It is shown that in the shrinking limit, fat graph boundary conditions reproduce those for the metric graph. Such a convergence is also shown on the basis of numerical treatment of NLSE on a fat graph. Detailed discussion of the potential application of the model to BEC in networks, branched optical materials, DNA double helix, conducting polymers and capillary networks is discussed. The model can be extended for other fat graph topologies, such as tree, ring and complete graphs. The above study allows one to determine the border between planar and linear motion in branched systems, where particle and wave transport is effectively considered as one dimensional. The results of this paper can be useful for problems of engineering materials and devices based on branched optical and electronic structures.

Acknowledgement

This work is supported by a grant from the Volkswagen Foundation. We thank Hannes Uecker for his valuable comments on the formulation of the problem and for the help in the numerical part of the work.

References

- [1] Albert R., Barabasi A-L. Statistical mechanics of complex networks. *Rev. Mod.Phys. A*, 2002, **74**, P. 47.
- [2] Cohen R., Havlin S. *Complex Networks: Structure, Robustness and Function*. Cambridge University Press, 2010.

- [3] Sobirov Z., Matrasulov D., Sabirov K., Sawada S., and Nakamura K. Integrable nonlinear Schrödinger equation on simple networks: Connection formula at vertices. *Phys. Rev. E*, 2010, **81**, P. 066602.
- [4] Adami R., Cacciapuoti C., Finco D., and Noja D. Fast solitons on star graphs. *Rev. Math. Phys.*, 2011, **23**, P. 409.
- [5] Adami R., Cacciapuoti C., Finco D., and Noja D. Stationary states of NLS on star graphs. *Europhys. Lett.*, 2012, **100**, P. 10003.
- [6] Adami R., Cacciapuoti C., Finco D., and Noja D. On the structure of critical energy levels for the cubic focusing NLS on star graphs. *J. Phys. A: Math. Theor.*, 2012, **45**, P. 192001.
- [7] Adami R., Noja D., and Ortoleva C. Orbital and asymptotic stability for standing waves of a NLS equation with concentrated nonlinearity in dimension three. *J. Math. Phys.*, 2013, **54**, P. 013501.
- [8] Sabirov K.K., Sobirov Z.A., Babajanov D., and Matrasulov D.U. Stationary nonlinear Schrödinger equation on simplest graphs. *Phys. Lett. A*, 2013, **377**, P. 860.
- [9] Noja D. Nonlinear Schrödinger equation on graphs: recent results and open problems. *Philos. Trans. R. Soc. A*, 2014, **372**, P. 20130002.
- [10] Cacciapuoti C., Finco D., and Noja D. Topology-induced bifurcations for the nonlinear Schrödinger equation on the tadpole graph. *Phys. Rev. E*, 2015, **91**, P. 013206.
- [11] Exner P., Post O. Approximation of quantum graph vertex couplings by scaled Schrödinger operators on thin branched manifolds. *J. Phys. A: Math. Theor.*, 2009, **42**, P. 415305.
- [12] Dell'Antonio G.F. and Costa E. Effective Schrödinger dynamics on ϵ -thin Dirichlet waveguides via quantum graphs: I. Star-shaped graphs. *J. Phys. A, Math. Theor.*, 2010, **43**, P. 474014, 23.
- [13] Exner P., Post O. A General Approximation of Quantum Graph Vertex Couplings by Scaled Schrödinger Operators on Thin Branched Manifolds. *Commun. Math. Phys.*, 2013, **322**, P. 207–227.
- [14] Uecker H., Grieser D., Sobirov Z., Babajanov D. and Matrasulov D. Soliton transport in tubular networks: Transmission at vertices in the shrinking limit. *Phys. Rev. E*, 2015, **91**, P. 023209.
- [15] Caputo J.-G., Dutykh D. Nonlinear waves in networks: a simple approach using the sine-Gordon equation. *Phys. Rev. E*, 2014, **90**, P. 022912.
- [16] Kosugi S. Semilinear Elliptic Equations on Thin Network-Shaped Domains with Variable Thickness. *Journal of Differential Equations*, 2002, **183**, P. 165.
- [17] Bianconi G., Barabasi A.-L. Bose-Einstein Condensation in Complex Networks. *Phys. Rev. Lett.*, 2001, **86**, P. 5632.
- [18] Burioni R., Cassi D., Meccoli I., Rasetti M., Regina S., Sodano P. and Vezzani A. Bose-Einstein condensation in inhomogeneous Josephson arrays. *Eur. Phys. Lett.*, 2000, **52**, P. 251.
- [19] Burioni R., Cassi Rasetti D., Sodano P. and Vezzani A. Bose-Einstein condensation on inhomogeneous complex networks. *J. Phys. B*, 2001, **34**, P. 4697.
- [20] Brunelli I., Giusiano G., Mancini F.P., Sodano P. and Trombettoni A. Topology-induced spatial Bose-Einstein condensation for bosons on star-shaped optical networks. *J. Phys. B*, 2004, **37**, P. S275.
- [21] Burioni R., Cassi D., Sodano P., Trombettoni A. and Vezzani A. Topological filters and high-pass/low-pass devices for solitons in inhomogeneous networks. *Phys. Rev. E*, 2006, **73**, P. 066624.
- [22] Castellanos E., Chacon-Acosta G. Polymer Bose-Einstein condensates. *Phys. Lett. B*, 2013, **722**, P. 119.
- [23] Leo G., Assanto G. Multiple branching of vectorial spatial solitary waves in quadratic media. *Opt. Commun.*, 1998, **146**, P. 356.
- [24] Heeger A.J., Kivelson S., Schrieffer J.R., and Su W.-P. Solitons in conducting polymers. *Rev. Mod. Phys.*, 1988, **60**, P. 781.
- [25] Heeger A.J. Semiconducting and metallic polymers: The fourth generation of polymeric materials. *Rev. Mod. Phys.*, 2001, **73**, P. 681.
- [26] Exner P. and Post O. Convergence of spectra of graph-like thin manifolds. *J. Geom. Phys.*, 2005, **54**, P. 77.
- [27] Molchanov S. and Vainberg B. Scattering Solutions in Networks of Thin Fibers: Small Diameter Asymptotics. *Commun. Math. Phys.*, 2007, **273**, P. 533.
- [28] Exner P. and Post O. Convergence of resonances on thin branched quantum wave guides. *J. Math. Phys.*, 2007, **48**, P. 092104.
- [29] Grieser D., *Analysis on graphs and its applications*. Isaac Newton Institute, Cambridge, UK, January 8 – June 29, 2007 (AMS, 2008), P. 565–593.
- [30] Post O. *Spectral analysis on graph-like spaces*. Berlin: Springer, 2012.
- [31] Jimbo S. Singular perturbation of domains and semilinear elliptic equations. *J. Fac. Sci., U. Tokyo, Sect. A. Math.*, 1988, **35** P. 27.
- [32] Gilbarg D., Trudinger N., *Elliptic Partial Differential Equations of Second Order*. Springer, 1977.
- [33] Butov L.V., Lai C.W., Ivanov A.L., Gossard A.C., Chemla D.S. Towards Bose-Einstein condensation of excitons in potential traps. *Nature*, 2002, **417**, P. 47.
- [34] Ben-Aryeh Y. Bose-Einstein Condensation of Excitons in Planar Systems and Superconductive Phase Transition Temperature. *J. Supercond. and Nov. Magn.*, 2015, **28**, P. 3211.
- [35] Gati R. and Oberthaler M.K. Molecular imaging using recolliding electrons. *J. Phys. B*, 2007, **40**, P. R61.
- [36] Carr L.D., Leung M.A. and Reinhardt W.P. Dynamics of the Bose-Einstein condensate: quasi-one-dimension and beyond. *J. Phys. B*, 2000, **33**, P. 3983.
- [37] Burger F.S.C.S., Fort C., Maddaloni P., Minardi F., Trombettoni A., Smerzi A., and Inguscio M. Josephson junction arrays with Bose-Einstein condensates. *Science*, 2001, **293**, P. 843.
- [38] Levy S., Lahoud E., Shomroni I., and Steinhauer J. The ac and dc Josephson effects in a Bose-Einstein condensate. *Nature*, 2007, **449**, P. 579.
- [39] Hasegawa A., *Optical Solitons in Fibers*. Springer, 1990.
- [40] Hall B.V., Whitlock S., Scharnberg F., Hannaford P. and Sidorov A. A permanent magnetic film atom chip for Bose-Einstein condensation. *J. Phys. B*, 2006, **39**, P. 27.
- [41] Rychtarik D., Engeser B., Nagerl H.-C., and Grimm R. Two-Dimensional Bose-Einstein Condensate in an Optical Surface Trap. *Phys. Rev. Lett.*, 2004, **92**, P. 173003.
- [42] De Luca R., Romeo F. Electrodynamic response of current-biased elementary cubic networks of Josephson junctions. *Phys. Rev. B*, 2002, **66**, P. 024509.
- [43] Giuliano D. and Sodano P. Pairing of Cooper pairs in a Josephson junction network containing an impurity. *Europhys. Lett.*, 2013, **103**, P. 57006.

- [44] Krasnov V.M., Ericsson O., Intiso S., Delsing P., Oboznov V.A., Prokofiev A.S., Ryazanov V.V. Planar SFS Josephson junctions made by focused ion beam etching. *Physica C*, 2005, **418**, P. 16.
- [45] Nussbaum J., Schmidt Th.L., Bruder Ch., and Tiwari R.P. Josephson effect in normal and ferromagnetic topological insulator planar, step and edge junctions. *Phys. Rev. B*, 2014, **90**, P. 045413.
- [46] Shandarov, Kip D., Wesner M. and Hukriede J. Observation of dark spatial photovoltaic solitons in planar waveguides in lithium niobate. *J. Opt. Soc. Am. B*, 2000, **2**, P. 500.
- [47] Eisenberg H.S., Morandotti R., Silberberg Y., Arnold J.M., Pennelli G., and Aitchison J.S. Optical discrete solitons in waveguide arrays. I. Soliton formation. *J. Opt. Soc. Am. B*, 2002, **19**, P. 2938.
- [48] Santos M.C. Dynamic Y-branched structures in quadratic nonlinear media. *Opt. Commun.*, 2000, **180**, P. 167.
- [49] Yakushevich L.V., *Nonlinear Physics of DNA*. Wiley, Chichester, 2004.
- [50] Peyrard M. Nonlinear dynamics and statistical physics of DNA. *Nonlinearity*, 2004, **17**, P. R1.
- [51] Zdravkovic S., Sataric M.V. Nonlinear Schrödinger equation and DNA dynamics. *Phys. Lett. A*, 2008, **373**, P. 126–132.
- [52] Rasmussen J. and Stiassnie M. Multiple gravity-capillary wave-forms near the minimum phase-speed. *J. Fluid. Mech.*, 1999, **384**, P. 93.
- [53] Sobirov Z.A., Akhmedov M.I., Karpova O.V., Jabbarova B. Linearized KdV equation on a metric graph. *Nanosystems: Physics, Chemistry, Mathematics*, 2015, **6**(6), P. 757–761.
- [54] Vidal E.J.G.G., Lima R.P.A., and Lyra M.L. Bose-Einstein condensation in the infinitely ramified star and wheel graphs. *Phys. Rev. E*, 2011, **83**, P. 061137.
- [55] de Oliveira I.N., dos Santos T.B., de Moura F.A.B.F., Lyra M.L., and Serva M. Critical behavior of the ideal-gas Bose-Einstein condensation in the Apollonian network. *Phys. Rev. E*, 2013, **88**, P. 022139.
- [56] Dalfovo F., Giorgini S., Pitaevskii L.P., and Stringari S. Theory of Bose-Einstein condensation in trapped gases. *Rev. Mod. Phys. A*, 1999, **71**, P. 463.
- [57] Muto V., Lomdahl P.S., and Christiansen P.L. Two-dimensional discrete model for DNA dynamics: Longitudinal wave propagation and denaturation. *Phys. Rev. A*, 1990, **42**, P. 7452.

Ultradiscretization of reaction-diffusion type partial differential equations exhibiting pulse propagation

Y. Yamazaki* and S. Ohmori

Department of Physics, Department of Physics, School of Advanced Science and Engineering,
Waseda University, Shinjuku, Tokyo 169-8555, Japan

*yoshy@waseda.jp

PACS 05.90.+m, 02.90.+p

DOI 10.17586/2220-8054-2017-8-1-38-41

Cellular automaton rules are derived from a set of reaction-diffusion partial differential equations by means of ultradiscretization method. The rules reproduce dynamical properties of pulse: annihilation, soliton-like preservation and periodic generation with a pacemaker.

Keywords: ultradiscretization, tropical discretization, pulse dynamics, cellular automaton, reaction-diffusion systems.

Received: 20 July 2016

Revised: 30 July 2016

1. Introduction: ultradiscretization

Now we carry out ultradiscretization of the following reaction-diffusion system [1,2]:

$$\begin{cases} \tau_u \frac{\partial u}{\partial t} = D_u \frac{\partial^2 u}{\partial x^2} - (u - \alpha)(u - \beta)(u - \gamma) - v, & (1) \\ \tau_v \frac{\partial v}{\partial t} = D_v \frac{\partial^2 v}{\partial x^2} + \kappa u - \lambda v + i, & (2) \end{cases}$$

where $\tau_u, \tau_v, D_u, D_v, \kappa, \lambda$, and i are positive constants. α, β , and γ are also positive and satisfy $0 < \alpha < \beta < \gamma$.

For Eq. (1), we first adopt the following tropical discretization [3,4]:

$$u_j^{n+1} = w_j^n \frac{w_j^n + F(w_j^n)\Delta t}{w_j^n + G(w_j^n, v_j^n)\Delta t}, \quad (3)$$

where $w_j^n = \mu(u_{j+1}^n + u_{j-1}^n) + (1 - 2\mu)u_j^n$ and $\mu = \frac{D_u \Delta t}{\tau_u (\Delta x)^2}$. F and G are defined as $F(u) = \frac{1}{\tau_u} [(\alpha + \beta + \gamma)u^2 + \alpha\beta\gamma]$ and $G(u, v) = \frac{1}{\tau_u} [u^3 + (\alpha\gamma + \alpha\beta + \beta\gamma)u + v]$, respectively. For Eq. (3), the ultradiscrete limits [5–8]:

$$\begin{cases} \lim_{\varepsilon \rightarrow +0} \varepsilon \log(e^{A/\varepsilon} + e^{B/\varepsilon} + \dots) = \max(A, B, \dots), & (4) \\ \lim_{\varepsilon \rightarrow +0} \varepsilon \log(e^{A/\varepsilon} \cdot e^{B/\varepsilon} \dots) = A + B + \dots \end{cases}$$

are carried out after the following variable transformations are performed:

$$\begin{cases} \Delta t / \tau_u = e^{T/\varepsilon} / (\mu^{n+1})^2, & u_j^n = \mu^n e^{U_j^n / \varepsilon}, & v_j^n = (\mu^{n+1})^3 e^{V_j^n / \varepsilon}, \\ \alpha = \mu^{n+1} e^{A/\varepsilon}, & \beta = \mu^{n+1} e^{B/\varepsilon}, & \gamma = \mu^{n+1} e^{\Gamma/\varepsilon}, \\ (1 - 2\mu) / \mu = e^{M/\varepsilon}. \end{cases} \quad (5)$$

Then, the ultradiscrete equation is obtained by considering $A < B < \Gamma$ as:

$$\begin{aligned} U_j^{n+1} &= W_j^n + \max\{W_j^n, T + \max(\Gamma + 2W_j^n, A + B + \Gamma)\} \\ &\quad - \max\{W_j^n, T + \max(3W_j^n, B + \Gamma + W_j^n, V_j^n)\}, \end{aligned} \quad (6)$$

where $W_j^n = \max(U_{j+1}^n, M + U_j^n, U_{j-1}^n)$.

Next, the discretized equation of Eq. (2):

$$\tau_v \frac{v_j^{n+1} - v_j^n}{\Delta t} = D_v \frac{v_{j+1}^n - 2v_j^n + v_{j-1}^n}{(\Delta x)^2} + \kappa u_j^n - \lambda v_j^n + i \quad (7)$$

can be rewritten as follows for ultradiscretization:

$$v_j^{n+1} = \theta(v_{j+1}^n + v_{j-1}^n) + \left(1 - 2\theta - \frac{\lambda\Delta t}{\tau_v}\right)v_j^n + \frac{\Delta t\kappa}{\tau_v}u_j^n + \frac{\Delta ti}{\tau_v}, \quad (8)$$

where $\theta = (D_v\Delta t)/((\Delta x)^2\tau_v)$. Applying the variable transformations

$$v_j^n = \theta^n e^{V_j^n/\varepsilon}, \quad \frac{1}{\theta} \left(1 - 2\theta - \frac{\lambda\Delta t}{\tau_v}\right) = e^{N/\varepsilon}, \quad \frac{\Delta t\kappa}{\tau_v} = \frac{\theta^{n+1}e^{S/\varepsilon}}{\mu^n}, \quad \frac{\Delta ti}{\tau_v} = \theta^{n+1}e^{I/\varepsilon}, \quad (9)$$

where $(\mu^{n+1})^3 = \theta^n$, we obtain the following ultradiscrete equation through Eq. (4):

$$V_j^{n+1} = \max(L_j^n, S + U_j^n, I). \quad (10)$$

Here, $L_j^n = \max(V_{j+1}^n, N + V_j^n, V_{j-1}^n)$. Then, we obtain the set of ultradiscrete equations (6) and (10) from Eqs. (1) and (2).

The transition from W_j^n to U_j^{n+1} using Eq. (6) is shown in Fig. 1 as a function of W_j^n and V_j^n . Fig. 1 shows that the convergence of U_j^n to A or Γ depends on the value of V_j^n . There is a time n at which the state U_j^n becomes A or Γ in regions I and IV. This fact reflects the ultradiscrete bistability in Eq. (6). Here, ultradiscrete bistability means that for the initial value U_j^0 , which is different from the two stable points, there exists a finite time n such that the state U_j^n becomes one of the two stable points. Note also that $U_j^{n+1} = A$ when $V_j^n = 3W_j^n + \Gamma - A$ for $W_j^n > (A + B)/2$ and $U_j^{n+1} = \Gamma$ when $V_j^n = 3W_j^n$ for $W_j^n > (B + \Gamma)/2$.

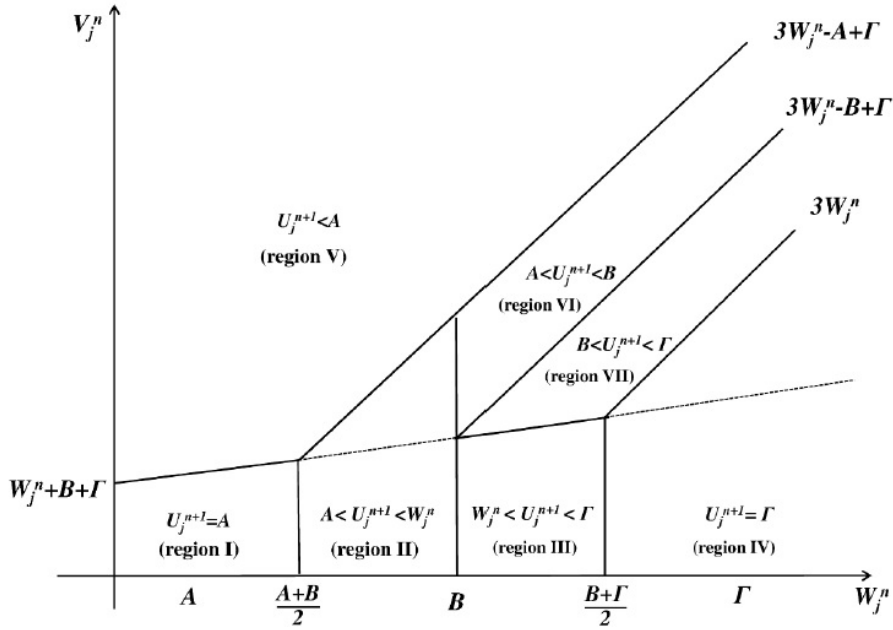


FIG. 1. Transition diagram of U_j^n from n to $n + 1$. The regions (I – VII) are separated by solid lines

2. Cellular automaton rules

In order to derive two-state cellular automaton (CA) rules from the above set of ultradiscrete equations (6) and (10), we assume the following additional relation:

$$\text{If } W_j^n = A, \text{ then } U_j^{n+1} \equiv A. \quad (11)$$

Now we consider the conditions $M = 0$ or $M \leq A - \Gamma$, $T \geq \max\{0, -(A + B + \Gamma)\}$, $N = 0$, $S = 3\Gamma - A$, and $I < 3\Gamma$. Under these conditions, $W_j^n, U_j^n \in \{A, \Gamma\}$ is confirmed.

When $V_{j\pm 1}^n, V_j^n \leq 3\Gamma - A + U_j^n$, we obtain from Eq. (10)

$$V_j^{n+1} = 3\Gamma - A + U_j^n. \quad (12)$$

From $W_j^n \in \{A, \Gamma\}$ and $T \geq \max\{0, -(A + B + \Gamma)\}$, Eq. (6) can be rewritten as

$$U_j^{n+1} = W_j^n + \max(T + \Gamma + 2W_j^n, T + A + B + \Gamma) - \max(T + 3W_j^n, T + B + \Gamma + W_j^n, T + V_j^n)$$

using the relation $\Gamma < T + 3\Gamma$. Considering Eq. (12), this equation is described as the following function of U_j^n , $U_{j\pm 1}^n$, and U_j^{n-1} :

$$U_j^{n+1} = W_j^n + \max(\Gamma + 2W_j^n, A + B + \Gamma) - \max(3W_j^n, B + \Gamma + W_j^n, 3\Gamma - A + U_j^{n-1}), \quad (13)$$

where $W_j^n = \max(U_{j+1}^n, U_j^n + M, U_{j-1}^n)$. Taking Eq. (11) into account, we obtain the following CA rules.

$$\text{If } W_j^n = \begin{cases} A, & \text{Eq.(11)} \\ \Gamma, & \text{Eq.(13)} \end{cases} \text{ is adopted.} \quad (14)$$

Note that Eq. (14) produces the following two CA rules depending on the conditions of M .

When $M = 0$, the rule shown in Table 1 is obtained from Eq. (14). The values of $\{U_j^0\}$ and $\{U_j^1\}$ have to be given as the initial conditions. Fig. 2 shows the spatiotemporal patterns obtained from Table 1 for two different initial conditions. Black and white cells correspond to Γ and A , respectively. The initial conditions are set as follows. (a) For j and k ($> j$), $U_j^0 = U_j^1 = \Gamma$ and $U_k^0 = U_k^1 = \Gamma$. Otherwise, $U^0 = U^1 = A$. (b) Using the same j and k as in (a), $U_j^0 = U_j^1 = \Gamma$ and $U_{k+1}^0 = U_{k+1}^1 = \Gamma$. Otherwise, $U^0 = U^1 = A$. It is found that the two pulse-like cells with $U = \Gamma$ are created periodically from the initial cell with $U = \Gamma$ and that the two pulse-like cells propagate in both directions. The difference between Figs. 2(a) and 2(b) is the initial relative positions between the two pulse-like cells. Regardless of such a difference in the initial conditions, both Figs. 2(a) and 2(b) show that the two pulses are annihilated when they collide with each other.

TABLE 1. CA rule given by Eq. (14) with $M = 0$. A value of U_j^{n+1} in parentheses is calculated using the value of U_j^{n-1} in parentheses

| | | | | | | | | |
|-------------------------------|--------------------------|---------------------|---------------------|---------------------|----------------|----------------|----------------|-------------|
| U_j^{n-1} | $\Gamma(A)$ | $\Gamma(A)$ | $\Gamma(A)$ | $\Gamma(A)$ | $\Gamma(A)$ | $\Gamma(A)$ | $\Gamma(A)$ | $\Gamma(A)$ |
| $U_{j+1}^n, U_j^n, U_{j-1}^n$ | Γ, Γ, Γ | Γ, Γ, A | Γ, A, Γ | A, Γ, Γ | Γ, A, A | A, Γ, A | A, A, Γ | A, A, A |
| W_j^n | Γ | Γ | Γ | Γ | Γ | Γ | Γ | A |
| U_j^{n+1} | $A(\Gamma)$ | $A(\Gamma)$ | $A(\Gamma)$ | $A(\Gamma)$ | $A(\Gamma)$ | $A(\Gamma)$ | $A(\Gamma)$ | $A(A)$ |

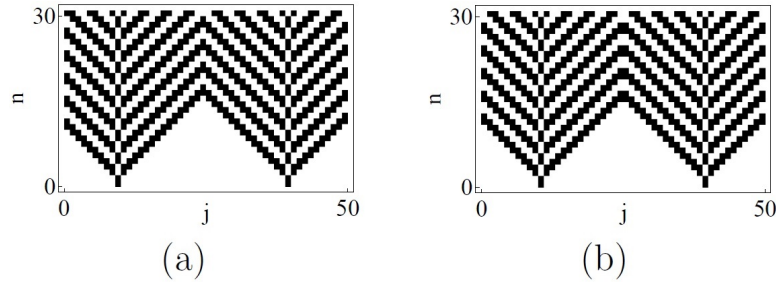


FIG. 2. Spatiotemporal patterns obtained according to Table 1 from two cells with $U = \Gamma$ (50 cells and 30 time steps). The difference between (a) and (b) is the initial relative position between the two cells with $U = \Gamma$. Time steps proceed from bottom to top. Black and white cells correspond to Γ and A , respectively

Alternatively, when $M \leq A - \Gamma$, $W_j^n = \max(U_{j+1}^n, U_{j-1}^n)$, the rule shown in Table 2 is obtained from Eq. (14). Fig. 3 shows spatiotemporal patterns obtained from Table 2 for two different initial conditions. Black and white cells correspond to Γ and A , respectively. As the initial conditions, we set the followings: (a) For j and k ($> j + 2$), $U_j^0 = U_{j+1}^1 = \Gamma$ and $U_k^0 = U_{k-1}^1 = \Gamma$. Otherwise, $U^0 = U^1 = A$. (b) Using the same j and k as in (a), $U_j^0 = U_{j+1}^1 = \Gamma$ and $U_{k+1}^0 = U_k^1 = \Gamma$. Otherwise, $U^0 = U^1 = A$. Figs. 3(a) and 3(b) show that there are two types of collision of propagating cells with $U = \Gamma$, namely, soliton-like preservation and annihilation, respectively. The emergence of these two different types of collision depends on the relative positions between the two pulse-like cells. If a pulse-like cell at U_j^n encounters another one at U_{j+1}^n , they pass through each other, and the pulses are preserved. However, if the two pulses exist at the same position at the same time, they annihilate.

TABLE 2. CA rule given by Eq. (14) with $M \leq A - \Gamma$. A value of U_j^{n+1} in parentheses is calculated using the value of U_j^{n-1} in parentheses

| | | | | | | | | |
|-------------------------------|--------------------------|---------------------|---------------------|---------------------|----------------|----------------|----------------|-------------|
| U_j^{n-1} | $\Gamma(A)$ | $\Gamma(A)$ | $\Gamma(A)$ | $\Gamma(A)$ | $\Gamma(A)$ | $\Gamma(A)$ | $\Gamma(A)$ | $\Gamma(A)$ |
| $U_{j+1}^n, U_j^n, U_{j-1}^n$ | Γ, Γ, Γ | Γ, Γ, A | Γ, A, Γ | A, Γ, Γ | Γ, A, A | A, Γ, A | A, A, Γ | A, A, A |
| W_j^n | Γ | Γ | Γ | Γ | Γ | A | Γ | A |
| U_j^{n+1} | $A(\Gamma)$ | $A(\Gamma)$ | $A(\Gamma)$ | $A(\Gamma)$ | $A(\Gamma)$ | $A(A)$ | $A(\Gamma)$ | $A(A)$ |

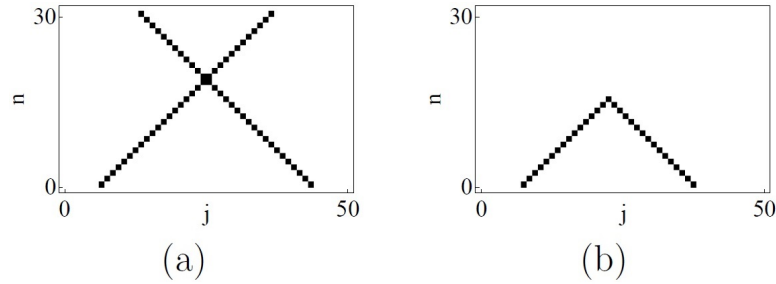


FIG. 3. Spatiotemporal patterns obtained from Table II. (a) soliton-like preservation and (b) pulse annihilation (50 cells and 30 time steps). Time steps proceed from bottom to top. Black and white cells correspond to Γ and A , respectively

3. Conclusion

We have derived the ultradiscretized equations [Eqs. (6) and (10)] from the reaction-diffusion system Eqs. (1) and (2). By considering the V dependence on the state transition of U , we have obtained the CA rules from the ultradiscretized equations. It was shown that some CA rules reproduce the spatiotemporal properties of pulse dynamics: pulse annihilation, periodic pulse generation from a pacemaker and soliton-like preservation. (More details are shown in ref. [9].)

Acknowledgements

The authors are grateful to Professor Daisuke Takahashi, Professor Tomoyuki Yamamoto, and Emeritus Professor Akihiko Kitada for useful discussions and encouragement.

References

- [1] Ohta T., Hayase Y., and Kobayashi R. Spontaneous formation of concentric waves in a two-component reaction-diffusion system. *Phys. Rev. E.*, 1996, **54**, P. 6074.
- [2] Hayase Y. Collision and Self-Replication of Pulses in a Reaction Diffusion System. *J. Phys. Soc. Jpn.*, 1997, **66**, P. 2584.
- [3] Murata M. Tropical discretization: ultradiscrete FisherKPP equation and ultradiscrete AllenCahn equation. *J. Differ. Equations Appl.*, 2013, **19**, P. 1008.
- [4] Murata M. Multidimensional traveling waves in the AllenCahn cellular automaton. *J. Phys. A.*, 2015, **48**, P. 255202.
- [5] Tokihiro T., Takahashi D., Matsukidaira J. and Satsuma J. From Soliton Equations to Integrable Cellular Automata through a Limiting Procedure. *Phys. Rev. Lett.*, 1996, **76**, P. 3247.
- [6] Grammaticos B., Ohta Y., Ramani A., Takahashi D. and Tamizhmani K.M. Cellular automata and ultra-discrete Painlevé equations. *Phys. Lett. A.*, 1997, **226**, P. 53.
- [7] Matsuya K. and Murata M. Spatial pattern of discrete and ultradiscrete Gray-Scott model. *Discrete Contin. Dyn. Syst. Ser. B.*, 2015, **20**, P. 173.
- [8] Takahashi D., Shida A. and Usami M. On the pattern formation mechanism of (2+1)D max-plus models. *J. Phys. A.*, 2001, **34**, P. 10715.
- [9] Ohmori S., Yamazaki Y. Cellular Automata for Spatiotemporal Pattern Formation from ReactionDiffusion Partial Differential Equations. *J. Phys. Soc. Jpn.*, 2016, **85**, P. 014003.

Tunable wave packet transport in branched periodic lattices with time-dependent external field

Jambul Yusupov

Turin Polytechnic University in Tashkent, 17. Niyazov Str., 100095, Tashkent, Uzbekistan

j.yusupov@polito.uz

PACS 03.65.Aa, 37.10.Jk, 05.60.Gg

DOI 10.17586/2220-8054-2017-8-1-42-47

We study the dynamics of a Gaussian wave packet in a branched system of periodic lattices driven by an external time-dependent field. Motivated by recent numerical experiments with the manipulation of wave packet transmission in quantum star graph, we provide further discussion based on some achievements obtained from one-dimensional tight-binding models with arbitrary external time-dependent fields and on numerical calculations.

Keywords: quantum graph, periodically-driven system, directed transport, wave packet dynamics.

Received: 12 August 2016

Revised: 3 September 2016

1. Introduction

Quantum particle dynamics in discrete and branched structures is of importance for many topics in condensed matter and nanoscale physics. Over past two decades a powerful method based on the use of so-called quantum graphs has been developed and has found numerous applications (see, e.g., [1,2] for review). This approach uses wave equations with the boundary conditions given on metric graphs. The latter are the set of bonds connected to each other at branching points often called vertices [1,3]. Such a method allows one to obtain complete solution of the problem for a given network topology and different boundary conditions. The main issue appearing in the study of particle transport in such systems is the problem of vertex scattering and/or transmission which plays crucial role in the manifestation of diffusive or ballistic transport in networks and discrete systems. Then, a key problem in the study of particle in branched systems becomes tunable transport where the tuning of particle motion from ballistic to diffusive or vice-versa is possible. Such a goal can be achieved by acting on the system with an external perturbation, such as electric or magnetic fields. For example, under the influence of static force, the system (called also tilted lattice in literature) may exhibit coherent oscillations, which is well-studied in tight-binding approach [4] and was experimentally confirmed by several groups [5–8]. The time-dependent tilted lattice allows one to direct the wave packet, which can be achieved by the modulation of the lattice amplitude [9–11] and/or by the modulation of an external field [12–16].

Recent progress made in the fabrication of quantum devices that can be modeled by branched and discrete structures motivate the study transport problems in quantum graphs [3]. Quantum particle dynamics in graphs have been studied in several works [17,18]. The concept of directed transport has been extended to quantum graphs and the possibility to manipulate the direction of the motion of Gaussian wave packet (GWP) through the bifurcation point of a quantum star graph has been shown in a recent numerical experiment [19].

In this paper, we study a GWP dynamics in branched periodic lattices under the influence of different external time-dependent fields. Branching is considered as being in the form of a metric star graph. In particular, we apply the results from the Ref. [16], where expression for trajectory of GWP center in the infinite chain driven by a time-dependent homogeneous field is obtained using the tight-binding model. We compare these results with the solution in the continuous model, which is considered in [19]. This paper is organized as follows. In the next section, we briefly recall the model for quantum star graph. In section 3, we discuss in detail wave packet dynamics in connected lattices with different modulated external fields. Finally, section 4 presents some concluding remarks.

2. Model

Our model is the same as that considered in Ref. [19], where directed transport in driven star graph has been studied. Each of the arms of the star graph is vested with a periodic lattice potential given by $V(x) = V_0 \cos(2\pi x/d)$, and they are connected at a common (central) vertex. We assign the coordinate x to each arm, which indicates the position along the arm; x takes the value 0 at the common vertex. Moreover, each arm is

driven by a time-dependent external field $F_j(t) = f_j \sin(\omega t + \phi_j)$, also being arm-dependent, and the parameters f_j and ϕ_j are used to manipulate the GWP transition through the central vertex.

The time-dependent Schrödinger equation (in the units $\hbar = 2m = 1$) for a star graph with N arms is:

$$i \frac{\partial}{\partial t} \Psi_j(x, t) = -\frac{\partial^2}{\partial x^2} \Psi_j(x, t) + [V(x) + F_j(t)x] \Psi_j(x, t), \quad \forall t, \quad 0 \leq x \leq L_j, \quad j = 1, \dots, N. \quad (1)$$

The imposed conditions are:

$$\begin{cases} \Psi_1(L_1, t) = \Psi_2(L_2, t) = \dots = \Psi_N(L_N, t) = 0, \\ \Psi_1(0, t) = \Psi_2(0, t) = \dots = \Psi_N(0, t), \\ \sum_{j=1}^N \frac{\partial}{\partial x} \Psi_j(x, t) \Big|_{x=0} = 0, \end{cases} \quad (2)$$

which imply Dirichlet boundary conditions at the non-connected edges in the form of continuity and current conservation at the vertex.

Referring to the results of the paper presented in Fig. 1, one can see dispersion of the packet after collision with vertex. This phenomenon is the starting point for the study of bifurcation at the graph vertex. Numerical method used in this work for the solution of the Schrödinger equation is the same as that in [19].

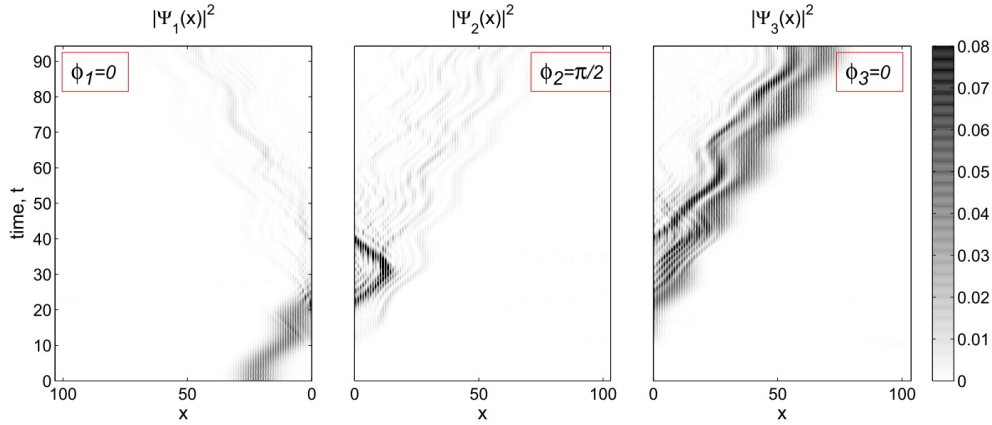


FIG. 1. Contour plot of the probability density for the three arm star graph, where the driving external field is given by $F_j(t) = f_j \sin(\omega t + \phi_j)$ with $f_1 = -f_2 = -f_3 = \pi/10$, $\omega = 0.2$. The three columns correspond to the arms of the star graph. The x -coordinate of the first arm is reversed. (Fig. from [19])

3. Wave packet dynamics

The time evolution of Gaussian wave packet (GWP):

$$\Psi(x, t = t_0) = \frac{1}{\sqrt{\sqrt{\pi}\sigma_0}} \exp\left(-\frac{(x-x_0)^2}{2\sigma_0^2} + ik_0x\right),$$

in a system driven by an arbitrary time-dependent external field was studied in [16] using the tight-binding approximation. According to this paper, in the case of a chain, momentum changes as:

$$k = k_0 - I(t, t_0), \quad (3)$$

where

$$I(t, t_0) = \int_{t_0}^t F(\tau) d\tau, \quad (4)$$

for arbitrary $F(t)$. As we consider the time-dependence of the external field given as $F(t) = f \sin(\omega t + \phi)$, one obtains:

$$I(t, t_0) = -\frac{f}{\omega} [\cos(\omega t + \phi) - \cos(\omega t_0 + \phi)]. \quad (5)$$

In the case of a wide wave packet, for the group velocity we have:

$$v_G(t) = 2J \sin [k_0 - I(t)], \quad (6)$$

where J is hopping amplitude. Consequently, the displacement is given by:

$$D(t) = \int_0^t v_G(\tau) d\tau. \quad (7)$$

Furthermore, this expression is used for the calculation of GWP trajectory, which is compared with the solution of the Schrödinger equation in continuous model.

3.1. Trajectory of GWP center

Without the loss of generality, we can consider the case of two bonds connected at one common vertex. Each bond is vested with periodic potential and driven by the modulated external field. For this system, we have no reflection at the common vertex (due to the Neumann boundary conditions), and when parameters of the fields are chosen as $f_1 = -f_2 = \pi/10$, $\phi_1 = \phi_2 = 0$, $\omega = 0.2$ one is faced with the chain problem. The signs of parameters f_1 and f_2 are chosen such that the field points globally in one direction. According to the above derivations, one can evaluate the trajectory of the GWP center and compare them with the solution of the Schrödinger equation (Fig. 2).

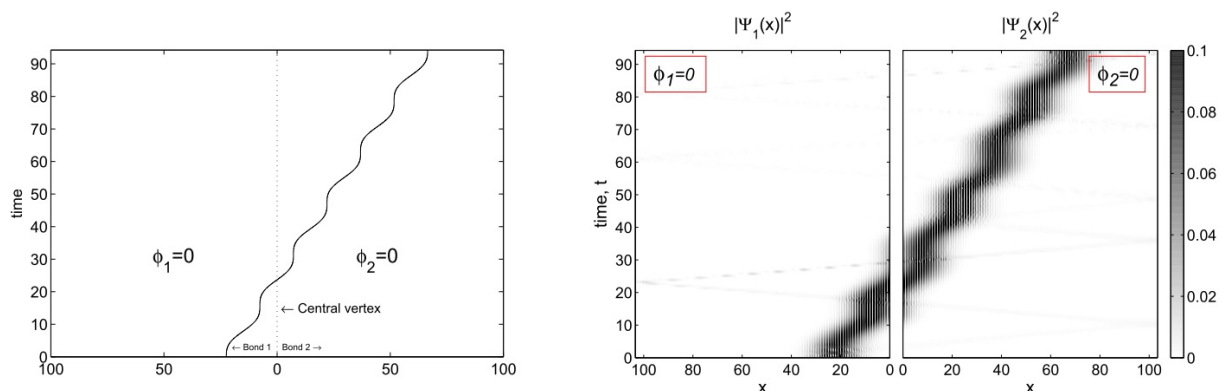


FIG. 2. A GWP center's trajectory (left) and the solution of the Schrödinger equation for two connected bonds (right) for $F_j(t) = f_j \sin(\omega t + \phi_j)$ with $f_1 = -f_2 = \pi/10$, $\phi_1 = \phi_2 = 0$, $\omega = 0.2$ and $V_0 = 16.7875$ (corresponding to the hopping amplitude $J = 1$ in the tight-binding model)

The situation changes when we introduce phases ϕ_j being different for each bond. Starting to move from one bond, a wave packet reaches the common vertex. After collision, the particle falls into another medium with a different external field. In our case, the difference is in the phase ϕ . Each time when reaching a common boundary, the wave packet starts a “new” trajectory in a corresponding external field with “new initial” momentum k , which makes the dynamics strongly dependent on the initial state of the GWP. Comparison of results for the two approaches is presented in Fig. 3 for the same parameters as in Fig. 2 with the only difference in $\phi_2 = \pi/2$.

As one can see from these results, we still have dissipation of the wave packet at the vertex. The same dynamics are seen from the first and second bonds in Fig. 1. The difference is on the small fraction of the packet, which appears from reflection on the common vertex. Thus, for a system of connected lattices, the expression for the GWP center's trajectory is not valid. This can be explained by the localization of wave packets on the lattice sites (Fig. 4).

Now, based on this idea, we can compute trajectories for the localized wave packets separately. Of course, this does not mean that a single wave packet localized in one site behaves in this way. We again note that we consider here a set of localized GWPs enveloped in a wide Gaussian wave packet. In Fig. 5, trajectories of localized wave packets are presented. The gray gradient in the left figure introduced in order to depict wave packets with different amplitudes; darker colors correspond to larger amplitudes. These results can be compared with the solution of the Schrödinger equation for two connected bonds.

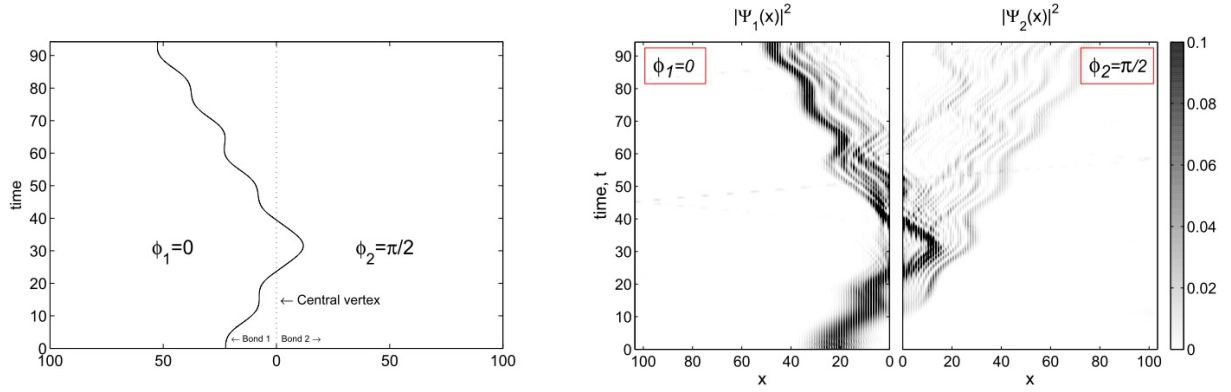


FIG. 3. A GWP center's trajectory (left) and the solution of the Schrödinger equation for two connected bonds (right) for the same parameters as in Fig. 2 with the only difference in $\phi_2 = \pi/2$.

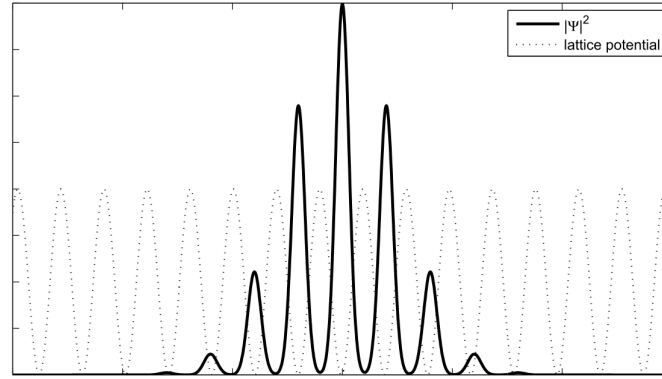


FIG. 4. Sketch of the profile of GWP in the lattice given by a cosine potential

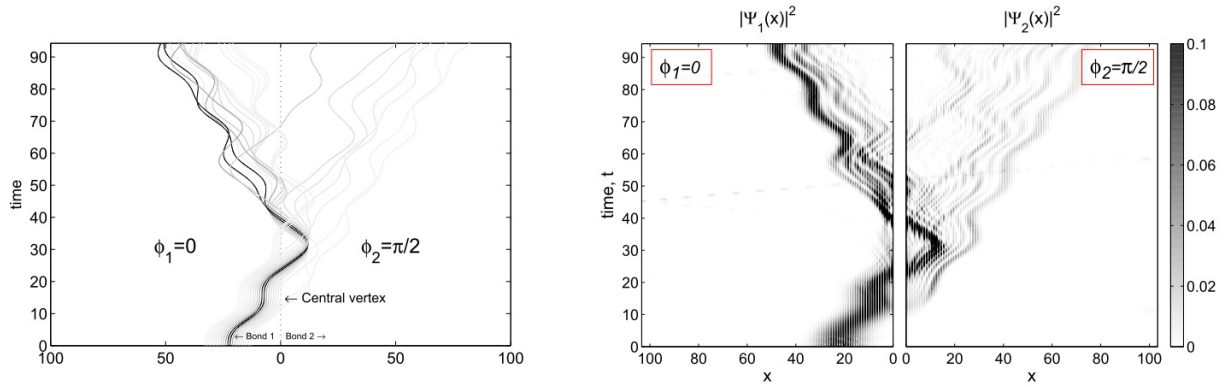


FIG. 5. Trajectories of localized wave packets (left) compared with the solution of the Schrödinger equation for two connected bonds (right). Gray gradient in the left figure; darker colors correspond to larger amplitudes

3.2. Manipulating GWP dynamics

A naive trial to bring to stop a GWP in the central vertex can be done in the following way. According to Eq. (6), in order to bring to a stop a wave packet, one needs in general:

$$k_0 + \frac{f}{\omega} (\cos(\omega t + \phi) - \cos(\omega t_0 + \phi)) = \pm \pi n, \quad n = 0, 1, \dots$$

Therefore, one of the solutions is $k_0 = \pm \pi n$ and $f = 0$ (or $\omega \gg f$) at the same time. In this case, k_0 is the initial momentum to the second bond and consequently $f_2 = 0$. Selecting $k_0 = \pm \pi n$ means selecting proper

initial position x_0 . So, for the initial momentum $k_0 = 0$ in the first bond, we can obtain periodically this value in each time $t_n = 2\pi n/\omega$. Then, in order the target position to be 0 (to stop at the common vertex), one can compute $x_0 = D(t_n)$. Thus, direct computations for parameters $f_1 = \pi/10$, $f_2 = 0$, $\omega = 0.2$ result in Fig. 6, where $x_0 = 29.2166$.

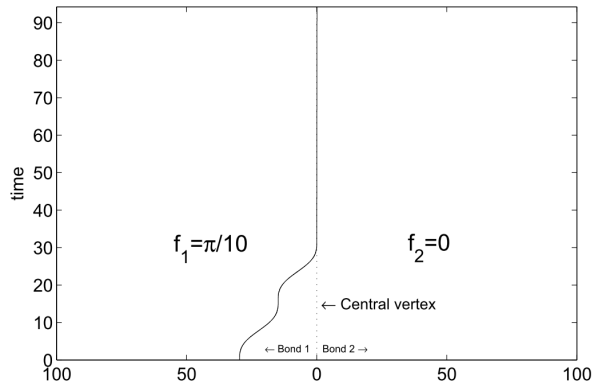


FIG. 6. Vanishing displacement of GWP center: $f_1 = \pi/10$, $f_2 = 0$, $\omega = 0.2$ and $x_0 = 29.2166$.

Another possibility to block transition can be achieved by choosing parameters as $f_1 = -f_2 = \pi/10$, $\phi_1 = 0$, $\phi_2 = -\pi$, $\omega = 0.2$ and $x_0 = 29.6567$ is the initial position of GWP's center, which correspond to having $k = 0$ on the common vertex. In such a case, one expects the trajectory shown in Fig. 7.

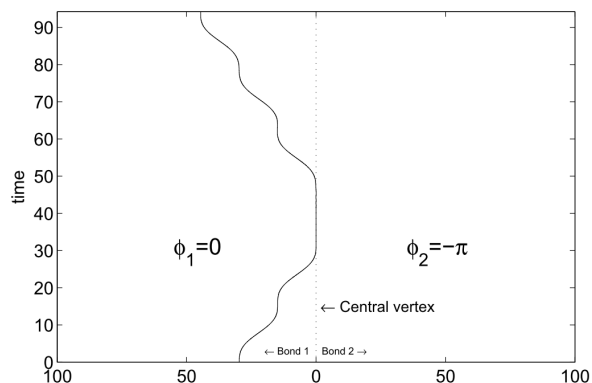


FIG. 7. Total reflection of a GWP in the central vertex: $f_1 = -f_2 = \pi/10$, $\phi_1 = 0$, $\phi_2 = -\pi$, $\omega = 0.2$ and $x_0 = 29.2166$.

At first glance, it seems easy that we found parameters to stop or totally reflect GWP at the vertex. However, solving the Schrödinger equation for these parameters results in different dynamics (see Fig. 8).

Thus, in order to be able to control GWP dynamics, one needs initialize localized wave packets with different precalculated group velocities. Despite the fact that this set up is experimentally unrealizable, theoretically it is possible to control GWP in this way.

4. Conclusion

In this paper, we have studied Gaussian wave packet dynamics in connected lattices under influence of different external time-dependent fields. It is shown that the dispersion of the wave packet at the bifurcation point is not only caused by reflection and transmission rules but also by the localization of the wave packet in the lattice sites. It was determined that the trajectory of a GWP should be computed for localized wave packets in order to obtain a complete picture of the dynamics and its calculation for branched lattices with different modulated fields is not valid. Even if this paper dealt with two connected lattices, the concept also holds true for many bond star graphs.

According to this approach, it is theoretically possible to control transmission or reflection of the GWP by selecting proper initial conditions (for example by assigning proper initial momentum to the each localized wave packet, which would be practically impossible to do) and parameters of the field, which will be studied in future works.

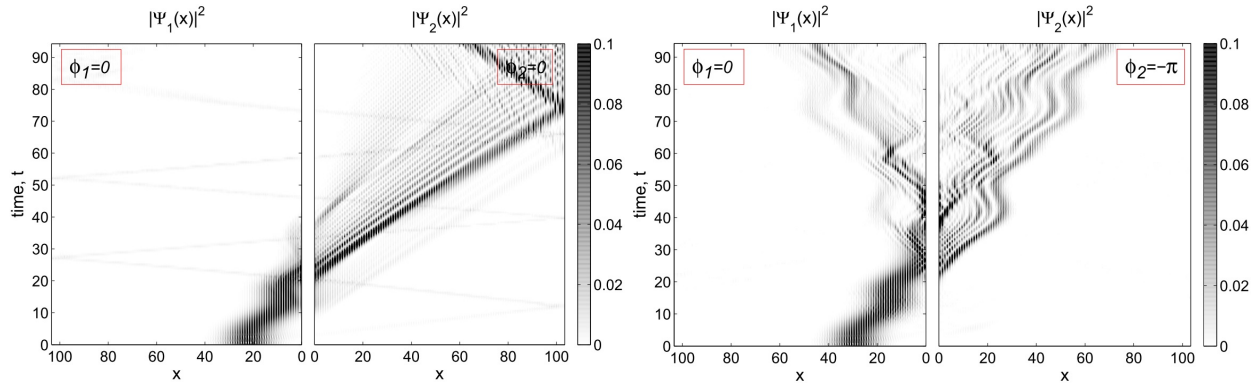


FIG. 8. Solution of the Schrödinger equation for cases considered in Fig. 6 (left) and Fig. 7 (right).

Acknowledgements

This work is supported by a grant of the Committee for Coordination of the development of Science and Technology of Uzbekistan (Grant No F-2-003).

References

- [1] Gnuzmann S., Smilansky U. Quantum graphs: Applications to quantum chaos and universal spectral statistics. *Adv. Phys.*, 2006, **55** (5–6), P. 527–625.
- [2] Exner P., Kovařík H. *Quantum waveguides*. Springer, 2015.
- [3] Kottos T., Smilansky U. Periodic orbit theory and spectral statistics for quantum graphs. *Ann. Phys.*, 1999, **274** (1), P. 76–124.
- [4] Hartmann T., Keck F., Korsch H.J., Mossmann S. Dynamics of Bloch oscillations. *New J. Phys.*, 2004, **6**, 2.
- [5] Dekorsy T., Ott R., Kurz H., Köhler K. Bloch oscillations at room temperature. *Phys. Rev. B*, 1995, **51**, P. 17275–17278.
- [6] Ben Dahan M., Peik E., Reichel J., et al. Bloch oscillations of atoms in an optical potential. *Phys. Rev. Lett.*, 1996, **76**, P. 4508–4511.
- [7] Haller E., Hart R., et al. Inducing transport in a dissipation-free lattice with super Bloch oscillations. *Phys. Rev. Lett.*, 2010, **104**, P. 200403.
- [8] Lehtinen J.S., Zakharov K., Arutyunov K.Yu. Coulomb blockade and Bloch oscillations in super-conducting Ti nanowires. *Phys. Rev. Lett.*, 2012, **109**, P. 187001.
- [9] Alberti A., Ferrari G., et al. Atomic wave packets in amplitude-modulated vertical optical lattices. *New Journal of Physics*, 2010, **12**, P. 065037.
- [10] Mülken O., Bauer M. Directed excitation transfer in vibrating chains by external fields. *Phys. Rev. E*, 2011, **83**, P. 061123.
- [11] Thommen Q., Garreau J.C., Zehnlé V. Quantum motor: Directed wave-packet motion in an optical lattice. *Phys. Rev. A*, 2011, **84**, P. 043403.
- [12] Thommen Q., Garreau J.C., Zehnlé V. Theoretical analysis of quantum dynamics in one-dimensional lattices: Wannier-stark description. *Phys. Rev. A*, 2002, **65**, P. 053406.
- [13] Thommen Q., Garreau J.C., Zehnlé V. Atomic motion in tilted optical lattices: an analytical approach. *J. Opt. B*, 2004, **6** (7), P. 301.
- [14] Arlinghaus S., Holthaus M. Controlled wave-packet manipulation with driven optical lattices. *Phys. Rev. A*, 2011, **84**, P. 063617.
- [15] Creffield C.E., Sols F. Directed transport in driven optical lattices by gauge generation. *Phys. Rev. A*, 2011, **84**, P. 023630.
- [16] Hu W.H., Jin L., Song Z. Dynamics of one-dimensional tight-binding models with arbitrary time-dependent external homogeneous fields. *Quantum Inf. Process.*, 2013, **12** (11), P. 3569–3585.
- [17] Matrasulov D.U., Yusupov J.R., Sabirov K.K., Sobirov Z.A. Time-dependent quantum graph. *Nanosystems: Physics, Chemistry, Mathematics*, 2015, **6** (2), P. 173–181.
- [18] Yusupov J., Eshniyozov V., Karpova O., Saidov D.Sh. Kicked particle dynamics in quantum graphs. *Nanosystems: Physics, Chemistry, Mathematics*, 2015, **6** (6), P. 773–778.
- [19] Yusupov J., Dolgushev M., Blumen A., Mülken O. Directed transport in quantum star graphs. *Quantum Information Processing*, 2016, **15** (4), P. 1765–1777.

Metal-insulator (fermion-boson)-crossover origin of pseudogap phase of cuprates I: anomalous heat conductivity, insulator resistivity boundary, nonlinear entropy

B. Abdullaev¹, C.-H. Park², K.-S. Park³, I.-J. Kang⁴

¹Institute of Applied Physics, National University of Uzbekistan, Tashkent 100174, Uzbekistan

²Research Center for Dielectric and Advanced Matter Physics, Department of Physics, Pusan National University, 30 Jangjeon-dong, Geumjeong-gu, Busan 609-735, Korea

³Department of Physics, Sungkyunkwan University, 2066, Seoburo, Jangangu, Suwon, Gyeonggido, Korea

⁴Samsung Mobile Display, Suwon, Kyunggido, Korea

bakhodir.abdullaev@yandex.ru, cpark@pusan.ac.kr, pmpark@skku.edu, hacret@hanmail.net

PACS 74.72.-h, 74.20.Mn, 74.25.Fy, 74.25.Bt

DOI 10.17586/2220-8054-2017-8-1-48-58

Among all the experimental observations of cuprate physics, the metal-insulator-crossover (MIC), seen in the pseudogap (PG) region of the temperature-doping phase diagram of copper-oxides under a strong magnetic field when the superconductivity is suppressed, is most likely the most intriguing one. Since it was expected that the PG-normal state for these materials, as for conventional superconductors, is conducting. This MIC, revealed in such phenomena as heat conductivity downturn, anomalous Lorentz ratio, insulator resistivity boundary, nonlinear entropy, resistivity temperature upturn, insulating ground state, nematicity- and stripe-phases and Fermi pockets, unambiguously indicates on the insulating normal state, from which high-temperature superconductivity (HTS) appears. In the present work (article I), we discuss the MIC phenomena mentioned in the title of article. The second work (article II) will be devoted to discussion of other listed above MIC phenomena and also to interpretation of the recent observations in the hidden magnetic order and scanning tunneling microscopy (STM) experiments spin and charge fluctuations as the intra PG and HTS pair ones. We find that all these MIC (called in the literature as non-Fermi liquid) phenomena can be obtained within the Coulomb single boson and single fermion two liquid model, which we recently developed, and the MIC is a crossover of single fermions into those of single bosons. We show that this MIC originates from bosons of Coulomb two liquid model and fermions, whose origin is these bosons. At an increase of doping up to critical value or temperature up to PG boundary temperature, the boson system undergoes bosonic insulator – bosonic metal – fermionic metal transitions.

Keywords: high critical temperature superconductivity, cuprate, metal-insulator-crossover, temperature-doping phase diagram, anomalous heat conductivity, insulator resistivity boundary, nonlinear entropy.

Received: 2 August 2016

Revised: 3 September 2016

1. Introduction

The origin of PG and HTS phases in copper oxides (cuprates) is one of the most puzzling and challenging problem in condensed matter physics. Despite being almost three decades since their discovery, intensive experimental and theoretical studies have yielded little clear understanding of these phases so far. The experimental studies of HTS and PG in cuprates have provided physicists with numerous interesting and fascinating materials with unconventional properties. Among the most puzzling and thus far most intriguing is the observation of the MIC, seen in the underdome region of a temperature-doping phase diagram in the absence [1–4] or presence [5–9] of a strong external magnetic field. The MIC, detected after suppression of the HTS by a strong magnetic field, results in a number of different phenomena: heat conductivity downturn and anomalous Lorentz ratio [10, 11], insulator resistivity boundary [6], nonlinear entropy [12, 13], insulating ground state (see Refs [1–4] and [5–9]), dynamic nematicity [14] and static stripe phases [15, 16] and Fermi pockets [15–17]. This reveals the highly unconventional dielectric properties of the PG-normal phase of these superconductors. Since superconductivity appears

in conventional superconductors from the conducting normal state only, the understanding of how HTS arises from an insulating state becomes a fundamental problem, and thus, the keystone for cuprate physics. This MIC also separates previously applied mechanisms and models for conventional superconductors from consideration.

Being previously introduced for the description of an electron transport transition of metals into insulators, as we see below in this and also in the second II papers, a concept of the MIC provides an opportunity to encompass various properties of the famous cuprate PG physics in the understanding within a single treatment. This treatment might be our Coulomb single boson and single fermion two liquid model, which was developed in Ref. [18].

Analyzing the electric charge and percolation of the visualized in STM real space PG and HTS nanoregions (NRs) of the $\text{Bi}_2\text{Sr}_2\text{CaCu}_2\text{O}_{8+\delta}$ compound [19,20] which exhibited an energy gap, we showed in [18] that NRs with minimal size are PG and HTS pairs and furthermore, they are single bosons, and percolation of these NRs occurs from the first critical doping, from which the HTS begins. In [18] we were also able to qualitatively understand all elements for the temperature-doping phase diagram of the copper-oxide. If the experiment [19] clearly showed, through the visualization of pair formation in the PG region, the precursor mechanism of the bulk HTS, we have successfully realized that the later appears due to percolative overlapping of the separated NRs. All positions of the Coulomb single boson and single fermion two liquid model are listed in Ref. [21]. This model is semi-phenomenological, since if the microscopic formation of single bosons, through the anyon bosonization of 2D fermions, is rigorously proven and after that experimentally confirmed in [18], then the size of these bosons and the percolative nature of the HTS are the results of Refs. [19,20] data analysis.

In the present paper, we describe the low-temperature (low- T) non-Fermi liquid behavior of the heat-transport and entropy. As will be seen below, the central role in this calculation plays the temperature T dependence of the electronic specific heat c . This T dependence of c is a result of the insulating ground state of 2D gas of plasmons, which consisted of charged single bosons, deformed and pinned by cuprate parent compound lattice ferroelectric atoms (the nematicity electronic state (see for details Ref. [21] and paper II)). Since, according to the Bogoliubov approach for gas of charged bosons [22], at high gas density, where this approach is valid, the ground state energy consists of components for the Bose-Einstein condensate and a gas of quasi-particle-plasmons. Following March *et al.* [23], who showed that the Bogoliubov approach can be nicely applied to the description of the liquid He II, we believe that this approach may at least qualitatively describe the intermediate densities of 2D Coulomb boson gas, at which the HTS takes place. At high magnetic fields or at lower dopings, close to the first critical doping, for which MIC phenomena are measured, the Bose-Einstein condensate vanishes and there only a gas of quasi-particle-plasmons exists. However, the latter, the individual charges of which being fixed by ferroelectric atoms, is insulating therefore, the insulator is the whole ground state of copper oxides. Typically, the experiment detects the MIC up to the critical value of doping [6–8], which, for some cuprates, is close to the optimal doping, where the T_c is maximum in the temperature-doping phase diagrams. There also exists the case of $\text{Bi}_2\text{Sr}_2\text{CaCu}_2\text{O}_{8+\delta}$ compound [19], for which this critical doping almost coincides with the second critical doping, at which the HTS vanishes.

We start with the description of existing experimental data for the heat-transport and PG-normal state specific heat of copper-oxides. Hill and collaborators [10] reported that the heat conductivity of the electron doped copper-oxide $\text{Pr}_{2-x}\text{Ce}_x\text{CuO}_4$ measured at low- T deviated from the one predicted by the Landau Fermi liquid theory (LFLT), i.e., as the temperature decreases, the temperature dependence of the heat conductivity (κ) is changed from the normal linear $\kappa \sim T$ behavior into an anomalous $T^{3.6}$ one, which was described by the ‘downturn’ behavior of the heat conductivity. They also reported another important non-Fermi liquid behavior: the Lorentz ratio of the Wiedemann – Franz law (WFL) in the region of the linear T -dependence of κ was significantly larger (1.7 times) than Sommerfeld’s value. These violations were also observed in the heavily over-doped non-superconducting compound $\text{La}_{2-x}\text{Sr}_x\text{CuO}_4$ by Nakamae *et al.* [24] and in $\text{Bi}_{2+x}\text{Sr}_{2-x}\text{CuO}_{6+\delta}$ copper-oxide in the vicinity of the MIC by Proust *et al.* [11]. Smith *et al.* suggested that the downturn behavior of κ results solely from the

decoupling of the heat carrying thermal phonons and electrically conducting charge carriers [25] at low- T , while Hill *et al.* have indicated that the downturn of κ should be intrinsic for copper-oxides (see Ref. [10]).

The normal state electronic specific heat c of superconductors $\text{YBa}_2\text{Cu}_3\text{O}_{6+x}$ and $\text{La}_{2-x}\text{Sr}_x\text{CuO}_4$ above the HTS transition temperature T_c was experimentally investigated in [12] and [13], respectively. A magnetic field dependence of c has considered in [26] for $\text{Y}_{0.8}\text{Ca}_{0.2}\text{Ba}_2\text{Cu}_3\text{O}_{6+x}$ compound. Due to existence of HTS, it is impossible to extract the information on the low- T dependence of the normal state c . On the other hand, Loram *et al.* [12] showed the T -dependence of the entropy (\mathcal{S}) $\mathcal{S} \sim T^i$ with $i > 1$ for the underdoped (insulating) material, which was driven from the measured electronic specific heat of HTS superconductors $\text{YBa}_2\text{Cu}_3\text{O}_{6+x}$, ignoring the superconducting effects, while for the optimal doping compound, $\mathcal{S} \sim T$ was measured. The simple Drude model for the heat conductivity κ will connect in our consideration the kinetic heat-transport property of PG region of HTS superconductors with its thermodynamic quantity – the electronic specific heat c . The entropy \mathcal{S} is a result of c .

The low- T MIC was observed firstly by Ando *et al.* [5] in the hole doped $\text{La}_{2-x}\text{Sr}_x\text{CuO}_4$ compound through the measurement of the resistivity in CuO_2 plane. This paper suggested the low- T MIC is an intrinsic property rather than one induced by the 2D localization of carriers. The doping versus T diagram of the insulating state up to near-optimal-doping was obtained in the extensive investigation by Boebinger *et al.* [6]. A similar (near-optimal-doping) observation of the low- T MIC was reported for the electron doped $\text{Pr}_{2-x}\text{Ce}_x\text{CuO}_4$ by Fournier *et al.* [7] and for the 1/8-doped $\text{Bi}_2\text{Sr}_{2-x}\text{La}_x\text{CuO}_{6+\delta}$ by Ono *et al.* [8]. The low- T MIC were clearly measured in a La-free hole-doped $\text{Bi}_{2+x}\text{Sr}_{2-x}\text{Cu}_{1+y}\text{O}_{6+\delta}$ of the doping $x = 0.13$ (while optimal doping was $x = 0.16$) by Vedenev and Maude [27] through the measurement of the in-plane resistivity. Although in some papers (see, for example, Ref. [27]) authors tried to invoke the 2D carrier localization approach to explain the phenomenon, the material-independent and universal character of the low- T MIC for all cuprates indicates that effect is intrinsic and may be related to a fundamental property of cuprates.

It was already mentioned above that according to Ref. [25] the downturn of the heat conductivity is related to a decoupling of charges and phonons. However, the paper [25] does not clarify the origin of this decoupling. Observations of the low- T MIC, and the downturn for the same compound and under same experimental conditions are not occasional and indicate on the MIC origin of the decoupling, when charges localized in the insulating state cease to do a scattering with phonons. Therefore, the non-linear insulating $\mathcal{S} \sim T^i$ with $i > 1$ dependence of entropy, the downturn behavior $\kappa \sim T^{3.6}$ and the low- T MIC are results of the same underlying physics of the insulating ground state and MIC for cuprates.

In this work, we demonstrate that the unified description of the three MIC phenomena is possible. In Sec. 2, we derive the specific heat of the ideal gas of Bogoliubov quasi-particles (IGBQ) and demonstrate that it is obtained from the contributions of plasmons at low- T and free quasi-particles at high- T temperatures. We will find in the section T , at which one part of the specific heat transits into another one. In Sec. 3, the low- T dependence and the downturn temperature of the heat conductivity κ will be determined. In this section, we also obtain the Lorentz ratio of the WFL and discuss the arguments supporting our approach for the explanation of the observed insulating ground state (IGS) and low- T MIC. Analysis of the experimental data on the specific heat for copper-oxides and their possible relation to c described in the present paper will be made in Sec. 4. In this section we obtain also the expression for entropy \mathcal{S} . We conclude and summarize the paper by Sec. 5.

2. Specific heat of IGBQ

As was indicated in the first section, the ground state for the low dopings of cuprates is HTS from charged bosons. However, under strong magnetic fields, which were used for the measurements of the heat conductivity κ and the IGS and low- T MIC, the HTS is suppressed and for PG normal state at low- T we have only the excited

state – IGBQ, which is not effected by magnetic field (see Sec. 4 below). Therefore, in order to investigate the T dependence of c for this low doping and low- T , we calculate the specific heat of IGBQ.

The thermodynamic free energy [28] of an ideal boson gas is:

$$F = T \int \frac{d^2 p d^2 x}{(2\pi\hbar)^2} \ln(1 - e^{-\varepsilon(p)/T}). \quad (1)$$

Here, the temperature T is described by the energy scale. We use a relation between the quasi-particle (QP) energy ε and momentum p of IGBQ, which was derived previously [22]: $\varepsilon(p) = (ap + (p^2/2m)^2)^{1/2}$, where ap is the square of QP energy of plasmon, and $a = 2\pi e^2 n \hbar / m$. Here, e and n are the charge and 2D density, respectively, of real particles with mass m .

One can separate the integral of Eq. (1) over the absolute value of momentum p into two parts: $\int_0^\infty = \int_0^q + \int_q^\infty$. Here q gives the maximum of the momentum distribution function of non-condensate real particles [29] at $T = 0$ under the Bogoliubov approximation. Thus, the contributions of the plasmon (dominant for $p < q$) and of the kinetic energy (dominant for $p > q$) to the energy of QPs are approximately separated at the boundary ($p = q$), where:

$$(aq)^{1/2} = q^2/(2m). \quad (2)$$

For the first (second) integral, if we introduce the variable $x = (ap)^{1/2}/T$ ($x = p^2/(2mT)$), we obtain:

$$F \approx \frac{TS}{2\pi\hbar^2} \left[\frac{2T^4}{a^2} \int_0^{(aq)^{1/2}/T} dx x^3 \ln(1 - e^{-x}) + mT \int_{(aq)^{1/2}/T}^\infty dx \ln(1 - e^{-x}) \right], \quad (3)$$

where S is defined to be the area of 2D system. (i) At lower temperatures, one can have $(aq)^{1/2}/T \gg 1$, and one can replace the upper limit of first integral in Eq. (3) by infinity sign, and the second integral becomes zero. (ii) At high temperature, we can have $(aq)^{1/2}/T \ll 1$, then the lower limit of second integral can be replaced by zero and the first integral is removed. Following the calculational scheme of Ref. [28], we thus find that the specific heat per area can be expressed at low- T by:

$$c_1 = -\frac{20T^4 A}{\pi\hbar^2 a^2} \quad (4)$$

with the ideal gas of the plasmons and at high- T by:

$$c_2 = -\frac{TmB}{\pi\hbar^2} \quad (5)$$

with the ideal gas of free QPs. Here,

$$A = -(1/4) \int_0^\infty x^4 dx / (e^x - 1) = -(1/4)\Gamma(5)\zeta(5) \quad \text{and} \quad B = - \int_0^\infty x dx / (e^x - 1) = -\Gamma(2)\zeta(2),$$

where $\Gamma(y)$ and $\zeta(y)$ are Gamma and the Riemann Zeta functions, respectively.

We define a temperature T_d^c , at which the low- T dependence of c_1 transforms into that of c_2 at high- T . It can approximately be determined by setting equal the approximate equations for c_1 and c_2 . It has the expression:

$$T_d^c = \left(\frac{\Gamma(2)\zeta(2)}{5\Gamma(5)\zeta(5)} \right)^{1/3} (ma^2)^{1/3}. \quad (6)$$

One can show that $(ma^2)^{1/3} = 2(2/r_s^2)^{2/3} Ry$, where r_s is the mean distance between particles in Bohr a_B radius ($a_B = \hbar^2/(me^2)$) and Ry is Rydberg ($Ry = me^4/(2\hbar^2)$) energy. We use the relation [30, 31] $n_{ab} = 6.747 \cdot 10^{14} t/\text{cm}^2$ between the density of charges in cuprate 1 cm^2 area of $a - b$ plane and fraction t of charge per Cu atom. Expressing the density in $1/a_B^2$ units we find r_s as function of t . Therefore, T_d^c is:

$$T_d^c \approx 0.114 t^{2/3} Ry. \quad (7)$$

The specific heat at an arbitrary temperature is obtained from Eq. (1), which has the form:

$$c = \frac{q^2}{2m} \frac{m}{4\pi\hbar^2} \int_0^\infty \frac{dy}{z^2} \frac{y^2(1+y^3)}{\sinh^2(y^{1/2}(1+y^3)^{1/2}/(2z))}, \quad (8)$$

where $z = T/(aq)^{1/2}$ and $y = p/q$. Fig. 1 shows the c/z (in $q^2/(8\pi\hbar^2)$ units) calculated by using Eq. (8). Here, it is remarkable that the curve can nicely describe the downturn behavior of the specific heat. The downturn occurs around $z = 0.5$, indicating that $T_d^c = 0.5(aq)^{1/2}$. Here, $(aq)^{1/2} = 8(2^{1/2}/(3r_s^2))^{2/3}Ry$ and expressing r_s through t , $(aq)^{1/2} = 0.737 \cdot t^{2/3}Ry$. By the numerical estimation of the downturn temperature T_d^c , the coefficient in Eq. (7) becomes 0.368 instead of 0.114.

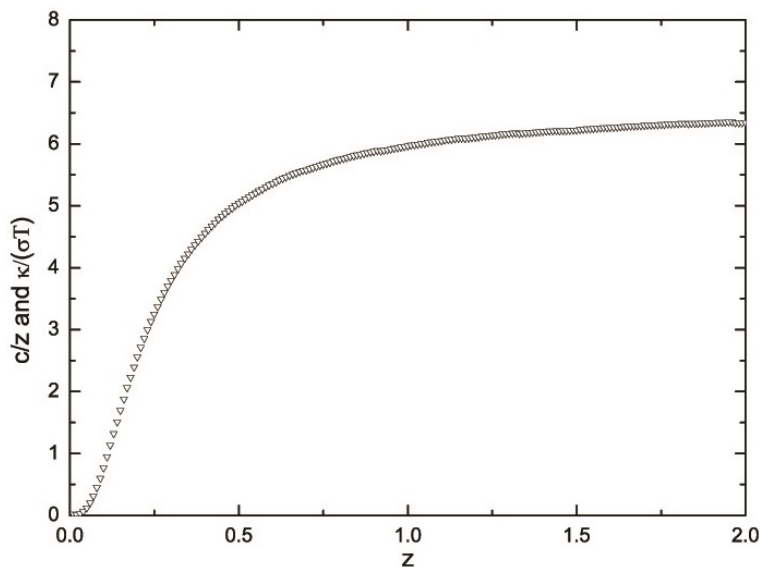


FIG. 1. The specific heat c/z (in $q^2/(8\pi\hbar^2)$ units) and $\kappa/(\sigma T)$ (in $k_B m v l / (2\pi\hbar^2 \sigma)$ units) as function of z . The definition of z : $z = T/(aq)^{1/2}$ for c/z and $z = K^{1/3}T/(aq)^{1/2}$ for $\kappa/(\sigma T)$, where $K \sim 10^{12}$ (see text)

3. Heat conductivity and MIC

The downturn behavior for the heat conductivity κ deviated from the WFL can be explained by a crossover of freely penetrating QPs of IGBQ into localizing individual particles collective plasmon state. As mentioned in the first section, the $a - b$ plane cuprate atoms deform the intra charge structure of single bosons and pin them (fixed nematicity phase). However, they become free (free QPs) at the bosonic insulator – bosonic metal transition temperature and doping (see below). At the same time, despite the fact that the charged single bosons are pinned before this transition, the plasmon gas is free for a penetrating.

The plasmon gas, which becomes dominant at low- T , does not carry the charge and is electrically insulating, therefore the formation of plasmons at low- T significantly affects the behavior of κ . One can approximately estimate the downturn temperature T_d^κ of κ as a temperature, where WFL of electrically conducting free QPs with electrical conductivity σ_2 transits into WFL of plasmons (with the electrical conductivity σ_1). We apply the WFL in the region of this nearly insulating gas (mainly consisted of plasmons) to calculate σ_1 from the κ and specific heat. Although the WFL is not conventionally applicable for insulators, we will demonstrate in this section that in the case of cuprates σ_1 for plasmons equals σ_2 of conductor with infinitely small numerical prefactor. Thus for plasmon gas as conductor with very small electrical conductivity the WFL is formally valid. On the other hand, this "bad" conductor satisfies the formal definition of insulator given in the classical electrodynamics as a

conductor having its conductivity close to zero. While the Lorentz ratio in our paper calculates only for free QPs of IGBQ, i.e., for conductor above the downturn T_d^κ temperature. We cannot, strictly saying, apply the WFL for insulating plasmon gas to calculate the Lorentz ratio. This our result for Lorentz ratio, Fig. 2 is in correspondence with experiment of Proust *et al.* [11].

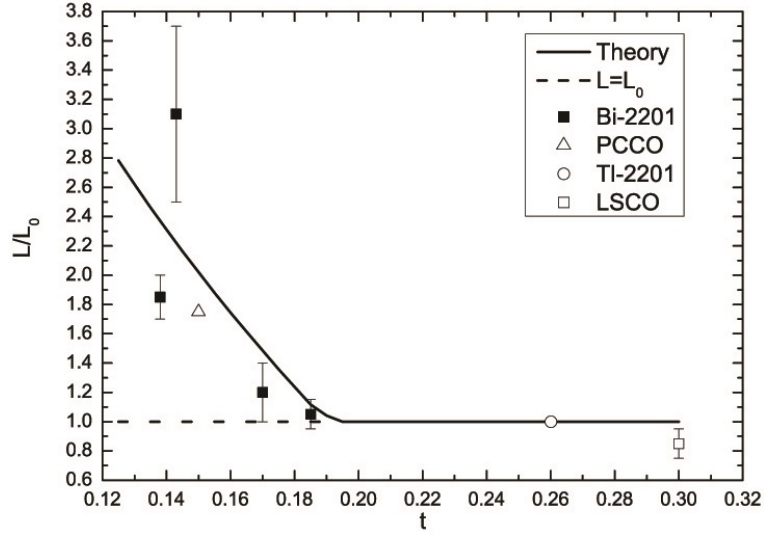


FIG. 2. The Lorentz ratio L/L_0 (Eq. (14)) vs. t (values for $t \geq 1$ are added artificially). Observed dots are from Ref. [11]

According to the Drude model, which we will apply for the description of heat conductivity κ , only two quantities (except the specific heat c) contribute in κ (see below): mean velocities and free penetration lengths of QPs. For the low- T regime, at which the experiments on κ are measured, one can ignore the T dependence of these two (if the mean velocity is determined by concentration of charges, then the free penetration length is determined for low- T by scattering of charges on impurities). Therefore, the qualitative T dependence of κ (together with downturn T_d^κ) is determined only by the specific heat c .

Following the Drude model, we have $\kappa_1(T) = (1/2)c_1(T)v_1l_1$ for gas of plasmons and $\kappa_2(T) = (1/2)c_2(T)v_2l_2$ for gas of free QPs with corresponding mean velocities and free penetration lengths $v_{1,2}$, and $l_{1,2}$, respectively. To obtain the value of T_d^κ , we express the specific heat Eq. (8):

$$c_1 = \frac{q^2}{2m} \frac{m}{\pi\hbar^2} z^4 10\Gamma(5)\zeta(5) \quad (9)$$

for $z \ll 1$ and

$$c_2 = \frac{q^2}{2m} \frac{m}{\pi\hbar^2} z\Gamma(2)\zeta(2) \quad (10)$$

for $z \gg 1$. Substituting $z = T/(aq)^{1/2}$ and using Eq. (2), it is found that Eq. (9) reduces to Eq. (4) and Eq. (10) to Eq. (5).

Therefore, WFL is expressed as:

$$\frac{\kappa_1}{\sigma_1 T} = \frac{k_B m v_1 l_1}{2\pi\hbar^2 \sigma_1} z^3 10\Gamma(5)\zeta(5) \quad (11)$$

for gas of plasmons and

$$\frac{\kappa_2}{\sigma_2 T} = \frac{k_B m v_2 l_2}{2\pi\hbar^2 \sigma_2} \Gamma(2)\zeta(2) \quad (12)$$

for gas of free QPs.

At the downturn temperature T_d^κ , it should be $\kappa_1(T_d^\kappa)/(\sigma_1 T_d^\kappa) = \kappa_2(T_d^\kappa)/(\sigma_2 T_d^\kappa)$. However, due to the non-equality $v_1 l_1 / \sigma_1 \neq v_2 l_2 / \sigma_2$, we cannot express Eq. (11) and Eq. (12) as single function of WFL, which transforms

from low- T limit into high- T limit with the increase of T . On the other hand, if we write $v_1 l_1 / \sigma_1 = K_{\sigma_1, \sigma_2} v_2 l_2 / \sigma_2$, where K_{σ_1, σ_2} is numerical factor, and if we introduce the definition $vl / \sigma = v_2 l_2 / \sigma_2$ for gas of free QPs, the single WFL for new parameter can be expressed by $z = K_{\sigma_1, \sigma_2}^{1/3} T / (aq)^{1/2}$. This can describe the WFL of the free QPs gas at all T . In Fig. 1, we plot the $\kappa / (\sigma T)$, (expressed in $k_B m v l / (2\pi \hbar^2 \sigma)$ units) as function of z , which is valid at low- T , where v , l and σ are T independent.

We estimate the electrical conductivity σ_1 for a case of $t \sim 0.1$. From the expression for $(aq)^{1/2}$, one derives $(aq)^{1/2} / k_B \sim 10^4$ K (in K – Kelvin temperature units). Thus, the downturn of the specific heat takes place at $T_d^c \sim 10^4$ K. The observed downturn- T of the heat conductivity [10, 11] is $T_{d,exp}^\kappa / k_B \sim 0.1$ K. By using the downturn coordinate $z = 0.5$ from Fig. 1 for $\kappa / (\sigma T)$ and by substituting in this z values of $(aq)^{1/2} / k_B$ and $T_{d,exp}^\kappa / k_B$, we obtain $K_{\sigma_1, \sigma_2} \sim 10^{12}$. This means that $\sigma_1 v_2 l_2 / (\sigma_2 v_1 l_1) \sim 10^{-12}$. We compare v_1 with v_2 and l_1 with l_2 . Free QPs crossover into plasmons at momentum q determined by Eq. (2). However, this expression for q is similar to the expression for the critical momentum for the Landau damping of electrons [32], which decay plasmons being generated or absorbed. Thus, we can apply the Landau damping approach in our case. However, except an energy conservation law – Eq. (2), this approach requires an equality of the plasmon phase velocity and electron velocity. Therefore, for an estimate, one can assume at T_d^κ that $v_1 \sim v_2$ and $l_1 \sim l_2$ (here we take that the plasmon phase velocity is roughly equal to the plasmon group velocity and the lifetime of plasmon and electron against to decay is the same), i.e., mean velocities and free penetration lengths for plasmons and free QPs have the same order of magnitude. Hence, we obtain $\sigma_1 / \sigma_2 \sim 10^{-12}$. This result supports the above supposed assumption of the IGS, in which the insulating plasmon gas formed from the charge conducting free QP gas transits at low- T .

This analysis allow us to suggest that the downturn of heat conductivity may be a result of the MIC at low- T . In addition to coincidence of experimental parameters for the doping and of magnetic field strength at the measurements of κ and the IGS, and low- T MIC for the same copper-oxide, as discussed above, the MIC boundary described by Boebinger *et al.* (see Ref. [6]) (at higher T) has qualitatively the same doping dependence as the PG boundary. In Ref. [30], we limited the existence region of anyon-related Coulomb interacting bosons below the PG boundary because close to PG boundary bosons were transformed to fermions. This observation of Boebinger *et al.* supports the frame of our approach on the nature of PG phase as a mixture of single particle bosons and normal fermions. In our description the region below Boebinger *et al.* MIC boundary is dominated by plasmons, while close and right above of this boundary by free QPs of IGBQ.

This scenario for MIC corresponds to the bosons of the Coulomb single boson and single fermion two liquid model and fermions, whose origin is these bosons. At an increase of doping up to a critical value or temperature up to PG boundary temperature, this boson system undergoes bosonic insulator – bosonic metal – fermionic metal transitions. While there also exists a small part of the model fermion component, which is not related to single bosons and at the same variation of doping or temperature undergoes insulator – metal crossover [18,21] and does not contribute to the MIC.

We determine the Boebinger *et al.* MIC boundary for temperature and doping in the doping-temperature phase diagram. This boundary defines temperature as function of doping, at which bosonic insulator – bosonic metal transition occurs. The analytic form for the transition temperature is expressed by Eq. (7) with coefficient 0.368 instead of 0.114 for the downturn temperature T_d^c of the specific heat. In the next paper, part II, we will demonstrate that the low- T dependence of a resistivity is determined by the specific heat. However, in Eq. (7), we used the expression for the entire density of charges n_{ab} . While one needs to separate in it the contributions from single boson and single fermion parts. We write the formula $n_{ab} = n_{ab}(1 - t/t_c) + n_{ab}t/t_c$, in which the first term describes the approximate single boson density and the second one the approximate single fermion density. Our interest is in the single bosons therefore, the expression for the bosonic insulator – bosonic metal transition

temperature is:

$$T_{bIM} \approx 0.368 \left[t \left(1 - \frac{t}{t_c} \right) \right]^{2/3} Ry. \quad (13)$$

Eq. (13) describes the temperature and doping boundary for the MIC of resistivity, found in the experiment of Boebinger *et al.* [6].

We now calculate the Lorentz ratio for free QPs of IGBQ. The WFL, $\kappa/(\sigma T) = L_0$, of heat transport for QPs of LFLT can be expressed by the Lorentz ratio L_0 and Sommerfeld's value $L_0 = (\pi^2/3)(k_B/e)^2$. We note that this value of L_0 corresponds to the three dimensional (3D) case. A simple calculation shows that it can be also applied for 2D case. For the IGBQ, it can be assumed that the mean kinetic energy of QPs is $mv^2/2 = (aq)^{1/2}$ (Eq. (2), because, as was pointed out above, at $T = 0$ the most part of non-condensate particles has this energy). Then $\kappa/(\sigma T) = mv^2c/(2ne^2T)$, with c determined from Eq. (5) for free QPs of IGBQ, reduces to a form $\kappa/(\sigma T) = 3.106 \cdot L_0/t^{1/3}$. This expression corresponds to the WFL of bosons, when there is no mixture of bosons with Fermi QPs of LFLT. However, at the increasing of concentrations of holes or electrons t to the direction of the critical doping t_c , fermions appear in the PG region [30] and this mixture occurs. Therefore, at $T \rightarrow 0$ we can phenomenologically write the expression $\kappa/(\sigma T) = L$ with:

$$L = L_0 \left[\frac{3.106}{t^{1/3}} \left(1 - \frac{t}{t_c} \right) + \frac{t}{t_c} \right], \quad (14)$$

which takes into account the transformation of L from one of free QPs of IGBQ to one of LFLT QPs, when the concentration t tends to (but below) critical concentration $t_c \approx 0.19$ [33]. In Fig. 2, we compare our estimated L/L_0 with the experimental data taken from Fig. 7 (a) of [11] for several cuprate compounds. It is remarkable that the calculated curve is in good agreement with the observed values of L/L_0 .

4. Specific heat and entropy

The qualitative features [12,13,33] of the observed cuprate electronic specific heat and entropy are as follows. The increment coefficient $\gamma = c/T$ of the specific heat in the HTS-to-normal-state phase transition (PT) point has weakly apparent and washed out peak in the lightly underdoped side. The peak of γ and its form become higher and sharper, respectively, when t increases. Peak is maximal (with the sharpest form) at t_c and then does not almost change the form for $t > t_c$. There is no influence on the normal state c by the external magnetic field [26]. At last, γ is independent from doping for $t > t_c$ [12].

In general, the weakly apparent peak of γ is attributed [28] to the first order PT, which is close to the second order one. Sharpening of γ at t_c might characterize the transition of PT into the second order type, where conventional superconductivity scenario with Cooper pairs becomes effective. The hypothesis in accordance with this description was pointed out in [30].

The non-dependence of the normal state c on the magnetic field might be a result that QP energy $\varepsilon(p)$ of IGBQ, by analogy with Cooper pair energy $\varepsilon_{Cp}(p)$, is independent of magnetic field. Abrikosov [34] has shown that $\varepsilon_{Cp}(p)$ being the result of canonical Bogoliubov transformation is function of scalar quantities u_p and v_p . However, the latter ones, as scalars, in the magnetic field with gauge $\vec{\nabla} \cdot \vec{A}(\vec{r}) = 0$ can be function of only zero scalar product $\vec{k} \cdot \vec{A}_{\vec{k}} = 0$, where \vec{k} and $\vec{A}_{\vec{k}}$ are Fourier transforms of vector-coordinate \vec{r} and vector-potential $\vec{A}(\vec{r})$, respectively. The independent from the magnetic field PG normal state was also observed in the resistivity measurement of the MIC [35], thus sustaining the possible role of $\varepsilon(p)$ of IGBQ.

For the specific heat c_F of 2D gas of LFLT QPs one obtains the same linear T dependence as in Eq. (5), but with ratio $c_F/c_2 = 2$ (due to two directions of spins for fermions instead of bosons). The non- t -dependence observation of γ for $t > t_c$ might be a result of the non-concentration dependence for Eq. (5).

We obtain the expression of the electronic normal state entropy \mathcal{S} through the calculation of integral $\mathcal{S} = \int_0^T (c/T_1) dT_1$ for PG, $T \leq T^*$, region. Here T^* is temperature of PG boundary. Typical experimental scale of T^* is $T^*/k_B \sim 10^2$ K, while $(aq)^{1/2}/k_B \sim 10^4$ K, therefore, in Eq. (8) one can assume $z \ll 1$ and use Eq. (4) as approximate expression of the specific heat of IGBQ. For arbitrary T (in the interval of $T \leq T^*$), we write the phenomenological expression:

$$\frac{c}{T} = \frac{c_1}{T} \left(1 - \frac{5}{4} \frac{T}{T^*} \right) + \frac{2c_F}{T} \frac{T}{T^*}. \quad (15)$$

The factor $5/4$ in front of first T/T^* term was introduced for convenience purpose. The integration over T_1 gives:

$$\mathcal{S} = \frac{c_1}{4} \left(1 - \frac{T}{T^*} \right) + c_F \frac{T}{T^*}. \quad (16)$$

We compare the T dependence of our \mathcal{S} with experimental one of [12]. It is convenient to express \mathcal{S} in mJ/(mol K) units and T in K units (we use the approximate PG boundary $T^* = 900 - 4736.8421 \cdot t$ taken from Fig. 11 of Ref. [33] and at calculating of \mathcal{S} we assume that value of charge is t). In this case, the increment coefficient γ from Fig. 4 of [12], being multiplied by T , gives \mathcal{S} as function of T , analogous to Fig. 6 of [26]. However, if Fig. 6 describes only the metallic t of holes, we obtain the data and for the insulating t . Comparing in Fig. 3 the plot of \mathcal{S} obtained from Eq. (16) with one from Fig. 6 of [26] we see (i) the general nonlinear, $\sim T^i$ with $i > 1$, behavior of all curves for $t < t_c$, (ii) all curves for $T > T^*$ have a linear behavior with the same slope, $\gamma \approx 1.46$, as for 2D fermion gas, (iii) in contrast to experimental result our curves for $T > T^*$ are not parallel. However, the parallelism of the observed curves indicated in the last point is inconsistent with the clear tendency of γ to approach the fixed value as T goes to infinity (more obviously it is seen in [13] for $\text{La}_{2-x}\text{Sr}_x\text{CuO}_4$ compound, although, in this paper $\gamma \approx 1.0$ was obtained). Finally, the alternative T/T^* dependencies are considered in [36] for T just after T_c of HTS and near the optimal doping, and in [37] close to T^* .

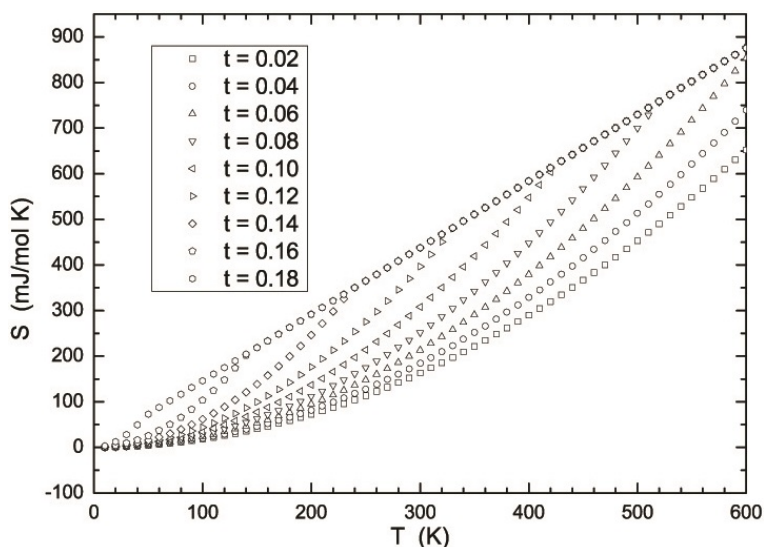


FIG. 3. The entropy \mathcal{S} (Eq. (16)) vs. T at various t (values of \mathcal{S} behind the crossing of linear and nonlinear parts of \mathcal{S} are added artificially).

However, irrespective the quality of t/t_c and T/T^* laws in Eqs. (14) and (16) one can say that at small values for these parameters the single particle boson contribution into κ and \mathcal{S} properly describes the experiment.

5. Summary and conclusion

We have carried out an attempt to describe in the unified anyon-related boson approach the PG phase electronic low- T heat conductivity κ , entropy \mathcal{S} and the IGS, and low- T MIC of cuprates. We have argued that the observed $\kappa \sim T^{3.6}$ and $\kappa \sim T$ is a result of $c \sim T^4$ and $c \sim T$ dependencies, respectively, while $\mathcal{S} \sim T^i$ with $i > 1$ originates from $c \sim T^4$ of the specific heat c for IGBQ of 2D Coulomb-interacting boson gas. Providing by the qualitative and quantitative arguments, we have attributed the downturn behavior of κ to the MIC and transition into the IGS. Assuming that the PG phase consisted from the mixture of IGBQ and 2D LFLT QP gas, we have obtained the Lorentz ratio values of WFL, which were close to experimental ones. We have clarified the origin of the decoupling of charge carriers with phonons as transition of free QPs of IGBQ into plasmons.

We have shown that the total MIC originates from bosons of the Coulomb single boson and single fermion two liquid model and fermions, whose origin is these bosons. At an increase of doping up to the critical value (Eq. (14)) or temperature up to PG boundary temperature (Eq. (16)), this boson system undergoes bosonic insulator – bosonic metal – fermionic metal transitions. It is interesting that this MIC behavior of the doping and temperature resembles the right-angled triangle rule, in which variables vary along horizontal and vertical legs, respectively. We note that there also exists a small part of the model fermion component, which is not related to single bosons and at the same variation of doping or temperature undergoes insulator – metal crossover and does not contribute to the MIC (see Ref. [18]). We have succeeded in describing of the Boebinger *et al.* experimental temperature and doping MIC boundary of resistivity.

The good agreement of the calculated within Coulomb two liquid model results for heat conductivity downturn, anomalous Lorentz ratio, and nonlinear entropy with experimental ones may indicate on the correctness of this model's concepts. In paper II of this series, we will try to understand within our model the physics of other MIC phenomena: resistivity temperature upturn, insulating ground state, nematicity- and stripe-phases, and Fermi pockets. The next important issue obtained in paper II will be a demonstration that the recently observed in the hidden magnetic order and STM experiments spin and charge fluctuations are the intra PG and HTS pair fluctuations.

Some results of the presented paper, without derivation and detail discussion, have partially been published in Ref. [21].

Acknowledgement

Authors B. Abdullaev and C.-H. Park acknowledge the support of the research by the National Research Foundation (NRF) Grant (NRF-2013R1A1A2065742) of the Basic Science Research Program of Korea.

References

- [1] Takagi H. et al. Systematic evolution of temperature-dependent resistivity in $\text{La}_{2-x}\text{Sr}_x\text{CuO}_4$. *Phys. Rev. Lett.*, 1992, **69**, P. 2975–2979.
- [2] Keimer B. et al. Magnetic excitations in pure, lightly doped, and weakly metallic La_2CuO_4 . *Phys. Rev. B*, 1992, **46**, P. 14034.
- [3] Wuyts B., Moshchalkov V.V., Bruynseraede Y. Resistivity and Hall effect of metallic oxygen-deficient $\text{YBa}_2\text{Cu}_3\text{O}_x$ films in the normal state. *Phys. Rev. B*, 1996, **53**, P. 9418.
- [4] Abe Y. et al. Normal-state magnetotransport in $\text{La}_{1.905}\text{Ba}_{0.095}\text{CuO}_4$ single crystals. *Phys. Rev. B*, 1999, **59**, P. 14753.
- [5] Ando Y. et al. Logarithmic Divergence of both In-Plane and Out-of-Plane Normal-State Resistivities of Superconducting $\text{La}_{2-x}\text{Sr}_x\text{CuO}_4$ in the Zero-Temperature Limit. *Phys. Rev. Lett.*, 1995, **75**, P. 4662–4665.
- [6] Boebinger G. S. et al. Insulator-to-Metal Crossover in the Normal State of $\text{La}_{2-x}\text{Sr}_x\text{CuO}_4$ Near Optimum Doping. *Phys. Rev. Lett.*, 1996, **77**, P. 5417–5420.
- [7] Fournier P. et al. Insulator-Metal Crossover near Optimal Doping in $\text{Pr}_{2-x}\text{Ce}_x\text{CuO}_4$: Anomalous Normal-State Low Temperature Resistivity. *Phys. Rev. Lett.*, 1998, **81**, P. 4720–4723.
- [8] Ono S. et al. Metal-to-Insulator Crossover in the Low-Temperature Normal State of $\text{Bi}_2\text{Sr}_{2-x}\text{La}_x\text{CuO}_{6+\delta}$. *Phys. Rev. Lett.*, 2000, **85**, P. 638–641.

- [9] Ando Y. et al. Supporting evidence of the unusual insulating behavior in the low-temperature normal-state resistivity of underdoped $\text{La}_{2-x}\text{Sr}_x\text{CuO}_4$. *J. Low Temp. Phys.*, 1996, **105**, P. 867–875.
- [10] Hill R. W. et al. Breakdown of Fermi-liquid theory in a copper-oxide superconductor. *Nature*, 2001, **414**, P. 711–715.
- [11] Proust C. et al. Heat transport in $\text{Bi}_{2+x}\text{Sr}_{2-x}\text{CuO}_{6+\delta}$: Departure from the Wiedemann-Franz law in the vicinity of the metal-insulator transition. *Phys. Rev. B*, 2005, **72**, P. 214511.
- [12] Loram J. W. et al. Electronic specific heat of $\text{YBa}_2\text{Cu}_3\text{O}_{6+x}$ from 1.8 to 300 K. *Phys. Rev. Lett.*, 1993, **71**, P. 1740–1743.
- [13] Loram J. W. et al. Evidence on the pseudogap and condensate from the electronic specific heat. *J. Phys. Chem. Solids*, 2001, **62**, P. 59–64.
- [14] Fujita K. et al. Simultaneous Transitions in Cuprate Momentum-Space Topology and Electronic Symmetry Breaking. *Science*, 2014, **344**, P. 612–616.
- [15] Vojta M. Lattice symmetry breaking in cuprate superconductors: stripes, nematics, and superconductivity. *Adv. Phys.*, 2009, **58**, P. 699–820.
- [16] Vojta M. Stripes and electronic quasiparticles in the pseudogap state of cuprate superconductors. *Physica C*, 2012, **481**, P. 178.
- [17] Sebastian S.E., Harrison N., Lonzarich G.G. Towards resolution of the Fermi surface in underdoped high- T_c superconductors. *Rep. Prog. Phys.*, 2012, **75**, P. 102501.
- [18] Abdullaev B., Park C.-H., Musakhanov M.M. Anyon bosonization of 2D fermions and single boson phase diagram implied from experiment on visualizing pair formation in superconductor $\text{Bi}_2\text{Sr}_2\text{CaCu}_2\text{O}_{8+\delta}$. *Physica C*, 2011, **471**, P. 486–491.
- [19] Gomes K.K. et al. Visualizing pair formation on the atomic scale in the high- T_c superconductor $\text{Bi}_2\text{Sr}_2\text{CaCu}_2\text{O}_{8+\delta}$. *Nature*, 2007, **447**, P. 569–572.
- [20] Pan S.H. et al. Microscopic electronic inhomogeneity in the high- T_c superconductor $\text{Bi}_2\text{Sr}_2\text{CaCu}_2\text{O}_{8+x}$. *Nature*, 2001, **413**, P. 282–285.
- [21] Abdullaev B., Abdullaev D.B. Park C.-H., Musakhanov M.M. Intra pseudogap- and superconductivity-pair spin and charge fluctuations and underdome metal-insulator (fermion-boson)-crossover phenomena as keystones of cuprate physics. *Nanosystems: Phys. Chem. Math.*, 2015, **6**, P. 803–824.
- [22] Abdullaev B., Roessler U., Musakhanov M. An analytic approach to the ground state energy of charged anyon gases. *Phys. Rev. B*, 2007, **76**, P. 075403(1-7).
- [23] March N.M., Young W.H., Sampanthar S. *The Many Body Problems in Quantum Mechanics*. Cambridge, University Press, 1967.
- [24] Nakamae S. et al. Electronic ground state of heavily overdoped nonsuperconducting $\text{La}_{2-x}\text{Sr}_x\text{CuO}_4$. *Phys. Rev. B*, 2003, **68**, P. 100502(R).
- [25] Smith M.F., et al. Origin of anomalous low-temperature downturns in the thermal conductivity of cuprates. *Phys. Rev. B*, 2005, **71**, P. 014506.
- [26] Luo J.L., et al. The magnetic field dependence of the electronic specific heat of $\text{Y}_{0.8}\text{Ca}_{0.2}\text{Ba}_2\text{Cu}_3\text{O}_{6+x}$. ArXiv: cond-mat/0112065, 2001, 7 p.
- [27] Vedenev S.I., Maude D.K. Metal-to-insulator crossover and pseudogap in single-layer $\text{Bi}_{2+x}\text{Sr}_{2-x}\text{Cu}_{1+y}\text{O}_{6+\delta}$ single crystals in high magnetic fields. *Phys. Rev. B*, 2004, **70**, P. 184524.
- [28] Landau L.D., Lifshitz E.M. *Statistical Physics, Part 1*. Oxford, Pergamon Press, 1980.
- [29] Lifshitz E.M., Pitaevskii L.P. *Statistical Physics, Part 2*. Oxford, Pergamon Press, 1980.
- [30] Abdullaev B. Implicit Anyon or Single Particle Boson Mechanism of HTCS and Pseudogap Regime. In *Trends in Boson Research*, edit. by A.V. Ling. N.Y.: Nova Science Publisher Inc., 2006, P. 139–161.
- [31] Abdullaev B., Park C.-H. Bosonization of 2D Fermions due to Spin and Statistical Magnetic Field Coupling and Possible Nature of Superconductivity and Pseudogap Phases Below E_g . *J. Korean Phys. Soc.*, 2006, **49**, P. S642–S646.
- [32] Ichimaru S. *Plasma Physics: An Introduction to Statistical Physics of Charged Particles*. New York, Benjamin/Cummings, 1986, Chap. 7.
- [33] Tallon J.L., Loram J.W. The doping dependence of T^* – what is the real high- T_c phase diagram? *Physica C*, 2001, **349**, P. 53.
- [34] Abrikosov A.A. *Fundamentals of the Theory of Metals*. Amsterdam, Elsevier Science, 1988.
- [35] Daou R., et al. Linear temperature dependence of resistivity and change in the Fermi surface at the pseudogap critical point of a high- T_c superconductor. *Nature Phys.*, 2009, **5**, P. 31.
- [36] Kim D.H., Lee P.A., Wen X.-G. Massless Dirac Fermions, Gauge Fields, and Underdoped Cuprates. *Phys. Rev. Lett.*, 1997, **79**, P. 2109.
- [37] Varma C.M. Theory of the pseudogap state of the cuprates. *Phys. Rev. B*, 2006, **73**, P. 155113.

Normal state pair nematicity and hidden magnetic order and metal-insulator (fermion-boson)- crossover origin of pseudogap phase of cuprates II

B. Abdullaev¹, D. B. Abdullaev¹, C. -H. Park², M. M. Musakhanov³

¹Institute of Applied Physics, National University of Uzbekistan, Tashkent 100174, Uzbekistan

²Research Center for Dielectric and Advanced Matter Physics, Department of Physics, Pusan National University, 30 Jangjeon-dong, Geumjeong-gu, Busan 609-735, Korea

³National University of Uzbekistan, Tashkent 100174, Uzbekistan

bakhodir.abdullaev@yandex.ru, cpark@pusan.ac.kr, yousufmm@list.ru

PACS 74.72.-h, 74.20.Mn, 74.25.Fy, 74.25.Bt, 74.25.Jb, 74.25.Ha

DOI 10.17586/2220-8054-2017-8-1-59-70

In the present paper II, we will gain an understanding of the nematicity, insulating ground state (IGS), nematicity to stripe phase transition, Fermi pockets evolution, and resistivity temperature upturn, as to be metal - insulator (fermion-boson)- crossover (MIC) phenomena for the pseudogap (PG) region of cuprates. While in the paper I [Abdullaev B., et al. arXiv:cond-mat/0703290], we obtained an understanding of the observed heat conductivity downturn, anomalous Lorentz ratio, insulator resistivity boundary, nonlinear entropy as manifestations of the same MIC. The recently observed nematicity and hidden magnetic order are related to the PG pair intra charge and spin fluctuations. We will try to obtain an answer to the question; why ground state of YBCO is Fermi liquid oscillating and of Bi-2212 is insulating? We will also clarify the physics of the recently observed MIC results of Lalibert et al. [arXiv:1606.04491] and explain the long-discussed transition of the electric charge density from doping to doping+1 dependence at the critical doping. We predict that at the upturns this density should have the temperature dependences $n \sim T^3 n_2$ for $T \rightarrow 0$, where n_2 is density for dopings close to the critical value. We understood that the upturns before and after the first critical doping have the same nature. We will find understanding of all above mentioned phenomena within PG pair physics.

Keywords: high critical temperature superconductivity, cuprate, metal-insulator-crossover, temperature-doping phase diagram, resistivity temperature upturn, insulating ground state, nematicity and stripe phases, Fermi pockets evolution.

Received: 2 August 2016

Revised: 6 August 2016

1. Introduction

Information about the normal state radius of localization for each electron or hole, or its wave function, may play an important role for high temperature T_c cuprate superconductors. The size of this radius may lead to an understanding of the physics of, for example, nematicity and stripe phases. The minimal size for square form nanoregions (NRs) (or of pseudogap (PG) and high T_c superconductivity (HTS) pairs), recently measured in the scanning tunneling microscopy (STM) experiments of Gomes et al. [1] and Pan et al. [2] for visualization of the energy gap formation in the cuprate $\text{Bi}_2\text{Sr}_2\text{CaCu}_2\text{O}_{8+\delta}$, has varied between nearly $4.5 a$ and $2.6 a$ of the $a - b$ plane crystal spacing constant a , when doping varies between two critical values in the doping-temperature phase diagram. Electric charge analysis of these NRs, made by Abdullaev et al. [3], reveals that at the first critical doping we have one boson inside of each NR, while at the second critical doping, one boson and one fermion. The wide spatial spreading of particle-charge in the underdoped region indicates that the role of the dielectric parent compound of cuprates is unimportant, which leads to universality of the properties of all underdoped copper-oxides with the same a .

The concept of Landau Fermi-liquid quasi-particles (QPs) plays a central role in the understanding of the normal state physics for conventional electric conducting materials [4, 5]. Typically, the energies of these QPs depend on momentum and they appear close to the Fermi surface.

For the HTS cuprates (copper-oxides), the normal PG state exhibits highly non-Fermi liquid properties (see, for example, our papers: I [6] and [7], for a comprehensive list of references) and it is unclear whether QPs defined in the momentum space are essential for the PG physics or not. However, as it will be shown in this paper, the real space PG pairs mentioned above and observed in the STM experiment are essential for an understanding of this physics.

In our first paper I [6] we gained an understanding of the following observed MIC phenomena: heat conductivity downturn, anomalous Lorentz ratio, insulator resistivity boundary, and nonlinear entropy. In the present paper (II), we will try to understand of other observed MIC phenomena: IGS, nematicity- and stripe-phases, Fermi pockets evolution, and resistivity temperature upturn. A question can appear about the relation of Fermi pockets evolution to the MIC phenomenon. This question is experimentally studied in detail in the Ref. [8] for $\text{La}_{1.6-x}\text{Nd}_{0.4}\text{Sr}_x\text{CuO}_4$ copper-oxide. However, the origin of Fermi pockets and what is origin of their evolution with doping has still not been adequately explained in the literature. We will see below that the disconnected Fermi pockets may just be indication of a (fermion) IGS and this state's evolution with doping coincides with these pockets' evolution, while the real origin of the MIC may be bosonic.

The seminal STM experiments of Gomes et al. [1] and Pan et al. [2] on the visualization of the real space PG and HTS NRs, which exhibited an energy gap, together with their electric charge and percolation analysis, made by Abdullaev et al. [3], have deeply extended our understanding of the HTS cuprate physics. The theoretical calculation, shown in the Ref. [3], has further justified the possible existence of single bosons in two-dimensional systems as $a - b$ planes of cuprates. The QPs, PG and HTS pairs-single bosons, have become the fundamental particles in our semi-phenomenological Coulomb single boson and single fermion two liquid model, which positions are formulated in the following list [7].

1. The doping charges, in the form of individual NRs, are embedded in the insulating parent compound of HTS copper oxides.
2. Before the first critical doping x_{c1} with NR size $\xi_{coh} = 17 \text{ \AA}$, they are not percolated single bosons.
3. The origin of single bosons is in the anyon bosonization of 2D fermions.
4. At the first critical doping x_{c1} , the percolation of single boson NRs and thus HTS appears; there appear also from x_{c1} doping single fermions, but up to second critical doping, x_{c2} , their NRs do not percolate, thus single fermions between x_{c1} and x_{c2} are insulating.
5. The value $x_{c1} = 0.05$ is universal for all copper oxide HTSs, since percolating single boson NRs cover 50 % of the 2D sample area (like connecting squares in a chessboard); the same situation takes place with NRs for fermions at x_{c2} .
6. The normal phase charge conductivity appears from x_{c2} at $T = 0$ or above PG temperature boundary $T = T^*$, where the percolation of single fermions appears, while for temperatures between T_c and T^* , there exists (fermion-boson) MIC.
7. The spatially rare charge density object, single boson, with NR size between $\xi_{coh} = 17 \text{ \AA}$ and $\xi_{coh} = 10 \text{ \AA}$, which correspond to x_{c1} and x_{c2} dopings, has zero total but fluctuating inside of NR spin (this rareness leads also to fluctuating charge inside of NR).
8. The increase of boson spin fluctuations with doping or temperature results in a transition of bosons into fermions, which occurs at PG T^* or at x_{c2} .
9. At zero external magnetic field, the HTS is a result of the Bose-Einstein condensate of single bosons.
10. At high external magnetic field strengths, the PG insulating ground state is the result of a plasmon gas consisting of these bosons. We note here that $a \approx 3.8 \text{ \AA}$.

The majority of these positions are the result of experimental data analysis. Below, when we will discuss positions from this list, we refer to experimental papers, which confirm the validity of these positions, or use the physical arguments for their support. The background of our model, existence of single bosons, has been derived in our microscopic anyon calculation and found its confirmation in the Gomes et al. and Pan et al. [1,2] STM

experiments. Results of this analysis together with microscopical single boson picture have been combined in the Coulomb two liquid model.

The first two points of these positions have been supported by the experimental paper [9], the authors of which reported on the emergent transition for superconducting fluctuations in the deep antiferromagnetic phase at a remarkably low critical doping, $x_c = 0.0084$, for ruthenocuprates, $\text{RuSr}_2(\text{R,Ce})_2\text{Cu}_2\text{O}_{10-\delta}$ with $\text{R} = \text{Gd, Sm, Nd}$. In this paper, it was claimed that those fluctuations have an intrinsic electronically-inhomogenous nature and provide new support for bosonic models of the superconducting mechanism.

In the introduction section of Ref. [7], we have described a qualitative understanding of the cuprate physics within our Coulomb single boson and single fermion two liquid model. The present paper will be devoted to application of PG pairs for understanding of MIC phenomena listed above. In the Sec. 2 we will give an understanding of the nematicity, IGS, nematicity-stripe phases transition, and Fermi pockets evolution with doping. We explain in detail the physical origin of each phenomenon using the NRs concept. To understand of the resistivity temperature upturn effect, we will use the Sec. 3. In the Sec. 4 we will discuss about the nematicity and hidden magnetic order as manifestations of the intra PG pair charge and spin fluctuations. We argue in this section why these fluctuations may be an indication of the PG pairs. In the Sec. 5, we formulate an interesting question: “Why is the ground state of YBCO an oscillating Fermi liquid and for Bi-2212 is insulating?” This is taken from the experimental analysis and we attempt to answer to it. For interpretation of the recently published experimental MIC results, from the point of view of our Coulomb two liquid model, we will devote the Sec. 6. And we conclude our paper with the Sec. 7.

2. Nematicity, IGS, Nematicity-stripe phases transition, and Fermi pockets evolution

The definition of the intra-unit-cell nematicity order in the copper-oxides is given in the Ref. [10] and it means the breaking of rotational C_4 symmetry by the electronic structure within CuO_2 unit cell, while the translational symmetry over all cells is conserved. The elemental structure for cuprate’s unit cells has square form with C_4 rotational symmetry. Authors of Ref. [10] have detected in the STM experiment the prominent electronic structure (charge distribution) along of some sides of this cell, in which the two closest oxygen atoms O_2 to the Cu atom played an important role, for the underdoped $\text{Bi}_2\text{Sr}_2\text{CaCu}_2\text{O}_{8+\delta}$.

However, for underdoped cuprate the area of NR is largest. Thus, a single boson unit charge is spread over the whole NR, which covers several unit cells, giving a very low regional charge density for the NR. The connection of Cu and O atoms in the unit cell of parent compound is electrically polarized. It redistributes and fixes a charge inside of the NR. As a result, a pinning of the NR occurs. The pattern of NRs with random pinning of their charges in real space yields the pattern for the electronic nematicity. On the other hand, the soft pinning of NR charges does not destroy the system’s translational symmetry.

The pinning of single boson charges in a strong magnetic field (we remember that this magnetic field destroys the HTS and experiment detects IGS (see our paper I)) by the cuprate parent compound is similar to the Wigner crystal of 2D electrons pinning in a disorder potential and in the same magnetic field. However, this Wigner crystal, under the same external potentials, results in the IGS of electrons (see Refs. [11, 12]). Therefore, the plasmon gas of pinned 2D charged single bosons has the IGS. Thus, if the pinned charged bosons are insulating, then the plasmons of this gas is also insulating. The last leads to the IGS of bosonic insulator or to IGS of cuprates (see Refs. [13–17] and point 10. in the above list of our model positions). This can be detected by measuring of this plasmon gas frequency using method described in [11, 12]. Then, the bosonic insulator - bosonic metal transition can experimentally be observed at a point for this frequency when it goes to zero. Physically, this transition corresponds to the changing of the charged boson gas elementary excitation spectrum from a plasmon part into a free particle one [6].

Authors of Ref. [18] have displayed in their Fig. 8 the schematic evolution of the nematic and stripe charge order phases with doping. They showed that a nematic charge order, with violation of the system's rotational symmetry and small spatial size of this order, dominates at initial dopings of the HTS dome phase diagram. While the stripe phase, with violation of the system's translational symmetry, appears for dopings close to the optimal (critical) level.

The fact that the system's translational symmetry is violated means that a factor, which violates this symmetry, has the same spatial size as CuO_2 unit cell. With an increase of doping in the interval between two critical levels and close to the optimal one, the spatial sizes of NRs decrease and single bosons transform into single fermions [3]. Together with insulating single fermions, appearing at the first critical doping (see point 4. of the model positions), the concentration of fermions becomes dominant in the mixture of bosons and fermions. Therefore, for violation of the system's translational symmetry, and thus for a stripe phase, the responsible the NRs occupied by charged single fermions (the real space size of the fermion NR is close to a).

The schematic evolution of the nematic and stripe charge order phases with doping resembles the bosonic insulator – bosonic metal transition crossover. The temperature-doping boundary of both these evolutions is described by the formula (see Eq. 13 of Ref. [6]):

$$T_{bIM} \approx 0.368[x(1 - x/x_c)]^{2/3} Ry, \quad (1)$$

where x_c and Ry are the critical doping and Rydberg atomic energy unit, respectively.

Now, it is worthwhile to discuss about Fermi pockets evolution with doping as an additional signature of the MIC. Fermi pockets and stripe phases belong to a very controversial subject of PG cuprate physics. There is a widely accepted belief that there is a relationship between these two objects and furthermore, through Fermi surface reconstruction, stripe phases induce the formation of Fermi pockets (see reviews [19,20] and references therein).

All the problems with understanding of experimental data result from the fact that the QPs, which determine the cuprate physics have so far been considered as fermions. A fermion statistics signature of these QPs has been detected by observation of Fermi pockets, as constituents of a Fermi surface. However, the manifestation of fermions in a parent compound's Brillouin zone starts at low dopings in the form of Fermi arcs. Then, upon evolution with doping, it acquires Fermi pockets, and, finally, after optimal doping, it becomes circle like, as for a homogenous Fermi gas [21].

However, the PG and thus the HTS cuprate physics is closely related with the MIC mechanism discussed in the present paper. As seen from the list of the Coulomb two liquid model positions, the electric current properties, between the first and second critical dopings, are determined by two percolation channels. The first one is conducting channel with percolation of NRs and thus particles inside of each NR; to this channel belongs the bosonic insulator-bosonic metal-fermionic metal transitions.

The second one belongs to the non-percolative, insulating channel. All fermions for dopings between the first and second critical concentrations are from this channel. These charged fermions do not contribute to the PG current properties and physics, therefore, we call them insulating fermions. The experimental information on these fermions cannot be used for clarification of anything in the PG phase physics. Only from the second critical doping, when the percolation of NRs of these fermions together with fermions obtained in the percolative channel starts on, the charged fermions begin to play a role. Everything stated here for insulating fermions is actually for temperatures below the PG boundary T^* . Percolation starts here from T^* .

The information about the evolution of Fermi pockets with doping also finds understanding within the insulating fermions. Two critical doping values in the phase diagram temperature-doping of cuprates exactly relate with two maximal and minimal sizes of NRs, which means that distances between particles-fermions varies between these two NR sizes. If we denote the NR size at a given doping x as $\xi_{coh}(x)$, then two limiting values for the Fermi pocket

wave vector are approximately determined as $k_{F1} \approx 2\pi/\xi_{coh}(x_{c2})$ and $k_{F2} \approx 2\pi/\xi_{coh}(x_{c1})$. Variation of these two values for the wave vector with doping x is given by formulas $k_{F1} \approx 2\pi/\xi_{coh}(x_{c2})$ and $k_{F2} \approx 2\pi/\xi_{coh}(x)$.

Finally, we note that a Fermi surface in the form of disconnected arcs or pockets is a signature of an insulator rather than a conductor. Because, for the conductor, the wave vector of a charge carrier can be arbitrary inside of a Fermi surface: from zero value up to one of the finite Fermi wave vector [5].

3. Resistivity temperature upturn

The validity of the low-temperature (low- T) heat transport Wiedemann – Franz law (WFL):

$$\kappa/(\sigma T) = L_0 , \quad (2)$$

where L_0 is the Lorentz ratio with Sommerfeld's value $L_0 = (\pi^2/3)(k_B/e)^2$ and κ and σ are the heat and electric charge conductivities, respectively, has been perfectly proven for many conventional metals [4]. We note that the L_0 value corresponds to the three dimensional (3D) case. Simple calculation shows that it can be also applied for the 2D case. An explanation of the WFL for metals was based on the exploitation of the simple Drude model for κ and σ involving Fermi liquid QPs [4]. This model suggests the relation:

$$\kappa = (1/2)cvl \quad (3)$$

for 2D heat conductivity κ (for the 3D case the factor should be 1/3) and

$$\sigma = e^2 n\tau/m \quad (4)$$

for the charge conductivity σ . Here c , v and l in Eq. (3) are the specific heat, mean velocity and mean free penetration length, respectively, and e , n and τ in Eq. (4) are the charge, 2D density and mean lifetime, respectively, of Fermi liquid QPs with mass m . For the low- T limit the T dependence of κ is entirely determined by the specific heat c . Since the velocity v (as a velocity on the Fermi surface) is a function of n and the length $l \approx v\tau$ is also T independent due to τ being characterized by scattering of QPs with impurities [5] for these temperatures. For Fermi liquid QPs $c \sim T$ (see Ref. [5]), therefore, $\kappa \sim T$ and this leads to Eq. (2) for WFL of that gas of QPs (T independence of σ is obvious from Eq. (4)).

Hill et al. have reported on the first WFL measurement of electron-doped copper-oxide $\text{Pr}_{2-x}\text{Ce}_x\text{CuO}_4$ in the pioneer paper [22]. They suppressed the HTS by the strong magnetic field and measured the low- T dependence of the heat conductivity κ for the PG QPs of cuprate. The observed κ deviated from the normal linear $\kappa \sim T$ behavior into an anomalous $T^{3.6}$ with the decrease of T . This behavior, called in the literature as downturn, has also been observed in the other hole-doped copper-oxides (see for references Refs. [6, 7]). The measurement of κ was performed in these hole-doped copper-oxides likewise after suppression of the HTS by a strong magnetic field.

Smith et al. [23] have suggested by phenomenological treatment that the downturn of κ is a result of the decoupling of the heat carrying phonons and electrical charge carriers at low- T , while Hill et al. [22] have noted that the downturn is a fundamental intrinsic property of copper oxides. The downturn has been widely accepted as a characteristic of non-Landau Fermi liquid behavior. As the next evidence for the non-Fermi liquid QPs property was recognized the fact that the cuprate Lorentz ratio was significantly larger than Sommerfeld's value [24].

In our preceding paper (Ref. [6]) we have shown that these non-Landau Fermi liquid behaviors of the low- T heat conductivity and Lorentz ratio are results of the MIC property of the cuprate PG regions, in which the IGS originates from a plasmon gas of 2D charged single bosons, pinned by a ferroelectric field of parent compound atoms (see also previous section). In this section, we show that the downturn T dependence carries the important information on the low- T scale of the MIC charge conductivity or resistivity. It will be demonstrated that this scale of the charge conductivity is driven by that of the specific heat. One should note that the physics of the MIC low- T scale of copper-oxides was far from the clear understanding.

As we argued in Ref. [6], the magnetic field does not affect on the energy of elementary excitations, i.e., plasmons, of gas of charged single bosons. The weak ferroelectric field effect of the cuprate atoms is also negligible for this energy. Therefore, we can use here results for the low- T heat conductivity κ and the specific heat c , obtained in [6] for the above-mentioned gas of plasmons. Namely, we assume that there exists a some downturn temperature T_d^κ of κ , which separates the linear $\kappa \sim T$ dependence from the downturn $\kappa \sim T^4$ one, in the PG phase of cuprates. Irrespective of the QP nature we consider, one may suppose the validity of WFL, Eq. (2), and Drude model, i.e., Eq. (3) and Eq. (4), for these QPs. However, it is necessarily to replace in these formulas $L_0 \rightarrow L$, since L has the explicit doping dependence (see Refs. [6, 24]).

On the other hand, the linear dependence $\kappa \sim T$ for $T > T_d^\kappa$ resembles the case of conventional metals, in which freely penetrating QPs are fermion-like and have $c \sim T$ dependence for the specific heat. Additionally, for low- T and $T > T_d^\kappa$ we may again apply the above arguments for the T independence of v and l for these QPs as well as conjecture that the temperature dependent κ arises from the T dependence of the specific heat $c(T)$.

We introduce the notations $c_1 \sim T^4$ and $c_2 \sim T$ for specific heats with T^4 and T dependencies, respectively, and σ_2 for charge conductivity, when $c_2 \sim T$. Hence, the total specific heat c transits from c_1 to c_2 as T increases. The $c \sim T^4$ dependence is consistent with the function $\mathcal{S} \sim T^i$ with $i > 1$ of an entropy (integral $\mathcal{S} = \int_0^T (c/T_1) dT_1$) observed in Ref. [25] for the insulating $\text{YBa}_2\text{Cu}_3\text{O}_{6+x}$ compound.

In the experimental papers on the WFL of cuprates, authors use the residual value for the charge conductivity σ_2 , which is the intercept of σ_2 , measured for $T \geq T_d^\kappa$ range, by extrapolation to the $T \rightarrow 0$ limit. It was previously shown (see Refs. [5]) that the typical low- T σ_2 is nearly constant, which is in accordance with the above assumption regarding the scattering of freely penetrating QPs with impurities. Therefore, one assumes $\sigma = \sigma_2 \approx \text{const}$ in WFL, Eq. (2), in the experimental measurements in this subject. We substitute the expressions for κ , Eq. (3), and σ_2 , Eq. (4), in the left hand side of Eq. (2). Then recalling that κ is expressed by the total specific heat c , one obtains the formula

$$\kappa/(\sigma_2 T) = cL/c_2 \quad (5)$$

for the measured WFL of cuprates, where the constant L is defined by the expression $L = c_2 m v^2 / (2e^2 n T)$. It is clear that L is determined for the $T \geq T_d^\kappa$ temperatures, for which the “metallic” QPs are well defined. We cannot calculate the numerical value of L . Since numerical data of empirical quantities, through which it is expressed, are unknown. However, from the paper [24] of Proust et al. we know that L is constant for fixed doping. Therefore, Eq. (5) demonstrates that for fixed doping, the T dependence of WFL is provided by c/c_2 factor and vice versa, the observed data on WFL determine the T dependent c/c_2 .

Let us suppose that the WFL for copper-oxides is temperature, T , independent as for conventional metals and defined by the relation $\kappa/(\sigma T) = L$, where σ varies now in the whole interval of T . Multiplying and dividing the left hand side of this relation by σ_2 and using Eq. (5) we obtain the expression

$$\sigma = c\sigma_2/c_2, \quad (6)$$

which is the main result of the present section. Then, Eq. (6) has two asymptotic limits: $\sigma = \sigma_2$ for $T > T_d^\kappa$, when $c = c_2$, and $\sigma \sim T^3 \sigma_2$ for $T < T_d^\kappa$ and $T \rightarrow 0$, when $c \sim T^4$. While for the first limit, the charge conductivity σ equals that of the conductor σ_2 (since $\sigma_2 = \text{const} \neq 0$). For the second limit, due to vanishing of σ at $T \rightarrow 0$, we have the conductor to insulator transition or the MIC. The important thing is the insulator charge conductivity has the $\sigma \sim T^3$ dependence. This T dependence for σ may be used in the experiment for the indication of the insulating state.

We may clarify the origin of the MIC crossover. For this we extend the Drude formula, Eq. (4), for the charge conductivity σ to the all considered temperatures (including the $T < T_d^\kappa$ interval) and define the concentration of charge carriers n , which corresponds to the σ . Let the “metallic” conductivity σ_2 be defined by Eq. (4) itself with the charge concentration n_2 . Substituting both the Drude formulas for σ and σ_2 in the Eq. (6) we obtain

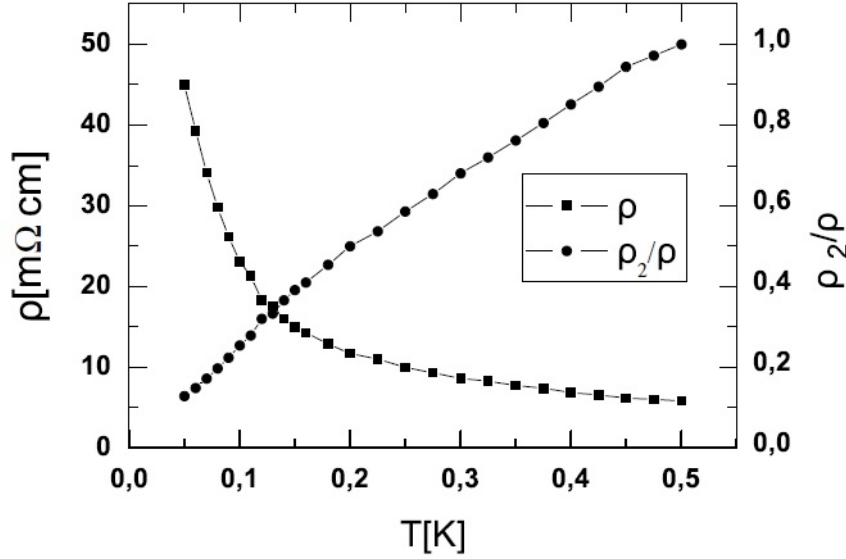


FIG. 1. The low- T dependence of a resistivity ρ for $\text{La}_{2-x}\text{Sr}_x\text{CuO}_{4+\delta}$ copper-oxide with $x = 0.06$ (from Fig. 3 (a) of Ref. [26]) and constructed on the base of this ρ our ratio ρ_2/ρ . It was assumed that metallic $\rho_2 = \rho$ ($T = 0.5$ K)

$n = cn_2/c_2$. In the last equation, we have implied the reasonable argument that other parameters of the gas of QPS (except the concentration n) should not change in the MIC. From this expression for n , we see that $n = n_2$ for $T \geq T_d^*$, when all charge carriers are the freely penetrating QPs, and $n \sim T^3 n_2 \rightarrow 0$ for $T < T_d^*$ and $T \rightarrow 0$. The second limit of n corresponds to vanishing of QPs. The decrease in the density of the conducting carriers is a reason for the MIC of cuprates. It is also the origin of the decoupling of the heat-carrying thermal phonons with these charge carriers [23].

The dependence for the concentration of carries, $n \sim T^3 n_2$, as a function of temperature, T , and at fixed doping, x , can be experimentally measured for any copper-oxide by using the method, described, for example, in the Ref. [27].

In Fig. 1, we plot the low- T dependence of a resistivity ($\rho = 1/\sigma$) taken from Fig. 3(a) of Ref. [26] for $\text{La}_{2-x}\text{Sr}_x\text{CuO}_{4+\delta}$ copper-oxide with $x = 0.06$. It is also shown in this figure the ratio $\rho_2/\rho = \sigma/\sigma_2$, where we assumed that $\rho_2 = \rho$ ($T = 0.5$ K). The observed in [26] result for ρ corresponds to the insulating normal state of the compound obtained by suppression of HTS by a strong magnetic field. As seen from Fig. 1, ρ_2/ρ line has the downturn behavior below $T = 0.5$ K and an obvious non-linear dependence for $T \leq 0.15$ K. This downturn relates to an MIC. However, since the slope of the depicted $\rho(T)$ is negative at $T = 0.5$ K, the $\rho_2/\rho = 1$ assumption is approximate, and the copper-oxide is still in the crossover state at this T . The downturn region of ρ_2/ρ extends for higher temperatures.

In Fig. 2, we compare in the semi-log scale the low- T dependence of $\rho(T)$ measured for purely insulating state $x = 0.05$ (without magnetic field) of the same copper-oxide (the insert of Fig. 3 (a) in Ref. [26]) with our empirically found $(aT)^{-3}$ function, where $a = 0.464 \text{ K}^{-1}$. As is evident from this figure, our function satisfactorily fits the non-linear part of the observed $\rho(T)$ for the lowest temperatures. This non-linear T dependence of $\rho(T)$ is also seen in Fig. 1 for lowest T . One may assume both insulating states have the same origin and for both, the T^{-3} dependence of $\rho(T)$ is valid.

At the end of this section, we note that the IGS of copper-oxides, the origin of which is the plasmon gas of 2D charged single bosons, results in the resistivity temperature upturn at the low- T limit as at strong magnetic field and $x > x_{c1}$, when the HTS is suppressed by this field, so and for purely insulating state with $x < x_{c1}$ and

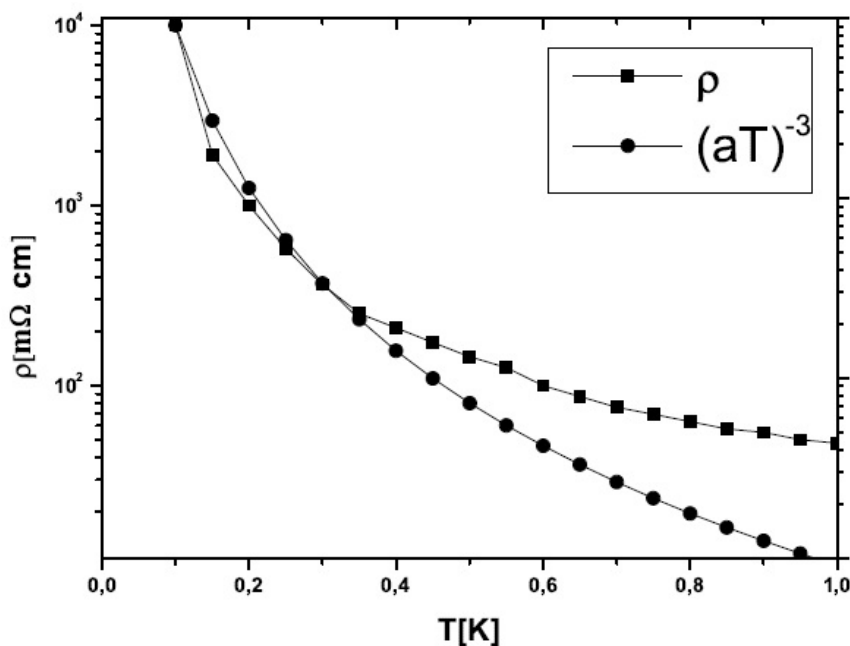


FIG. 2. The semi-log scale of the low- T dependence of ρ for $\text{La}_{2-x}\text{Sr}_x\text{CuO}_{4+\delta}$ copper-oxide with $x = 0.05$ (measured without a magnetic field and below the first critical doping) (the insert of Fig. 3 (a) of Ref. [26]) and our empirically fitted function, $-3 \log(aT)$, with $a = 0.464\text{K}^{-1}$. It is seen that our function satisfactorily represents the non-linear part of the observed ρ at lowest T

without field. This is in accordance with point 10 of the Coulomb two liquid model positions and confirms the point 1, which means that, even though at $x < x_{c1}$ the electric charges and their NRs are not percolating, due to plasmon origin of the IGS, the resistivity displays the upturn behavior. In principle, the last argument can also be applied for insulating fermions for dopings in the interval $x_{c1} \leq x \leq x_{c2}$. It seems that they should give a similar upturn in the resistivity. However, the weight of their concentration with respect to one of single bosons for the same dopings is not high.

4. Nematicity and hidden magnetic order as intra PG pair charge and spin fluctuations

First observed in $\text{YBa}_2\text{Cu}_3\text{O}_{6+x}$ (Y123) compound, using polarized elastic neutron diffraction [28], the hidden magnetic order has been observed in three other copper-oxide families: $\text{HgBa}_2\text{CuO}_{4+\delta}$ (Hg1201) [29, 30], $\text{La}_{2-x}\text{Sr}_x\text{CuO}_4$ (La214) [31] and $\text{Bi}_2\text{Sr}_2\text{CaCu}_2\text{O}_{8+\delta}$ (Bi-2212) [32] (see for references also [33]). Since the size of detection was a few structural cells, it was called the intra-unit-cell (IUC) hidden magnetic order.

These interesting experiments have revealed the existence of IUC objects in the PG phase with fluctuating spin components inside, which exactly cancel each other, so that the total spin of the every object was zero. Despite the authors of Ref. [28] having interpreted the physics of both, total and intra, spins either by invoking of a pair of oppositely flowing intra structural cell charge loop-currents or of staggered spins in the same cell, the role of these objects in the physics of copper-oxides was not understood [34].

This role becomes unambiguously clear, if we connect these objects with the visualization of NRs which exhibit the energy gap in the STM experiment [1]. Since, as NRs, they exist in the PG region and disappear in the PG temperature boundary T^* [28]. There is no doubt that their evolution with temperature will be the same as for NRs. While their evolution with doping (see Refs. [28–30]) qualitatively coincides with that of the NRs, described in [3]. However, minimal size NRs are single bosons, therefore, the IUC hidden magnetic order objects are also

single bosons and PG and HTS pairs. On the other hand, the spin fluctuation inside of the single boson was introduced in our original papers on the single boson mechanism of HTS [35,36]. Furthermore, the increase of this fluctuation with temperature below PG boundary T^* and doping below the second critical x_{c2} and transformation of these single bosons into single fermions in T^* and x_{c2} was physical origin of T^* and x_{c2} .

The spatially intra rare charge density of each single boson allows one to understand the nature of the intra unit cell electronic nematicity, observed recently in the STM experiment [10], as the intra PG pair dynamic charge fluctuation. The strong ferroelectric crystal field of the parent compound forms an atomic scale charge distribution within an individual NR (see for details the Sec. 2).

The evolution of the dynamic charge fluctuation with doping resembles that of the IUC hidden magnetic order [21] (Ref. [21] contains a very thorough up-to-date list of references on the subject of IUC spin and charge fluctuations).

5. Why ground state of YBCO is Fermi liquid oscillating and of Bi-2212 is insulating?

The Fermi liquid like behavior of conducting QPs have been observed through the measurement of magnetoresistance oscillations at high magnetic fields in the underdome region of the temperature-doping phase diagram. The authors of these quantum oscillation experiments have succeeded in measuring a Fermi surface, which had a form of Fermi pockets. This effect was found for the YBCO family of cuprates for dopings up to the optimal level (see the review of Ref. [19,20] for references).

However, the quantum oscillations were not found in other copper-oxides, whose ground states were insulating in the same magnetic fields (see Refs. [13–17]). There appears the question: Why the ground state of some copper-oxide compounds is Fermi liquid oscillating and of other cuprates is insulating and can this discrepancy be understood within the framework of a single model?

If we look on the Table 1, we see that the critical doping for the YBCO cuprate is $x_c = 0.19$, while for the Bi-2212 one is $x_c = 0.28$. The lowest critical x_c provides the percolation for the single fermion NRs at the lower dopings, close to x_c . Thus the YBCO cuprate has the Fermi liquid oscillating ground state. While for Bi-2212, i.e., $\text{Bi}_2\text{Sr}_2\text{CaCu}_2\text{O}_{8+\delta}$ HTS compound, the single fermion NRs are not percolating for almost all x between x_{c1} and x_{c2} . Therefore, the ground state of Bi-2212 material in a strong magnetic field is insulating (see Ref. [37]). However, it is worthwhile to note here that the cuprate *LSCO* with low critical doping $x_c = 0.18$ (see Table 1) has, for unknown reasons to us, an insulating ground state (see Refs. [13–17]).

6. Interpretation of experimental MIC results 2016

The resistivity of cuprates at low temperatures and in high magnetic fields revealed the appearance of an insulator-like upturn in its temperature dependence [13–17], which we already discussed in Sec. 3. This upturn (MIC) behavior is still considered puzzle in the literature.

Using high-field resistivity measurements on $\text{La}_{2-x}\text{Sr}_x\text{CuO}_4$, Lalibert F. et al. [27] have tried to experimentally show that this MIC upturn property is due to a drop in carrier density n associated with the onset of the PG phase at the critical doping x_c . Namely, authors of Ref. [27] proposed that the upturns are quantitatively consistent with a drop from $n = 1 + x$ above x_c to $n = x$ below x_c . Based on that idea, the explanations of the upturns for other copper-oxides are also given in [27]. Here, we note that this transition in carrier density n dependence is the long term discussed in a literature issue (see [27] for references).

First, we start with mentioning (see Sec. 2) that all electric current properties of cuprates should be considered within the conducting percolation channel. Therefore, the resistivity temperature upturn is a result of this channel, more exactly, as we demonstrated in Sec. 3, of the plasmon gas of 2D charged single bosons. No charged single fermions below the critical doping x_c play a role. Their NRs are not percolating, thus these fermions are insulating.

TABLE 1. Carrier density as function of normalized to x_c doping for LSCO= $\text{La}_{2-x}\text{Sr}_x\text{CuO}_4$, YBCO= $\text{YBa}_2\text{Cu}_3\text{O}_y$ and Nd-LSCO= $\text{La}_{1.6-x}\text{Nd}_{0.4}\text{Sr}_x\text{CuO}_4$, taken from Ref. [27], and for fermion carrier density for Bi-2212= $\text{Bi}_2\text{Sr}_2\text{CaCu}_2\text{O}_{8+\delta}$, taken from Ref. [3]. For the comparison, in the brackets we showed numerical values for Bi-2212, if the function was measured in the experiment

| x/x_c | 0.2 | 0.4 | 0.6 | 0.8 | 1.0 |
|------------------------|--------|---------|---------|---------|-------------------|
| LSCO, $x_c = 0.18$ | | | | | |
| $n(x/x_c)$ | 0.04 | 0.07 | 0.1 | 0.14 | 1.18 |
| YBCO, $x_c = 0.19$ | | | | | |
| $n(x/x_c)$ | 0.04 | 0.08 | 0.11 | 0.15 | 1.4 ± 0.4 |
| Nd-LSCO, $x_c = 0.235$ | | | | | |
| $n(x/x_c)$ | 0.05 | 0.09 | 0.14 | 0.188 | 1.3 ± 0.4 |
| Bi-2212, $x_c = 0.28$ | (0.06) | (0.112) | (0.168) | (0.224) | (1.3 ± 0.4) |
| $f(x) = n(x/x_c) - 1$ | -0.103 | 0.170 | 0.341 | 0.524 | 0.939 |

Secondly, one needs to make clear the definition of a carrier density. Because it does not simply indicate the fraction of charge x per Cu atom. As we already discussed in previous sections, only the NR, i.e. the PG pair, carries the charge n in the normal state. And for doping x between critical x_{c1} and x_{c2} we have $n = 1 + f(x)$, where the charge of boson is 1 and the charge of fermion is $f(x)$. Here, the function $f(x)$ is phenomenological and taken from the STM experimental data for NRs (see Table 1 for Bi-2212). Therefore, the fraction $f(x)$ indicates the charge of fermion inside the PG pair. At the approach of x to x_{c2} , or for PG pair size approaching that of $2a$, the charge of fermion tends to 1 and thus each Cu atom contains one doped fermion-hole. This is reason why at critical doping x_c in Ref. [27] the charge density adds 1 or becomes $n = 1 + x$.

Lalibert F. et al. claim in the Ref. [27] that the transition $n = 1 + x$ into $n = x$ for the carrier density n has a sharp, like in a second order phase transition, form and it occurs exactly at the critical doping x_c . However, the original Refs. [13–17] result on the upturns was MIC, which means a soft gradual transition, and it occurred according to [13–17] at “near optimal doping”, i.e., below critical doping x_c . Furthermore, Boebinger et al. demonstrated in the Ref. [17] that this MIC temperature-doping boundary resembles the PG boundary T^* but located below T^* . This MIC boundary approximately describes by Eq. (1) and corresponds to bosonic insulator-bosonic metal transition boundary, as was discussed in our Ref. [6], while the total PG phase MIC corresponds to bosonic insulator-bosonic metal-fermionic metal transitions [7]. The last transition occurs at T^* .

One needs to note at the end of this section that the fraction of dopings corresponding to single bosons is hidden from the Luttinger sum rule investigations of copper oxides. This rule investigates only fermions, however, there is a variety of publications, which supports or violates the Luttinger sum rule for these materials. Refs. [38, 39], for example, violates this rule.

7. Conclusion

In conclusion, we have found an understanding for the nematicity, IGS, nematicity to stripe phase transition, Fermi pockets evolution, and resistivity temperature upturn, as to be MIC phenomena for the PG region of cuprates. While in our initial paper, we have found an understanding of the observed heat conductivity downturn, anomalous Lorentz ratio, insulator resistivity boundary, nonlinear entropy as manifestation of the same MIC. The observed nematicity and hidden magnetic order have been related to the PG pair intra charge and spin fluctuations. Probably, we could understand the answer on the question: Why ground state of YBCO is Fermi liquid oscillating and of

Bi-2212 is insulating? We have also analyzed the physics of the recently observed MIC result of Lalibert et al. [27] and explained the long term discussed in the literature transition of the electric charge density from doping to doping+1 dependence at the critical doping. We predict that at the upturns this density should have a temperature dependence of $n \sim T^3 n_2$ for $T \rightarrow 0$, where n_2 is density for dopings close to the critical level. We understood that the upturns before and above first critical doping have the same nature. We found understanding of all above mentioned phenomena within the PG pair physics.

Acknowledgements

Authors B. Abdullaev, D.B. Abdullaev and M.M. Musakhanov acknowledge the support of the research by the Volkswagen Foundation of Germany and C.-H. Park by the National Research Foundation of Korea (NRF) grant funded by the Korean Government (2015M3D1A1070639).

References

- [1] Gomes K.K. et al. Visualizing pair formation on the atomic scale in the high- T_c superconductor $\text{Bi}_2\text{Sr}_2\text{CaCu}_2\text{O}_{8+\delta}$. *Nature*, 2007, **447**, P. 569–572.
- [2] Pan S.H. et al. Microscopic electronic inhomogeneity in the high- T_c superconductor $\text{Bi}_2\text{Sr}_2\text{CaCu}_2\text{O}_{8+x}$. *Nature*, 2001, **413**, P. 282–285.
- [3] Abdullaev B., Park C.-H., Musakhanov M.M. Anyon bosonization of 2D fermions and single boson phase diagram implied from experiment on visualizing pair formation in superconductor $\text{Bi}_2\text{Sr}_2\text{CaCu}_2\text{O}_{8+\delta}$. *Physica C*, 2011, **471**, P. 486–491.
- [4] Ashcroft N.W., Mermin N.D. *Solid State Physics*. Philadelphia, HRW, 1976.
- [5] Abrikosov A.A. *Fundamentals of the Theory of Metals*. Amsterdam, Elsevier Science, 1988.
- [6] Abdullaev B., Park C.-H., Park K.-S., Kang I.-J. Metal-insulator (fermion-boson)-crossover origin of pseudogap phase of cuprates I: anomalous heat conductivity, insulator resistivity boundary, nonlinear entropy. ArXiv e-prints, 2007, arXiv:cond-mat/0703290, 8 pp.
- [7] Abdullaev B., Abdullaev D.B. Park C.-H., Musakhanov M.M. Intra pseudogap- and superconductivity-pair spin and charge fluctuations and underdome metal-insulator (fermion-boson)-crossover phenomena as keystones of cuprate physics. *Nanosystems: Phys. Chem. Math.*, 2015, **6**, P. 803–824.
- [8] Collignon C. et al. Fermi-surface transformation across the pseudogap critical point of the cuprate superconductor $\text{La}_{1.6-x}\text{Nd}_{0.4}\text{Sr}_x\text{CuO}_4$. ArXiv e-prints, 2016, arXiv: 1607.05693, 11 pp.
- [9] McLaughlin A.C., Attfield J.P. Emergent Transition for Superconducting Fluctuations in Antiferromagnetic Ruthenocuprates. *Phys. Rev. B*, 2014, **90**, P. R220509.
- [10] Lawler M.J. et al. Intra-unit-cell electronic nematicity of the high- T_c copper-oxide pseudogap states. *Nature*, 2010, **466**, P. 347–351.
- [11] Drichko I.L. et al. Melting of Wigner crystal in high-mobility n-GaAs/AlGaAs heterostructures at filling factors $0.18 > \nu > 0.125$: Acoustic studies. ArXiv e-prints (2016), ArXiv: 1607.01918, 6 pp.
- [12] Shayegan M. *Flatland electrons in high magnetic fields*. In High Magnetic Fields: Science and Technology, Vol. 3, edited by F. Herlach and N. Miura, Singapore, World Scientific Co, 2006, P. 31–60, ArXiv e-prints, 2005, ArXiv: cond-mat/0505520.
- [13] Ando Y. et al. Logarithmic Divergence of both In-Plane and Out-of-Plane Normal-State Resistivities of Superconducting $\text{La}_{2-x}\text{Sr}_x\text{CuO}_4$ in the Zero-Temperature Limit. *Phys. Rev. Lett.*, 1995, **75**, P. 4662–4665.
- [14] Fournier P. et al. Insulator-Metal Crossover near Optimal Doping in $\text{Pr}_{2-x}\text{Ce}_x\text{CuO}_4$: Anomalous Normal-State Low Temperature Resistivity. *Phys. Rev. Lett.*, 1998, **81**, P. 4720–4723.
- [15] Ono S. et al. Metal-to-Insulator Crossover in the Low-Temperature Normal State of $\text{Bi}_2\text{Sr}_{2-x}\text{La}_x\text{CuO}_{6+\delta}$. *Phys. Rev. Lett.*, 2000, **85**, P. 638–641.
- [16] Ando Y. et al. Supporting evidence of the unusual insulating behavior in the low-temperature normal-state resistivity of underdoped $\text{La}_{2-x}\text{Sr}_x\text{CuO}_4$. *J. Low Temp. Phys.*, 1996, **105**, P. 867–875.
- [17] Boebinger G.S. et al. Insulator-to-Metal Crossover in the Normal State of $\text{La}_{2-x}\text{Sr}_x\text{CuO}_4$ Near Optimum Doping. *Phys. Rev. Lett.*, 1996, **77**, P. 5417–5420.
- [18] Caprara S. et al. Signatures of nematic quantum critical fluctuations in the Raman spectra of lightly doped cuprates. *Phys. Rev. B*, 2015, **91**, P. 205115.
- [19] Vojta M. Lattice symmetry breaking in cuprate superconductors: stripes, nematics, and superconductivity. *Adv. Phys.*, 2009, **58**, P. 699–820.
- [20] Vojta M. Stripes and electronic quasiparticles in the pseudogap state of cuprate superconductors. *Physica C*, 2012, **481**, P. 178.
- [21] Fujita K. et al. Simultaneous Transitions in Cuprate Momentum-Space Topology and Electronic Symmetry Breaking. *Science*, 2014, **344**, P. 612–616.
- [22] Hill R.W. et al. Breakdown of Fermi-liquid theory in a copper-oxide superconductor. *Nature*, 2001, **414**, P. 711–715.

- [23] Smith M.F. et al. Origin of anomalous low-temperature downturns in the thermal conductivity of cuprates. *Phys. Rev. B*, 2005, **71**, P. 014506.
- [24] Proust C. et al. Heat transport in $\text{Bi}_{2+x}\text{Sr}_{2-x}\text{CuO}_{6+\delta}$: Departure from the Wiedemann-Franz law in the vicinity of the metal-insulator transition. *Phys. Rev. B*, 2005, **72**, P. 214511.
- [25] Loram J. W. et al. Electronic specific heat of $\text{YBa}_2\text{Cu}_3\text{O}_{6+x}$ from 1.8 to 300 K. *Phys. Rev. Lett.*, 1993, **71**, P. 1740–1743.
- [26] Hawthorn D.G. et al. Field-Induced Thermal Metal-to-Insulator Transition in Underdoped $\text{La}_{2-x}\text{Sr}_x\text{CuO}_{4+\delta}$. *Phys. Rev. Lett.*, 2003, **90**, P. 197004.
- [27] Lalibert F. et al. Origin of the metal-to-insulator crossover in cuprate superconductors. ArXiv e-prints, 2016, arXiv:1606.04491, 16 pp.
- [28] Fauque B. et al. Magnetic order in the pseudogap phase of high- T_C superconductors. *Phys. Rev. Lett.*, 2006, **96**, P. 197001.
- [29] Li Y et al. Unusual magnetic order in the pseudogap region of the superconductor $\text{HgBa}_2\text{CuO}_{4+\delta}$. *Nature*, 2008, **455**, P. 372.
- [30] Li Y et al. Magnetic order in the pseudogap phase of $\text{HgBa}_2\text{CuO}_{4+\delta}$ studied by spin-polarized neutron diffraction. *Phys. Rev. B*, 2011, **84**, P. 224508.
- [31] Baledent V. et al. Two-Dimensional Orbital-Like Magnetic Order in the High-Temperature $\text{La}_{2-x}\text{Sr}_x\text{CuO}_4$ Superconductor. *Phys. Rev. Lett.*, 2010, **105**, P. 027004.
- [32] De Almeida-Didry S. et al. Evidence for intra-unit-cell magnetic order in $\text{Bi}_2\text{Sr}_2\text{CaCu}_2\text{O}_{8+\delta}$. *Phys. Rev. B*, 2012, **86**, P. 020504.
- [33] Mangin-Thro L. et al. Characterization of the intra-unit-cell magnetic order in $\text{Bi}_2\text{Sr}_2\text{CaCu}_2\text{O}_{8+\delta}$. *Phys. Rev. B*, 2014, **89**, P. 094523.
- [34] Norman M. Fermi-surface reconstruction and the origin of high-temperature superconductivity. *Physics*, 2010, **3**, P. 86 (6 pp).
- [35] Abdullaev B., Park C.-H. Bosonization of 2D Fermions due to Spin and Statistical Magnetic Field Coupling and Possible Nature of Superconductivity and Pseudogap Phases Below E_g . *J. Korean Phys. Soc.*, 2006, **49**, P. S642–S646; arxiv:cond-mat/0404668.
- [36] Abdullaev B. *Implicit Anyon or Single Particle Boson Mechanism of HTCS and Pseudogap Regime*. In Trends in Boson Research, edit. by A. V. Ling. N. Y.: Nova Science Publisher Inc., 2006, P. 139–161.
- [37] Zavaritsky V.N. et al. Giant normal state magnetoresistances of $\text{Bi}_2\text{Sr}_2\text{CaCu}_2\text{O}_{8+\delta}$. *EPJ B*, 2004, **42**, P. 367–371.
- [38] Mei Jia-Wei et al. Luttinger-volume violating Fermi liquid in the pseudogap phase of the cuprate superconductors. *Phys. Rev. B* 2012, **85**, P. 134519.
- [39] Yoshida T. et al. Systematic doping evolution of the underlying Fermi surface of $\text{La}_{2-x}\text{Sr}_x\text{CuO}_4$. *Phys. Rev. B*, 2006, **74**, P. 224510.

Simulation of DIBL effect in 25 nm SOI-FinFET with the different body shapes

A. E. Atamuratov¹, A. Abdikarimov¹, M. Khalilloev¹, Z. A. Atamuratova¹,
R. Rahmanov¹, A. Garcia-Loureiro², A. Yusupov³

¹Urganch State University, Kh. Olimjan, 14, Urganch, 220100, Uzbekistan

²University of Santiago de Compostela, Ra de Jenaro de la Fuente Domnguez,
15782 – Santiago de Compostela, Spain

³Tashkent Automobile and Road Institute, 100060 Tashkent, st. A. Temur 20, Uzbekistan

atabek.atamuratov@yahoo.com, ayus@mail.ru

PACS 85.30.Tv

DOI 10.17586/2220-8054-2017-8-1-71-74

Short channel effects, such as DIBL are compared for SOI-FinFETs with different silicon body geometries. The original device considered was straight without narrowing at the top and a set of devices that exhibit the mentioned narrowing, up to the extreme case where the top of the gate has no surface and so the body cross-section is essentially a triangle. We have studied five different variations from the original geometry of a 25 nm gate length SOI-FinFET device with 1.5 nm thick oxide layer. The P-type channel had a doping concentration of 10^{15} cm^{-3} and n-type S/D areas are doped at concentrations of 10^{20} cm^{-3} . The silicon body of the device accordingly had a height of 30 nm and a width of 12 nm. Simulation results show the source-drain barrier decreasing with increasing the upper body thickness. The DIBL effect of the considered FinFETs depends on upper body thickness, tending to increase with thicker upper body widths. Results of a comparison of two devices with different shapes but with the same cross-sectional area shows the relationship mainly depends on the shape rather than the cross-section area of the device body.

Keywords: FinFET, DIBL, potential barrier.

Received: 8 July 2016

Revised: 25 August 2016

1. Introduction

MOSFET scaling induces different effects that tend to degrade device performance. Among the most important are: technological variability of parameters [1], short channel effects (SCEs) [2], influence of single defects in oxide or oxide-semiconductor interface [3]. The use of multiple-gate topologies significantly enhances the electrostatic integrity of the device and provides increased immunity from SCEs [4]. As the devices are scaled down, new sources of variability appear, while other ones might gain more importance [5, 6]. One type of variability is the narrowing of the body which might appear in a multiple-gate FinFET. Previous works on SOI-FinFET [1] have investigated the impact of the device body shape on the electric characteristics, such as threshold voltage, subthreshold swing, on-current, and off-current. In this work, we analyze the influence of body width narrowing in FinFET on short channel effects such as DIBL. The impact of the device body shape on the DIBL of a 25 nm SOI-FinFET was studied using Sentaurus TCAD simulations [7].

2. Device structure

SOI-FinFETs are currently considered one of the most promising solutions to avoid SCEs of MOSFETs, but because the body is aligned in a vertical fashion which allows self-aligned gate contacts, a body narrowing appears at the top of the gate. This will have an effect on the channel, as well as the threshold voltage, off-current, on-current and subthreshold swing [5]. We have studied five different variations from the original geometry of a 25 nm gate length SOI-FinFET device with oxide thickness 1.5 nm. The P-type channel has a doping concentration of 10^{15} cm^{-3} and n-type S/D areas are doped with concentrations 10^{20} cm^{-3} . The silicon body of the device has height and width of 30 nm and 12 nm accordingly. For each device, we had simulated the device using Synopsis Sentaurus software in a local computation cluster. Our objective was to modify the original device, which is straight without narrowing at the top, with a set of devices that exhibit the mentioned narrowing, up to the extreme case where the top of the gate has no surface and so the body cross-section is triangular in shape (Fig. 1).

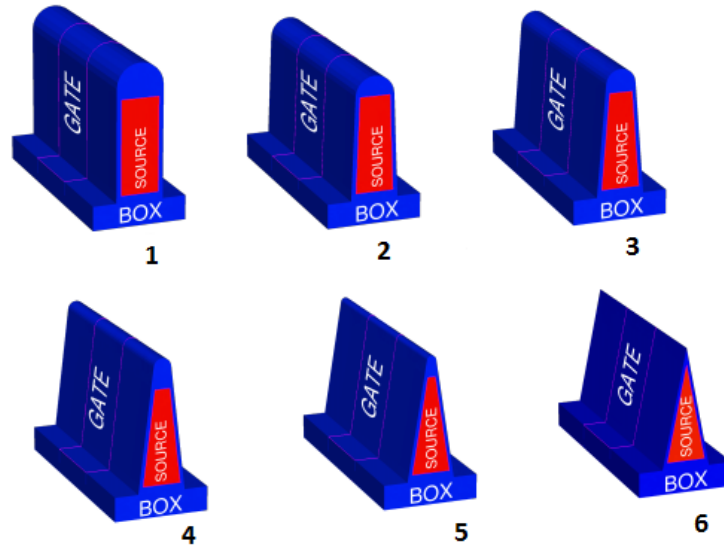


FIG. 1. Cross-section of SOI-FinFETs simulated, with different body top thickness, silicon body cross-section is modified from rectangle shape (a structure 1 with maximal body top thickness) up to triangle geometry (structure 6 with zero body top thickness)

3. Results of simulation and discussion

We have analyzed the influence of varying the geometry of a 25 nm gate length FinFET device to DIBL. This study has been done via drift-diffusion simulations that include quantum corrections.

For calculating DIBL, we simulated I_d - V_g characteristics of FinFET devices with the geometrical parameters mentioned in Section 2. The DIBL was calculated as the change of threshold voltage per 1 V change of drain voltage. The characteristics were simulated for $V_{ds} = 0.05$ V and 0.75 V. In Fig. 2, the I_d - V_g characteristics, normalized to cross-section area for FinFET, with different upper body widths, are shown.

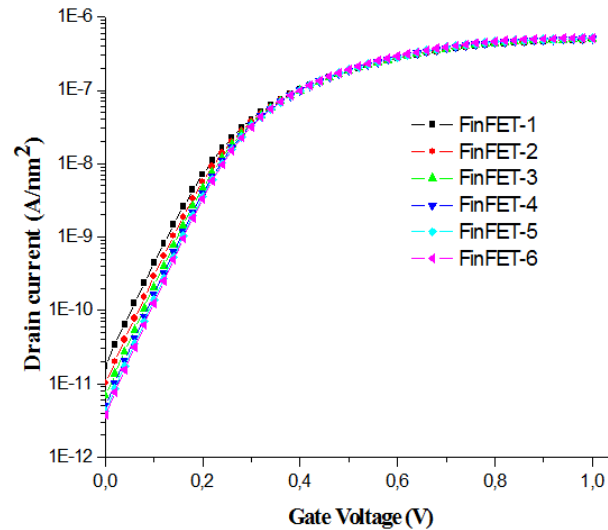


FIG. 2. The normalized transfer characteristics for FinFETs with different body top thickness at $V_{ds} = 0.75$ V

The DIBL effect had a strong influence on the device geometry of FinFET and increased with increased upper body thickness (Fig. 3). This means that the threshold voltage was controlled more by the gate voltage than by the drain voltage for devices with narrower upper bodies.

Such behavior of DIBL for FinFETs with different upper body widths may be connected with changing of parasitic capacitive coupling between source (drain) and gate of the device structure; this results in a changing of potential distribution between the source and the drain for devices with different upper body widths (Fig. 4).

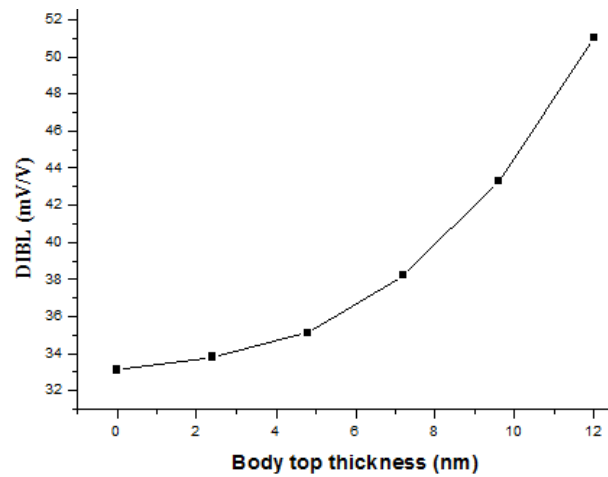


FIG. 3. SOI-FinFET DIBL dependence on body top thickness

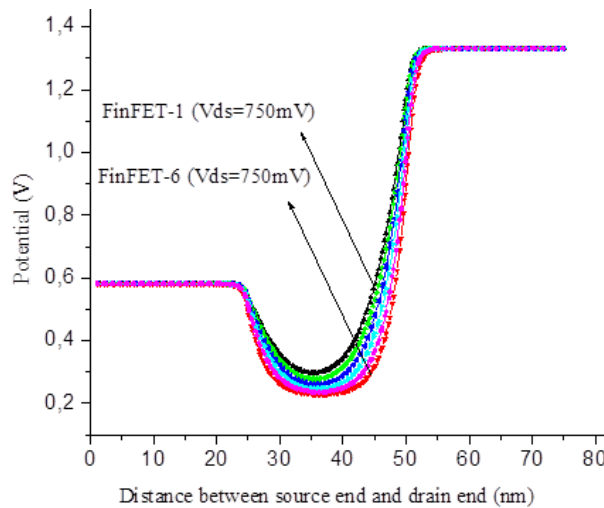


FIG. 4. Potential distribution in the center of the body between source and drain ends of FinFETs with different body top thickness. $V_{ds} = 750$ mV

In Fig. 4, the potential barrier between source and drain is shown to be lowered with increasing upper body thickness. The potential distribution and the potential barrier between the source and drain depend on the drain-source voltage (Fig. 5), which shows the DIBL effect.

In the considered FinFET devices, under conditions of constant height with decreasing upper body thickness, the cross section area also decreased. In order to verify the effect that the change in cross section area had on DIBL, the value was obtained for the initial device with rectangle top and compared to that of a device with triangle top, but with the same cross-section area (i.e. different height). The results showed that the DIBL value for the triangular device was 34 mV/V, which was less than the value obtained for the rectangular geometry device (51 mV/V). This indicates that the change in shape had more of an effect on the DIBL than the change of cross-section area of the device.

4. Conclusion

Simulation of SOI-FinFETs was performed with different upper body widths, starting with the original device, which was straight without narrowing at the top and a set of devices that exhibit the mentioned narrowing, up to the extreme case where the top of the gate had no surface and so the body cross-section was a triangle. These results showed source-drain barrier decreasing with increased upper body thickness. The DIBL effect of the considered FinFETs depended on upper body thickness, increasing with increased upper body width. Such behavior of the dependence is mainly connected with the shape rather than the cross-section area of the device's body.

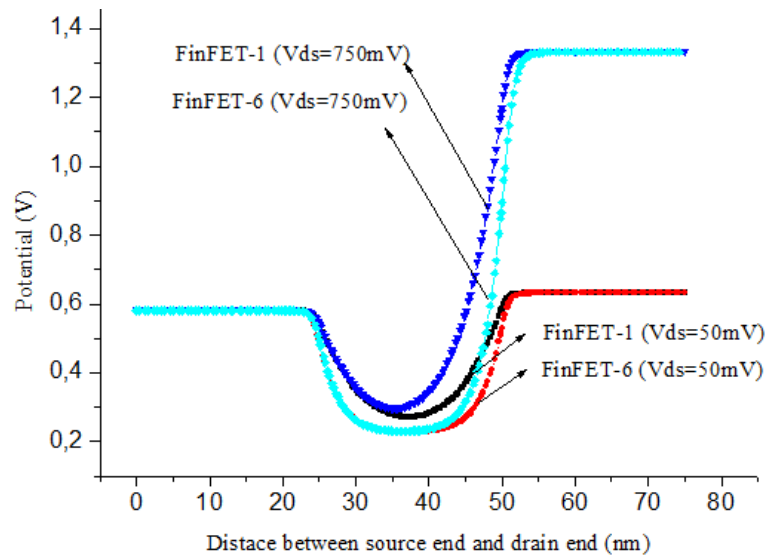


FIG. 5. Potential distribution in the center of body between source and drain ends of FinFETs with body top thickness 12 nm and 0 nm for $V_{ds} = 750$ mV and 50 mV

References

- [1] Abdikarimov A., Indalecio G., et al. Influence of device geometry on electrical characteristics of a 10.7 nm SOI-FinFET. *Proceeding of the 17th International Workshop on Computational Electronics (IWCE-17)*, Paris, France, 3–6 June 2014, P. 247–248.
- [2] Veeraraghavan S., Fossum J.G. Short-channel effects in SOIMOSFETs. *IEEE Transactions on Electron Devices*, 1989, **36** (3), P. 522–528.
- [3] Atamuratov A.E., Aminov U.A., et al. The lateral capacitance of nanometer MNOSFET with a single charge trapped in oxide layer or at $\text{SiO}_2 - \text{Si}_3\text{N}_4$ interface. *Nanosystems: Physics, Chemistry, Mathematics*, 2015, **6** (6), P. 837–842.
- [4] Ferain I., Colinge C.A., Colinge J.-P. Multigate transistors as the future of classical metal-oxide-semiconductor field-effect transistors. *Nature*, 2011, **479**, P. 310–316.
- [5] Asenov A., Kaya S., Brown A. Intrinsic parameter fluctuations in decananometer MOSFETs introduced by gate line edge roughness. *IEEE Transactions on Electron Devices*, 2003, **50** (5), P. 1254–1260.
- [6] Wang X., Brown A.R., Cheng B., Asenov A. Statistical variability and reliability in nanoscale FinFETs. *Electron Devices Meeting, 2011 IEEE International*, 2011, 5-7 Dec. 2011, P. 5.4.1–5.4.4.
- [7] URL: <http://www.synopsys.com>.

Simulation of DIBL effect in junctionless SOI MOSFETs with extended gate

A. E. Atamuratov¹, M. Khalilloev¹, A. Abdikarimov¹, Z. A. Atamuratova¹,
M. Kittler², R. Granzner², F. Schwierz²

¹Urganch State University, Kh. Olimjan, 14, Urganch, 220100, Uzbekistan

²Technical University of Ilmenau, Ehrenbergstrasse, 29, 98693 Ilmenau, Germany

atabek.atamuratov@yahoo.com, frank.schwierz@tu-ilmenau.de

PACS 85.30.Tv

DOI 10.17586/2220-8054-2017-8-1-75-78

Short channel effects such as DIBL are compared for trigate SOI Junctionless MOSFET with extended and non-extended lateral part of the gate. A trigate SOI JLMOSFET with gate length L_{gate} , a silicon body width W_{tin} and thickness of 10 nm are simulated. In order to calculate the DIBL, the transfer characteristics of JLMOSFETs was simulated at a donor concentration of $5 \cdot 10^{19} \text{ cm}^{-3}$ in the silicon body. The equivalent oxide thicknesses of the HfO_2 gate insulator used in simulation was 0.55 nm. Simulation result showed the DIBL for the trigate JLMOSFET depended on the length of the lateral part of the gate L_{ext} . DIBL is high for devices with gates having extended lateral parts. This is a result of parasitic source (drain)-gate capacitance coupling which is higher for longer L_{ext} .

Keywords: Junctionless MOSFET, DIBL, parasitic capacitance.

Received: 8 July 2016

Revised: 30 August 2016

1. Introduction

In very short-channel MOSFET devices ($L = 10 \text{ nm}$ or less) the formation of ultra-sharp source and drain junctions imposes orders of magnitude of variation in doping concentration over a distance of a few nanometers. Such concentration gradients impose drastic conditions on doping techniques and thermal budget. To avoid these conditions, recently, junctionless MOSFETs have been proposed [1,2]. The proposed devices would be fabricated without the need for forming junctions. Since the channel doping concentration and type are the same as in the source and drain extensions, there would be no doping concentration gradient, and therefore, no impurity diffusion during thermal processing steps. This should tremendously relax the thermal budget. The electrical characteristics of JLMOSFETs are identical to those of normal MOSFETs, however, the physics is quite different [3].

The main problems associated with MOSFET scaling are different effects which tend degrade device characteristics. Among the more important ones are: technological variability of parameters [4], short channel effects [5], influence of single defects in oxide or oxide-semiconductor interface [6]. The use of multiple-gate topologies significantly enhances the electrostatic integrity of the device and provides increased immunity from SCEs [7], however, in many simulation studies connected with short channel effects research do not take consider parasitic capacitance. In this work, the DIBL effect for trigate SOI Junctionless MOSFET with a gate length of 10 nm has been investigated in 3D simulation and the influence of parasitic capacitance connected with gate lateral extensions was considered.

In many practical cases for Integrated Circuits (MOSFET memory, CMOS based logic gates) a linear array of MOSFETs (Fig. 1), instead of single device, is used. In these cases all MOSFETs in a line can be covered by a common gate. This can lead to the extension L_{ext} of the lateral part of MOSFET's gate in the line compared to the gate of the single MOSFET (Fig. 2, a, b). The extended gate can alter the parasitic capacitances, and as a consequence, change the short channel effects in the nanometer MOSFET. For estimation of the influences of the extension of the gate lateral part on short channel effects, the DIBL effect in trigate SOI JLMOSFET with extended and unextended gates have been compared. For simulations, an Advanced TCAD Sentaurus device simulator has been used [8].

2. Results of simulation and discussion

A trigate SOI JLMOSFET with gate length $L_{gate} = 10 \text{ nm}$ and with silicon body width $W_{fin} = 10 \text{ nm}$ (Fig. 2) are simulated. We have considered transistors with an unextended gate as a simple contact (Fig. 2a) and with the extended polysilicon gate (Fig. 2b). The equivalent oxide thicknesses of the HfO_2 gate insulator used in simulation was 0.55 nm.

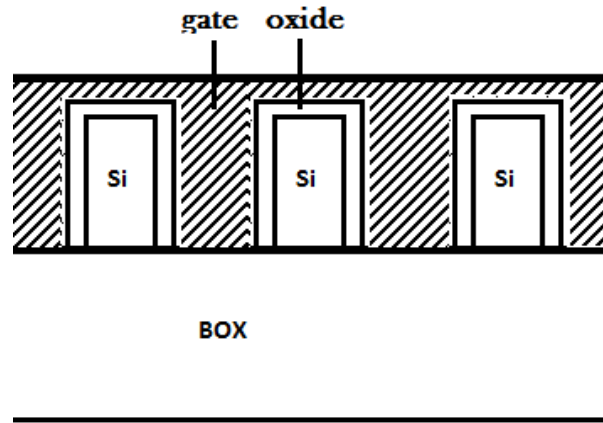


FIG. 1. SOI JLMOSFETs in the line

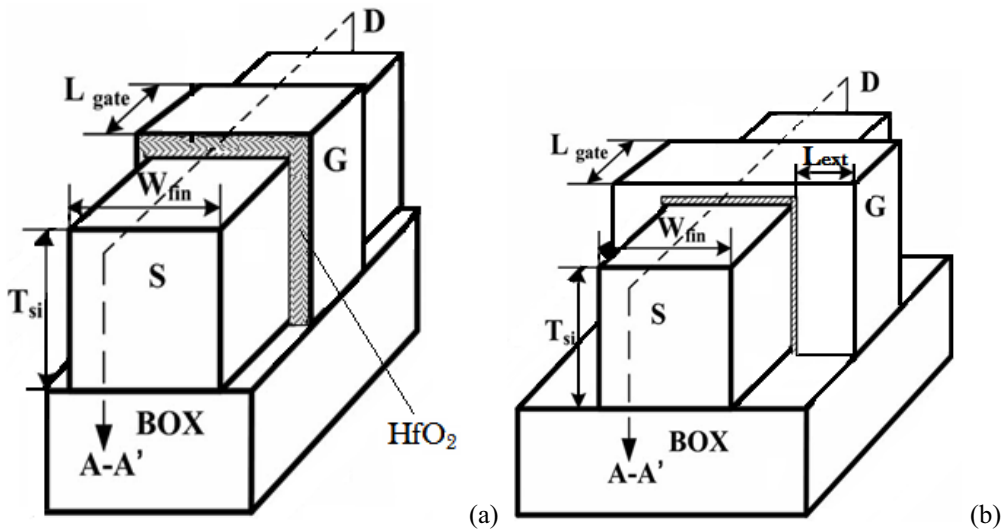


FIG. 2. Trigate SOI JLMOSFET with not extended (a) and extended (b) gate

For calculation of DIBL, we simulated transfer characteristics of JLMOSFETs with donor concentration in silicon layer $5 \cdot 10^{19} \text{ cm}^{-3}$, an active layer thickness $T_{si} = 10 \text{ nm}$. DIBL was calculated as change of threshold voltage per 1 V changing of drain voltage. The transfer characteristics were simulated for $V_{ds} = 0.05 \text{ V}$ and 0.75 V . In Fig. 3 the transfer characteristics for the trigate JLMOSFETs with extended and unextended lateral gate part are shown. I_d - V_g characteristics in Fig. 3 shows lateral extending of the gate leads to a change in the threshold voltage. DIBL effect are different for trigate SOI JLMOSFETs with extended and unextended gates. The value is higher in case of trigate JLMOSFETs with extended gate in all the considered range of L_{ext} (Fig. 4). It means that in the cases of trigate; for MOSFET with unextended gate, the threshold voltage was more controlled by the gate than by drain voltage. Such behavior for DIBL might cause additional change in the source (drain)-gate parasitic capacitance (Fig. 5) of the device structure.

In the considered case, an additional potential is induced in the source (drain) part of substrate by the lateral part of the gate through the parasitic source (drain)-gate capacitance coupling. It is expected that this influence is higher at high parasitic coupling capacitance. The parasitic source (drain)-gate capacitance can be considered as capacitance between two perpendicular bodies, i.e. the device's silicon body and gate (Fig. 5). This parasitic capacitance may be estimated using the non-parallel thick-plate capacitor approach [9]. According to this methodology, the parasitic capacitance is proportional to $\ln(1 + l/d)$, where l may be considered as a length of the gate extension L_{ext} , and d is some constant. As it can be seen from the expression, with increasing gate extension, the parasitic capacitance, as well as its influence on the source (drain) potential, is increased logarithmically and should reach saturation at higher gate extensions, L_{ext} . Such dependence is coordinated with the dependence of

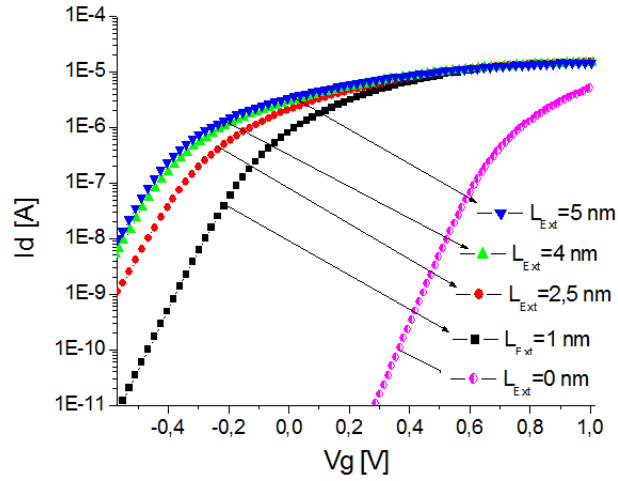


FIG. 3. Transfer characteristics for tri-gate JLMOSFETs with extended and not extended lateral part of gate, $V_{ds} = 0.75$ V

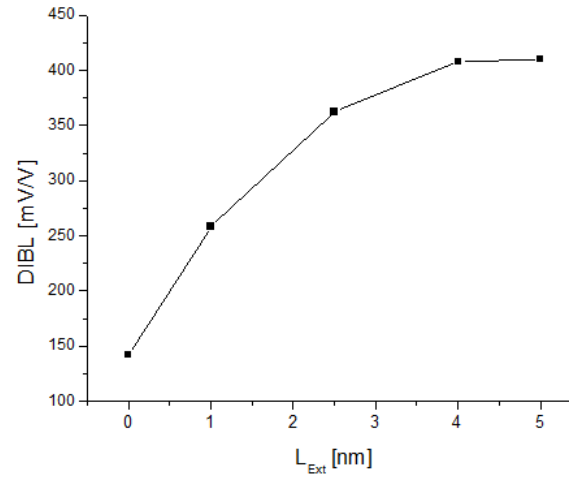


FIG. 4. DIBL dependence on length of lateral extension of the gate L_{ext}

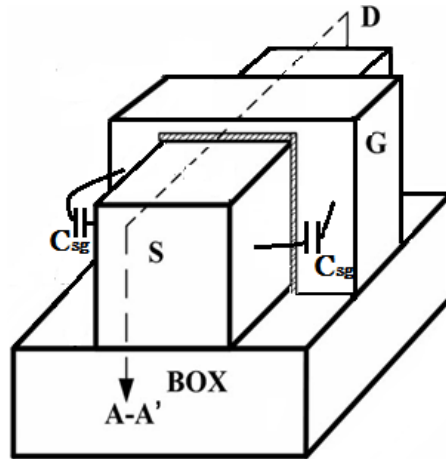


FIG. 5. Tri-gate JLMOSFET with the indicated source(drain)-gate parasitic capacitance C_{sg}

DIBL on the gate lateral extension L_{ext} , which is shown in Fig. 4. In Fig. 6, potential distributions from source end to drain end along the center of silicon body for different L_{ext} at drain-source voltage $V_{ds} = 50$ mV are shown. As it is seen from the figure the potential barrier between source and drain is lowered with increasing the lateral gate extension L_{ext} . In addition, the potential barrier between the source and drain also depends on drain-source voltage, too (see Fig. 7). In Fig. 7, the potential barrier was shown to change more for high L_{ext} with the same change of V_{ds} . Such behavior of potential in the body results in DIBL dependence on the L_{ext} which is shown in Fig. 4.

3. Conclusion

Simulation of SOI JLMOSFET with a gate length of 10 nm, silicon body thicknesses and width of 10 nm shows that short channel effects such as DIBL for tri-gate devices with extended lateral gate portions are higher than those of the devices not having extended gates. The difference of DIBL for the devices with extended and unextended gates depends on lateral extension of gate L_{ext} and it occurs as a result of the influence of parasitic source (drain)-gate capacitance to the device body potential.

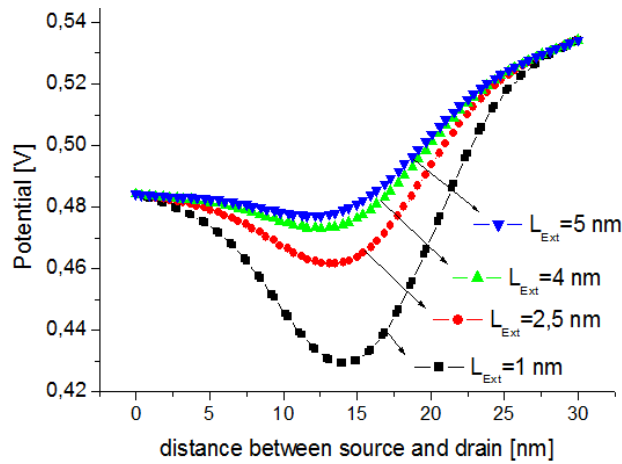


FIG. 6. Potential distribution along center of transistor's substrate from source end to drain end at different gate lateral extensions

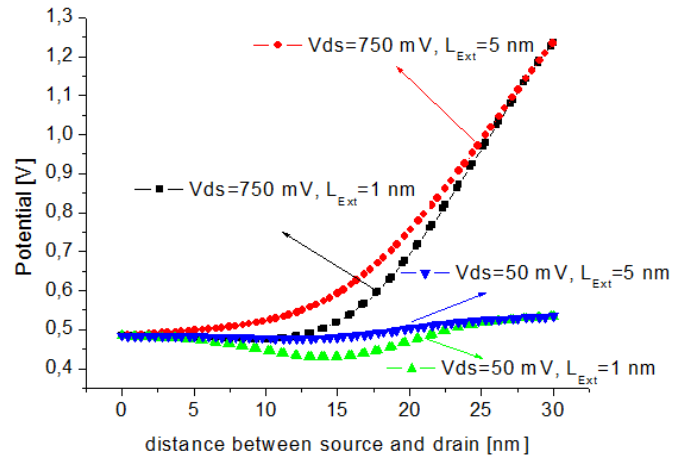


FIG. 7. Potential distribution along center of transistor's body from source end to drain end at gate lateral extensions 1 nm and 5 nm for $V_{ds} = 50$ mV and $V_{ds} = 750$ mV

References

- [1] Park J.-T., Colinge J.-P., Diaz C.H. Pi-Gate SOI MOSFET. *IEEE Electron Device Letters*, 2001, **22** (8), P. 405–406.
- [2] Lee C.-W., et al. Performance estimation of Junctionless multigate transistors. *Solid-State Electronics*, 2009, **54**, P. 97–103.
- [3] Colinge J.-P. Conduction mechanisms in thin-film, accumulation-mode p-channel SOI MOSFETs. *IEEE Trans. Electron Devices*, 1990, **37**, P. 718.
- [4] Abdikarimov A., Indalecio G., et al. Influence of device geometry on electrical characteristics of a 10.7 nm SOI-FinFET. *Proceeding of the 17th International Workshop on Computational Electronics (IWCE-17)*, Paris, France, 3–6 June 2014, P. 247–248.
- [5] Veeraraghavan S., Fossum J.G. Short-channel effects in SOIMOSFETs. *IEEE Transactions on Electron Devices*, 1989, **36** (3), P. 522–528.
- [6] Atamuratov A.E., Aminov U.A., et al. The lateral capacitance of nanometer MNOSFET with a single charge trapped in oxide layer or at $\text{SiO}_2 - \text{Si}_3\text{N}_4$ interface. *Nanosystems: Physics, Chemistry, Mathematics*, 2015, **6** (6), P. 837–842.
- [7] Ferain I., Colinge C.A., Colinge J.-P. Multigate transistors as the future of classical metal-oxide-semiconductor field-effect transistors. *Nature*, 2011, **479**, P. 310–316.
- [8] URL: <http://www.synopsys.com>.
- [9] Bueno-Barrachina J.M., Cañas-Peñuelas C.S., Catalan-Izquierdo S. Capacitance Evaluation on Non-parallel Thick-Plate Capacitors by Means of Finite Element Analysis. *Journal of Energy and Power Engineering*, 2011, **5**, P. 373–378.

Digital holographic interferometry in physical nanomeasurements

Z. T. Azamatov¹, N. A. Akbarova¹, I. A. Kulagin¹, V. E. Gaponov², V. I. Redkorechev¹, A. M. Isayev³

¹National University of Uzbekistan, 100074, Tashkent, Uzbekistan

²Krypton Ltd., Snezhinsk, Russia

³Center of Laser Technologies Scientific Firm, Almaty, Kazakhstan

ilya_kulagin@list.ru, zakir.azamatov@mail.ru, gorani@bk.ru

PACS 07.60.-j

DOI 10.17586/2220-8054-2017-8-1-79-84

The possibility of using digital holographic interferogram obtained via laser radiation at different wavelengths and different pulse lengths in different times for the reconstruction of dynamic phase changes was explored. The opportunities for applying the digital holographic interferometry method to the study of resonant mode shapes in resonant acoustic spectroscopy are shown. The results of experimental measurements and analytical calculations are submitted.

Keywords: information transmission, digital holographic interferometry.

Received: 10 August 2016

Revised: 6 September 2016

1. Algorithm Description

Ranges of resonant acoustic vibrations and their form bear information on the internal structure of the studied solid. From a range of resonance frequencies of known form for a sample, the elasticity tensor can be measured and areas of localization of defects can be defined. One of the most sensitive methods for determining resonance frequencies and studying the form of resonant fluctuations is digital holographic interferometry (DHI). The method of DHI is based on comparing the phases of two object waves recovered from the digital holograms corresponding to different phases of process of a surface deflection of object. For registration of the digital hologram, the radiation of the laser is divided into the object bunch covering object, and the basic bunch which is directly arriving on a receiving sensor of a digital video camera. The object bunch covers object in the direction of \mathbf{k}_i . The part of the world reflected by object in the direction of \mathbf{k}_v , called ‘the direction of supervision’, passes through optical system of the interferometer and creates the image of object on the receiving sensor of a digital video camera. The hologram of the focused image forms on the CCD array of the digital camera as result of an interference between basic and object bunches. For allocation of measuring information, the algorithm of processing digital hologram1 was used.

Let $R(x, y)$ be a smooth basic wave, and $U(xy)$ is an object wave proceeding from object. Then, the intensity registered on the CCD array of a receiving video camera is described by expression:

$$I_H(x, y) = |R_H(x, y)|^2 + |U_H(x, y)|^2 + R_H(x, y)U_H^*(x, y) + R_H^*(x, y)U_H(x, y), \quad (1)$$

where, H – the index designating the hologram plane, and an index * designates complex interface. The intensity described by the equation (1) is registered on the two-dimensional electronic device consisting of ranks of the sensitive cells-pixels ($M \times N$ cells) having the sizes $\Delta x \times \Delta y$ that allows one to write down value of intensity in the form of the IH function ($m\Delta x, n\Delta y$) where m and n – integers. The last two terms of Eq. (1) contain information on amplitude and phase of an object wave. By the Fourier transformation to the registered array, it is possible to allocate and filter one of two last terms of Eq. (1). After filtering and Fourier transformation return the complex amplitude of the object wave front is obtained. From the complex amplitude of U_H received in a digital form ($m\Delta x, n\Delta y$), the phase of the wave front of an object wave can be calculated:

$$\Phi_n(m\Delta x, n\Delta y) = \text{atan} \frac{I_m[U_H(m\Delta x, n\Delta y)]}{R_m[U_H(m\Delta x, n\Delta y)]}. \quad (2)$$

By subtraction of the phase values for the object field, we obtain the difference of phases, which allows us to calculate the shift of points of object of \mathbf{d} in the directions, giving:

$$\Delta\Phi = \frac{2\pi}{\lambda} \mathbf{d} \cdot \mathbf{s}, \quad (3)$$

where, λ is the laser wavelength, \mathbf{s} is the vector interferometer sensitivity defined by the expression $\mathbf{s} = \mathbf{k}_i - \mathbf{k}_v$, \mathbf{k}_i and \mathbf{k}_v are the unit vectors of illumination and observation, respectively.

2. Scheme of measurements, results and discussion

2.1. The stroboscopic-holography method

The stroboscopic-holography method [1] was utilized for quantitative measurements of the vibrational movement fields. At the same time, the digital holograms of the vibrating object for each resonance frequency are registered by accumulation (over 1/10 – 1/1000 s) exposures on the receiving sensor of a digital camera in the light of the short repeating impulses of laser radiation synchronized with the set phases of fluctuation processes. Comparison of the object waves' phases to those obtained from two digital stroboscopic holograms registered in different vibration phases allows one to receive the two-exposition interferogram, which is given to quantitative interpretation. Application of long pulse exposures to the principle eliminates the need for synchronization of time intervals for exhibition of the camera's receiving sensor with the process phase, permitting the use of low-frequency digital cameras for measurements and providing an increase in the data on the studied objects. Holograms registered in the laser radiation were diffracted by the optical-acoustic modulator (OAM), which for the continuous laser radiation ($\lambda = 0.53$ mm, 50 mW), allocated the impulses synchronized with the chosen phase having a fluctuation of 2 ms. The metal plate 5×5 cm fixed in the center was object of study. The plate was excited by the piezo vibrator at frequencies up to 20 kHz. Acoustic vibrations of a plate were registered by the vibration sensor and were processed by a range analyzer for determination of resonance frequencies. Then, at the fluctuations of a resonance frequency, the phase of resonant fluctuation was chosen and the hologram was removed. Digital holograms were removed on a matrix 1000×1000 pixels with a pixel size 5×5 mm and were processed by the program in the MATLAB-12 environment in real time. The scheme of experiment is depicted in Fig. 1.

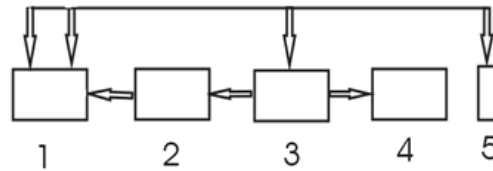


FIG. 1. Scheme of measurements: 1 – PC laptop; 2 – Interferometer in structure with the laser, the camera and OAM; 3 – Generator and analyzer of a range; 4 – A piezo vibrator and the studied sample; 5 – Sensor of vibrations

The measuring accuracy was defined by comparison with controlled movement and was 0.01 mm. In Fig. 2, results of quantitative measurements of the vibrational movement fields at resonance frequencies are presented. At each resonance frequency, two digital holograms corresponding to two amplitude conditions of an object in opposite phases were registered.

An upper row contained the fluctuation forms obtained by calculation by method of final elements, while an average row displayed results for the experimental determination of resonance frequencies, visualization of forms of own fluctuations and localization of nodal lines in real time.

The lower row contained results for the measurement of vibrational movement fields at resonant fluctuations. On axes x and y – coordinates in pixels, on an axis z – amplitude of fluctuations in mm. The maximum amplitude of movement of points of a surface is equal to 1 mm and the accuracy of measured movements was 0.01 mm.

2.2. Dynamic phase changes in photorefractive crystals of lithium niobate

The digital holographic interferometer (DHI) 'interferes' with the digital field derived from the actual field by digital holography (PG) [2]. These methods are based on the Huygens–Fresnel principle, the mathematical formalism of the Fourier transform, numerical algorithms for deployment phase and the digital image processing algorithms [3]. Unlike the conventional interferometer, which requires two or more coherent phase fields to obtain a phase interferogram, in the DHI, one can calculate them by obtaining the interference field incoherent phase fields (e.g. fields that existed at different times and thus cannot interfere with each other). As a result of digital 'interference' such fields produce a virtual interferogram. A necessary condition for the implementation of single-wave DHI is the appropriate smallness of the optical path difference between adjacent pixels (less than half a wavelength ($\Delta \leq \lambda/2$)). In cases where this condition is violated, in the recovery process (deployment), an uncertainty arises in the phase field equal to modulo 2π . The conditions $\Delta \leq \lambda/2$ puts a hard limit on the range of single wavelength measurements in the DHI in relation to the natural spatial resolution of modern radiation detectors.

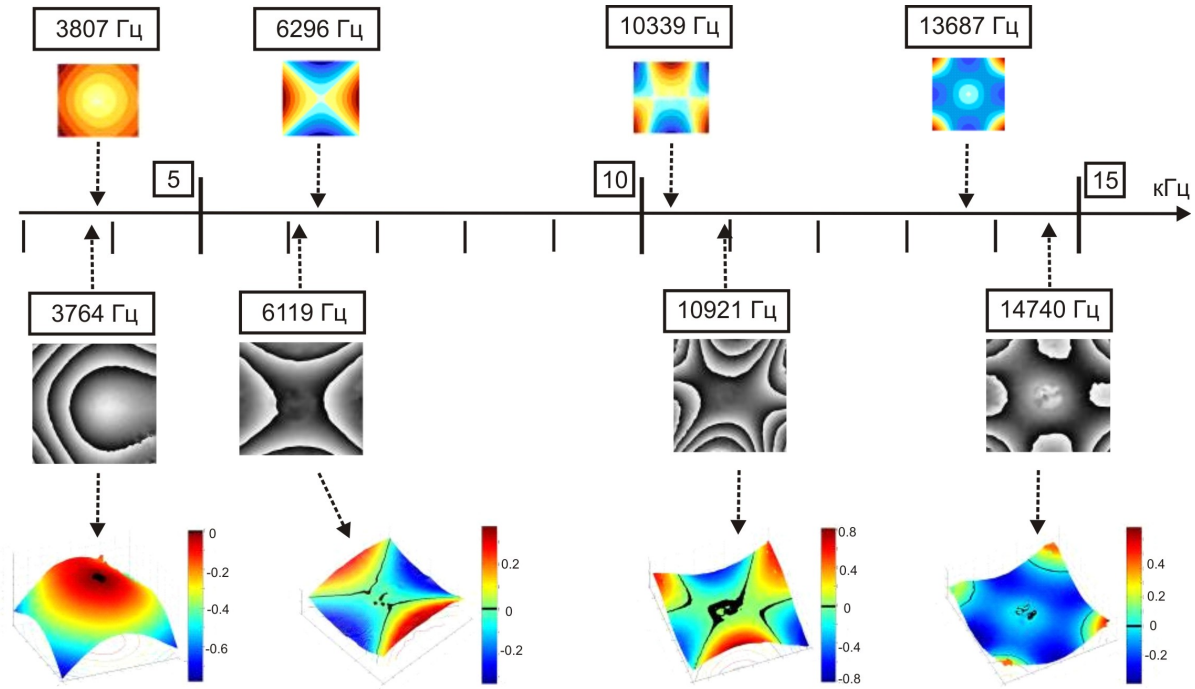


FIG. 2. The stroboscopic-holography method

One way to eliminate this uncertainty is the use of far infrared rays. However, the practical implementation of this method is limited due to the long-wave threshold of the detectors' sensitivity. Another method is the use of two waves of the visible range of different frequencies [4, 5]. Two-tone CGI uses two data sets obtained at different wavelengths λ_1 and λ_2 . The recovery phase of the field is carried out on an equivalent wavelength $\Lambda_{12} = \lambda_1 \lambda_2 / |\lambda_1 - \lambda_2|$, the greater the wavelength used real light in the visible range. Thus, the use of two-tone DHI significantly softens demands on spatial resolution radiation detectors, reduces uncertainty in the recovery phase of the field and increases the sensitivity. However, enhancements in this effect also result in increased noise. In order to find an acceptable compromise, one must use different combinations of virtual and real wavelengths Λ_{12} , λ_1 , λ_2 as a reference and object waves in the reconstruction phase of the interferogram. Thus, the developed technology to date information about the interference of multi-colored fields aimed at solving the problem of the uncertainty inherent in all 2π interference measuring techniques are used as measures of real measuring radiation wavelength.

In this paper, we used two methods of digital exposure interferometry – phase difference obtaining a surface carrying information about the changes in the test object during the time between exposures. These compared hologram phase fronts were shot at different wavelengths in pulses of varying duration. In our studies of virtual interferogram, we used Mach–Zehndera and Michelson collected under the scheme. The primary digital hologram was recorded in the laser radiation with a wavelength of 1.064 mm, 1.054 mm, 0.532 mm, 0.357 mm, in pulses with a duration of 30 ns to 50 ps to 200 fs and emission of continuous He–Ne laser with a digital camera such as the TM-1020-15CL a pixel size 9×9 mm.

The objects used in the shooting: a plate of non-linear optical crystal and LiNbO₃ plate photorefractive crystal LiNbO₃: Fe (0.01 %). On multicolored holograms recorded by two exposition digital interferometer [6] were obtained digital interferogram different stages of relaxation phase in homogeneities recorded in the volume of the photorefractive crystal LiNbO₃: Fe, as well as the nonlinear optical LiNbO₃ crystal. According to the interferograms' recovered phase fronts, supporting quantitative information about the sample was obtained. A comparison of the obtained information – the value of the angle of inclination, a change in the refractive index, the amplitude and length of the surface acoustic waves in various combinations of primary colored phase fronts was performed.

Figure 3 shows a diagram of a recording phase holograms. The radiation of a neodymium laser ($\lambda_1 = 1.06$ mm) length of 30 ns and 50 ps with a mirror (1) directed to a non-linear optical crystals (2,3), in which the generation of the second and third harmonics of laser radiation with wavelengths $\lambda_2 = 0.532$ mm and $\lambda_3 = 0.357$ mm.

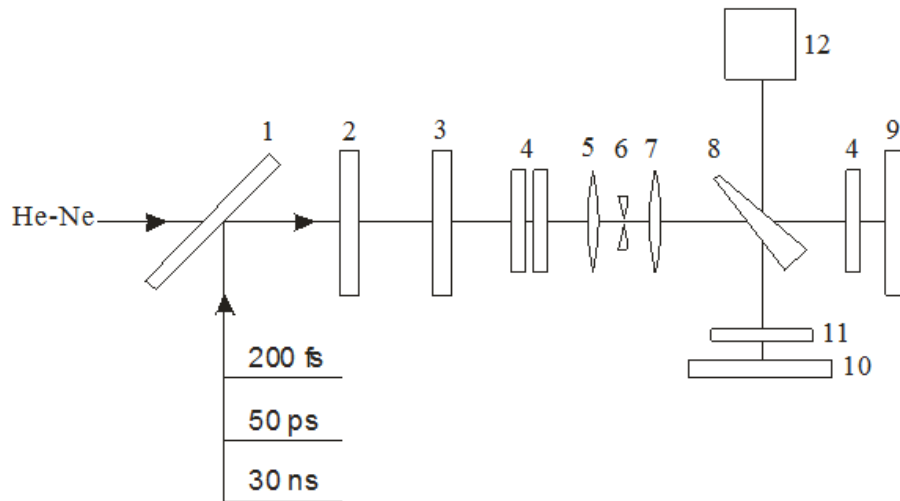


FIG. 3. Scheme of the recording phase holograms: 1 –mirror; 2,3 –nonlinear crystal frequency multiplication; 4 – filters; 5,7 –linza; 6 – spatial filter; 8 – optical wedge; 10 – mirror; 11 – the sample; 12 – CCD camera

Isolation of radiation at a particular wavelength and emission intensity change was carried out by means of filters (4). The emission of He–Ne lasers, at femtosecond levels, would not convert the frequency. Spatial filtering of the radiation was performed by the lenses (5, 7) and the diaphragm (6). At the output of the phase front of the spatial filter, the radiation was close to flat. Then, the radiation directed into the interferometer formed by the optical wedge (8) and mirrors (9, 10). The sample (11) is located in one of the arms of the interferometer. Register holograms were obtained using a CCD camera (12) connected to a personal computer. Based on the processing of the obtained holograms, the interferogram was constructed.

The resulting phase homogeneity in the laser field in a photorefractive crystal is determined by the intensity of the laser radiation $I(t)$, the exposure time τ , sensitivity photorefractive material K and the absorption coefficient α . Fig. 4 shows the calculated phase in homogeneity image in a photorefractive $\text{LiNbO}_3:\text{Fe}$ crystals with different exposure times corresponding to the interference pattern in a digital format. The spatial intensity distribution of the laser radiation was supposed to be Gaussian. The exposure time for the image illustrated in Fig. 4b, 3.5 times higher than the exposure time for the image shown in Fig. 4a, as well. The figure shows that with increasing exposure times, the phase in the homogeneity image becomes more complex, resulting in increased interference fringes.

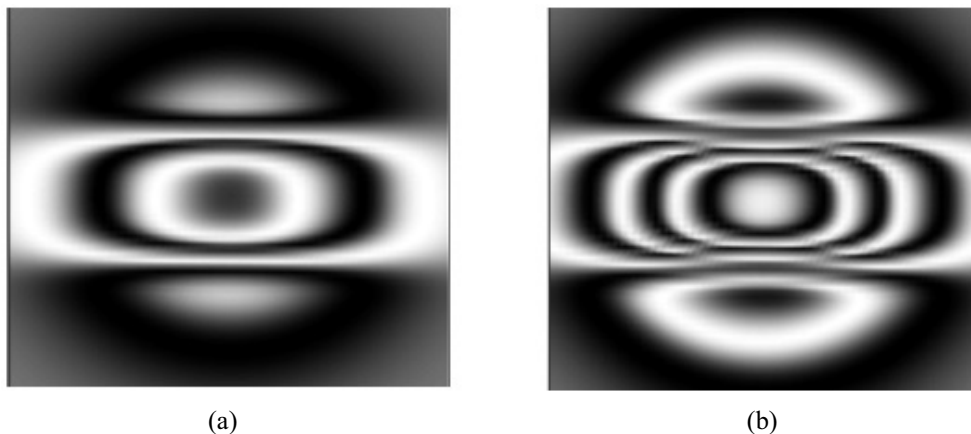


FIG. 4. Calculation of photorefractive crystal structure in $\text{LiNbO}_3:\text{Fe}$

Figure 5 shows the magnified view of the bulk phase in homogeneity induced in the waist of the focused laser beam, as well as three-dimensional reconstruction phase in homogeneities recorded in $\text{LiNbO}_3:\text{Fe}$ radiation with a wavelength of 532 nm. This image is received in the nanosecond laser pulses. The polarization of the

laser radiation was directed parallel to the optical axis of the crystal. When you rotate the polarization by 90° pattern has not changed. From the analysis of the recorded phase in homogeneity shown in this figure, it follows that its view qualitatively coincides with the calculated phase distribution (Fig. 4). Some discrepancy may be due to the difference of the beam of laser radiation from the Gaussian. In this case, the main role was played by photorefractive heterogeneity.

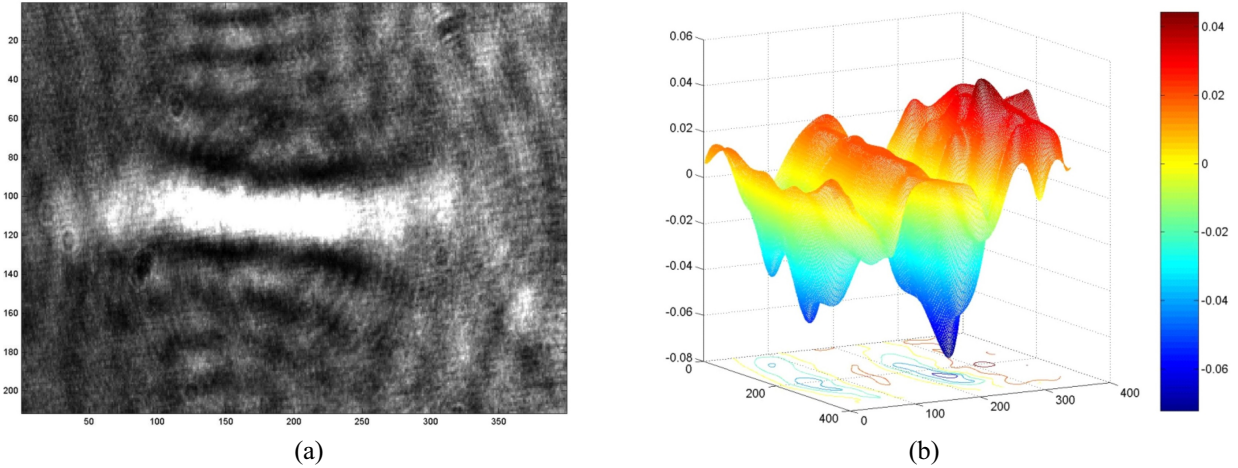


FIG. 5. Interferogram and phase reconstruction photorefractive structure

In the picoseconds laser phase, change occurs due to the influence of the heterogeneity of the Kerr nonlinearity. Kerr nonlinearity (and hence nonlinear addition to the refractive index) is a tensor quantity that links the components of the third order polarization and the corresponding components of the electromagnetic field. The LiNbO₃ nonlinear optical crystal with no loss of Kerr nonlinearity is generally determined by four components [7]. The value of the Kerr nonlinearity depends on the angle of propagation with respect to the main optical axis. To calculate the Kerr nonlinearity values in this case, we used a semi-empirical model. This model is based on taking into account the contribution of the transition in the discrete spectrum.

In this approximation, the Kerr nonlinearity is expressed as a function of the refractive index and its second derivative with respect to wavelength. The expression also includes the density of oscillators N , which is defined as the average density of the atoms in the crystal. Fig. 6 shows a simulation of the calculated dependence of the magnitude of the phase shift induced by the intensity of the spatial coordinates at an angle of radiation spread to the main axis of the crystal equal to 72° at the wavelength $\lambda = 532$ nm. The initial distribution of the laser intensity was assumed to be Gaussian. The calculations used the following relationship between the components of the non-linearities $\chi_{12} : \chi_{14} : \chi_{23} : \chi_{33} = 1 : 0.1 : 0.2 : 6.0$. Note that in this case the components χ_{14} and χ_{23} made only a small contribution. From these figures it is clear that the induced nonlinearity has the form of an ellipse, which is approaching the axis of the beam is converted into a dumbbell structure elongated along the z -axis of the crystal.

Figure 7, shows a central part of the interferogram fragments obtained by passing the laser radiation with a wavelength of 1.06 mm X-cut LiNbO₃ crystal is 0.2 cm thick at two different radiation intensities. Radiation polarization direction coincides with the axis y . The density of radiation power was 10 GW/cm².

According to the Fig. 4, the central part of the phase difference expressed in units of wavelength, was 0.085 mm. The calculation showed that the value of the non-linear refractive index γ was 1.8×10^{-19} m²/W. When the crystal orientation of the nonlinear susceptibility of the crystal is determined by the class 3m full tensor component χ_{12} , and thus possible to determine the components of the nonlinearity tensor.

We note that for X-cut crystal nonlinear refractive index change may be due to the inverse energy transfer process of the second harmonic of the main emission of laser radiation. Using the known values of the second-order nonlinearity, the refractive index and the correction value were determined by a direct non-linear refractive index, due to the Kerr nonlinearity, which amounted to 1.12×10^{-19} m²/W.

Similar measurements of the induced optical nonlinearity were performed for other wavelengths and for different crystal orientations with respect to the laser light polarization. Fig. 7b shows a fragment of the central part of an interferogram obtained using the radiation wavelength of the second harmonic of Nd: YAG laser; the nonlinearity size was ~ 1.4 times higher than the fundamental nonlinearity frequency.

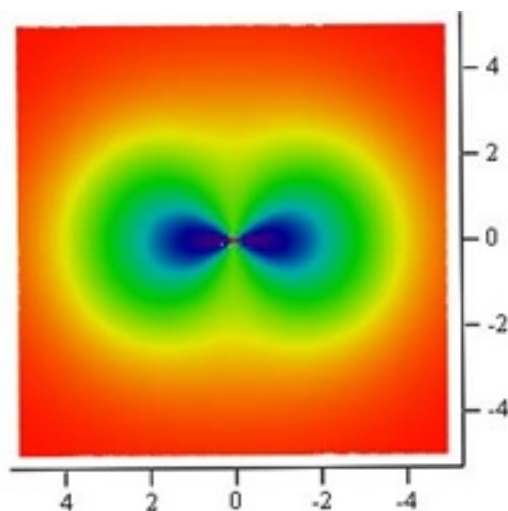


FIG. 6. Calculated dependence of the shift in chip phase difference with the symmetry 3m, due to the change in the refractive index depending on the intensity of laser radiation

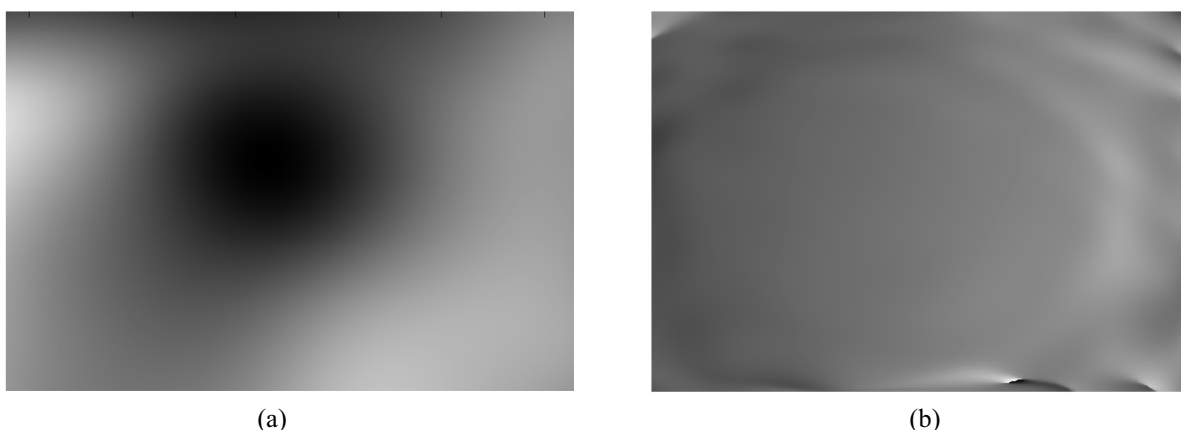


FIG. 7. Fragments central interferogram recorded to 1.064 (a) and 0.532 (b) microns

The analysis showed the potential for using a double-exposure digital holographic interferometer for direct measurement of the dynamic emerging in a strong laser field in homogeneity phase and, therefore, made the measurement of non-linear refractive index coefficient photorefractive sensitive material and Kerr nonlinearity perceivable.

Thus, the above study has shown that the digital holographic interferogram obtained using the laser radiation at different wavelengths and durations may possibly be used for the reconstruction of dynamic phase changes occurring in the samples. The most promising practical application of multicolor DHI is the measuring of nanometer-length displacements (nanotechnology, digital microscopy) along with the possibility of using the tunable laser sources in the femtosecond range and the measurement with high temporal resolution, or using cheap laser diodes in the spectral ranges.

References

- [1] Gurevich V.S., Gaponov V.Y., et al. Limit opportunities of a digital holographic interferometry at measurement of midjet movements. *Control probing devices and automatic equipment in Kazakhstan*, 2008, **3** (21), P. 13–14.
- [2] Jueptner W., Schnars U. *Digital Holography*. Springer, Berlin, 2004.
- [3] Vizilter Y., et al. *Processing and analysis of digital images with examples in LabVIEW and IMAQ Vision*. DMK Press, Moscow, 2007.
- [4] Cheng Y.-Y., Wyant J.C. Two-Wavelength Phase Shifting Interferometry. *Appl Opt.*, 1984, **23**, P. 4639.
- [5] Schwider J., et al. Digital wave-front measuring interferometry: Some systematic error sources. *Appl. Opt.*, 1983, **22**, P. 3421–3427.
- [6] Redkorechev V.I., et al. Digital picosecond tricolor holographic interferometry. *Optics and Spectroscopy*, 2009, **107**, P. 435–439.
- [7] Kulagin I.A. Analysis of third-order nonlinear susceptibilities of quadratic nonlinear optical crystals. *J. Opt. Soc. Am. B*, 2006, **23**, P. 75–80.

Fast-forward of standard dynamics with use of electromagnetic field

G. Babajanova¹, K. Nakamura^{1,2}

¹Faculty of Physics, National University of Uzbekistan,
Vuzgorodok, Tashkent 100174, Uzbekistan

²Department of Applied Physics, Osaka City University,
Sumiyoshi-ku, Osaka 558-858, Japan
gobabajanova@gmail.com

PACS 03.65.Ge, 03.65.Vf

DOI 10.17586/2220-8054-2017-8-1-85-91

We introduce Khujakulov and Nakamura's scheme for the exact fast-forwarding of standard quantum dynamics for a charged particle. The idea allows the acceleration of both amplitude and phase of the wave function throughout the fast-forwarding time range. Firstly we shall apply the proposed method to 1-D free wave packet dynamics and obtain the electromagnetic field to ensure its rapid propagation and diffusion. Then we proceed to study 1-D quantum tunneling phenomenon, namely a rapid penetration of wave function through a delta-function type barrier. We elucidate the distribution of the tunneling current density to show the remarkable enhancement of the tunneling rate (tunneling power) due the fast-forwarding. We introduce two types of time-magnification factors and confirm the stability of fast-forward against the variation of such factors.

Keywords: acceleration of standard dynamics, free wave packets, quantum tunneling.

Received: 14 July 2016

Revised: 2 September 2016

1. Introduction

Masuda and Nakamura [1–3] investigated a method of acceleration quantum dynamics with use of a characteristic driving potential determined by the additional phase of the wave function. One can accelerate a given quantum dynamics to obtain a target state in any desired short period. This kind of acceleration is called the fast-forward of quantum dynamics, which constitutes one of the more promising ways of attaining a shortcut to adiabaticity [4–9]. The relationship between the fast forward and the shortcut to adiabaticity is currently clear [10, 11]. Before embarking upon the main part of the text, we briefly summarize the theory of the fast-forward of quantum dynamics updated by Khujakulov and Nakamura [12]. The Schrödinger equation on standard time scale is represented as:

$$i\hbar \frac{\partial \psi_0}{\partial t} = -\frac{\hbar^2}{2m} \nabla^2 \psi_0 + V_0(\mathbf{x}, t) \psi_0, \quad (1)$$

$\psi_0 \equiv \psi_0(\mathbf{x}, t)$ is a known function of space \mathbf{x} and time t and is called a standard state. For any long time T called a standard final time, we choose $\psi_0(x, t = T)$ as a target state that we are going to generate.

Let $\tilde{\psi}_0(\mathbf{x}, t)$ be a fast-forwarded state of $\psi_0(\mathbf{x}, t)$ as defined by

$$\tilde{\psi}_0(\mathbf{x}, t) \equiv \psi_0(\mathbf{x}, \Lambda(t)) \equiv \Psi_{FF}(\mathbf{x}, t) \quad (2)$$

with

$$\Lambda(t) = \int_0^t \alpha(t') dt'. \quad (3)$$

$\alpha(t)$ is a magnification scale factor defined by

$$\begin{aligned} \alpha(0) &= 1, \\ \alpha(t) &> 1 \quad (0 < t < T_{FF}), \\ \alpha(t) &= 1 \quad (t \geq T_{FF}). \end{aligned} \quad (4)$$

T_{FF} is the final fast-forward time defined by

$$T = \int_0^{T_{FF}} \alpha(t) dt. \quad (5)$$

At the final time of the fast-forward (T_{FF}) and we can obtain the exact target state

$$\psi_{FF}(T_{FF}) = \psi_0(T). \quad (6)$$

The explicit expression for $\alpha(t)$ in the fast-forward range ($0 \leq t \leq T_{FF}$) is proposed by Masuda and Nakamura [1, 3] as:

$$\alpha(t) = \bar{\alpha} - (\bar{\alpha} - 1) \cos\left(\frac{2\pi}{T/\bar{\alpha}}t\right), \quad (7)$$

where $\bar{\alpha}$ is the mean value of $\alpha(t)$ and is given by $\bar{\alpha} = T/T_{FF}$. Besides the time-dependent scaling factor in Eq. (7) in the fast-forward range, we can also have recourse to the uniform scaling factor:

$$\alpha(t) = \bar{\alpha} \quad (0 \leq t \leq T_{FF}), \quad (8)$$

which may be useful in the quantitative analysis of fast forward. Khujakulov and Nakamura [12] tried to realize ψ_{FF} by applying the electromagnetic field, \mathbf{E}_{FF} and \mathbf{B}_{FF} .

Let's assume ψ_{FF} is the solution of the time-dependent Schrödinger equation for a charged particle in the presence of additional vector $\mathbf{A}_{FF}(\mathbf{x}, t)$ and scalar $V_{FF}(\mathbf{x}, t)$ potentials:

$$\begin{aligned} i\hbar \frac{\partial \psi_{FF}}{\partial t} &= \left(\frac{1}{2m} \left(\frac{\hbar}{i} \nabla - \mathbf{A}_{FF} \right)^2 + V_{FF} + V_0 \right) \psi_{FF} \\ &= -\frac{\hbar^2}{2m} \nabla^2 \psi_{FF} + \frac{i\hbar}{2m} (\nabla \cdot \mathbf{A}_{FF}) \psi_{FF} \\ &\quad + \frac{i\hbar}{m} \mathbf{A}_{FF} \cdot \nabla \psi_{FF} + \frac{\mathbf{A}_{FF}^2}{2m} \psi_{FF} + (V_{FF} + V_0) \psi_{FF} \end{aligned} \quad (9)$$

where, for simplicity, we employ the prescription of a positive unit charge ($q = 1$) and the unit velocity of light ($c = 1$). The driving electromagnetic field is given by:

$$\mathbf{E}_{FF} = -\frac{\partial \mathbf{A}_{FF}}{\partial t} - \nabla V_{FF}, \quad \mathbf{B}_{FF} = \nabla \times \mathbf{A}_{FF}. \quad (10)$$

Substituting Eqs. (1) and (2) into Eq. (9) and taking its real and imaginary parts, we obtain a pair of equations:

$$\nabla \cdot \mathbf{A}_{FF} + 2\text{Re} \left[\frac{\nabla \tilde{\psi}_0}{\tilde{\psi}_0} \right] \mathbf{A}_{FF} + \hbar(\alpha - 1) \text{Im} \left[\frac{\nabla^2 \tilde{\psi}_0}{\tilde{\psi}_0} \right] = 0 \quad (11)$$

and

$$V_{FF} = -(\alpha - 1) \frac{\hbar^2}{2m} \text{Re} \left[\frac{\nabla^2 \tilde{\psi}_0}{\tilde{\psi}_0} \right] + \frac{\hbar}{m} \mathbf{A}_{FF} \text{Im} \left[\frac{\nabla \tilde{\psi}_0}{\tilde{\psi}_0} \right] - \frac{1}{2m} \mathbf{A}_{FF}^2 + (\alpha - 1) V_0. \quad (12)$$

Now, we write $\tilde{\psi}_0$ as:

$$\tilde{\psi}_0 = \rho e^{i\eta} \quad (13)$$

with use of the real amplitude ρ and phase η defined by:

$$\begin{aligned} \rho &\equiv \rho(\mathbf{x}, \Lambda(t)), \\ \eta &\equiv \eta(\mathbf{x}, \Lambda(t)). \end{aligned} \quad (14)$$

Then, one finds that:

$$\mathbf{A}_{FF} = -\hbar(\alpha - 1) \nabla \cdot \eta \quad (15)$$

satisfies Eq. (11), and that

$$V_{FF} = -(\alpha - 1) \hbar \frac{\partial \eta}{\partial \Lambda(t)} - \frac{\hbar^2}{2m} (\alpha^2 - 1) (\nabla \eta)^2. \quad (16)$$

With use of the driving vector \mathbf{A}_{FF} and scalar V_{FF} potentials in Eqs. (15) and (16), we can obtain the fast-forwarded ψ_{FF} in Eq.(2)

Noting $\mathbf{B}_{FF} = \nabla \times \mathbf{A}_{FF} = 0$, only the electric field \mathbf{E}_{FF} is required to accelerate a given dynamics. With use of Eqs. (10), (15) and (16), \mathbf{E}_{FF} is given explicitly by [13]:

$$\mathbf{E}_{FF} = \hbar \dot{\alpha} \nabla \eta + \hbar \frac{\alpha^2 - 1}{\alpha} \partial_t \nabla \eta + \frac{\hbar^2}{2m} (\alpha^2 - 1) \nabla (\nabla \eta)^2. \quad (17)$$

A remarkable issue of the present scheme is the enhancement of the current density \mathbf{j}_{FF} . Using a generalized momentum which includes a contribution from the vector potential in Eq. (15), we see:

$$\begin{aligned}\mathbf{j}_{FF}(\mathbf{x}, t) &\equiv \psi_{FF}^*(\mathbf{x}, t) \frac{1}{m} \left(\frac{\hbar}{i} \nabla - \mathbf{A}_{FF} \right) \psi_{FF}(\mathbf{x}, t) \\ &= \frac{\hbar}{m} \alpha(t) \rho^2(\mathbf{x}, \Lambda(t)) \nabla \eta(\mathbf{x}, \Lambda(t)),\end{aligned}\quad (18)$$

where we employ the prescription of a positive unit charge. Noting the current density in the standard dynamics:

$$\mathbf{j}(\mathbf{x}, t) \equiv \text{Re} \left[\psi_0^*(\mathbf{x}, t) \frac{\hbar}{im} \nabla \psi_0(\mathbf{x}, t) \right] = \frac{\hbar}{m} \rho^2(\mathbf{x}, t) \nabla \eta(\mathbf{x}, t), \quad (19)$$

we find [12]

$$\mathbf{j}_{FF}(\mathbf{x}, t) = \alpha(t) \mathbf{j}(\mathbf{x}, \Lambda(t)). \quad (20)$$

Thus, the standard current density at each of spatial points becomes both squeezed and magnified by a time-scaling factor $\alpha(t)$ in Eq. (7) or Eq. (8) as a result of the exact fast forwarding which enables acceleration of both amplitude and phase of the wave function throughout the time evolution.

2. Free wave packet dynamics

The time evolution of a free electron wave packet in 1 dimension is described by the time-dependent Schrödinger equation:

$$i\hbar \frac{\partial \Psi}{\partial t} = -\frac{\hbar^2}{2m} \frac{d^2 \Psi}{dx^2}. \quad (21)$$

Let's consider the initial state of electron as

$$\Psi_0(x, t=0) = \pi^{-1/4} \Delta^{-1/2} \exp \left(-\frac{x^2}{2\Delta} + i \frac{p_0}{\hbar} x \right). \quad (22)$$

Then, the time evolution of Ψ_0 is given by

$$\Psi_0(x, t) = \int_{-\infty}^{\infty} dx' K(x, t; x', 0) \Psi_0(x', t=0). \quad (23)$$

Where K is the kernel propagator defined by:

$$K(x, t; x', 0) = \left(\frac{m}{2\pi i \hbar t} \right)^{1/2} \exp \left[\frac{im(x-x')^2}{2\hbar t} \right] \quad (24)$$

$\Psi_0(x, t)$ in Eq.(23) becomes:

$$\begin{aligned}\Psi_0(x, t) &= \pi^{-1/4} \Delta^{-1/2} \left[1 + \frac{i\hbar t}{m\Delta^2} \right]^{-1/2} \times \\ &\exp \left[-\frac{(x - \frac{p_0}{m}t)^2}{2\Delta^2(1 + (\hbar t/m\Delta^2)^2)} + i \left[\frac{p_0}{\hbar} \left(x - \frac{p_0}{m}t \right) + \frac{p_0^2}{2\hbar m} t + \frac{\hbar t(x - \frac{p_0}{m}t)^2}{2m\Delta^4(1 + (\hbar t/m\Delta^2)^2)} \right] \right].\end{aligned}\quad (25)$$

From Eq. (23), the probability amplitude $|\Psi|^2$ and the phase η is given by:

$$|\Psi|^2 = \pi^{-1/4} \Delta^{-1/2} \left[1 + \left(\frac{\hbar t}{m\Delta^2} \right)^2 \right]^{-1/4} \exp \left[-\frac{(x - \frac{p_0}{m}t)^2}{2\Delta^2(1 + (\hbar t/m\Delta^2)^2)} \right] \quad (26)$$

and

$$\eta = \frac{p_0}{\hbar} \left(x - \frac{p_0}{m}t \right) + \frac{p_0^2}{2\hbar m} t + \frac{\hbar t(x - \frac{p_0}{m}t)^2}{2m\Delta^4(1 + (\hbar t/m\Delta^2)^2)} - \frac{1}{2} \arctan \left(\frac{\hbar t}{m\Delta^2} \right), \quad (27)$$

respectively.

Figure 1 shows $|\Psi|^2$ of the standard wave packet as a function of x and t .

Now, we shall proceed to analyze the fast-forward the above dynamics. The fast-forward state is given by:

$$\Psi_{FF} = \Psi_0(x, (\Lambda(t))), \quad (28)$$

Figure 2 shows $|\Psi_{FF}|^2$ where the mean time-magnification factor $\bar{\alpha} = 5$ is used.

To realize the fast-forward state, the electric field is given by Eq. (17). Using Eqs. (17) and (27), we can evaluate \mathbf{E}_{FF} , which is depicted in Fig. 3.

Now, we shall apply the present scheme to tunneling phenomena in quantum mechanics.

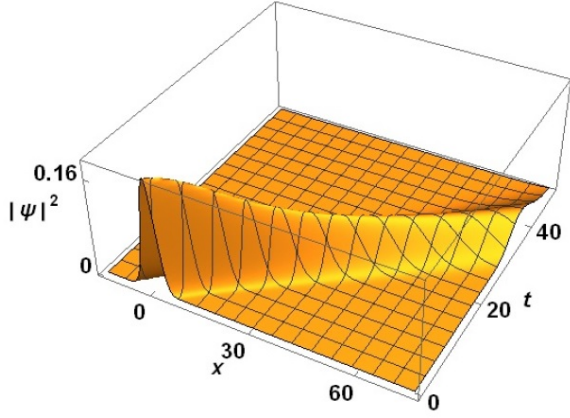


FIG. 1. 3D plot of $|\Psi|^2$ for a standard wave packet as a function of x and t . The final time $T = 50$

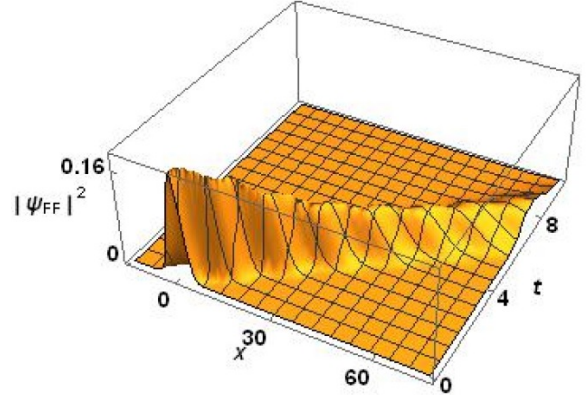


FIG. 2. 3D plot of $|\Psi_{FF}|^2$ fast-forward wave packet with $\bar{\alpha} = 5$ as a function of x and t for the $\bar{\alpha} = 5$, $T_{FF} = 10$

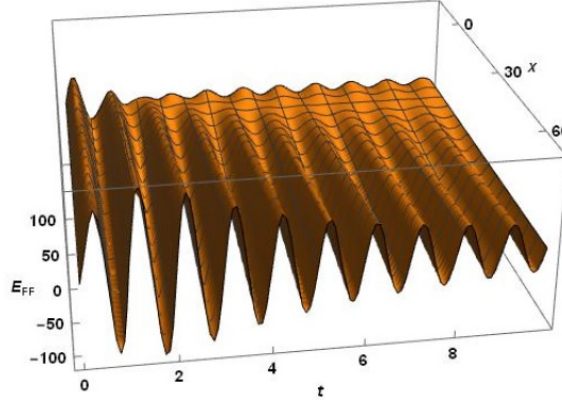


FIG. 3. 3D plot of E_{FF} as a function of x and t , $\bar{\alpha} = 5$

3. Fast-forward of tunneling of wave packet dynamics

Confining ourselves again to 1-D motion, we now investigate the time evolution of a localized wave packet when it runs through a delta-function barrier. The initial wave packet centered at $x = -x_0$ and having a momentum k is expressed as:

$$\psi^{(0)}(x, 0) = \sqrt{\beta} e^{-\beta|x+x_0|} e^{ik(x+x_0)}. \quad (29)$$

$\psi^{(0)}(x, 0)$ satisfies the normalization condition $\int_{-\infty}^{\infty} |\psi^{(0)}(x, 0)|^2 dx = 1$. Therefore, $\langle x \rangle = -x_0$ and $\langle p \rangle = k$ at $t = 0$.

The time-dependent Schrödinger equation with a δ function barrier at $x = 0$ is given by

$$[i\hbar\partial_t + (\hbar^2/2m)\partial_x^2] \psi_0(x, t) = V(x)\psi_0(x, t), \quad (30)$$

with $V(x) = V_0\delta(x)$. In order to simplify notation, we shall use “natural unit” ($\hbar = m = 1$).

The time evolution of ψ_0 follows for $t > 0$ from:

$$\psi_0(x, t) = \psi^{(0)}(x, t) - V_0 \int_{-\infty}^{\infty} dx' \times M(|x| + |x'|; -iV_0; t) \psi_0(x', 0). \quad (31)$$

Here $M(x; k; t)$ is “Moshinsky” function defined in terms of the complementary error function by

$$M(x; k; t) = \frac{1}{2} e^{i(kx - k^2 t/2)} \operatorname{erfc} \left(\frac{x - kt}{\sqrt{2it}} \right), \quad (32)$$

which is interpreted as the wave function of a monochromatic particle that is confined to the left half-space $x \leq 0$ at $t = 0$. On the other hand, $\psi^{(0)}(x, t)$ is the free-particle wave function:

$$\psi^{(0)}(x, t) = \int_{-\infty}^{\infty} dx' K(x, t|x', 0) \psi^{(0)}(x', 0), \quad (33)$$

with K the free-particle propagator given in Eq. (24).

The explicit solution for $t > 0$ was given by Elberfeld and Kleber [13] as:

$$\begin{aligned} \psi_0(x, t) = & \sqrt{\beta} [M(x + x_0; k - i\beta; t) + M(-x - x_0; -k - i\beta; t)] \\ & + V_0 \sqrt{\beta} [S(x_0, \lambda^*; t) - S(x_0, -\lambda; t) + e^{-\lambda x_0} [S(0, -\lambda; t) + S(0, \lambda; t)]], \end{aligned} \quad (34)$$

where $\lambda = \beta - ik$ and $S(\xi, \lambda; t)$ is defined by:

$$S(\xi, \lambda; t) = [1/(V_0 - \lambda)] [M(|x| + \xi; -iV_0; t) - M(|x| + \xi; -i\lambda; t)]. \quad (35)$$

The first bracket on r.h.s. of Eq. (34) describes the time evolution of the free ($V_0 = 0$) wave packet, and the second bracket denotes the sum of reflected and transmitted waves.

The tunneling current density is:

$$j(x, t) = \text{Im}[\psi_0^*(x, t) \partial_x \psi_0(x, t)]. \quad (36)$$

Now, we analyze the fast forward of tunneling of wave packets, and find the corresponding current density. Here we shall present the results not investigated by Khujakulov and Nakamura [13]. By extracting the space-time dependent phase η of the wave function in Eq. (34), one can obtain both vector and scalar potentials in Eqs. (15) and (16). Under these driving potentials, one can generate the fast-forward state of a tunneling wave packet through the barrier as:

$$\psi_{FF}(x, t) \equiv \psi_0(x, \Lambda(t)), \quad (37)$$

which accelerates both amplitude and phase of Eq. (34) exactly. From Eq. (20), the tunneling current density for

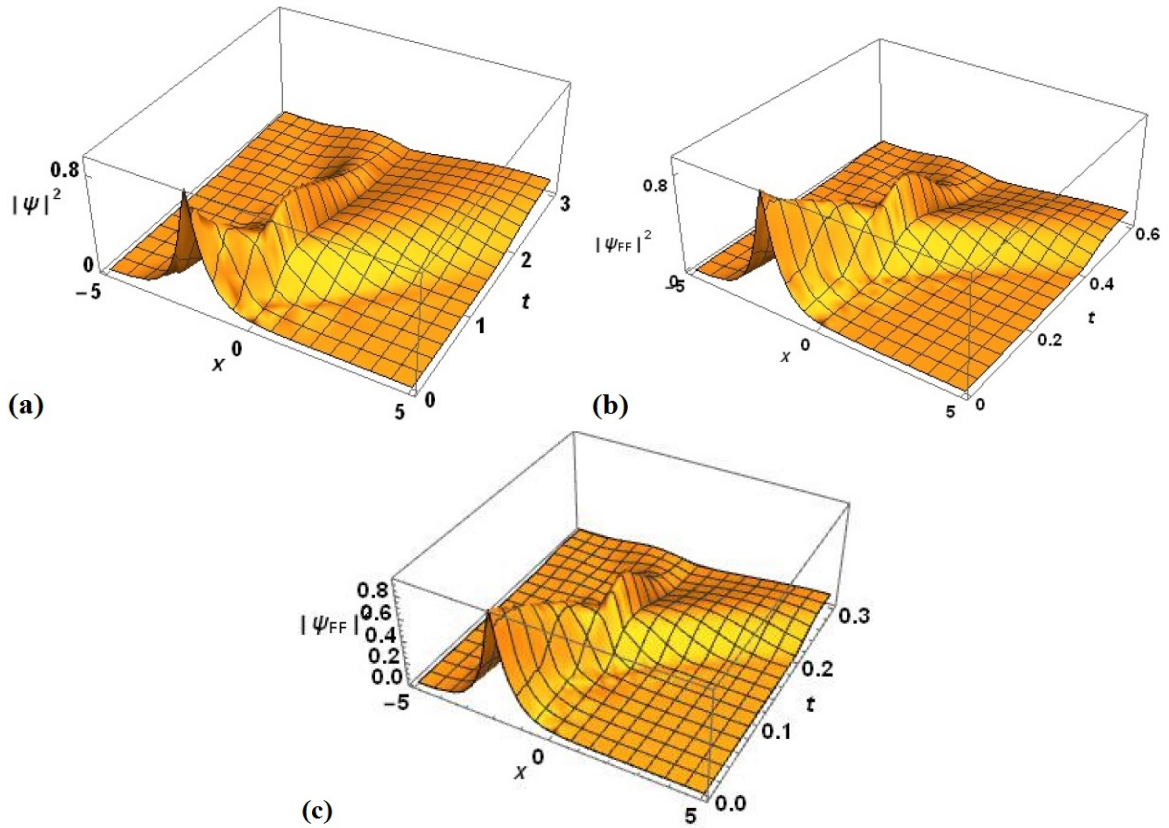


FIG. 4. 3D plot of wave function amplitude (a) $|\Psi|^2$; (b) $|\Psi_{FF}|^2$ with $\bar{\alpha} = 5$; (c) $|\Psi_{FF}|^2$ with $\bar{\alpha} = 10$

the fast-forward tunneling phenomenon is:

$$j_{FF}(x, t) = \alpha(t)j(x, \Lambda(t)). \quad (38)$$

Figure 4 shows the probability amplitude as a function of x and t . In our numerical analysis we choose $x_0 = 2, k = 2$ and $\beta = 1$. We use typical space and time scales like $L = 10^{-2} \times$ the linear dimension of a device and $\tau = 10^{-2} \times$ the phase coherent time and put $\frac{\hbar}{m} = 1(\times L^2 \tau^{-1})$. Therefore, the above choice means $x_0 = 2(\times L), k = 2(\times L^{-1})$ and $\beta = 1(\times L^{-1})$. We shall show the standard dynamics up to $T = 3(\times \tau)$ and its fast-forward version up to $T_{FF} \equiv \frac{T}{\bar{\alpha}}(\tau)$ with use of the mean time acceleration factor $\bar{\alpha} = 5$ and $\bar{\alpha} = 10$.

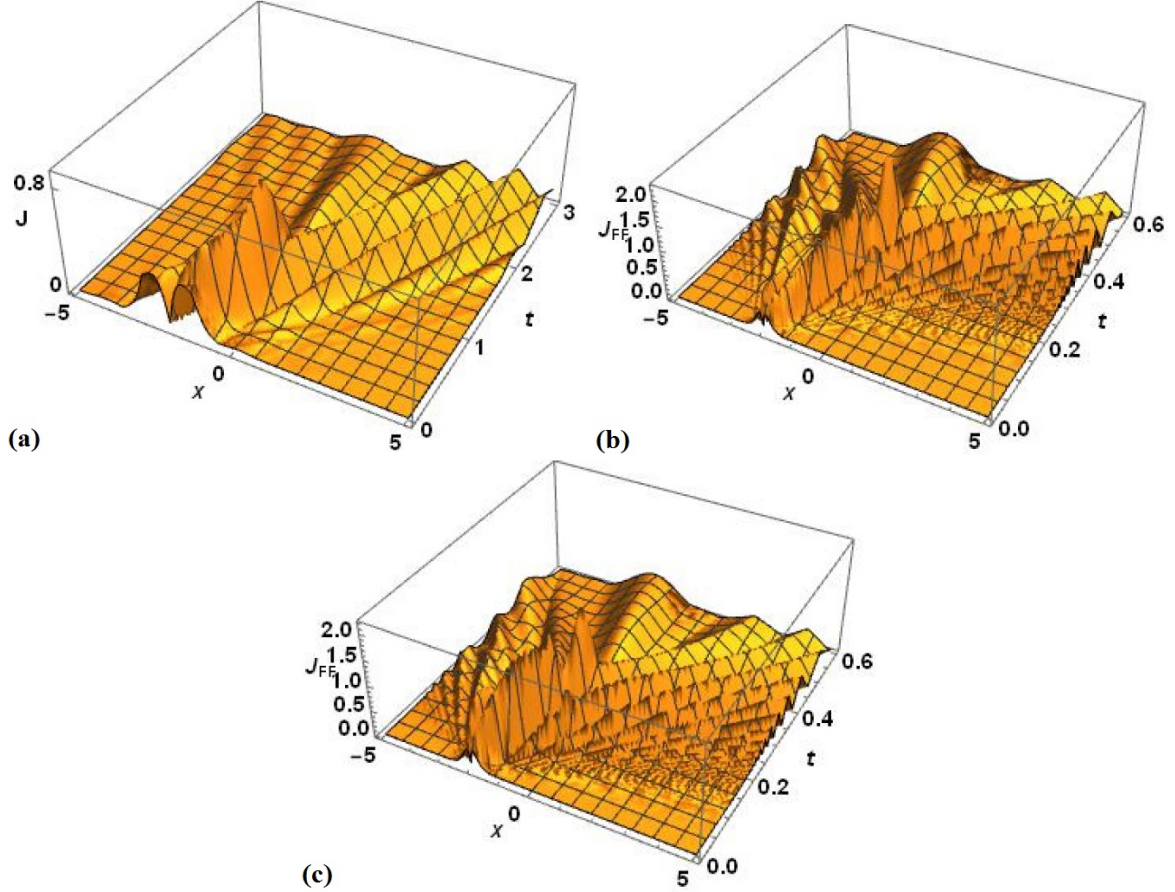


FIG. 5. 3D plots of current density as a function of x and t (a) standard current density $j(x, t)$ in Eq. (36); (b) fast-forward current in Eq. (38) with $\alpha = \bar{\alpha} - (\bar{\alpha} - 1) \cos(\frac{2\pi}{T_{FF}} t)$ and $\bar{\alpha} = 5$; (c) fast-forward current in Eq. (38) with $\alpha = 1 + 6(\bar{\alpha} - 1) \frac{t}{T_{FF}} (1 - \frac{t}{T_{FF}})$ and $\bar{\alpha} = 5$

We see the exponential wave function partially goes through the barrier and is partially reflected back. The dynamics up to T on the standard time scale is reproduced in the fast-forward dynamics up to T_{FF} . The phenomena in the latter time scale is just the squeezing (along the time axis) of those in the former time scale.

Figure 5 shows the standard and fast-forwarded tunneling currents as a function of x and t . Here, we choose $T = 5, T_{FF} = 1$ and $\bar{\alpha} = 5$.

As for fast-forwarding, we have employed two kinds of time-magnification factor: (i) cos-type, $\alpha = \bar{\alpha} - (\bar{\alpha} - 1) \cos(\frac{2\pi t}{T_{FF}})$ and (ii) parabola-type, $1 + 6(\bar{\alpha} - 1) \frac{t}{T_{FF}} (1 - \frac{t}{T_{FF}})$. We find the temporal behavior of the current density is both squeezed and amplified, as compared to the standard version of j . We also see this result is not affected by the functional form of $\alpha(t)$. Fig. 6 shows E_{FF} for two kinds of time-magnification factors, which also shows that E_{FF} is not sensitive to the functional form of $\alpha(t)$.

4. Conclusion

By using the fast-forward theory which makes possible the exact acceleration of the phase and amplitude of a standard wave function, we investigated fast-forward of wave packet dynamics with and without a potential

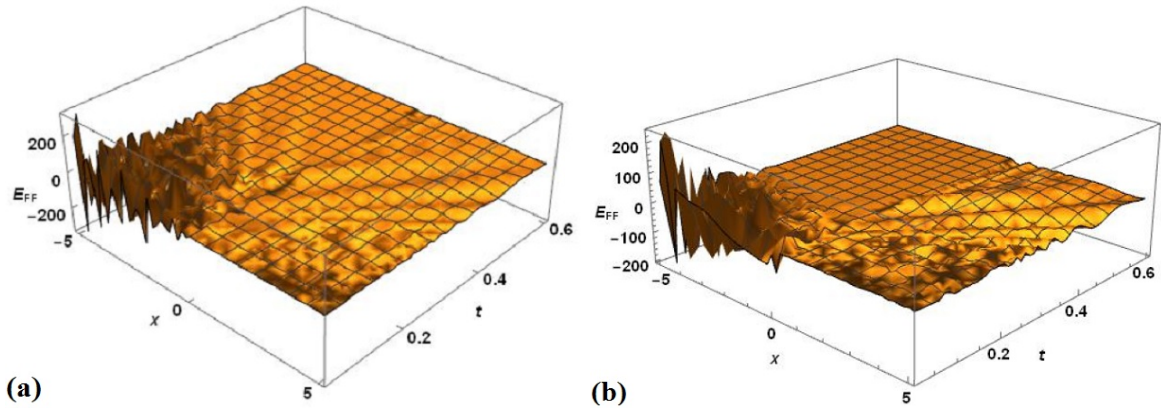


FIG. 6. Electric field E_{FF} : (a) cos-type time-magnification factor; (b) parabola-type time-magnification factor

barrier. We choose two kinds of time-magnification scaling factors $\alpha(t)$ ((i) cos type and (ii) parabolic type). The fast-forwarded current density distribution and the driving electromagnetic field have proved to be unaffected by the details of $\alpha(t)$, which indicate the stability of fast-forwarding mechanism.

Acknowledgements

We are grateful to Anvar Khujakulov for kind and helpful comments and to Iwan Setiawan for technical assistance.

References

- [1] Masuda S., Nakamura K. Fast-forward problem in quantum mechanics. *Phys. Rev. A*, 2008, **78**, P. 062108.
- [2] Masuda S., Nakamura K. del Campo A. High-fidelity rapid ground-state loading of an ultracold gas into an optical lattice. *Phys. Rev. Lett.*, 2014, **113**, P. 063003.
- [3] Masuda S., Nakamura K. Fast-forward of adiabatic dynamics in quantum mechanics. *Proc. R. Soc. A*, 2010, **466**, P. 1135–1154.
- [4] Demirplak M., Rice S.A. Adiabatic population transfer with control fields. *J. Phys. Chem. A*, 2003, **89**, P. 9937.
- [5] Demirplak M., Rice S.A. Assisted adiabatic passage revisited. *J. Phys. Chem. B*, 2005, **109**, P. 6838.
- [6] Berry M. V. Transitionless quantum driving. *J. Phys A : Math. Theor.*, 2009, **42**, P. 365303.
- [7] Lewis H.R., Riesenfeld W.B. An exact quantum theory of the time-dependent harmonic oscillator and of a charged particle in a time-dependent electromagnetic field. *J. Math. Phys A*, 1969, **10**, P. 1458.
- [8] Chen X., Ruschhaupt A., et al. Fast optimal frictionless atom cooling a harmonic traps: Shortcut to adiabaticity. *Phys. Rev. Lett.*, 2010, **104**, P. 063002.
- [9] Torrontegui E., Ibanez M., et al. Shortcut to adiabaticity. *Adv. At. Mol. Opt. Phys.*, 2013, **62**, P. 117.
- [10] Torrontegui E., Martinez-Garaot M., Ruschhaupt A., Muga J.G. Shortcut to adiabaticity: fast-forward approach. *Phys. Rev. A*, 2012, **86**, P. 013601.
- [11] Takahashi K. Fast-forward scaling in a finite-dimensional Hilbert space. *Phys. Rev. A*, 2014, **89**, P. 042113.
- [12] Khujakulov A., Nakamura K. Scheme for accelerating quantum tunneling dynamics. *Phys. Rev. A*, 2016, **93**, P. 022101.
- [13] Elberfeld W., Kleber M. Time-dependent tunneling through thin barriers: A simple analytical solution. *Am. J. Phys.*, 1998, **56**, P. 154.

Fractal structures in perovskite-based solar cells

B. L. Oksengendler¹, N. R. Ashurov¹, S. E. Maksimov¹, I. Z. Uralov¹, O. V. Karpova^{2,3}

¹Polymer Chemistry and Physics Research Center at The National University of Uzbekistan named after Mirzo Ulugbek, 100128, A. Kadyri Str., 7b, Tashkent, Uzbekistan

²Turin Polytechnic University in Tashkent, 17 Kichik Halka Yuli, Tashkent, 100095, Uzbekistan

³Faculty of Physics, National University of Uzbekistan, Tashkent, Uzbekistan
oksengendlerbl@yandex.ru

PACS 05.45.Df

DOI 10.17586/2220-8054-2017-8-1-92-98

Interface engineering plays important role in the fabrication of tandem and perovskite-based solar cells. Recent experiments show that the interface effects are caused by the coupling of the electron bands and the pairing of surface contact geometry. In particular, it has been experimentally revealed that the transition from a planar to a rough interface improves many photoelectric parameters of the device. This means that the value of the fractal dimension of the interface may be key factor in device performance. It is possible to formulate two problems: firstly, the understanding on simple models why the electrical properties are improved with fractal interfaces, and, secondly, to discuss one of the most promising approaches in modern electronics, namely technology of radiation applications in the creation of rough interfaces.

Keywords: solar cells, perovskite, interface, fractal.

Received: 27 July 2016

Revised: 2 September 2016

1. Introduction

Thin film photovoltaic materials based on polymers and tandem structures have attracted much attention due to their flexibility, environmental safety and low cost. However, to compete with silicon based solar cells, conversion efficiency and stability of organic and tandem solar cells need to be improved considerably. To address these concerns, in particular, perovskite based solar cells have been developed whose conversion efficiencies have monotonically increased over the last 3–4 years [1–3].

Fabrication of highly efficient solar cells (SC) based on organic-inorganic perovskites requires basic studies related to such issues as the physical and chemical aspects of cell morphology [4], the architecture of device structures [5], stability and degradation of photovoltaic materials and devices [6], thermodynamics and electronics of defects [7], homologous composition of perovskites [8], the role of the organic component of perovskites [9], mechanisms of photophysics [10] in organic and tandem structures.

All these issues can be classified as the “problem of interface engineering for photovoltaics” [11]. In this paper, we address the problem of rough interfaces in the charge dynamics and conversion efficiency of the perovskite based tandem solar cells. This problem is of special importance for perovskites because of their multi-component nature. Earlier, in the study of similar problem in thin film silicon solar cells, it was found that the surface “landscape” plays an important role causing the multiple reflection of the light [12]. Similar effects in organic-inorganic perovskite solar cells were studied in [13], where the cells with rough interface surfaces were fabricated.

In particular, in [13], additional power conversion efficiency should be gained without increasing the thickness and the complexity of the devices for practical applications. This result has been checked in [13] for 20 samples. A rough interface between perovskite and hole-conducting material (HTM) was fabricated in perovskite solar cells to enhance the light scattering effect and improve the charge transport [13]. The parameters related to the morphology have been systematically investigated by sequential deposition. The control of the roughness degree of the interface was realized by two ways: a) reaction temperature control and b) pre-wetting time control (see, Fig. 1). Simultaneous enhancements of short-circuit current and power conversion efficiency were observed in both $\text{CH}_3\text{NH}_3\text{PbI}_3$ and $\text{CH}_3\text{NH}_3\text{PbI}_{3-x}\text{Cl}_x$ devices containing the rough interface, with power conversion efficiencies of 10.2 % and 10.8 %, respectively, additionally, the enhancement of the short-circuit current was more than 13 %.

Here it is important to note that the increase of the total surface for the fractal interface should decrease the current through the device, since the interface has electron traps. However, this is in contradiction with the experimental results of [13]. This may imply that the fractal structure at the interfaces plays an important role. Therefore, the theoretical analysis of such structures and their role in photovoltaic conversion is important for deeper understanding of the mechanisms for charge carrier generation and dynamics.

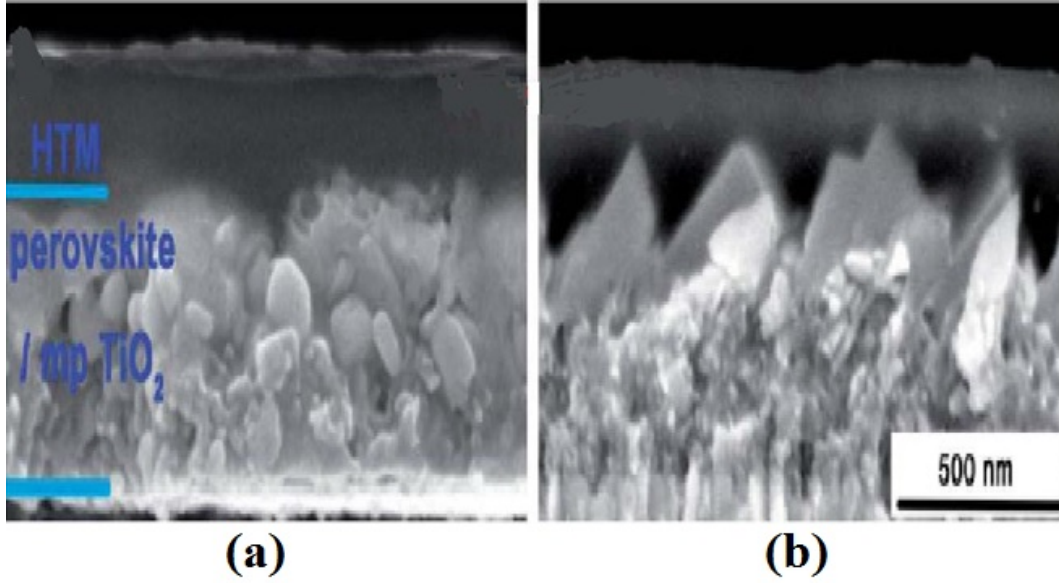


FIG. 1. Scanning electron microscope images of cross-sections of perovskite/HTM interface: (a) planar, (b) rough relief (a picture taken from [13])

These theoretical and experimental results highlight an efficient and universal way to control the morphology and further optimize perovskite solar cells for devices by sequential deposition with various structures.

2. Light passage through the fractal interface

The interaction of electromagnetic waves with the fractal (“rough”) surfaces has attracted much attention earlier within different models. However, the geometric structures of the rough surfaces considered in these models are very far from that of the perovskite cells studied in [13]. Therefore, we consider a simple model of the “perovskite particles/ HTM film” interface, which is more close to the interface structures studied by the SEM method. Let us assume that the interface contains the tightly contacting perovskite balls with radii R and the dense HTM film. The light beam falls vertically on the interface inside perovskite cell from the side of the balls (see Fig. 2). It is obvious that there is a distance $\rho^* = Y_0$ measured from the central diameter of the ball (see, Fig. 2a), further, which the light beam undergoes the total internal reflection and remains inside the perovskite. From the simplest constructions, the following expression for the part of the total interactions of parallel rays with the spherical surface of the perovskite ball, when the light rays remain in the ball and cannot transit into the HTM film can be obtained: $F = (1 - \eta^2)^{3/2}$ (here $\eta = \sin \alpha^*$ is the light refraction index in the transition from the more dense medium of perovskite into the less dense HTM medium).

Now, suppose that the interface is formed from the ellipsoidal perovskite particles (with semi-axes a , b , $c=b$) and the HTM film (Fig. 2b). The calculations for ellipsoidal particles are similar to those for the spherical particles and allow one to obtain the part of rays falling initially parallel to the major axis of the ellipsoid but undergoing total internal reflection: $\tilde{F} = \tilde{Z}^3 / 2(1 + \tilde{Z}^2)^{3/2}$; here $\tilde{Z} = \left(\frac{a}{b}\right) \text{ctg} \alpha^*$. It is important to note that in the case of the spherical particles ($a = b$), the expression for \tilde{F} transforms into that of F . Therefore we can conclude that in the case of the surface consisting of ellipsoidal grains, the probability of total internal reflection of light beams is greater than in the case of spherical particles of perovskites. From this conclusion, it follows that the number of electron-hole pairs generated per one second in the subsurface particles of perovskite increases with increased interface roughness. Of course, this leads to the increase of the current through the interface. Note that these results are in agreement with the concept of “true fractal interfaces”. Indeed, as a result of technological operations, a large set of perovskite particles with varying degrees of ellipticity (i.e. with different $\frac{a}{b}$ relations) is presented at the interface. If we introduce the idea about the value of the particle deformability, $\tilde{\beta} = 2\frac{a-b}{a+b}$, then at the small degrees of deformability, we obtain $\frac{a}{b} \approx 1 + \tilde{\beta}$. In this way, in the expression for \tilde{F} we can introduce the dependence on $\tilde{\beta}$, and then we consider it distributed in agreement with the fractal laws. This case corresponds

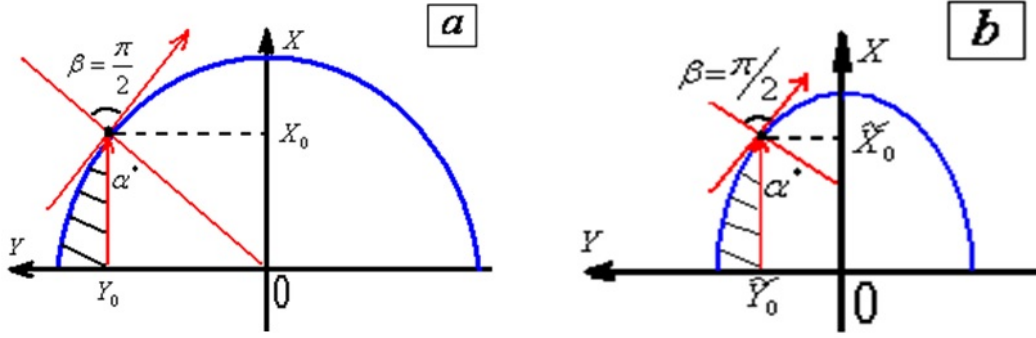


FIG. 2. Schematic representation for the total internal reflection inside the round (a) and ellipsoidal (b) particles of perovskite; in the case (b) the shaded area is greater than in (a) $\left(\frac{Y_0}{R} > \frac{\tilde{Y}_0}{R}\right)$, which corresponds to the larger number of generated e - h -pairs for the ellipsoidal particles

to the change of the shape of perovskite particles under the influence of some type of technology, but with the preservation of its volume. Thus we can assume that the growth of the fractal dimension (roughness) of interface causes a decrease of the current due to the enhanced electron-hole recombination at the interface.

3. Current on the fractal interface

The effect of the interface fractal dimension on the photocurrent should be resolved in terms of the interaction of electron de Broglie waves with a fractal. Due to the lack of such investigations (see [14]), we restrict our study by considering the simple quantum mechanical model. Since the fractal interface is characterized by non-uniform density of matter, it is reasonable to use the approach “on average” for the first approximation when the interface can be characterized by a spatial value $2a$, which is mean-square deviation of the value of roughness at the interface. Then $2a \approx \sigma$ and the potential acting on electron can be chosen as $V(\tilde{x}) = \frac{1}{2}V_0 \left(1 + \text{th} \frac{\tilde{x}}{2}\right)$ [15, 16] (see, Fig. 3). Then, for the transmission coefficient (of the wave through the interface), we have:

$$\tilde{T} = 1 - \left[\frac{\text{sh}\pi(k - k')a}{\text{sh}\pi(k + k')a} \right]^2 \approx 1 - \left(\frac{\pi a V_0}{\hbar} \right)^2 \frac{2m}{E} \exp\left(-\frac{4\pi a}{\hbar} \sqrt{2mE}\right). \quad (1)$$

Here V_0 is the difference of the potential energy of electrons between the particles of perovskite and the film covering the interface: $k = \frac{2m}{\hbar^2}E$; $k' = \frac{2m}{\hbar^2}(E - V_0)$; E is the electron energy. The formula for \tilde{T} demonstrates clearly that $d\tilde{T}/da > 0$. Since the interface fractal dimension D is symbatical to σ^2 , then $d\tilde{T}/dD = (d\tilde{T}/da) \cdot (da/d\sigma) \cdot (d\sigma/dD) > 0$. This shows the electron transport through the interface is enhanced by increasing of its fractal dimension. It is important to note that the opposite difference of the potential relief for electrons facilitates the passage through the steps at its broadening in the direction perpendicular to the interface which is consistent with the experimental results of the Ref. [13].

4. Controlling of the interface fractal structure by radiation

Consider a planar boundary in the characteristic architecture of perovskite based solar elements (Fig. 4a).

The interface roughness (including the fractal structure) can be designed by ion bombardment. Earlier, such models have been discussed in the Refs. [17, 18].

The interface between the surface of hole transporting material (HTM) and perovskites, made in the form of fine particles can be considered as quasi-plane (Fig. 4a). Such a “weakly rough” surface may be characterized by the surface height (Z) at its different points along a certain direction. Then, a portion of representative surfaces can be characterized by the relation:

$$\sigma^2 = \langle Z^2(y) \rangle. \quad (2)$$

Here, the brackets denote averaging over the interface area, the reference point on a vertical is chosen such that $\langle Z(y) \rangle = 0$. An important measure of the statistical properties for the surface is the correlation function given by:

$$C(\Delta y) = \langle Z(y + \Delta y) * Z(y) \rangle. \quad (3)$$

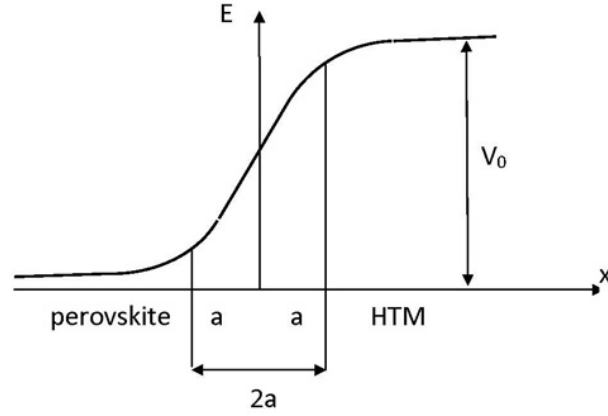


FIG. 3. Potential relief modelling the energy barrier at the transition of an electron through a “fuzzy” interface

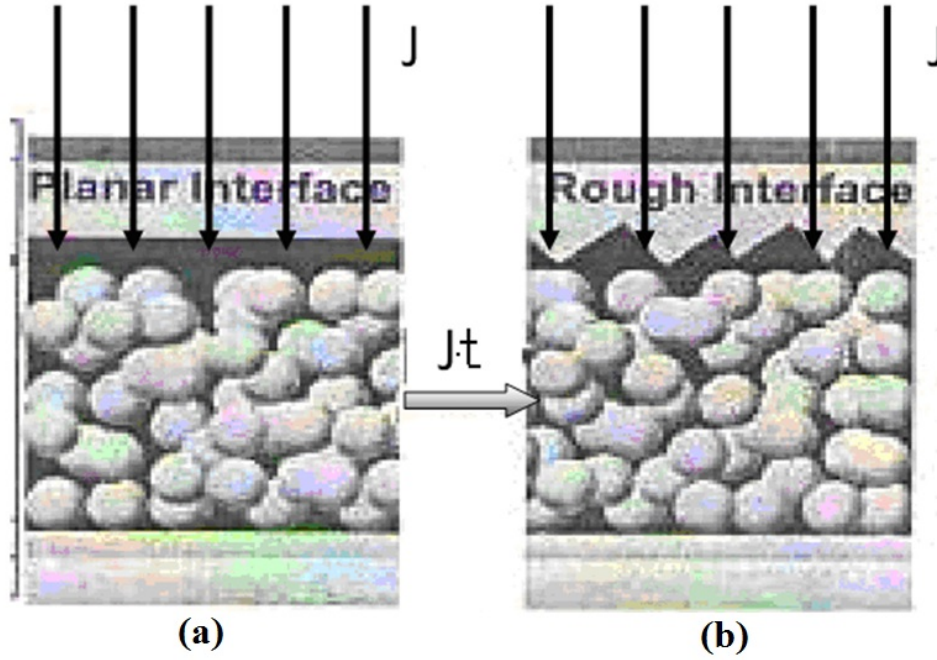


FIG. 4. Diagram of the perovskite solar cells on the planar (left) and rough (right) interface under irradiation with the intensity of ion irradiation J

It can be expressed in terms of “power spectrum” $G(f)$ by Fourier transformation:

$$C(\Delta y) = \int_{f_{\min}}^{\infty} G(f) \exp(2\pi i f \Delta y) df \quad (4)$$

Here, f is the spatial frequency which is inversely proportional to the wavelength corresponding to the rough surface. It is clear that $f_{\min} = 1/M_{\max}$, where M_{\max} is the physical length of the entire interface. Choosing the “fractal spectrum” of power $G(f) = \frac{\chi}{f^\alpha}$ (where χ is the coefficient surface irregularity), we have:

$$\sigma^2 = \langle Z^2(y) \rangle = \int_{f_{\min}}^{\infty} G(f) df = \frac{\chi M_{\max}^{\alpha-1}}{(\alpha-1)}. \quad (5)$$

From the Mandelbrot relation [19] $\alpha = 7 - 2D$, we obtain the expression of fractal dimension (D) for rough surface with its dispersion:

$$D = 3 - \frac{const}{\sigma^2} \quad (6)$$

Eq. (6) is valid in the interval of $2 < D < 3$ and was tested on a huge number of surface types (see, e.g., [19]).

Note that the constant in the last formula allows one to obtain the correct value of D for extreme cases: perfectly smooth ($\sigma \rightarrow \infty$) and absolutely rough ($\sigma \rightarrow 0$) surfaces; formally, it is sufficient in the upper limit of the integrals used to replace infinity f_{max} , expressed in terms of the minimum size of a representative portion of the surface. Thus, to verify in the growth of D under the action of radiation (Fig. 4b) it is necessary to prove an increase in the spread of height “hills” on the surface (i.e., increasing its roughness). Let us return to the original formulation of the problem and use the results of Mullins (1959) (see in [20]) to describe the evolution of the groove on the border of the two grains (Fig. 5).

Under the influence of the difference in the chemical potential $\Delta\mu = \gamma_s \Omega \tilde{K}$, for certain constraints, there is a material removal from the contact between two grains (in our case from two adjacent particles of perovskite) on the border of the groove (here, γ_s is the surface tension of the free surface, Ω is the atomic volume, \tilde{K} is the curvature of the surface). As a result, the groove depth d increases over time.

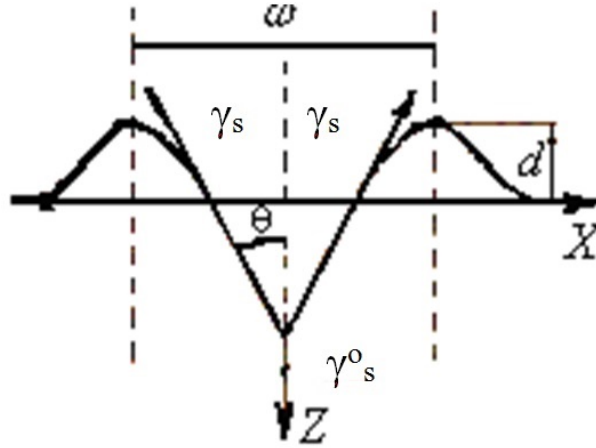


FIG. 5. Profile of “groove” in place of the output of the boundary of two particles on the surface of the interface under irradiation. (see [20])

For the case of surface diffusion, we obtain:

$$d = 2(ctg\theta)(Bt)^{1/4} \quad (7)$$

where $B = \frac{D_s \delta \gamma_s \Omega}{k_B T}$, D_s is the surface radiation enhanced atom diffusion coefficient, δ is the width of the surface layer having a high rate of diffusion; θ is the angle of the original groove before its recess (at $t = 0$), (Fig. 5).

Thus, the value d at different points of the surface is determined by the angle θ at a predetermined growth time (t). When θ is increased from 0 to $\pi/2$ rate of groove deepening decreases. The speed of growth is determined by depending on the irradiation parameters and increases with increasing δ and D_s : managing them, you can change the value of d . Obviously, the larger B , the difference in the initial increases $\{d\}$, i.e. it increases the degree of roughness and hence the fractal dimension D . This qualitative picture can easily be translated into the language of mathematics, if we take into account that the original set of θ has a different fractal distribution, averaging on which allows to give all the necessary statistical values.

5. Photodegradation of solar cells with fractal interfaces

Since the presence of fractal interface leads to its excessive area, the exposure by ionizing light (as such as by any type of ionizing radiation in general), taking into account the semiconductor nature of the perovskite, can lead to the surface radiation-stimulated atomic diffusion. This diffusion takes place by recharge of local electron levels and should lead to the smoothing of the roughness of the interface; this, in turn, should eliminate the extra value

of 13 % of the photocurrent. The effect of radiation smoothing of fractal has been observed already on a BaF₂ surface [21].

However, to realize such surface smoothing by surface atom diffusion, it is necessary to release them from their regular surface layer of perovskite, i.e. the action of some mechanism for the formation of defects on the surface under exposition of light, UV-radiation (as well as the X- and gamma-rays in the case of work of device in space) must take place. The most important mechanism of the radiation defect may be the so-called mechanism of Dexter-Varley, including his variations in form of Knotek-Feibelman [22]. Its essence is the ionization of deep shell of surface negative ion by X-rays, resulting that the deep-level hole rises to higher levels by Auger transition with “breeding”; the negative ion is converted into the positive one losing electrons (in our case it is $I_s^- \rightarrow I_s^+$). Such a transformation makes the ion I_s^+ Coulomb unstable and it then leaves its site. This process is probabilistic in nature and is governed by the ratio of the reverse Debye frequency $1/\omega_D$ and of the time τ_e of life of hole on the I_s^+ ion, so that the cross section of the destruction is proportional to $\eta \sim \exp\left(-\frac{1}{\omega_D\tau_e}\right)$ (see [22]). Since the surface ions I_s^- form area of Tamm states [23], the delocalization of the holes takes place on Tamm zone, so $\tau_e \approx \frac{\hbar}{\Delta E_T}$, where ΔE_T is the width of the Tamm zone [23]. Turning to the fractal surface of the interface where the convexes alternate with the cavities (see. Fig. 1), we see that electron wave functions overlap on neighboring ions I_s^- in the areas of convexity worse than on a flat surface, whereas in the area of the cavities the situation is opposite. The result is the variation of ΔE_T on the convexities and the concavities, but the time τ_e is higher on the convexities than on the concavities. This, in turn, leads one to the conclusion that the probability of convex domain destruction is greater. Consequently, under the X-rays (and under the corresponding UV-radiation) the smoothing of the relief takes place that reduces the fractal dimension of the interface and leads to the degradation of the device as lost an additional 13 % found in [13].

6. Conclusion

In this paper, we proposed a model which explains experimentally established effect of photovoltaic parameter enhancement for perovskite-based solar cells in the transition from a planar to a rough interface. The model is based on the assumption that the surface perovskite interface has the fractal structure that may cause an increase in the mobility of the electrons. The rigorous analysis the problem can be done by modeling the interaction of the waves of different nature with fractal surfaces. The above model can be used for the comprehensive description of the problem of charge carrier generation, separation and transport in perovskite-based tandem solar cells.

Acknowledgements

This work was supported by the Committee for Coordinating the Development of Science and Technology under the Cabinet of Ministers of the Republic of Uzbekistan, contract No. F3-003.

References

- [1] Giorgi G., Yamashita K. Organic-inorganic perovskites: an ambipolar class of materials with enhanced photovoltaic performances. *J. Mater. Chem. A*, 2015. DOI: 10.1039/c4ta05046k.
- [2] Yin W.-J., Yang J.H., Kang J. et al. Halide perovskite materials for solar cells: a theoretical review. *J. Mater. Chem. A*, 2014. DOI: V. 10.1039/c4ta05033a.
- [3] Ashurov N.R., Oksengendler B.L., Rashidova S.Sh., Zakhidov A.A. State and Prospects of Solar Cells Based on Perovskites. *Appl. Solar Energy*, 2016, **52** (1), P. 5–15.
- [4] Salim T., Sun S., Abe J., et.al. Perovskite-based solar cells: impact of morphology and device architecture on device performance. *J. Mater. Chem. A*, 2015. DOI: 10.1039/c4ta05226a.
- [5] Liu Ch., Oiu Zh., Meng W. et.al. Effect of interfacial characteristics on photovoltaic performance in CH₃NH₃PbBr₃-based bulk perovskite solar cells with core/shell nanoarray as electron transporter. *Nano Energy*, 2015, **12**, P. 59–68.
- [6] Oksengendler B.L., Ismailova O.B., Marasulov M.B., Urolov I.Z. On the degradation mechanism of functioning solar cells based on organic-inorganic perovskites. *Appl. Solar Energy*, 2014, **50** (4), P. 255–259.
- [7] Du M.H. Efficient carrier transport in halide perovskites: theoretical perspectives. *J. Mater. Chem. A*, 2014, **2**, P. 9091–9098.
- [8] Shkrob I., Marin T. Charge trapping in photovoltaically active perovskites and related halogenoplumbate compounds. *J. Phys. Chem. Lett.*, 2014, **5**, P. 1066–1071.
- [9] Frost J., Butler K., Brivo F., et. al. Atomistic origins of high-performance in hybrid halide perovskite solar cells. arXiv: 1042.4980v3[Cond.-Mat.mtrl-sci] apl, 2014.
- [10] Sum T., Mathews N. Advancements in perovskite solar cells: photophysics behind the photovoltaics. *Energy and Environ. Sci.*, 2014, **7**, P. 2518–2534.
- [11] Graetzel M., Janssen R., Mitzi D., Sargent E.H. Materials interface engineering for solution-processed photovoltaics. *Nature*, 2012, **488**, P. 304–312.
- [12] Mueller J., Rech B., Springer J., Vanecek M. TCO and light trapping in silicon thin film solar cells. *Solar Energy*, 2004, **70**, P. 917–930.

- [13] Zheng L., Ma Y., Chu S., et al. Improved light absorption and charge transport for perovskite solar cells with rough interfaces by sequential deposition. *Nanoscale*, 2014, **6**, P. 8171–8176.
- [14] Jakeman E., in: Pietronero L., and Tosatti E., (ed.) *Fractals in Physics*. North Holland, Amsterdam-Oxford-New York-Tokyo, 1986, p. 82.
- [15] Flugge S. *Practical Quantum Mechanics I*, Springer-Verlag, Berlin-Heidelberg-New-York, 1971, 99 p.
- [16] Bohm D. *Quantum Theory*. Prentice-Hall Inc, New-York, 1952, 722 p.
- [17] Parilis E., Kishinevskiy L., Turaev N., et al. *Atomic Collisions on Solid Surfaces*. Elsevier Sci. Publ. North. Holl., Amsterdam, London, New York, Tokyo, 1993, 664 p.
- [18] Maksimov S.E., Oksengendler B.L. Turaev N.Yu. Synergetic Approach to Studying Material Sputtering under Ion Bombardment. *Journ. of Surf. Invest.*, 2013, **7** (2), P. 333–338.
- [19] Feder E. *Fractals*. Plenum Press, New York, 1988, 262 p.
- [20] Shewmon P.G. *Diffusion in solids*. McGraw-Hill Book Com., NY, San Francisco, Toronto, London, 1961, 189 p.
- [21] Yadav R.P., Kumar M., Mital A., et al. Fractal and multifractal characteristics of swift heavy ion induced self-affine nanostructured BaF₂ thin film surfaces. *Chaos*, 2015, **25**, P. 083115.
- [22] Oksengendler B.L., Maksimov S.E., Marasulov M.B. Degradation of perovskites and Dexter-Varley paradox. *Nanosystems: physics, chemistry, mathematics*, 2015, **6** (6), P. 825–832.
- [23] Tamm I.E. *Collection of scientific works in two volumes*. Moscow: Nauka, 1975, V.1. (in Russian)

Accelerated dynamics in adiabatically-tunable asymmetric double-well potential

I. Setiawan^{1,2,3}, B. E. Gunara¹, J. S. Kosasih¹ and K. Nakamura^{3,4}

¹Physics Department, Insitut Teknologi Bandung, Jalan Ganesha 10, Bandung 40132, Indonesia

²Physics Education Department, University of Bengkulu, Jalan WR, Supratman Kandang Limun, Bengkulu 38371, Indonesia

³Faculty of Physics, National University of Uzbekistan, Vuzgorodok, Tashkent 100174, Uzbekistan

⁴Department of Applied Physics, Osaka City University, Sumiyoshi-ku, Osaka 558-8585, Japan
isetiawan@unib.ac.id

PACS 03.65.Ge, 03.65.Vf

DOI 10.17586/2220-8054-2017-8-1-99-107

We study a scheme for the acceleration of adiabatic quantum dynamics. Masuda-Nakamura's theory of acceleration uses a strategy of combining two opposite ideas: infinitely-large time-magnification factor ($\bar{\alpha}$) and infinitely-small growth rate (ϵ) for the adiabatic parameter. We apply the proposed method to a system with a parameter-dependent asymmetric double-well potential which has no scale invariance, and obtain the electromagnetic field required to accelerate the system. The ground state wave function, initially localized in one well, quickly moves to another well. We investigate two kinds of ground-state wave functions: with and without space-dependent phase η . For the system with non-zero η , we show the fast-forward of the adiabatic change for current density distribution more clearly characterizes the well-to-well transport and is deformed as the finite renormalized time-multiplication factor ($\bar{v} = \epsilon\bar{\alpha}$) is varied.

Keywords: fast-forwarding, adiabatic quantum dynamics, asymmetric double-well potential.

Received: 14 July 2016

Revised: 2 September 2016

1. Introduction

The shorter production time in manufacturing products (e.g., electronics, automotives, plants, etc.) is becoming an important factor in nanotechnology. Currently, we can control even individual atoms [1] and macroscopic wave packets in BEC [2–5]. If we try to fabricate massive amounts of such nanoscale structures, we should shorten the dynamics of each atom or BEC to get its desired target states in shorter times. A theory to accelerate quantum dynamics is proposed by Masuda and Nakamura [6] with use of additional phase and driving potential. This theory aims to accelerate a known quantum evolution and to obtain the desired target states on shorter time scales, by fast forwarding the standard quantum dynamics. The theory of fast-forward can be developed to accelerate the adiabatic quantum dynamics [7], and constitutes one of the most promising means to obtain a shortcut to adiabaticity [8–14]. The relationship between the acceleration and the shortcut to adiabaticity is presently clear [15, 16]. Adiabaticity occurs when the external parameter of Hamiltonian is very-slowly changed. The quantum adiabatic theorem [17–21] states that if the system is initially in an eigenstate of the instantaneous Hamiltonian, it remains so during the adiabatic process. In section 2, we briefly summarize the theory of fast-forward of quantum adiabatic dynamics [6, 7].

2. The theory of fast-forward by Masuda and Nakamura

Let $\Psi_0(x, t)$ be a known function of space (x) and time (t). We shall call it a standard state. Let α the time magnification factor of the acceleration. Time evolution of the wave function (WF) is sped up if $\alpha > 1$ and slowed down if $0 < \alpha < 1$. In general α can be time dependent $\alpha = \alpha(t)$. The time evolution of the WF is accelerated and decelerated when $\alpha(t)$ is increases and decreases, respectively. The ideal accelerated state is defined as:

$$|\Psi_\alpha(t)\rangle \equiv |\Psi_0(\Lambda(t))\rangle, \quad (1)$$

where

$$\Lambda(t) = \int_0^t \alpha(t') dt', \quad (2)$$

but it proves difficult to realize $|\Psi_\alpha(t)\rangle$. Consequently, Nakamura and Masuda redefined the accelerated state with use of an additional phase factor $f(x, t)$ as:

$$|\Psi_{\text{FF}}(x, t)\rangle = \exp[i f(x, t)] |\Psi_\alpha(x, t)\rangle. \quad (3)$$

The dynamics for the standard state is assumed to be described by Schrödinger equation:

$$i\hbar \frac{d\Psi_0}{dt} = -\frac{\hbar^2}{2m_0} \nabla^2 \Psi_0 + V_0(x, t) \Psi_0. \quad (4)$$

The corresponding equation for the accelerated state is:

$$i\hbar \frac{d\Psi_{\text{FF}}}{dt} = -\frac{\hbar^2}{2m_0} \nabla^2 \Psi_{\text{FF}} + V_{\text{FF}} \Psi_{\text{FF}}, \quad (5)$$

where V_{FF} is the driving potential.

By using Eqs. (1)–(5), the expression for f and V_{FF} can be written, respectively, as:

$$f(x, t) = (\alpha(t) - 1)\eta(x, \Lambda(t)) \quad (6)$$

and

$$V_{\text{FF}} = V_0 - \hbar\eta \frac{d\alpha}{dt} - \hbar \frac{\alpha^2 - 1}{\alpha} \frac{\partial\eta}{\partial t} - \frac{\hbar^2}{2m_0} (\alpha^2 - 1)(\nabla\eta)^2, \quad (7)$$

where $\eta \equiv \eta(x, \Lambda(t))$ is the phase of the standard state Ψ_0 .

Next, we study the fast-forwarding of adiabatic quantum dynamics. Masuda and Nakamura [7] proposed a theory to accelerate the adiabatic quantum dynamics by using a combination of opposite ideas of infinitely-large time multiplication and infinitesimally-slow evolution rate of adiabatic dynamics, to generate the finite driving potential, by which we obtain the final adiabatic state in any desired short time. To apply the theory of accelerated standard dynamics, it is necessary to regularize the adiabatic state so that it satisfies the time-dependent Schrödinger equation. A regularized potential and WF is written a

$$V_0^{\text{reg}} = V_0 + \epsilon \tilde{V}(x, t), \quad (8)$$

$$\Psi_0^{\text{reg}}(x, t, R(t)) = \phi_n(x, R(t)) e^{(-i/\hbar) \int_0^t E_n(R(t')) dt'} e^{i\epsilon\theta(x, t)}, \quad (9)$$

where R is a time-dependent adiabatic parameter as:

$$R(t) = R(0) + \epsilon t \quad (10)$$

with $\epsilon \ll 1$, and: ϕ_n is the eigenstate of the time-independent Schrödinger equation,

$$H\phi_n = E_n\phi_n. \quad (11)$$

Formally, ϕ_n can be decomposed as:

$$\phi_n = \bar{\phi}_n e^{i\eta(x, t)}, \quad (12)$$

where $\bar{\phi}_n$ is a real positive amplitude and η is the phase. The Schrödinger equation for Ψ_0^{reg} is represented as:

$$i\hbar \frac{d\Psi^{\text{reg}}}{dt} = -\frac{\hbar^2}{2m_0} \nabla^2 \Psi^{\text{reg}} + V_0^{\text{reg}}(x, t) \Psi^{\text{reg}}. \quad (13)$$

Ψ_0^{reg} and V_0^{reg} are assumed to satisfy Eq. (13) up to $O(\epsilon)$. By substituting Eqs. (8), (9) and (12) into Eq. (13) and decomposing it into real and imaginary parts, we have θ and \tilde{V} as follows:

$$\bar{\phi}_n^2 \nabla^2 \theta + 2\bar{\phi}_n \nabla \bar{\phi}_n \nabla \theta + \frac{2m_0}{\hbar} \bar{\phi}_n \frac{\partial \bar{\phi}_n}{\partial R} = 0, \quad (14)$$

and

$$\tilde{V} = -\hbar(\partial_R \eta) - \frac{\hbar^2}{m_0} \nabla \eta \nabla \theta. \quad (15)$$

Here, θ can be solved as:

$$\nabla \theta = -\frac{m_0}{\hbar} \frac{1}{\bar{\phi}_n^2(x, R)} \frac{\partial}{\partial R} \int_{-\infty}^x \bar{\phi}_n^2(x', R) dx'. \quad (16)$$

Applying the general issue in Eqs. (6) and (7), we have:

$$f(x, t) = (\alpha(t) - 1)\epsilon\theta(x, R(\Lambda(t))). \quad (17)$$

With use of f in Eq. (17), the driving potential V_{FF} to realize fast-forward of adiabatic quantum dynamics can be written as:

$$\begin{aligned} V_{\text{FF}} = & -\alpha\epsilon\hbar(\partial_R \eta) - \alpha\epsilon \frac{\hbar^2}{m_0} \nabla \eta \nabla \theta \\ & -\hbar \frac{d\alpha}{dt} \epsilon\theta - \hbar\epsilon^2 \alpha^2 \frac{\partial\theta}{\partial R} - \frac{\hbar^2}{2m_0} \epsilon^2 \alpha^2 (\nabla\theta)^2 + V_0. \end{aligned} \quad (18)$$

The expression for driving electric field can be written as:

$$\begin{aligned} \hat{E}_{\text{FF}} \equiv & -\frac{\partial}{\partial x}(V_{\text{FF}} - V_0) = \hbar\epsilon\dot{\alpha}\nabla\theta + \hbar\epsilon^2\alpha^2\frac{\partial}{\partial R}(\nabla\theta) + \frac{\hbar^2}{m_0}(\alpha\epsilon)^2\nabla\theta\nabla^2\theta \\ & + \alpha\epsilon\hbar\partial_R(\nabla\eta) + \alpha\epsilon\frac{\hbar^2}{m_0}\nabla(\nabla\eta\nabla\theta). \end{aligned} \quad (19)$$

Taking the limit $\epsilon \rightarrow 0$, $\bar{\alpha} \rightarrow \infty$, with $\epsilon\bar{\alpha} = \bar{v}$, we can define $v(t)$ and $\dot{v}(t)$ as:

$$\alpha\epsilon = \bar{v}\left(1 - \cos\frac{2\pi t}{T_F}\right) \equiv v(t), \quad (20)$$

$$\dot{\alpha}\epsilon = \dot{v}(t). \quad (21)$$

Then, Ψ_{FF} becomes $\Psi_{\text{FF}} = \bar{\phi}_n e^{i(\eta+v(t)\theta)}$, and \hat{E}_{FF} is given by:

$$\begin{aligned} \hat{E}_{\text{FF}} = & \hbar\dot{v}(t)\nabla\theta + \hbar(v(t))^2\partial_R\nabla\theta + \frac{\hbar^2}{m_0}(v(t))^2\nabla\theta\nabla^2\theta \\ & + v(t)\hbar\partial_R(\nabla\eta) + v(t)\frac{\hbar^2}{m_0}\nabla(\nabla\eta\nabla\theta). \end{aligned} \quad (22)$$

The magnification factor α in Eq. (20) is commonly chosen for $0 \leq t \leq T_F$, where \bar{v} is the time average of $\alpha(t)\epsilon$ during the fast forwarding. The final time of the fast-forward T_F is related to the standard final time T as $T_F = \epsilon T/\bar{v}$, where T is taken as $T = 1/\epsilon (\gg 1)$ and $R(T) - R(0) = 1$.

The driving electric field (\hat{E}_{FF}) guarantees the fast-forward of adiabatic quantum dynamics [22]. Recently, Nakamura et al. [23] suggested a new theory for the fast-forwarding of the adiabatic dynamics without the additional phase f . But the present and new theories are compatible by using the gauge transformation as shown in Appendix A.

3. Accelerated dynamics in adiabatically tunable-asymmetric double-well potential: case of $\tilde{V} = 0$

We show the acceleration of the adiabatic quantum dynamics with use of a parameter-dependent asymmetric double-well potential, which does not satisfy the scale invariance such as dilation or translation invariance. Let's define the zero energy ($E_0 = 0$) eigen-function which is a superposition of a pair of Gaussian functions with their center at $x = 0$ and $x = d$, where d represents the distance between the two wells. To be explicit:

$$\Psi_0 = h(R) \left[(1 - R)e^{-\frac{x^2}{2a}} + Re^{-\frac{(x-d)^2}{2a}} \right], \quad (23)$$

changing in the range $0 \leq R \leq 1$. The potential $V_0(x)$ to realize Ψ_0 is written by:

$$V_0(x) \equiv \frac{\hbar^2}{2m} \frac{\Psi_0''}{\Psi_0} = \frac{\hbar^2}{2m_0} \left[-\frac{1-R}{a} \left(1 - \frac{x^2}{a}\right) - \frac{R}{a} \left(1 - \frac{(x-d)^2}{a}\right) f(x) \right] \times \frac{1}{(1-R) + Rf(x)}, \quad (24)$$

with $f(x) = e^{\frac{d}{a}(x-\frac{d}{2})}$. The normalization factor $h(R)$, determined by $\int_{-\infty}^{\infty} |\Psi|^2 = 1$, is given by:

$$h(R) = \frac{1}{(\pi a)^{1/4}} \left(1 - 2R + 2R^2 + 2R(1-R)e^{-\frac{d^2}{4a}} \right)^{-1/2}. \quad (25)$$

Figures 1 and 2 show the change of the potential and wave function for various values of R , between $R = 0$ and $R = 1$. As the potential minimum moves from $x = 0$ to $x = d$, the center-of-mass of WF also moves in the same direction. Fig. 3 shows the probability amplitude $|\Psi_0|^2$ in the adiabatic dynamics with $R(t) = \epsilon t$. Fig. 4 shows $|\Psi_{\text{FF}}|^2$ in the fast-forwarded adiabatic dynamics, where $R(\Lambda(t))$ is written as:

$$R(\Lambda(t)) = \epsilon \int_0^t \alpha(t') dt' = \int_0^t v(t') dt' = \bar{v} \left(t - \frac{T_F}{2\pi} \sin \frac{2\pi t}{T_F} \right). \quad (26)$$

The adiabatic standard dynamics evolves up to the final time $T = 10^2$ with use of $\epsilon = 10^{-2}$ and its accelerated version up to the shortened final time $T_F = T/\bar{\alpha} = \epsilon T/\bar{v} = 0.025$ with use of the mean acceleration factor $\bar{\alpha} = 4 \times 10^3$ and mean velocity $\bar{v} = \bar{\alpha}\epsilon = 40$.

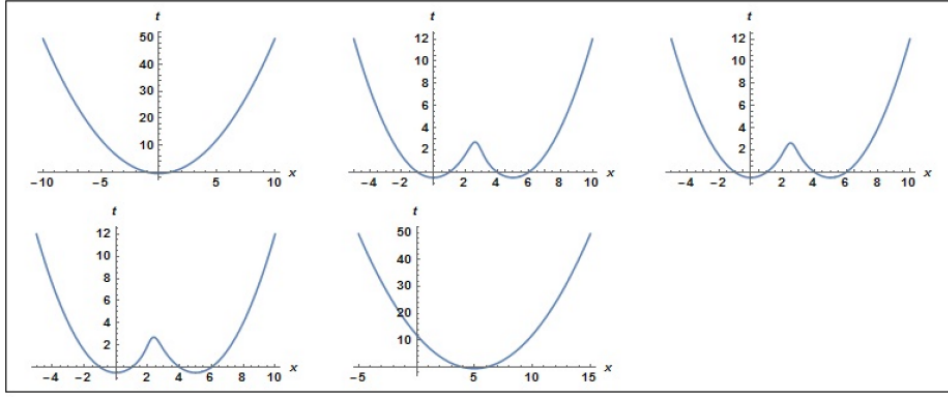


FIG. 1. The change of $V_0(x)$ with various values of R : $R = 0 \rightarrow 0.25 \rightarrow 0.5 \rightarrow 0.75 \rightarrow 1$ (from top left to bottom right), $d = 5$

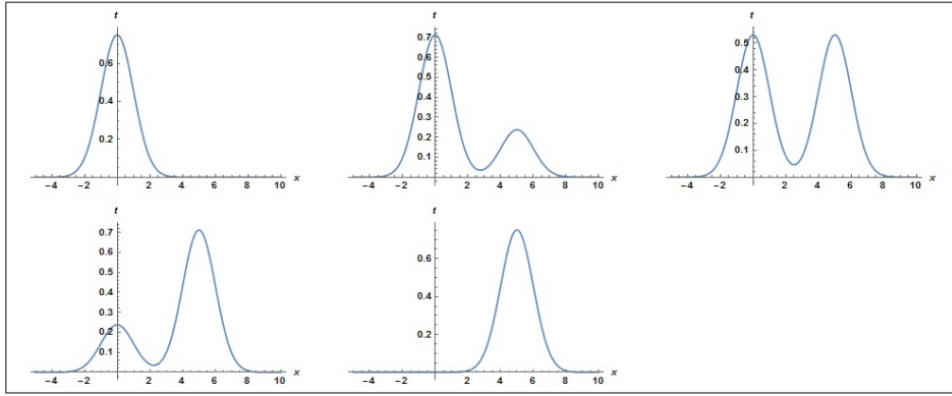


FIG. 2. The change of probability amplitude $|\Psi_0(x)|$ with various values of R : $R = 0 \rightarrow 0.25 \rightarrow 0.5 \rightarrow 0.75 \rightarrow 1$, $d = 5$

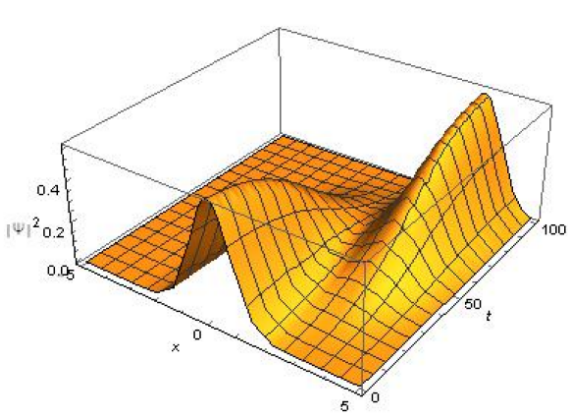


FIG. 3. 3D plot of $|\hat{\Psi}|^2$ with $\epsilon = 10^{-2}$, $T = 100$, $a = 1$, and $d = 3$

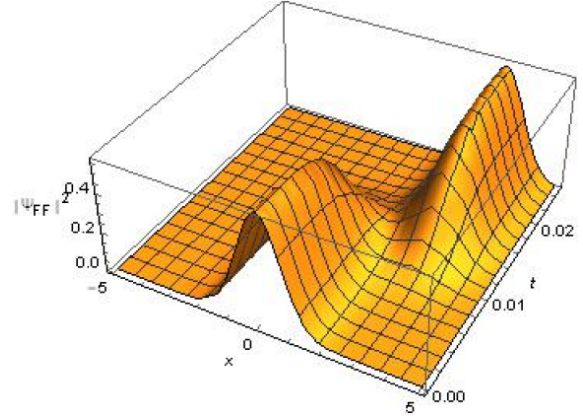


FIG. 4. 3D plot of $|\hat{\Psi}_{FF}|^2$ with $T_F = T/\bar{\alpha} = 0.025$

From Eqs. (16), $\nabla\theta$ is given by:

$$\nabla\theta = -\frac{1}{2}(\pi a)^{1/2} \left[\frac{\kappa}{\left((1-R)e^{-\frac{x^2}{2a}} + Re^{-\frac{(x-d)^2}{2a}} \right)^2} - \frac{(-2+4R+(2-4R)e^{-\frac{d^2}{4a}})\mu}{\left((1-R)e^{-\frac{x^2}{2a}} + Re^{-\frac{(x-d)^2}{2a}} \right)^2 g} \right], \quad (27)$$

with

$$\begin{aligned}\kappa &= (2 - 4R)e^{-\frac{d^2}{a}} \operatorname{erfc}\left(-\frac{x - \frac{d}{2}}{\sqrt{a}}\right) + 2R \operatorname{erfc}\left(-\frac{x - d}{\sqrt{a}}\right) + (2R - 2) \operatorname{erfc}\left(-\frac{x}{\sqrt{a}}\right), \\ \mu &= \left(2R(1 - R)e^{-\frac{d^2}{a}} \operatorname{erfc}\left(-\frac{x - \frac{d}{2}}{\sqrt{a}}\right) + R^2 \operatorname{erfc}\left(-\frac{x - d}{\sqrt{a}}\right) + (1 - R)^2 \operatorname{erfc}\left(-\frac{x}{\sqrt{a}}\right)\right),\end{aligned}$$

and

$$g = \left(2(1 - R)Re^{-\frac{d^2}{4a}} + 2R^2 - 2R + 1\right),$$

where the complimentary error function erfc is :

$$\operatorname{erfc}(x) = \frac{2}{\sqrt{\pi}} \int_x^{\infty} e^{-t^2} dt. \quad (28)$$

The driving electric field (\hat{E}_{FF}) to generate the acceleration is calculated by Eq. (22) and is shown in Fig. 5.

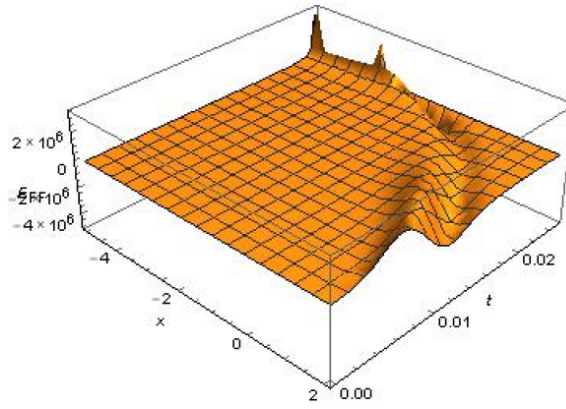


FIG. 5. \hat{E}_{FF} with $T_F = 0.025$

4. The case of $\tilde{V} \neq 0$

In the previous example, the right-hand side of Eq. (15) was always vanishing, because of the absence of a space-dependent phase η in the standard WF. In many practical cases, we have an adiabatic state with a space-dependent phase η . Choosing again the asymmetric double-well potential, we shall investigate the fast-forwarding with non-zero \tilde{V} by having recourse to a stationary state with a phase η . Here, the adiabatic state with the eigenvalue $E_{n=0} = 0$ is chosen as:

$$\Psi_0 = h(R) \left[(1 - R)e^{-\frac{x^2}{2a}} + Re^{-\frac{(x-d)^2}{2a}} \right] e^{i\eta}, \quad (29)$$

with η given as:

$$\eta = B \int_{-\infty}^x \exp \left[-\frac{1}{h(R) \left((1 - R)e^{-\frac{x^2}{2a}} + Re^{-\frac{(x-d)^2}{2a}} \right)^2} \right], \quad (30)$$

where B is a real constant. The potential that guarantees the eigenstate in Eq. (29) is written as:

$$\begin{aligned}V_0(x) &= \frac{\hbar^2}{2m_0} \left[\left(-\frac{1 - R}{a} \left(1 - \frac{x^2}{a} \right) - \frac{R}{a} \left(1 - \frac{(x-d)^2}{a} \right) f(x) \right) \right. \\ &\quad \left. \times \frac{1}{(1 - R) + Rf(x)} + \frac{1}{2} \exp \left(-\frac{1}{h(R) \left((1 - R)e^{-\frac{x^2}{2a}} + Re^{-\frac{(x-d)^2}{2a}} \right)^2} \right) \right],\end{aligned} \quad (31)$$

with $f(x) = e^{\frac{d}{a}(x - \frac{d}{2})}$, and $h(R)$ being given in Eq. (25). Eq. (31) is available from Eq. (24) by adding an extra term. $\nabla\theta$, which appears in the regularization procedure, is the same as in Eq. (27) because of the formula Eq. (16). From Eqs. (15) and (29), \tilde{V} is written as:

$$\begin{aligned} \tilde{V} = & -\hbar \frac{\partial}{\partial R} \left(B \int_{-\infty}^x \exp \left[-\frac{1}{h(R) \left((1-R)e^{-\frac{x^2}{2a}} + Re^{-\frac{(x-d)^2}{2a}} \right)^2} \right] \right) \\ & - \frac{\hbar^2}{m_0} B \exp \left[-\frac{1}{h(R) \left((1-R)e^{-\frac{x^2}{2a}} + Re^{-\frac{(x-d)^2}{2a}} \right)^2} \right] \nabla \theta. \end{aligned} \quad (32)$$

Figures 6 and 7 show the amplitude of the standard wave function and its fast-forward version with $\eta \neq 0$, respectively. \hat{E}_{FF} is evaluated by Eqs. (22), and is depicted in Fig. 8. We see no big difference of fast forward between the cases with $\eta = 0$ and $\eta \neq 0$.

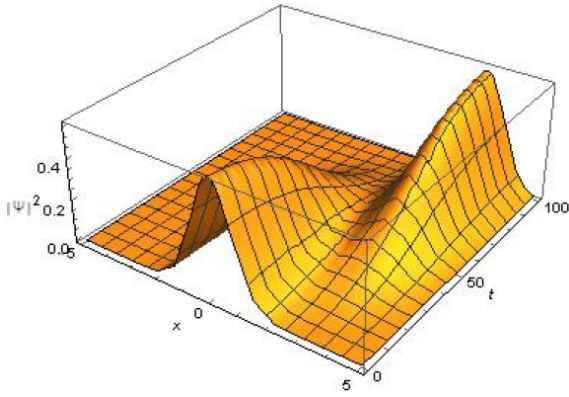


FIG. 6. 3D plot of $|\hat{\Psi}|^2$ with $\eta \neq 0$ and $B = 1$

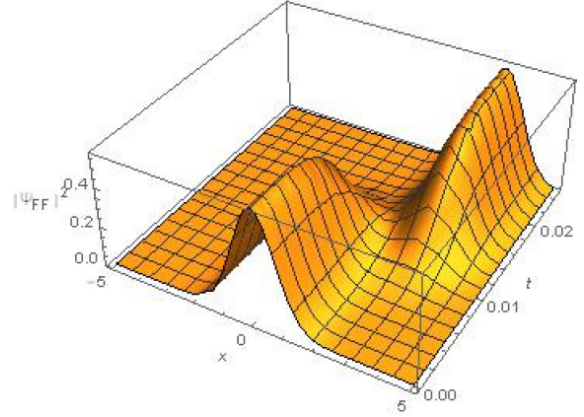


FIG. 7. 3D plot of $|\hat{\Psi}_{\text{FF}}|^2$ with $\eta \neq 0$, $T_F = T/\bar{\alpha} = 0.025$ and $B = 1$

The present scheme also introduces a current density j_{FF} . We see:

$$j_{\text{FF}}(x, t) = \text{Re} \left[\Psi_{\text{FF}} \frac{\hbar}{im} \nabla \Psi_{\text{FF}} \right] = \frac{\hbar}{m} \bar{\phi}_n^2(x, \Lambda(t)) [\nabla \eta(x, \Lambda(t)) + v(t) \nabla \theta(x, \Lambda(t))], \quad (33)$$

$$j(x, t) = \frac{\hbar}{m} \bar{\phi}_n^2(x, t) \nabla \eta(x, t), \quad (34)$$

and find the relationship:

$$j_{\text{FF}}(x, t) = j(x, \Lambda(t)) + \frac{\hbar}{m} v(t) \bar{\phi}_n^2(x, \Lambda(t)) \nabla \theta(x, \Lambda(t)). \quad (35)$$

Thus, j_{FF} has a non-adiabatic current in addition to the adiabatic one $j(x, \Lambda(t))$. Figs. 9 and 10 show the adiabatic current density and fast-forward current density respectively. We find : the adiabatic current density distribution in Fig. 9 is radically changed by the fast forwarding. This change, in particular, the increase of the current intensity becomes more marked as the control parameter \bar{v} associated with the fast forwarding is increased (see Fig. 10). At the end of the fast forwarding, the non-adiabatic current vanishes.

The asymmetric double-well potential in the present paper breaks the scale invariance. In the case of a scale-invariant single well, Lewis-Riesenfeld's invariant method [11] can also lead to the accelerated dynamics, which will be discussed in Appendix B.

5. Conclusion

The Masuda-Nakamura's scheme of accelerated adiabatic quantum dynamics is applied to the system with a tunable asymmetric double-well potential and the driving electric field is obtained. The potential here has no scale invariance. A combination of opposite ideas of infinitely-large time multiplication and infinitesimally-slow adiabatic dynamics generates a finite driving potential, by which we obtain the final adiabatic state in any desired short time. We investigated two kinds of ground state wave functions, with and without the space-dependent phase η . For the system with non-zero η , we see that the fast-forward of current density acquires a non-adiabatic

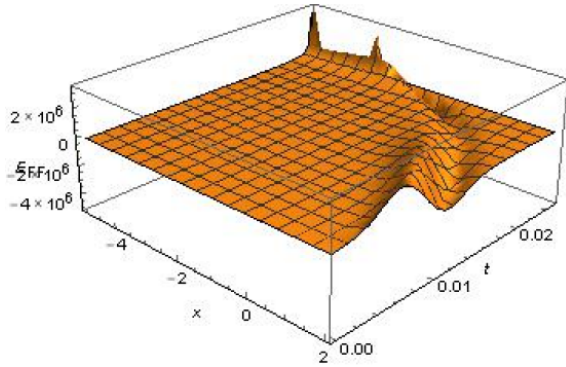


FIG. 8. \hat{E}_{FF} with $\eta \neq 0$, $T_F = T/\bar{\alpha} = 0.025$ and $B = 1$

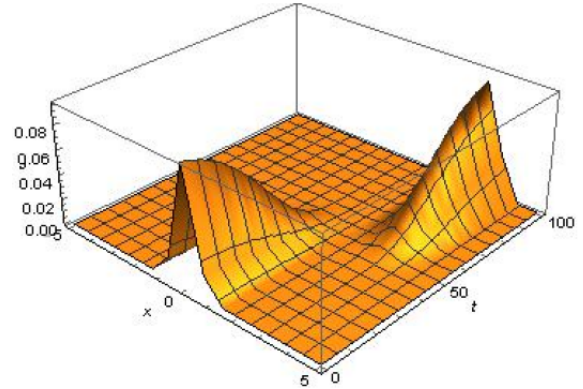


FIG. 9. 3D plot of j with $B = 1$

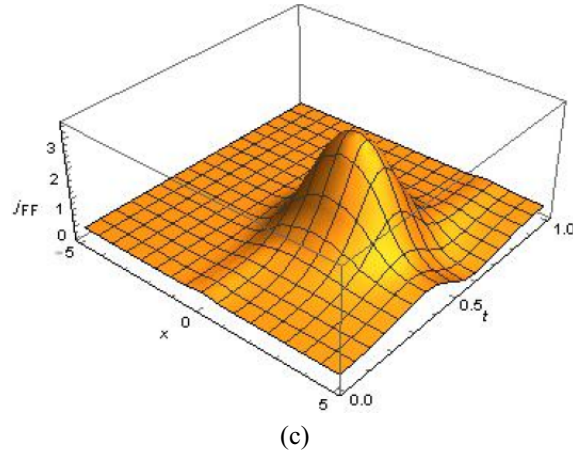
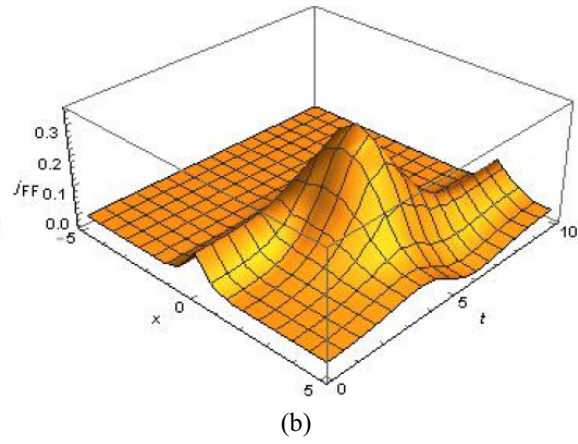
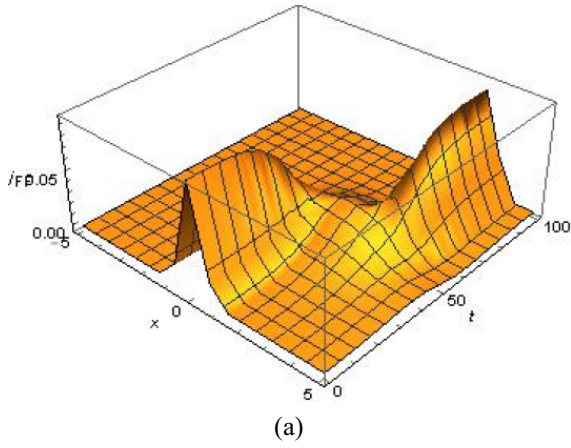


FIG. 10. 3D plot of j_{FF} with $\eta \neq 0$ and $B = 1$: (a) $\bar{\alpha} = 1$, $\bar{v} = 0.01$, $T_F = 100$; (b) $\bar{\alpha} = 10$, $\bar{v} = 0.1$, $T_F = 10$; (c) $\bar{\alpha} = 10^2$, $\bar{v} = 1$, $T_F = 1$

contribution besides the adiabatic current density and that the current intensity radically grows as the control parameter associated with fast forwarding is increased.

Acknowledgements

This work is funded by Riset KK ITB 2015–2016 and Hibah Desentralisasi ITB 2015–2016. I. S. is grateful to Prof. Davron Matrasulov for his great hospitality at Turin Polytechnical University at Tashkent.

Appendix A. Gauge transformation to the scheme without the additional phase

Let's consider the gauge transformation as follows :

$$\begin{aligned}\Psi_{\text{FF}} &\rightarrow \hat{\Psi}_{\text{FF}} e^{i\zeta} \\ V_{\text{FF}} &\rightarrow \hat{V}_{\text{FF}} - \frac{\hbar}{q} \dot{\zeta} \\ A_{\text{FF}} (= 0) &\rightarrow \hat{A}_{\text{FF}} + \frac{\hbar c}{q} \nabla \zeta,\end{aligned}$$

with

$$\zeta = \epsilon \alpha(t) \theta(x, R(\Lambda(t))) \quad (\text{A.1})$$

Then, the Schrödinger equation becomes that of a charge particle under the gauge potentials \hat{A}_{FF} and \hat{V}_{FF} :

$$i\hbar \frac{\partial \hat{\Psi}_{\text{FF}}}{\partial t} = \frac{1}{2m_0} \left(\frac{\hbar}{i} \nabla - \frac{q}{c} \hat{A}_{\text{FF}} \right)^2 \hat{\Psi}_{\text{FF}} + q \hat{V}_{\text{FF}} \hat{\Psi}_{\text{FF}}. \quad (\text{A.2})$$

The wave function becomes free from the additional phase :

$$\hat{\Psi}_{\text{FF}} = \phi_n(x, R(\Lambda(t))), \quad (\text{A.3})$$

and the scalar and vector potential are given by:

$$\hat{V}_{\text{FF}} = -\frac{\hbar^2}{2m_0} \epsilon^2 \alpha^2 (\nabla \theta)^2 - \alpha \epsilon \hbar (\partial_R \eta) - \alpha \epsilon \frac{\hbar^2}{m_0} \nabla \eta \nabla \theta, \quad (\text{A.4})$$

$$\hat{A}_{\text{FF}} = -\hbar \epsilon \alpha \nabla \theta \quad (\text{A.5})$$

respectively. Equations (A.2)–(A.5) are nothing but the scheme proposed in Ref. [23].

Appendix B. Relationship between Masuda-Nakamura's scheme and Lewis-Riesenfeld method

Let us consider the Hamiltonian for single well potential:

$$H = \frac{\hat{p}^2}{2m} + \frac{1}{2} m \omega^2(t) \hat{x}^2, \quad (\text{B.1})$$

where ω is a time-dependent parameter. The wave function at any time t can be deduced from Lewis-Riesenfeld theory of invariants [11]. By assuming the existence of a Hermitian invariant of the homogeneous, its quadratic form is given by:

$$I(t) = \frac{1}{2} [\alpha(t) \hat{x}^2 + \beta(t) \hat{p}^2 + \gamma(t) (\hat{x} \hat{p} + \hat{p} \hat{x})], \quad (\text{B.2})$$

where α , β , and γ are real function of time. $I(t)$ should satisfy the conditions:

$$\frac{dI}{dt} = \frac{\partial I}{\partial t} + \frac{1}{i\hbar} [I, H] = 0. \quad (\text{B.3})$$

In order to satisfy Eq. (B.3), it is convenient to introduce another function $\sigma(t)$, defined by:

$$\beta(t) = \sigma^2(t), \quad (\text{B.4})$$

where $\sigma^2(t)$ is a real function of time. By making the scale transformation $\sigma(t) = c^{1/4} \rho(t)$, the invariant may be written in the form:

$$I = \frac{1}{2} m \omega_0^2 (1/\rho^2) \hat{x}^2 + \frac{1}{2m} (\rho \hat{p} - m \dot{\rho} \hat{x})^2. \quad (\text{B.5})$$

Here, c is an arbitrary constant of integration and ρ satisfies the Ermakov equation:

$$\ddot{\rho} + \omega^2(t) \rho - \frac{\omega_0^2}{\rho^3} = 0. \quad (\text{B.6})$$

The eigenstates and the eigenvalues of the invariant operator $I(t)$ may be found by an operator technique. Thus the dynamical phase function may be written in the form:

$$\alpha_n(t) = -\frac{i}{\hbar} \left(n + \frac{1}{2} \right) \int_0^t dt' \frac{1}{\rho^2(t')}. \quad (\text{B.7})$$

For the Hamiltonian in Eq. (B.1), the general solution of time-dependent Schrödinger equation can be expanded as a linear combination with eigenvectors ψ_n of I as:

$$\psi(x, t) = \sum_n c_n e^{i\alpha_n} \psi_n(x, t) = \sum_n c_n \psi_n(x, t) e^{-\frac{i}{\hbar} (n + \frac{1}{2}) \int_0^t dt' \rho^{-2}(t')}. \quad (\text{B.8})$$

Formally ψ_n can be decomposed as $\psi_n = \bar{\psi}_n e^{i\zeta}$, where $\zeta = \frac{m}{2\hbar} \frac{\dot{\rho}}{\rho} x^2$.

By using ω in Eq. (B.6), the potential for the single well in Eq. (B.1) can be written as:

$$V(x, t) = \frac{1}{2} m \left[\frac{\omega_0^2}{\rho^4(t)} - \frac{\ddot{\rho}}{\rho(t)} \right] x^2. \quad (\text{B.9})$$

The corresponding V_0 is:

$$V_0(x, t) = \frac{1}{2} m \frac{\omega_0^2}{\rho^4(t)} x^2. \quad (\text{B.10})$$

Applying Eq. (16) to the adiabatic eigenstate of Eq. (B.1), we can show the equality:

$$\zeta = \epsilon \alpha(t) \theta(x, R(\Lambda(t))) = \frac{m}{2\hbar} \frac{\dot{\rho}}{\rho} x^2, \quad (\text{B.11})$$

where $\Lambda(t) = \int_0^t \alpha(t') dt'$. By making space and time derivatives of Eq. (B.11), the potential in Eq. (B.9) can be written as:

$$V(x, t) = V_0 - \hbar \frac{d\alpha}{dt} \epsilon \theta - \hbar \epsilon^2 \alpha^2 \frac{\partial \theta}{\partial R} - \frac{\hbar^2}{2m} \epsilon^2 \alpha^2 (\nabla \theta)^2, \quad (\text{B.12})$$

which is nothing but V_{FF} in Eq. (18) in the case $\eta = 0$. Therefore, Lewis-Riesenfeld scheme is equivalent to Masuda-Nakamura's. In contrast with [12] and [15], $\alpha(t)$ is an arbitrary and experimentally-accessible time scaling factor and is not necessary to satisfy the Ermakov equation with 6 boundary conditions. Besides this advantage, the Masuda-Nakamura's scheme is applicable to any kind of scale-noninvariant potentials.

References

- [1] Eigler D.E., Schweizer E.K. Positioning single atoms with a scanning tunnelling microscope. *Nature (London)*, 1994, **344**, P. 524.
- [2] Legget A.J., Schweizer E.K. Bose-Einstein condensation in the alkali gases: Some fundamental concepts. *Rev. Mod. Phys.*, 2001, **73**, P. 307.
- [3] Ketterle W. Nobel lecture: When atoms behave as waves: Bose-Einstein condensation and the atom laser. *Rev. Mod. Phys.*, 2002, **74**, P. 1131.
- [4] Learnhardt A.E., Chikkatur A.P., et al. Propagation of Bose-Einstein Condensates in a Magnetic Waveguide. *Phys. Rev. Lett.*, 2002, **89**, P. 040401.
- [5] Gustavson T.L., Chikkatur A.P., et al. Transport of Bose-Einstein Condensates with Optical Tweezers. *Phys. Rev. Lett.*, 2001, **88**, P. 020401.
- [6] Masuda S., Nakamura K. Fast-forward problem in quantum mechanics. *Phys. Rev. A*, 2008, **78**, P. 062108.
- [7] Masuda S., Nakamura K. Fast-forward of adiabatic dynamics in quantum mechanics. *Proc. R. Soc. A*, 2010, **466**, P. 1135-1154.
- [8] Demirplak M., Rice S.A. Adiabatic population transfer with control fields. *J. Phys. Chem. A*, 2003, **89**, P. 9937.
- [9] Demirplak M., Rice S.A. Assisted adiabatic passage revisited. *J. Phys. Chem. B*, 2005, **109**, P. 6838.
- [10] Berry M.V. Transitionless quantum driving. *J. Phys A: Math. Theor.*, 2009, **42**, P. 365303.
- [11] Lewis H.R., Riesenfeld W.B. An exact quantum theory of the time-dependent harmonic oscillator and of a charged particle in a time-dependent electromagnetic field. *J. Math. Phys. A*, 1969, **10**, P. 1458.
- [12] Chen X., Ruschhaupt A., et al. Fast optimal frictionless atom cooling in a harmonic trap: Shortcut to adiabaticity. *Phys. Rev. Lett.*, 2010, **104**, P. 063002.
- [13] Torrontegui E., Ibanez M., et al. Shortcut to adiabaticity. *Adv. At. Mol. Opt. Phys.*, 2013, **62**, P. 117.
- [14] Masuda S., Nakamura K., del Campo A. High-fidelity rapid ground-state loading of an ultracold gas into an optical lattice. *Phys. Rev. Lett.*, 2014, **113**, P. 063003.
- [15] Torrontegui E., Martinez-Garaot M., Ruschhaupt A., Muga J.G. Shortcut to adiabaticity: fast-forward approach. *Phys. Rev. A*, 2012, **86**, P. 013601.
- [16] Takahashi K. Fast-forward scaling in a finite-dimensional Hilbert space. *Phys. Rev. A*, 2014, **89**, P. 042113.
- [17] Kato T. On the Adiabatic Theorem of Quantum Mechanics. *J. Phys. Soc. Jpn.*, 1950, **5**, P. 435.
- [18] Messiah A. *Quantum Mechanics 2*. North-Holland, Amsterdam, 1962.
- [19] Berry M.V. Quantal Phase Factors Accompanying Adiabatic Changes. *Proc. R. Soc. London*, 1984, **392**, P. 45.
- [20] Aharonov Y., Anandan J. Phase change during a cyclic quantum evolution. *Phys. Rev. Lett.*, 1987, **58**, P. 1593.
- [21] Berry M.V. Geometric Amplitude Factors in Adiabatic Quantum Transitions. *Proc. R. Soc. London Ser. A*, 1990, **430**, P. 405.
- [22] Khujakulov A., Nakamura K. Scheme for accelerating quantum tunneling dynamics. *Phys. Rev. A*, 2016, **93**, P. 022101.
- [23] Nakamura K., Khujakulov A., et al. Fast forward of adiabatic control of tunneling states. Preprint submitted for publication.

Equilibrium properties of 3-arm star-shaped polyions: an entropic sampling Monte Carlo study

I. A. Silanteva¹, A. A. Yurchenko¹, P. N. Vorontsov-Velyaminov¹, A. P. Lyubartsev²

¹St. Petersburg State University, Universitetskaya nab., 7/9, St. Petersburg, 199034, Russia

²Stockholm University, Svante Arrhenius väg 16, Stockholm, 10691, Sweden

i.silanteva@spbu.ru, sila3@yandex.ru

PACS 02.70.-c, 02.70.Uu, 05.10.Ln, 05.70.-a, 05.70.Fh, 07.05.Tp, 36.20.-r, 36.20.Hb, 64.60.-i, 64.70.Nd, 64.70.km, 64.70.pj, 65.40.Ba, 65.80.+n, 81.07.Nb, 82.20.Wt, 82.35.Lr, 87.10.Rt, 87.15.ak, 87.16.aj, 87.53.Wz, 87.55.K

DOI 10.17586/2220-8054-2017-8-1-108-120

The entropic sampling Monte Carlo method within Wang-Landau algorithm is applied to investigate properties of a lattice model of strongly charged flexible 3-arm star-shaped polyelectrolyte. The density of states is calculated, from which the canonical properties of the system in a wide temperature range are obtained by simple integration. The effects of the arm length and the short-range monomer-monomer potential on the thermal and structural properties of star polyions are studied. We calculate such characteristics as mean square radius of gyration and its components, the radius vector of the center of mass, components of the tensor of inertia and parameters characterizing the shape of the polyion. In this work, we focus on how these characteristics are influenced by the change of the reduced temperature which, within the considered model, is a parameter combining the effect of real temperature, linear charge density and solvent dielectric permittivity. The coil-globule transition is observed in most of the considered cases, and for the polyions with the longest length of arms (24), the transition from a liquid globule to a solid-like state is observed. Comparison of polyelectrolyte models with neutral ones is given.

Keywords: star-shaped polymer, polyelectrolytes, lattice model, entropic sampling, Monte Carlo method, phase transition, solvent quality.

Received: 10 January 2017

Revised: 23 January 2017

1. Introduction

Recently, polyelectrolytes having star-like architecture have attracted significant attention being actively investigated by using both experimental [1–4] and theoretical [5–14] methods. These macromolecules are widely used in various fields of nanotechnology, for example as a template for the synthesis of nanoparticles [15] or as emitting devices [16–18]. Charged macromolecules easily interact through electrostatic forces with negatively charged DNA, forming stable complexes for further transporting it into a living cell. They may also be used in another area of biomedicine, particularly in diagnostics and tissue engineering, as antibacterial substances and implant materials [19]. So the investigation of such macromolecules is certainly an important issue.

Star polymers are the simplest among the branched ones. It is known that they are qualitatively different from their linear analogs: the increase of branching leads to an increase in the average concentration of monomers within the macromolecule [20–22]. Therefore, the volume effects for branched polymers are more significant than in the case of linear chains. The properties of stars with a small number of arms are close to those of linear polymers. With an increasing number of arms, the molecule approaches a spherical shape, and its properties become closer to those of nanoparticles. While uncharged models have been sufficiently studied, there is still a lack of understanding in the area of polyelectrolytes. There are at least two specific features of charged polymers in comparison with uncharged ones. First, electrostatic interactions are long-ranged, and secondly, the presence of counterions provides osmotic pressure.

Experiments deal mainly with the polydisperse systems with no clearly defined architecture; from these data, it is difficult to obtain the information on the microscopic state of the macromolecules. Analytical description of star shaped polymers is made difficult by their complex architecture, and is often based on simplifying assumptions; e.g. there exist quasi-planar and nonlocal theories [11] based on the assumption that all the ends of arms are fixed on a certain outer surface. Therefore, in this case, computer simulation methods such as molecular dynamics (MD) or Monte Carlo (MC) appear to be very helpful [5–10].

Investigation of equilibrium conformational properties of polyelectrolytes by standard Monte Carlo or molecular dynamics methods may suffer ergodicity problems due to steric hindrance for a polymer chain to cross another polymer chain. This makes achieving of equilibrium canonical distribution more difficult; evidently for star

polymers the problem becomes more severe with increasing the number of arms. In previous works, we have shown that the entropic sampling Monte Carlo method [23–25], modified for polymer simulations [26,27], provides the possibility to investigate conformational and thermodynamic properties of neutral polymers [26], polyelectrolyte chains [27] and uncharged star-shaped polymers [28,29] in a wide temperature range.

The major aim of our study is to use this advanced sampling method to explore equilibrium properties of the star-branched polyelectrolyte over a wide possible range of temperatures within a simple lattice model [26,27], and obtain insight how the length of arms, the monomer-monomer interactions in the polyion and the concentration of the whole system determine its thermal and structural properties. An additional advantage of the used approach is that it provides a means for obtaining results over a wide range of temperatures, including the area of possible structural transitions in a single computer run. Our independent data could be compared with the existing results of other authors obtained using different approaches [9, 11, 22, 30].

The outline of the paper is as follows: description of the model and of the used method is given in sections 2. Section 3 presents the results of research and discussion for two sets of data: a polyion with various length of arms and a polyion with various short-range monomer-monomer interactions. The conclusions are presented in the last, fourth, section.

2. Model and Method

Though lattice models were introduced some time ago, they still have not lost their relevance [31–35]. On the one hand, simple models allow us to run simulations quickly and efficiently, on the other hand absence of chemical details gives possibility to get insight into underlying physical background of the studied phenomena. In this study the model of flexible star shaped polyion on a simple cubic lattice with the lattice constant $a = 1$ is considered. This model was originally proposed in paper [36] and later used in work [27] to study the equilibrium behavior of a polyelectrolyte chain. In our case, the star shaped polyion (for convenience, we shall call it simply a “star”) is located in a cubic cell of the size d with periodic boundary conditions imposed. The regular star consists of f arms, each of which includes N_{arm} monomers; here, we limit ourselves by the cases of $f = 3$. The monomers are located at the lattice sites and are connected to each other in a proper way by rigid bonds of a unit length. The total number of monomers per polyion is $N = fN_{\text{arm}} + 1$, i. e. the arms’ monomers plus the central monomer connecting all the arms and fixed in the center of the periodic cell. We limit ourselves to cases when each monomer carries unchangeable (quenched) unit charge; although, if necessary, the simulation of a partially ionized molecule is also possible. In order to maintain electroneutrality in the cell, N ions (counterions), carrying unit charges of the opposite sign are also present and they can move freely within the cell. The counterions are located on sites of the lattice shifted by the vector $(0.5, 0.5, 0.5)$ relative to the lattice of the polyion location. This excludes overlaps of counterions with the polyion and hence makes the MC procedure more efficient. It should also be noted that the minimal distance of a counterion and a monomer is $\sqrt{3}/2 = 0.866$ while the minimal distance for monomer-monomer and counterion-counterion is 1.

The volume interactions are taken into account while modeling of the polyelectrolyte by forbidding any two monomer units, or any two ions to occupy the same lattice site. However, during the simulation, we allow the star’s monomers to overlap with each other (phantom random walks [37]), as well as overlaps of the mobile counterions, in order to improve sampling. This way, the system achieves compact conformations with extremely low probabilities but still contributing to the canonical averages at low temperatures, due to low energy of these conformations. The overlapping conformations are then excluded from the canonical averaging to obtain the correct statistics for the conformations without overlaps (intersections), according to the procedure described below.

Monomers of the polyion and counterions interact through Coulomb potential $U(r_{ij}) = q_i q_j / r_{ij}$, where q_i and q_j are charges and r_{ij} the distances between them. Thus, the energy of the entire system consists of three components: repulsion between the monomers of the polyion, repulsion between the counterions and attraction between monomers and counterions. All distances are measured in the lattice constant units a , the energy is expressed in units of $E_0 = e^2 / (\epsilon a)$, the temperature is in units of $e^2 / (\epsilon a k_B)$ where e is the elementary charge, ϵ is the dielectric constant of the solution, k_B is Boltzmann constant. So for the temperature in our units we have:

$$T = k_B T_K / E_0, \quad (1)$$

where T_K is temperature in Kelvins.

Let us determine the typical temperature range for aqueous solutions of a real polyelectrolyte system. If the lattice constant is taken equal to the distance between charged groups on the polyelectrolyte chain (for example, 2.8 Å for polyacrylic acid), dielectric constant for water is $\epsilon = 80$, the temperature $T_K = 293$ K would yield $T = 0.39$. Actually, ϵ of water decreases with temperature so that product ϵT_K shows a weak decrease with temperature also, that is why the increase of real temperature T_K in aqueous solution leads to some decrease of

the reduced temperature T . The dielectric permittivity can be also changed by addition of other organic solvents, and the polyelectrolyte linear charge density can be changed by pH of the solution. To summarize, the reduced temperature T of our model is a parameter expressing the collective effect of the polyion charge density, real temperature and properties of the solvent, with typical values 0.3–0.7 for strong polyelectrolytes and with higher values for weaker polyelectrolytes.

In order to present a complete picture of behavior for our model system we are going to obtain dependencies over a much broader temperature range so that we can see how our data are tending to athermal limits. Though not all the temperature range in which the results would be obtained and presented further is achievable in a real laboratory experiment. In order to take into account the long-range electrostatic interactions in presence of periodic boundary conditions the minimal image convention was used in calculating them. It was shown in [27] that it gives for our model the same result as the Ewald summation [38] over a wide range of parameters.

The quality of the solvent, defined by the parameter $\chi = \tilde{z}\Delta w_{12}/k_B T$, [39], where \tilde{z} is the number of nearest neighbors in the model, Δw_{12} is the change of energy in the formation of a contact polymer-solvent in the solution, such interaction also is straightforwardly included into our model (See part 3.2). It is modeled by assigning the energy u_0 to pairs of unbound monomers occupying neighboring lattice sites, $u_0 = -\Delta w_{12}$. The zero value of u_0 corresponds to conditions of a good solvent (See part 3.1). The smaller the parameter u_0 , values correspond to lower solvent qualities χ (χ also depends on the temperature).

The method that we used here is the entropic sampling (ES) method [23, 24] within Wang-Landau (WL) algorithm [25] initially applied to polymers in our simulation group [26] and successfully used later by us [27–29, 34, 37, 40, 41] and by other researchs [30, 33, 42–45] for studying different polymer systems. In the ES-WL computer experiment the density of states $g(E)$ is calculated just as it was done in [27] (see [27] for details). The density of states obtained by this procedure allows us to calculate the canonical averages of physical characteristics over a wide temperature range with the aid of simple summation:

$$\langle F \rangle (T) = \frac{\sum_{i=0}^M F_i g_i e^{-E_i/T}}{\sum_{i=0}^M g_i e^{-E_i/T}}, \quad (2)$$

where F_i is the calculated average of the corresponding physical quantity at conditions corresponding to the i -th energy interval, which is also determined within the simulation. The summation is over the whole energy range (divided into M intervals) that corresponds to conformations of the system without intersections. As the quantity F it can be taken: the configuration energy, the square of the radius of gyration and its components, the modulus of the radius vector of the center of mass, the components of the tensor of inertia. It is worth noting here that at $T \rightarrow \infty$ equation (2) gives the results for the athermal case taking into account the excluded volume interactions of the monomers (a non-charged polymer in a good solvent).

The heat capacity is calculated by the following relationship:

$$C(T) = \frac{\partial E}{\partial T} = \frac{\langle E^2 \rangle (T) - (\langle E \rangle (T))^2}{T^2}. \quad (3)$$

In order to ensure the correct work of the program, we have run it first for linear chains (star with two arms) with the number of monomers $N = 11, 31, 51, 81$ in the same way as it has been done in the previous paper [27]. The size of the cell was chosen so that the concentration c was constant, $d = 30, 42, 50, 58$ respectively. In this case the chain is attached by the center monomer at the center of the periodic cell, and cannot move freely as in [27]. In the presence of periodic boundary conditions, this distinction should not affect the final result. The obtained test data are consistent with the data of work [27], which means that the program can be used for subsequent calculations.

Next, we investigated how the concentration of the solution affected the properties of the studied system with its other parameters being kept constant. We consider the stars with three arms of the length $N_{\text{arm}} = 10$ and change the concentration by the corresponding variation of the periodic cell size d in the range (16, 50) which corresponds to concentrations $c \in [7.57 \cdot 10^{-3}, 2.48 \cdot 10^{-4}]$ respectively (see [46]). Thus, it is possible to confirm the assertion that increasing the concentration of the solution results in a decrease in the swelling of the polyelectrolyte star [22]. The change of concentration in the studied range does not lead to qualitative changes in the thermal and structural properties of the investigated system.

3. Results

3.1. The effect of the length of arms

In order to study how the properties of 3-arm polyelectrolyte star depend on the length of arms we consider the samples with the following length of arms: $N_{\text{arm}} = 10, 15, 19, 24$; respectively the total number of monomers is $N = 31, 46, 58, 73$. The size of the cell was selected so that the polymer concentration remains approximately the same for all the considered cases and its value is $c \approx 4.2 \cdot 10^{-4}$. The corresponding sizes of the cells are $d = 42, 48, 52, 56$. Short-range monomer-monomer interactions are not included.

Figure 1 shows the logarithm of the density of states function for conformations of stars with various N_{arm} . One can see that with an increase in the length of arms the maximum of the distribution shifts to higher energies, and the range of possible energies expands. The lowest energy corresponds to the conformation of a dense globule with built-in counterions; at increasing energy, the counterions leave the star polyion which is transferred to a swollen state; at a positive energy the star loses the counterions completely. At highly-positive energies, very compact conformations without counterions are observed, which do not contribute significantly to the canonical averaging.

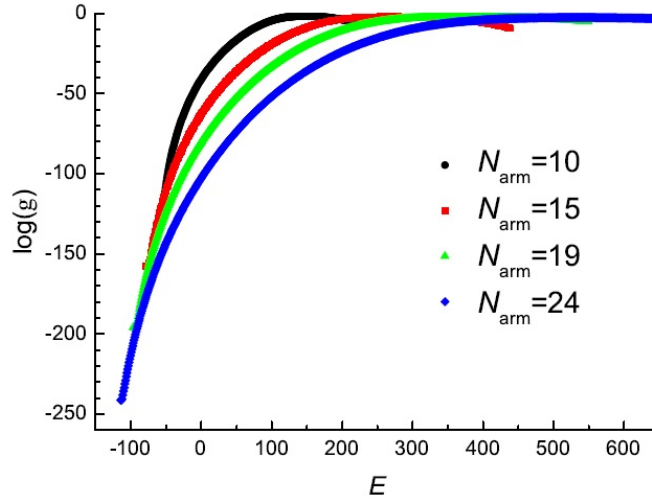


FIG. 1. The logarithm of the density of states as a function of energy for conformations of the 3-arm stars with different lengths of arms $N_{\text{arm}} = 10, 15, 19, 24$

Average configuration energy of stars (Fig. 2a) increases monotonously with increasing temperature. The same way as in the case of chains [27], there exists a point at which the graphs intersect, i.e. it is the temperature at which the energy does not depend on the number of monomers in the star. A similar behavior was observed for uncharged stars [41] with a contact negative interaction potential between monomers. It should especially be noted here that while for ordinary electrolyte solutions the equilibrium configurational energy is always negative with the limiting value being zero for $T \rightarrow \infty$, in the case of polyelectrolyte containing a polyion with rigid bonds the energy can become positive with an increase in temperature. This is because polymer bonds cannot dissociate and the energy of polyion-polyion interaction remains positive while polyion-ion and ion-ion interaction energies tend to zero, the case that we observe in our data.

Each dependency (Fig. 2b) has a broad non-smooth maximum for the heat capacity, which indicates a coil-globule transition. With an increase in the arm length, an additional maximum is observed at low temperatures, and in the case of the star with $N_{\text{arm}} = 24$ a sharp peak emerges. Similar peaks for long chain polyelectrolytes ($N > 50$) were observed by Volkov et. al. [27]. An analogous result was obtained in [30], where the bond-fluctuation lattice model for the uncharged star polymer was studied; the authors attributed this peak to a liquid \rightarrow crystal-like state transition. Also, with an increase of the N_{arm} , some small rippling on the curves appears, that could be apparently associated with the specific features of the lattice model or with discrete splitting of the energy range into intervals, and, we believe, they do not carry much physical sense.

Let us watch now the structural properties starting with the square of the radius of gyration:

$$R_g^2 = \frac{1}{2N^2} \sum_{i=1}^N \sum_{j=1}^N |r_{ij}|^2 = \frac{1}{N} \sum_{i=1}^N (r_i - \vec{R}_c)^2, \quad (4)$$

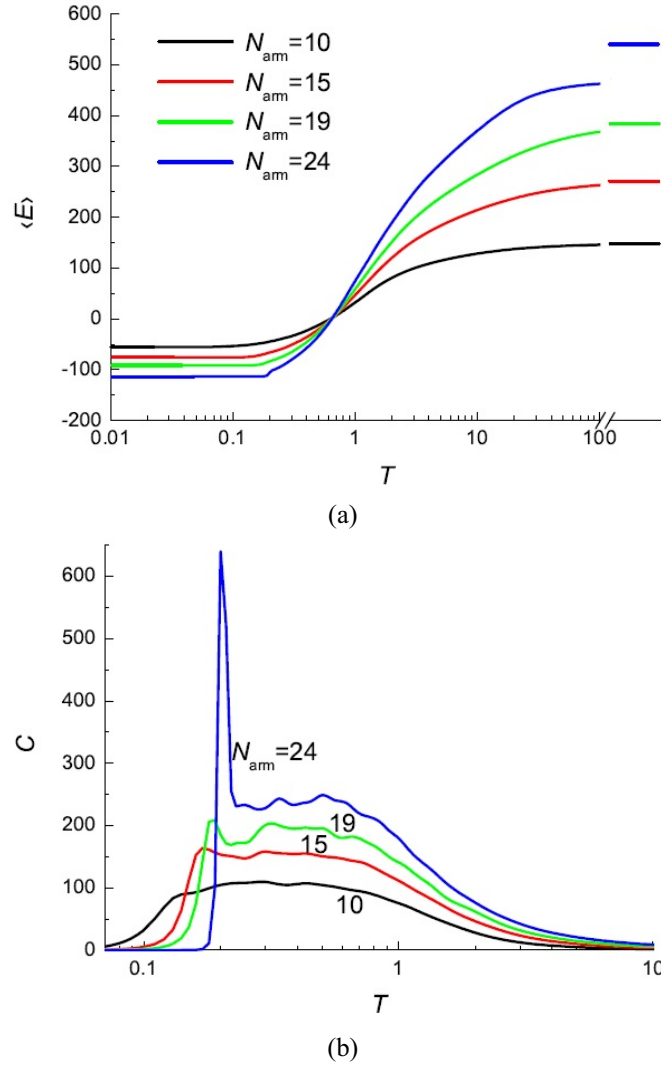
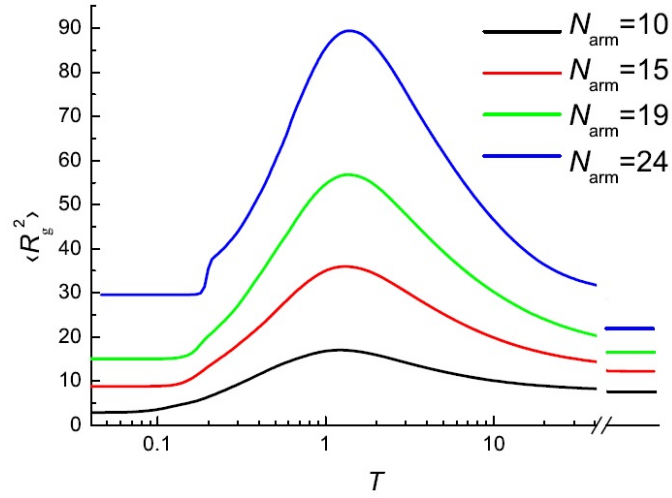


FIG. 2. The temperature dependence of the average configuration energy (a) and of heat capacity (b) for the stars ($f = 3$) with different lengths $N_{\text{arm}} = 10, 15, 19, 24$. The horizontal dashes on the right of this and the next graphics show the values at $T \rightarrow \infty$, i. e. the values for athermal case

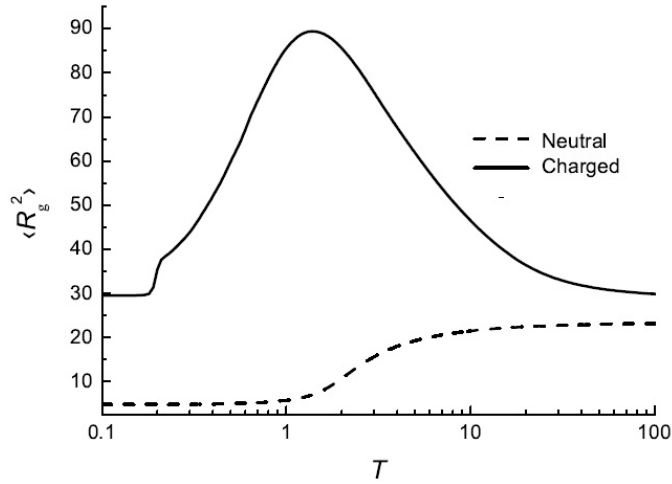
where \vec{R}_c is the radius vector of the center of mass. The temperature dependence of $\langle R_g^2 \rangle(T)$ has the following form (Fig. 3a): a single maximum in the vicinity of $T \approx 1.2$ (varies for different N_{arm}). Its value increases with increasing N_{arm} , and its position is slightly shifted to higher temperatures. In this range the polymer is in a swollen state, its size is several times larger than the size of the ideal polymer. It is worth noting here that for the uncharged model of a star (with a negative interaction potential) [28, 29] the dependence of $\langle R_g^2 \rangle(T)$ has a simple monotonic rise (Fig. 3b). So the maximum observed in the case of polyelectrolyte is caused by the presence of electrostatic interactions. At low temperatures ($T < 0.1$) the star polyion is in a compact state with built-in counterions, and its size is determined only by the total number of segments.

At high temperatures, when $k_B T$ is considerably higher than the energy of electrostatic interaction the effect of the latter is insignificant. This is the area of so-called athermal solvent in terms of Flory theory (Flory-Huggins parameter $\chi = 0$) [39]. The values of athermal limits ($T \rightarrow \infty$) for $\langle R_g^2 \rangle(T)$ dependence (dashes in Fig. 3a) can be approximated as $\langle R_g^2 \rangle(T) \propto N^{1.21}$, that coincides with scaling predictions from analytical theories [12, 20] for an uncharged star in a good solvent.

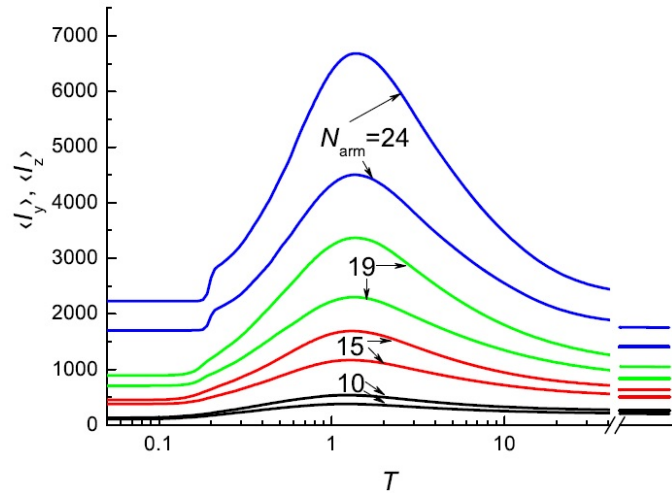
All the components of the inertia tensor were also obtained at each step and its matrix was reduced to a diagonal form to extract three main components. The averaged reduced components of the inertia tensor $\langle I_x \rangle < \langle I_y \rangle < \langle I_z \rangle$ are shown in Fig. 3c. It is evident that in the entire considered temperature range the components have different



(a)



(b)



(c)

FIG. 3. Temperature dependencies of the average values of: the mean square radius of gyration $\langle R_g^2 \rangle$ (a), the reduced components $\langle I_y \rangle$, $\langle I_z \rangle$ of the tensor of inertia, $\langle I_y \rangle < \langle I_z \rangle$ ($\langle I_x \rangle$ not shown for clarity, the form of dependence is similar to $\langle I_y \rangle$, $\langle I_z \rangle$) (c) for the stars ($f = 3$) with different length of arms $N_{\text{arm}} = 10, 15, 19, 24$. Comparison of $\langle R_g^2 \rangle(T)$ for charged and neutral stars, $f = 3$, $N_{\text{arm}} = 24$ (b)

values and by rotational properties each star can be described as a three-axial ellipsoid elongated along one axis (cucumber).

In order to characterize the shape in more detail, the components of the mean square radius of gyration were also calculated (Stockmayer [47, 48]) L_1^2, L_2^2, L_3^2 , so that $R_g^2 = L_1^2 + L_2^2 + L_3^2$, $L_1^2 < L_2^2 < L_3^2$. Firstly all the components of the tensor were calculated:

$$L_{lk}^2 = \frac{1}{N} \sum_{i=1}^N (r_{il} - R_{cl})(r_{ik} - R_{ck}), \quad l, k = 1, 2, 3, \quad (5)$$

where R_{cl} and R_{ck} are the l -th and k -th coordinates of the center of mass vector. Then the matrix of the tensor was reduced to a diagonal form and three components were determined. Knowledge of the three components provides possibility to determine the parameter that allows us to distinguish the oblate shape from the elongated one (Fig. 4a):

$$S^* = (3sf_1 - 1)(3sf_2 - 1)(3sf_3 - 1). \quad (6)$$

Here, the reduced components emerge $sf_1 = L_1^2/R_g^2$, $sf_2 = L_2^2/R_g^2$, $sf_3 = L_3^2/R_g^2$. Parameter S^* varies in the range $[-0.25, 2]$, and can be both negative (oblate shape) and positive (prolate shape) [32]. At $T \approx 1.2$ the star is in a swollen state, its shape is close to spherical ($S^* \approx 0$, Fig. 4a), and its conformation is asymmetric relative

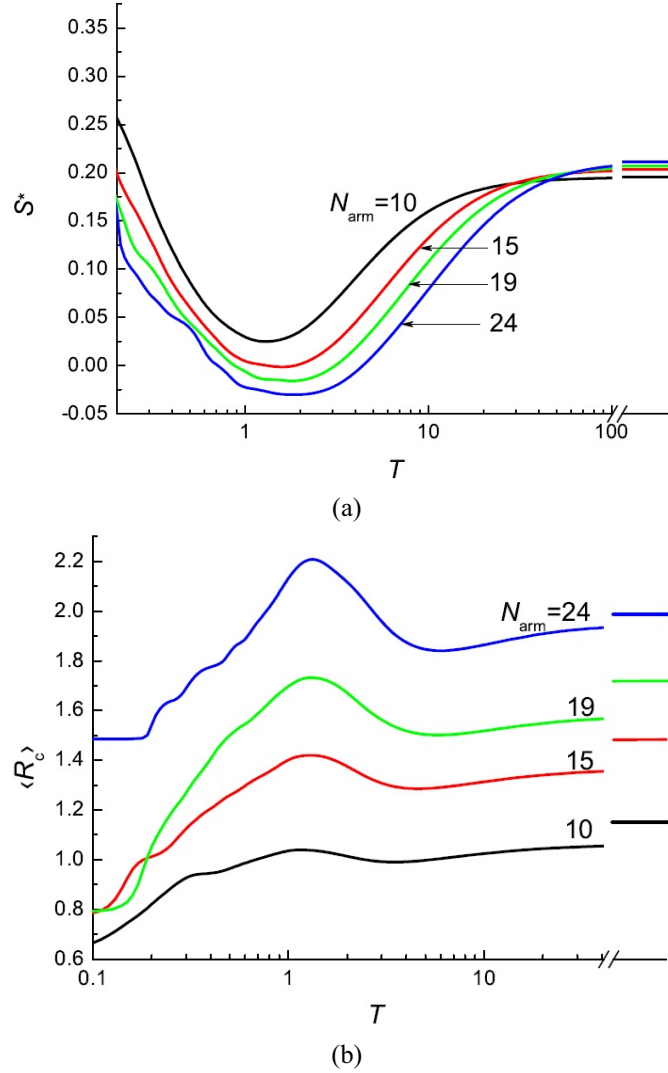


FIG. 4. Temperature dependencies of the parameter characterizing the shape S^* (a), of the average modulus of the radius vector of the center of mass $\langle R_c \rangle$ (b) for 3-arm stars with different length of arms $N_{\text{arm}} = 10, 15, 19, 24$

to its center (maximum $\langle R_c \rangle (T)$ Fig. 4b). At $T \rightarrow 0$ the size of the star decreases, the conformation becomes symmetric relative to the center (decreasing $\langle R_c \rangle (T)$).

The analytical theory for the salt-free dilute solution of star-shaped electrolyte was proposed in [22]. It gives the scaling relations that allow us to estimate the size of the stars R for separate regimes. The first is the unscreened regime, which is achieved if $Q \ll R/l_B$, where Q is the total charge of the star, $l_B = e^2/\epsilon k_B T$ is the Bjerrum length. In this case the star size is determined by the following relationship [22]:

$$R \cong N_{\text{arm}} m^{-2/3} l_B^{1/3} f^{1/3}, \quad (7)$$

where $1/m$ is the part of ionized monomers. In our case, the polymer is completely ionized, and $m = 1$. In this regime counterions surround the star and there is a dependence of the star size on the number of arms.

The second regime is osmotic, which is achieved when $Q \gg R/l_B$. In this case the star captures and holds the counterions from the solution. Its size does not depend on the number of arms and is determined by the relation:

$$R \cong N_{\text{arm}} m^{-1/2}. \quad (8)$$

If we consider the results of this theory in the framework of our model, we obtain the following. In the units of our model $l_B = 1/T$, and the first regime is reached when $RT \gg Q$, i. e. at high temperatures, and $R \cong N_{\text{arm}} T^{-1/3} 3^{1/3}$. This regime corresponds to the decreasing dependence of $\langle R_g^2 \rangle (T)$ (Fig. 3a). The osmotic regime is achieved when $RT \ll Q$ is provided.

We can qualitatively compare our results with work [9], where the classical MC simulation is carried out for star-branched micelles with $N_{\text{arm}} = 130$ and with the number of arms 6 and 27 in some range of temperatures. There, the dependence of R_g/N_{arm} on the parameter ζ is presented; ζ corresponds to $1/T$ in the units of our model. $R_g/N_{\text{arm}}(\zeta)$ dependence is not monotonic and has a maximum in the area around $\zeta = 1$ similar to our case (see $\langle R_g^2 \rangle (T)$ and its maximum in Fig. 3a). Each $\langle R_g^2 \rangle (T)$ dependence has a single broad maximum in the vicinity of $T \approx 1.2$, the height of the maximum is determined by the length of arms in a star. The unscreened regime is observed at $T \gg 1$ ($\zeta \ll 1$). With a decrease in temperature, when the Coulomb energy of counterions in the field, created by the corona radius [9] becomes of the order of $k_B T$, the regime of spherical condensation is achieved. It is performed at $\zeta_{\text{sph}} \approx 1/f$, i.e. $T_{\text{sph}} \approx f$. When all counterions are inside the star, the osmotic regime is observed [22], in [9] it occurs at $\zeta \gg 1/f$. In our case the number of arms is small and osmotic regime is observed around the maximum of $\langle R_g^2 \rangle (T)$, it becomes broader with increasing f . We analyzed $\langle R_g^2 \rangle$ values (Fig. 3a) in the area of $1 < T < 1.38$, and obtained that $\langle R_g^2 \rangle (T) \propto N_{\text{arm}}^2$, which agrees with eq. (8).

When the Manning criterion of cylindrical condensation [49] is satisfied, i.e. $\zeta > 1$ or $T < 1$ the counterion condensation around each arm of the star begins. In this regime, the condensed counterions partly compensate the charge of the star polyion, and the effective charge fraction of the star becomes $\alpha_{\text{eff}} = T$. So the size of the star at the same time is decreased, see Fig. 3a. With further decreasing of temperature the transition of polyion into the collapsed state that was predicted by Schissel and Pincus [50] for strongly charged chains is observed. We can see this state at $T < 0.1$, Fig. 3a. When the collapse energy dominates over the entropic contribution, each counterion is attached to a monomer and forms an electric dipole [9, 50, 51]. The attraction of the dipoles leads to a transition to a collapsed state. It can be noted here that in [9], the collapsed state is not achieved probably due to the consideration of a limited temperature range.

Thus, we can conclude that for star and linear polyions within the above considered model at the increasing the number of monomers there appears a transition from a liquid to a solid-like state in addition to the coil-globule transition. It is shown how strongly the polyelectrolyte star swells compared to the uncharged polymer.

3.2. The effect of the short-range interactions

In this series of simulations, we investigate how the short-range (contact) interactions influence the star polyion properties. We consider a 3-arm star with $N_{\text{arm}} = 10$ in the cell of size $d = 42$, that corresponds the concentration $c \approx 4.2 \cdot 10^{-4}$. The contact attraction of unbound monomers, located at a distance of the lattice constant are determined by the energy $u_0 < 0$, that is varied in the range $[-3; 0]$. Note that the smaller is the parameter u_0 is, the worse is the quality of the solvent χ .

The logarithm of the density of states as a function of energy is presented in Fig. 5. One can see that with decreasing of the parameter u_0 values, the range of possible energies significantly expands to the negative E -side, which is to be expected. Maximum of $g(E)$ shifts to the lower energies and the coordinates of maxima at the E -axis are 154.56, 145.55, 144.06, 141.93, 136.10, 131.09 for $u_0 = 0, -0.2, -0.5, -1, -2, -3$ respectively. It is not simply a left shift of $g(E)$ function for the case of $u_0 = 0$, the shape of the $g(E)$ changes with u_0 as well.

The temperature dependences of the average configuration energy $\langle E \rangle$, and of excess free energy ΔF are presented in Fig. 6a. One can see that the curves are qualitatively close to each other for different u_0 values and

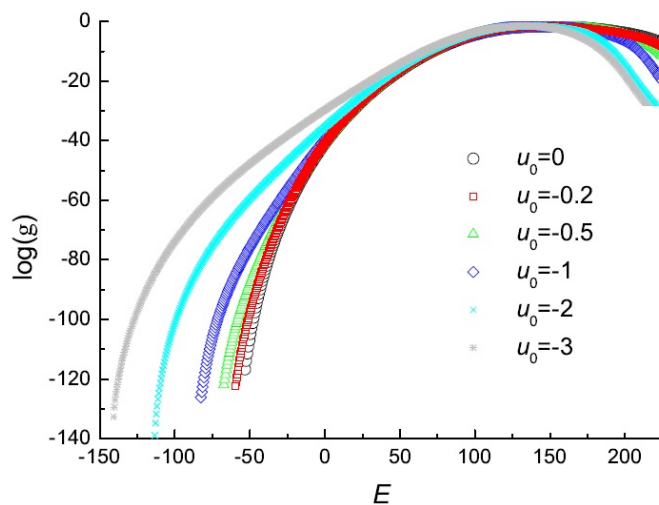


FIG. 5. The logarithm of the density of states as a function of energy for conformations of the 3-arm star ($N_{\text{arm}} = 10$) at different u_0 parameter values, $u_0 = 0, -0.2, -0.5, -1, -2, -3$

only the energy of the ground state becomes lower for lower u_0 . At $T \rightarrow 0$ the values of $\langle E \rangle$ and ΔF for each case tend to the common limits.

The maximum of $C(T)$ dependence (Fig. 6b) becomes sharper and noticeably shifts to the right at T axis with lowering of the parameter u_0 . One can see that the addition of the short-range attractive potential results in easier transition to the globule state, and this transition becomes not as smooth as in the case of $u_0 = 0$. The $\langle R_g^2 \rangle(T)$ dependence is presented in Fig. 7a; we can notice that the addition of the short-range attractive potential results in decreasing of the polyelectrolyte swelling. The coil-globule transition now occurs at higher temperatures. The maximum of $\langle R_g^2 \rangle(T)$ is shifted to the higher temperature region. At low T the values of $\langle R_g^2 \rangle(T)$ for $u_0 \neq 0$ tends to the common limit that is slightly lower than for the case of $u_0 = 0$. This slight difference could be caused by insufficient statistics for the low-energy conformations that was discarded at averaging. We suppose that the size of the globule must be independent of u_0 .

We consider the shape of the star using the asphericity parameter:

$$\delta = 1 - 3(sf_1sf_2 + sf_2sf_3 + sf_3sf_1). \quad (9)$$

Here, the reduced components are the same as in the equation (6). The asphericity parameter varies from zero (absolute symmetry, sphere) to one (form of a rigid rod).

$\delta(T)$ and $S^*(T)$ dependencies are presented in Fig. 7b,c. Before the transition to the globule state the shape of the star polyion becomes elongated that we can conclude from observing the maxima of $\delta(T)$ and $S^*(T)$. These maxima become significantly sharper with decreasing u_0 values.

It was shown how the addition of the short-range attraction potential affects the size and shape of a 3-arm star polyion. It was confirmed that the short-range attraction potential results in easier transition from a coil to a globule state. The greater the attraction, the stronger the asymmetric shape of the molecule is before transition into a globular state.

4. Conclusion

In this work, the entropic sampling Monte Carlo method is applied to study the lattice model of the 3-arm star-shaped polyelectrolyte with constant (quenched) charges and with short-range attractive interaction of the monomers in a salt-free solution. The applied approach allows us to trace the equilibrium state of the considered system over a wide temperature range, including athermal, unscreened, osmotic, Mannings condensation and collapsed regimes.

Two sets of calculations were performed. In the first set, the length of arms was modified at fixed overall density of the system. For comparatively short arms the temperature decrease results in the transition of the coil-globule type while with increasing the arm lengths there appears an additional transition from a liquid-like to a solid-like state. We can see that for the polyelectrolyte the $\langle R_g^2 \rangle(T)$ dependency has a maximum while it rises monotonously for the neutral ones, the swelling of the polyelectrolyte is much larger than that for neutral stars.

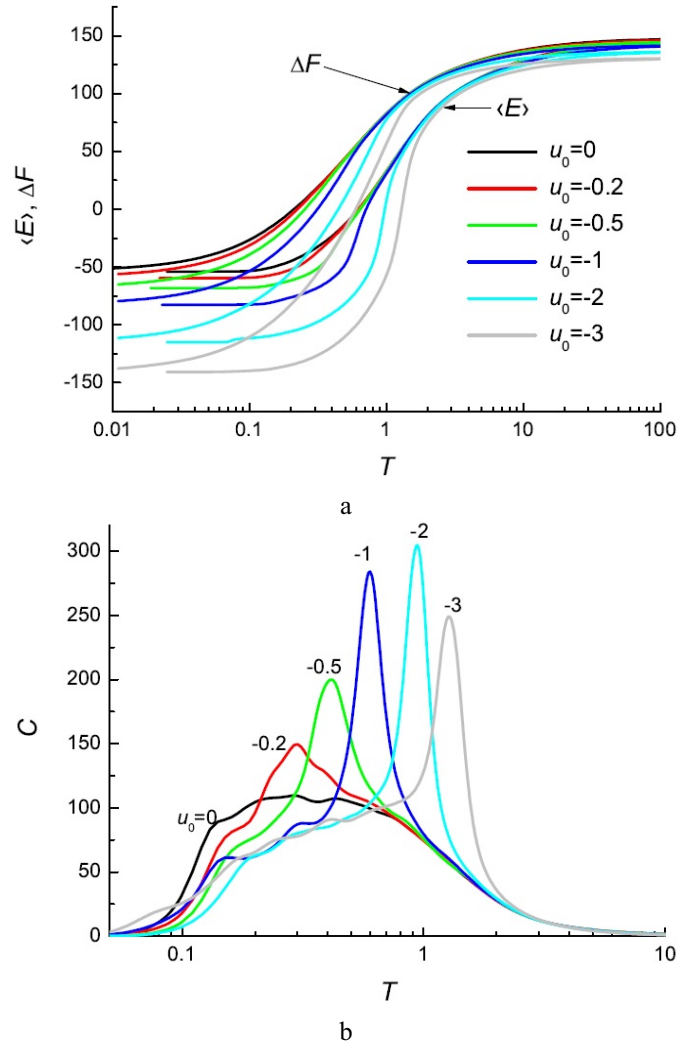


FIG. 6. The temperature dependence of the average configuration energy $\langle E \rangle$, of excess free energy ΔF (a) and of heat capacity C (b) of the 3-arm star ($N_{\text{arm}} = 10$) at different values of the parameter u_0 , $u_0 = 0, -0.2, -0.5, -1, -2, -3$

In the second set of simulations, the short-range monomer-monomer interactions that characterize the solvent quality are included. It is shown that short-range monomer-monomer attraction results in an easier transition from a coil to a globule state and with a more elongated molecule shape before transition into a globular state.

In this work, we have studied systems with comparatively small number of monomers $N < 73$ that can be considered as a starting point for further work. It can include increasing the number of arms, their length, as well as considering the system with the addition of salt ions of different valence. It should be pointed out here that the studied case without added salt is perhaps more difficult for simulations because the salt ions create additional screening of electrostatic interactions, and at high concentrations, the properties of charged macromolecules approach the properties of the neutral ones [13,22]. Change of the charge fraction on the polyion (which models change of solvent pH) can also be envisioned.

Considering continuous models and combining the method applied here with other approaches (MD, expanded ensemble MC, etc.) could be used as well. The algorithm can be straightforwardly parallelized with the use of multiwalker sampling which would allow us to use the method for substantially larger systems. Particularly, it would permit increasing the length of star arms and their number. This way, further study would seemingly yield new interesting results in the area of branched polyelectrolytes.

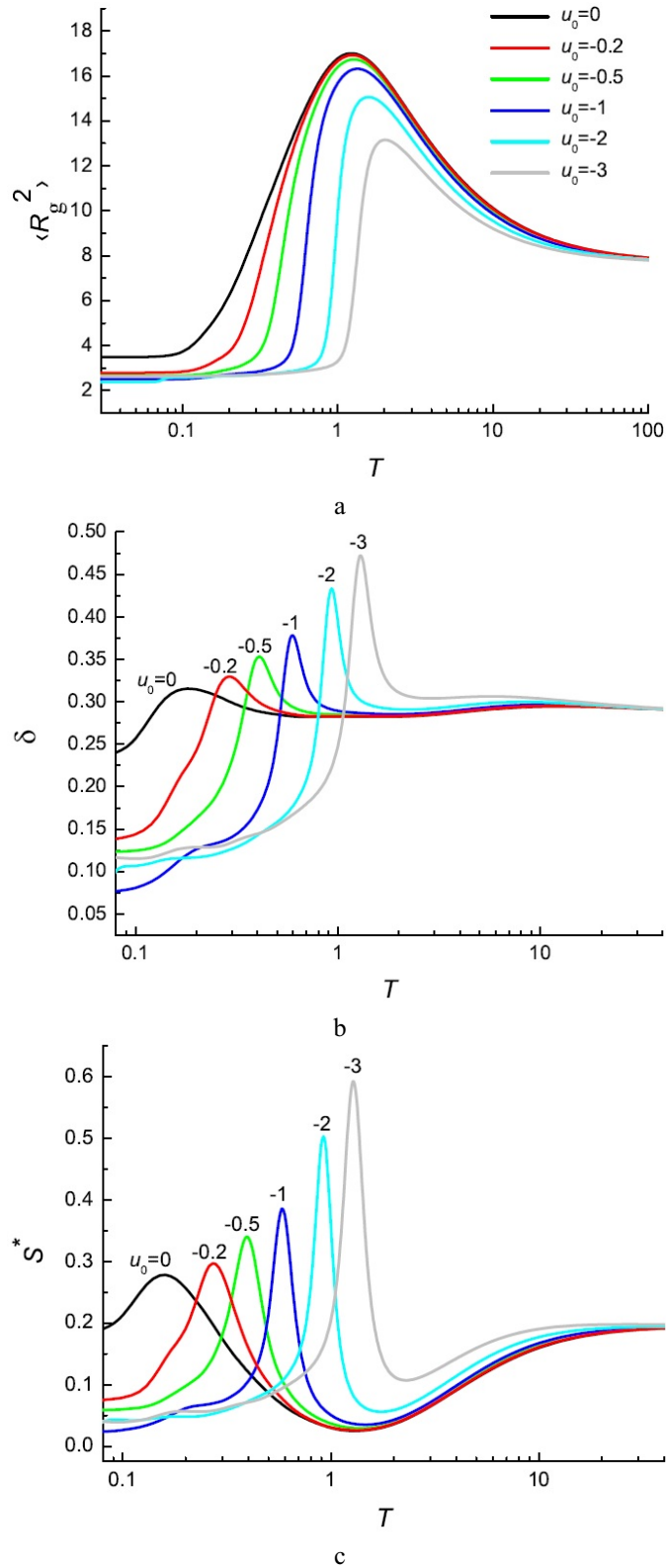


FIG. 7. Temperature dependencies of the averaged square radius of gyration $\langle R_g^2 \rangle$ (a), of the asphericity parameter δ (b), of the parameter characterizing the shape S^* (c) of the 3-arm star ($N_{\text{arm}} = 10$) at different u_0 parameter values, $u_0 = 0, -0.2, -0.5, -1, -2, -3$

Acknowledgements

This work is supported by the St. Petersburg State University, the project numbers 11.37.290.2015, 11.57.673.2014, 11.57.159.2016.

References

- [1] Alhoranta A. M., Lehtinen J. K., Urtti A. O., Butcher S. J., Aseyev V. O., Tenhu H. J. Cationic amphiphilic star and linear block copolymers: synthesis, self-assembly, and in vitro gene transfection. *Biomacromolecules*, 2011, **12**, P. 3213–3222.
- [2] Aryal S., Prabaharan M., Pilla S., Gong S. Biodegradable and biocompatible multi-arm star amphiphilic block copolymer as a carrier for hydrophobic drug delivery. *International Journal of Biomacromolecules*, 2009, **44**, P. 346.
- [3] Cameron D., Shaver M. Aliphatic polyester polymer stars: synthesis, properties and applications in biomedicine and nanotechnology. *Chemical Society Reviews*, 2011, **40**, P. 1761–1776.
- [4] Filippov A. P., Romanova O. A., Vinogradova L. V. Molecular and hydrodynamic characteristics of star-shaped polystyrenes with one or two fullerene (C₆₀) molecules as a branching center. *Polymer Science A*, 2010, **52** (3), P. 221–227.
- [5] Jusufi A., Likos C. N., Löwen H. Counterion-induced entropic interactions in solutions of strongly stretched, osmotic polyelectrolyte stars. *J. Chem. Phys.*, 2002, **116**, P. 11011.
- [6] Jusufi A., Likos C. N., Löwen H. Conformations and Interactions of Star-Branched Polyelectrolytes. *Phys. Rev. Lett.*, 2001, **88**, P. 018301.
- [7] Jusufi A., Likos C. N. Colloquium: Star-branched polyelectrolytes: The physics of their conformations and interactions. *Rev. Mod. Phys.*, 2009, **81**, P. 1753–1772.
- [8] Likos C. N., Blaak R., Wynveen A. Computer simulations of polyelectrolyte stars and brushes. *J. Phys.: Condens. Matter*, 2008, **20**, P. 494221.
- [9] Roger M., Guenoun P., Muller F., Belloni L., Delsanti M. Monte-Carlo simulations of star-branched polyelectrolyte micelles. *Eur. Phys. J. E.*, 2002, **9**, P. 313–326.
- [10] Košovan P., Kuldová J., Limpouchová Z., Procházka K., Zhulina E. B., Borisov O. V. Molecular dynamics simulations of a polyelectrolyte star in poor solvent. *Soft Matter*, 2010, **6**, P. 1872–1874.
- [11] Zhulina E. B., Birshtein T. M., Borisov O. V. Curved polymer and polyelectrolyte brushes beyond the Daoud-Cotton model. *Eur. Phys. J. E.*, 2006, **20**(3), P. 243–256.
- [12] Birshtein T. M., Mercurieva A. A., Leermakers F. A. M., Rud O. V. Conformations of polymer and polyelectrolyte stars. *Polymer Science A*, 2008, **50**(9), P. 992–1007.
- [13] Polotsky A. A., Zhulina E. B., Birshtein T. M. Effect of the ionic strength on collapse transition in star-like polyelectrolytes. *Macromol. Symp.*, 2009, **278**, P. 24–31.
- [14] Rud O. V., Mercurieva A. A., Leermakers F. A. M., Birshtein T. M. Collapse of Polyelectrolyte Star. Theory and Modeling. *Macromolecules*, 2012, **45**(4), P. 2145–2160.
- [15] Kytseval N. V., Rawiso M. Star-shaped dextran-polyacrylamide polymers. Features of the structure and prospects of application in nanotechnology. *Vestnik Kazanskogo Technologicheskogo Universiteta*, 2014, **17**(2), P. 164–169 (in Russian).
- [16] Montgomery N., Hedley G., Ruseckas A., Denis J., Schumacher S., Kanibolotsky A., Skabara P., Galbraith I., Turnbull G., Samuel I. Dynamics of fluorescence depolarisation in star-shaped oligofluorene-truxene molecules. *Phys. Chem. Chem. Phys.*, 2012, **14**, P. 9176–9184.
- [17] Swinarev A., Piekarnik B., Grobelny Z., Stolarzewicz A., Simokaitiene J., Andrikaityte E., Grazulevicius J. Star-Shaped Poly((9-carbazolyl)methylthiirane): A New Polymer for Optoelectronic Applications. *Macromol. Symp.*, 2011, **308**(1), P. 8–11.
- [18] Zang Z.-L., Zou L.-Y., Ren A.-M., Liu Y.-F., Feng J.-K., Sun C.-C. Theoretical studies on the electronic structures and optical properties of star-shaped triazatruxene/heterofluorene co-polymers. *Dyes and Pigments*, 2013, **96**(2), P. 349–363.
- [19] Wu W., Wang W., Li J. Star polymers: Advances in biomedical applications. *Progress in Polymer Science*, 2015, **46**, P. 55–85.
- [20] Likos C. N. Soft matter with soft particles. *Soft Matter*, 2006, **2**, P. 478–498.
- [21] Muzafarov A. M., Vasilenko N. G., Tatarinova E. A., Ignateva G. M., Myakushev V. M., Obrezkova M. A., Meshkov I. B., Voronina N. V., Novozhilov O. V. Macromolecular nano-objects as a promising direction of polymer chemistry. *Polymer Science C*, 2011, **53**(1) P. 48.
- [22] Klein Wolternik J., Leermakers F. A. M., Fleer G. J., Koopal L. K., Zhulina E. B., Borisov O. V. Screening in solutions of star-branched polyelectrolytes. *Macromolecules*, 1999, **32**, P. 2365–2377.
- [23] Berg B. A., Neuhaus T. Multicanonical ensemble: a new approach to simulate first-order phase transitions. *Phys. Rev. Lett.*, 1992, **68**, P. 9–12.
- [24] Lee J. New Monte Carlo algorithm: entropic sampling. *Phys. Rev. Lett.*, 1993, **71**, P. 211–214.
- [25] Wang F., Landau D. P. Efficient, multiple-range random walk algorithm to calculate the density of states. *Phys. Rev. Lett.*, 2001, **86**, P. 2050–2035.
- [26] Vorontsov-Velyaminov P. N., Volkov N. A., Yurchenko A. A. Entropic sampling of simple polymer models within Wang-Landau algorithm. *J. Phys. A*, 2004, **37**, P. 1573–1588.
- [27] Volkov N. A., Vorontsov-Velyaminov P. N., Lyubartsev A. P. Entropic sampling of flexible polyelectrolytes within the Wang-Landau algorithm. *Phys. Rev. E*, 2007, **75**, P. 016705.
- [28] Silantyeva I. A., Vorontsov-Velyaminov P. N. The calculation of the density of states and the thermal properties of the polymer chains and stars on a lattice by Monte Carlo method using the Wang-Landau algorithm. *Numerical Methods and Programming*, 2011, **12**, P. 397–408 (in Russian).
- [29] Silantyeva I. A., Vorontsov-Velyaminov P. N. Thermodynamic properties of star shaped polymers investigated with Wang-Landau Monte Carlo simulations. *Macromol. Symp.*, 2012, **317–318**, P. 267–275.
- [30] Wang Z., He X. Phase transition of a single star polymer: a Wang-Landau sampling study. *J. Chem. Phys.*, 2011, **135**, P. 094902.
- [31] Clisby N. Efficient implementation of the pivot algorithm for self-avoiding walks. *J. Stat. Phys.*, 2010, **140**, P. 349–392.
- [32] Zifferer G., Eggerstorfer D. Monte Carlo simulation studies of the size and shape of linear and star-branched copolymers embedded in a tetrahedral lattice. *Macromol. Theory. Simul.*, 2010, **19**, P. 458–482.

- [33] Wüst T., Lee Yu., Landau D. Unraveling the beautiful complexity of simple lattice model polymers and proteins using Wang-Landau sampling. *J. Stat. Phys.*, 2011, **144**, P. 638–651.
- [34] Yurchenko A. A., Antyukhova M. A., Vorontsov-Velyaminov P. N. Investigation of the interaction of the polymer with the surface by entropic modeling. *J. Structure Chemistry*, 2011, **52**(6), P. 1216–1223 (in Russian).
- [35] Vogel T., Bachmann M., and Janke W. Freezing and collapse of flexible polymers on regular lattices in three dimensions. *Phys. Rev. E*, 2007, **76**, P. 061803.
- [36] Lyubartsev A. P., Vorontsov-Velyaminov P. N. Monte-Carlo modeling of flexible polyelectrolytes. *Polymer Science U.S.S.R.*, 1990, **32**, P. 660–666.
- [37] Volkov N. A., Yurchenko A. A., Lyubartsev A. P., Vorontsov-Velyaminov P. N. Entropic sampling of free and ring polymer chains. *Macromol. Theory Simul.*, 2005, **14**, P. 491–504.
- [38] Frenkel D., Smit B. *Understanding molecular simulation: from algorithms to applications*. Academic Press, 2001.
- [39] Grossberg A. Yu., Khokhlov A. R. *Statistical physics of macromolecules*. AIP Press, Woodbury, 1994.
- [40] Silantyeva I. A., Vorontsov-Velyaminov P. N. Entropic sampling of star-shaped polymers with different number of arms: temperature dependencies of structural properties. *Nanosystems: physics, chemistry, mathematics*, 2015, **6**(4), P. 513–523.
- [41] Vorontsov-Velyaminov P. N., Yurchenko A. A., Antyukhova M. A., Silantyeva I. A., Antipina A. Yu. Entropic sampling of polymers: A chain near a wall, polyelectrolytes, star-shaped polymers. *Polymer Science C*, 2013, **55**(1), P. 112–124.
- [42] Janke W., Paul W. Thermodynamics and structure of macromolecules from flat-histogram Monte Carlo simulations. *Soft Matter*, 2016, **12**, P. 642–657.
- [43] Seaton D. T., Wüst T., Landau D. P. Collapse transition in a flexible homopolymer chain: application of the Wang-Landau algorithm. *Phys. Rev. E*. 2010. **81**. 011802.
- [44] Martemyanova J. A., Stukan M. R., Ivanov V. A., Müller M., Paul W., Binder K. Dense orientationally ordered states of a single semiflexible macromolecule: An expanded ensemble Monte Carlo simulation, *J. Chem. Phys.*, 2005, **122**, P. 174907.
- [45] Wang Z., Wang L., Chen Y., He X. Phase transition behaviours of a single dendritic polymer. *Soft Matter*, 2014, **10**, P. 4142–4150.
- [46] Silanteva I. A., Vorontsov-Velyaminov P. N. Entropic sampling study of star-shaped polyelectrolytes on a lattice. Proceedings of “Multiscale modeling of materials and molecules”, Uppsala, Sweden, 7–9 June 2016. P. 6.
- [47] Šolk K., Stockmayer W. H. Shape of a RandomFlight Chain. *J. Chem. Phys.*, 1971, **54**(6), P. 2756–2757.
- [48] Šolk K. Shape of a RandomFlight Chain. *J. Chem. Phys.*, 1971, **55**, P. 335–344.
- [49] Manning G. S. Limiting Laws and Counterion Condensation in Polyelectrolyte Solutions I. Colligative Properties. *J. Chem. Phys.*, 1969, **51**, P. 924–933.
- [50] Schiessel H., Pincus P. Counterion-Condensation-Induced Collapse of Highly Charged Polyelectrolytes. *Macromolecules*, 1998, **31**(22), P. 7953–7959.
- [51] Brilliantov N., Kuznetsov D., Klein R. Chain Collapse and Counterion Condensation in Dilute Polyelectrolyte Solutions. *Phys. Rev. Lett.*, 1998, **81**(7), P. 1433.

Adiabatic cycles in quantum systems with contact interactions

Atushi Tanaka, Taksu Cheon

Department of Physics, Tokyo Metropolitan University, Hachioji, Tokyo 192-0397, Japan
tanaka-atushi@tmu.ac.jp, taksu.cheon@kochi-tech.ac.jp**PACS 03.65.-w,03.65.Vf,02.40.Pc****DOI 10.17586/2220-8054-2017-8-1-121-126**

An adiabatic cycle involving the δ -function potential is shown to excite Bose particles confined in a one-dimensional box. We consider a cycle, during which a wall described by a δ potential is applied and its strength and position are slowly varied. When the system is initially prepared in the equilibrium ground state, the adiabatic cycle brings all bosons into the first excited one-particle state, leaving the system in a nonequilibrium state. The absorbed energy during the cycle is proportional to the number of bosons.

Keywords: Bose particles, adiabatic cycle, δ -function potential, boson.

Received: 10 July 2016

Revised: 30 July 2016

1. Introduction

Since the discovery of the geometric phase [1], it has been widely recognized that adiabatic cyclic parameter variation does not necessarily bring a quantum eigenstate of a system back to itself. In general, an “exotic” quantum holonomy [2,3], in which one eigenstate turns into another eigenstate belonging to the same Hamiltonian, can be observed after the cyclic variation of the system parameters. In this paper, we examine an adiabatic cycle that excites a system consisting of Bose particles confined in a one-dimensional box. During the cycle, we vary an additional wall adiabatically, while the interparticle interaction is kept fixed. This is in contrast to the scheme described in [4,5], where the interaction strength between Bose particles is an effective adiabatic parameter. In this study, we suppose that the wall is described by a δ -function shaped potential [6–8]. We show that the first excited one-particle state is occupied by all the bosons to achieve the population inversion completely, if the system is prepared to be in the ground state. Namely, the energy gained by the bosons during the adiabatic cycle is proportional to the number of bosons.

The adiabatic cycle described above has an immediate relevance to the population inversion in Bose gas system [9], particularly in the super-Tonks-Girardeau gas, which has attracted considerable recent attention in both experimental and theoretical studies [4,10–12]. In the super-Tonks-Girardeau gas, which may be described by the Lieb-Liniger model [13] with strongly attractive interaction, the population inversion is created through an “adiabatic” process, where the interaction strength is suddenly flipped from infinitely repulsive to infinitely attractive [4,14]. Such a population inversion can be induced even by an adiabatic cycle, which can be obtained with an extension of the adiabatic process that connects Tonks-Girardeau and super-Tonks-Girardeau gases both to weaker repulsive and weaker attractive regime. The repetitions of this adiabatic cycle transform the ground state of non-interacting bosons into their higher excited states and achieve the population inversion [5]. This is counterintuitive, since there is no external field to drive the final state of the bosons away from the initial state.

The paper is organized as follows: in Section 2, the basic setup of our model is presented in the simplest setting of one boson; Section 3 and 4 treat several interacting and non-interacting bosons, respectively; Section 5 contains the summary and the discussion.

2. A particle in a box with a δ -wall

In order to examine N Bose particles in a one-dimensional box with an additional δ -wall, we review the single particle case, i.e., $N = 1$ [8], where the system is described by the Hamiltonian:

$$H(g, X) = \frac{p^2}{2m} + V(x) + g\delta(x - X), \quad (1)$$

where m is the particle mass, $V(x)$ is the confinement potential, and g and X are the strength and position of δ -wall. In particular, we assume that $V(x)$ describes an infinite square well with the length L , i.e., $V(x) = 0$ for $0 < x < L$ and $V(x) = \infty$ otherwise [6,7].

We introduce an adiabatic cycle C , which consists of three adiabatic processes C_I , C_{II} and C_{III} , as shown in Fig. 1. We suppose that the δ -wall is initially absent, i.e., $g = 0$ in 1, and that the system is in a stationary state initially. In the first part of C , which will be called as C_I , an impenetrable wall is inserted at x_0 adiabatically. In

terms of the δ -wall, the strength g is slowly increased from 0 to ∞ , while its position X is fixed at x_0 during C_I . Subsequently, in the second part C_{II} , the position X of the impenetrable wall is adiabatically changed from x_0 to x_1 . In the last part C_{III} , the δ -wall at $X = x_1$ is adiabatically turned off. At the end of the cycle C , the δ -wall has no effect, again.

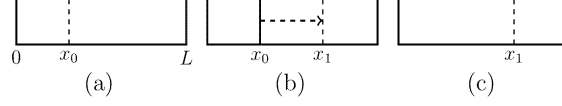


FIG. 1. The adiabatic cycle C of a one-dimensional box, which contains Bose particles. The strength and the position of an additional δ -wall is adiabatically varied during C

In Fig. 2, we depict the parametric dependence of eigenenergies of the single-particle Hamiltonian $H(g, X)$ (1) along C . Throughout this manuscript, we indicate the eigenenergy E using a normalized wavenumber \bar{k} :

$$\bar{k} \equiv \sqrt{\frac{E}{N\epsilon}}, \quad (2)$$

where $\epsilon = (\hbar\pi/L)^2/(2m)$ is the ground eigenenergy of the particle in the infinite square well.

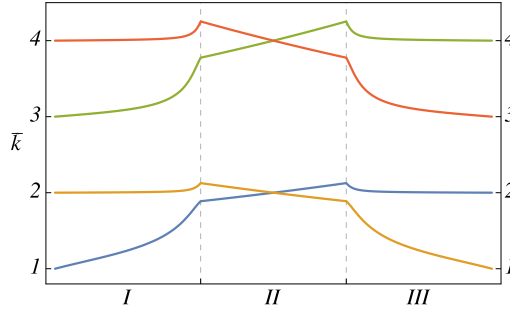


FIG. 2. Parametric evolution of eigenenergies with $N = 1$ along the cycle C , which consists of C_I (left part), C_{II} (middle part) and C_{III} (right part). The eigenenergies are depicted by their normalized wavenumber \bar{k} (2). We set $x_0 = 0.4703L$ and $x_1 = L - x_0$

The adiabatic time evolution of the single-particle system along C depends on x_0 and x_1 . In the following, we explain the case $\frac{2}{5}L < x_0 < \frac{1}{2}L < x_1 < \frac{3}{5}L$, which may be explained from Fig. 2. A more rigorous argument is found in [8].

First, let us consider the case that the initial state is the ground state $|1(g=0, X=x_0)\rangle$ of the particle in the infinite square well, where $|n(g, X)\rangle$ denotes the n -th adiabatic eigenstate of $H(g, X)$ during processes C_I and C_{III} . We will omit to indicate (g, X) in the following. After the completion of C_I , the state vector arrives at $|R_1\rangle$, the ground state of the right well, since we choose the right well in C_{II} is slightly larger than the left well. During C_{II} , there occurs a spectral degeneracy between $|R_1\rangle$ and $|L_1\rangle$, the ground state of the left well. This is because the size of the left (right) well is increasing (decreasing) during C_{II} , and these sizes coincide at $X = L/2$. At the end of C_{II} , $|R_1\rangle$ becomes the first excited state, which adiabatically continued to $|2\rangle$, which is the second excited state of the particle in an infinite square well, through C_{III} . Hence, the ‘‘population inversion’’ in the single-particle system occurs if the system is prepared to be in the ground state initially.

Second, we examine the case that the initial state is the first excited state $|2\rangle$, which offers the ‘‘inverse’’ of the population inversion. Through the adiabatic cycle C , the system arrives at $|L_1\rangle$ after the completion of C_I , and then arrives at $|1\rangle$ at the end of the cycle C . Namely, either $|1\rangle$ and $|2\rangle$ return to the initial states after the completion of the adiabatic cycle C twice.

Third, let us examine the cases that the initial states are $|3\rangle$ and $|4\rangle$, which are the first and second excited state, respectively. Now, C induces an interchange of these two states, through the intermediate states $|R_2\rangle$ and $|L_2\rangle$, which are localized the right and left well during the process II.

A similar interchange of initial eigenstates occurs as a result of the adiabatic cycle C , as long as we choose x_0 and x_1 appropriately. In general, the level crossing of the one-particle Hamiltonian (1) during the process C_{II}

plays an important role to determine which pairs of eigenstates are interchanged by C , while there is no level crossing generically during the processes C_I and C_{III} [8].

We will now comment on the stability of the present scheme for the one-body population inversion. A crucial point is the stability of the adiabatic time evolution across the level crossing during C_{II} . The level crossing may be lifted due to an imperfection of the impenetrable wall, i.e., the δ -wall with an infinite strength. If the level splitting is small enough, we may employ the diabatic process around the avoided crossing to realize the one-body population inversion. It has been shown that an open diabatic process made of a time-dependent potential well produces a second excited state from the ground state of a Bose particle [17]. This diabatic scheme is applied to create collective excitations of interacting bosons [17–19].

3. Non-interacting bosons

We first examine the case that the number of the Bose particles is N , assuming the absence of interparticle interaction. It is straightforward to extend the above result for $N = 1$, once we restrict the case that N bosons initially occupies the one-particle state $|n\rangle$. Hence, the system is in an adiabatic state of the N Bosons:

$$|n^{\otimes N}\rangle \equiv |nn\dots n\rangle, \quad (3)$$

where the one-particle adiabatic state $|n\rangle$ is occupied by N bosons, during C_I and C_{III} .

If there is no interparticle interactions, the parametric evolution of averaged wavenumber \bar{k} for the adiabatic N -particle state agrees with the one for the single-particle system. This suggests that the adiabatic cycle C of the N -particle system with no interaction delivers the ground state $|1^{\otimes N}\rangle$ to the excited state $|2^{\otimes N}\rangle$, i.e., the complete population inversion, as is seen in Figure 2. The energy that the particles acquire during the cycle C is proportional to the number of the particles.

4. Interacting bosons

We now examine the adiabatic cycle C for N interacting Bose particles. We mainly examine the case that the system is initially in the ground state. In order to confirm that the N -particle population inversion really occurs, we need to examine the effect of the interparticle interaction.

We assume that the interparticle interaction V consists of two-body contact interactions. Namely, we suppose that V takes the following form:

$$V(x_1, x_2, \dots, x_N) = \lambda \sum_{\langle i,j \rangle} \delta(x_i - x_j), \quad (4)$$

where λ is the interaction strength, and the summation is taken over pairs. We also assume that the interparticle interaction is weak enough so that the topology of the parametric dependence of eigenenergy remain unchanged, except around the level crossing points of the noninteracting bosons. Namely, when the gaps of the eigenenergies between neighboring levels in the noninteracting system are larger than a constant value, the interparticle interaction shifts the eigenenergy at most $\mathcal{O}(\lambda)$, according to the standard perturbation theory. For small enough perturbative energy correction, the corresponding adiabatic time evolution of the stationary state of the interacting bosons closely follows the evolution of noninteracting bosons.

Accordingly, under the weak interparticle interaction condition, the eigenstates of the interacting bosons can be labeled by the quantum numbers of the noninteracting bosons. For example, the ground state of the initial and final points of the adiabatic cycle C may be denoted as $|1^{\otimes N}(\lambda)\rangle$, whose overlapping integral with the unperturbed state $|1^{\otimes N}\rangle$ is large. Also, $|1^{\otimes N}(\lambda)\rangle$ can be constructed by the standard perturbation theory with a small parameter λ .

On the other hand, even a weak interparticle interaction can strongly influence the parametric evolution of energy levels in the vicinity of level crossings by making avoided crossings. Hence, we need to closely examine the level crossing of the non-interacting Bose particles.

In the following, we argue that the adiabatic time evolution closely follows that of the noninteracting system examined above, if the number of the particles is large enough. The key is the selection rule for the matrix element of V in the adiabatic representation in the vicinity of the level crossings of non-interacting Bosons.

4.1. “Tunneling” and direct contributions of the interaction in $N = 2$

We show that the effect of the interparticle interaction is significantly different, depending on whether a level crossing locates either in C_{II} , or in $C_I \cup C_{III}$, as for the two body case. In the former case, the relevant matrix elements may be small since it involves only tunneling processes through the impenetrable wall. On the other hand, in processes C_I and C_{III} , the matrix element cannot be negligible. However, it seems that there is no corresponding level crossing that affects the population inversion whose initial state is the ground state.

The parametric evolutions of eigenenergies of the noninteracting two particle system are depicted in Fig. 3, in terms of the averaged wavenumber \bar{k} (see, (2)). The parametric evolution of the eigenenergy that connects $|11\rangle$ and $|22\rangle$ has a level crossing with two eigenenergies during C_{II} . The initial states of these energy levels are $|22\rangle$ and $|12\rangle$, which are $|L_1L_1\rangle$ and $|R_1L_1\rangle$ during C_{II} , respectively.

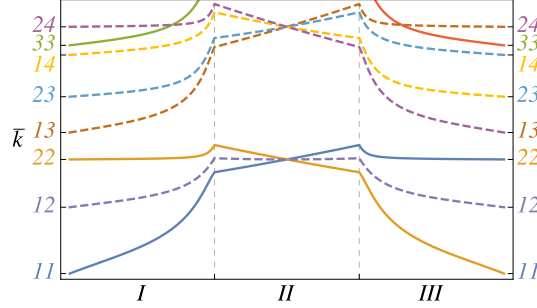


FIG. 3. Parametric evolution of normalized wavenumbers for $N = 2$. Full lines indicate the levels whose initial states are $|nn\rangle$ ($n = 1, \dots, 4$). Other levels are depicted by dashed lines. Parameters are the same as in Fig. 2

We examine the matrix elements of the interparticle interaction term V between the adiabatic basis vectors $|R_1R_1\rangle$, $|L_1L_1\rangle$ and $|R_1L_1\rangle$. Note that $|R_1R_1\rangle$ corresponds to the initial state $|11\rangle$ of the adiabatic cycle:

$$\langle R_1, L_1 | V | R_1, R_1 \rangle = \sqrt{2}\lambda \int_0^L \{\psi_{R_1}(x)\psi_{L_1}(x)\}^* \{\psi_{R_1}(x)\}^2 dx, \quad (5)$$

for example. Since the single-particle adiabatic eigenfunctions $\psi_{L_1}(x)$ and $\psi_{R_1}(x)$ are completely localized in the left and right wells, respectively, the overlapping integral is zero, if the δ -wall is completely impenetrable during C_{II} . The level crossing accordingly remains even in the presence of the interparticle interaction. Thus the adiabatic cycle C induces complete population inversion from $|11\rangle$ to $|22\rangle$, as in the non-interacting case.

Let us examine the case that the δ -wall during C_{II} allows the tunneling leakage of particles due to some imperfections. Still, we may expect that the matrix elements due to the tunneling corrections are exponentially small. Since the resultant energy gap of the avoided crossing is also exponentially small, we may expect that the diabatic process easily almost recovers the complete population inversion.

Also, during the second process C_{II} , the left and right part of the well may be separated. This allows us to make the tunneling correction arbitrarily small. Accordingly, the adiabatic limit that follows the extremely small avoided crossing would be difficult to realize.

Conversely, if the level crossing appears during C_I or C_{III} , the interparticle interaction destroys the level crossing. In Fig. 3, such an example is seen between the levels whose initial states are $|33\rangle$ and $|24\rangle$, which is delivered to $|R_2R_2\rangle$ and $|L_1L_2\rangle$, respectively, in the absence of V .

The matrix element $\langle 33 | V | 24 \rangle$ does not vanish in general, since the relevant single-particle adiabatic eigenfunctions extend the whole box. Accordingly, the level crossings are destroyed to form avoided crossing. Thus the adiabatic process C_I for example, delivers $|33\rangle$ and $|24\rangle$ at the initial point of C_I , to $|L_1L_2\rangle$ and $|R_2R_2\rangle$, respectively. This breaks the population inversion whose initial state is a higher excited state, e.g., the adiabatic cycle C delivers $|33\rangle$ to $|44\rangle$ in the absence of interparticle interaction.

4.2. Selection rule for $N = 3$

Here, we show that the interparticle interactions do not suppress the population inversion for $N > 2$ due to a selection rule of V .

We explain this with the case $N = 3$ (Fig. 4). Let us examine the level whose initial state is $|1^{\otimes 3}\rangle$ along C . The corresponding final state is $|2^{\otimes 3}\rangle$ in the absence of interparticle interaction.

First, the interparticle interaction has no, or exponentially small effect on the level crossing during C_{II} , as shown in the case of $N = 2$.

Second, we examine the level crossing in C_{III} , where the levels whose final states are $|2^{\otimes 3}\rangle$ and $|113\rangle$ exhibit crossing. We examine the matrix element of interparticle interaction $\langle 113 | V | 2^{\otimes 3} \rangle$, which vanishes since V is a two-body interaction, and the set of quantum numbers $(1, 1, 3)$ and $(2, 2, 2)$ has no common quantum number.

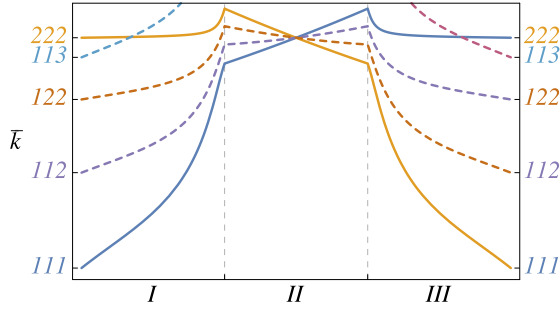


FIG. 4. Parametric evolution of normalized wavenumbers for $N = 3$. Other parameters are the same as in Fig. 3

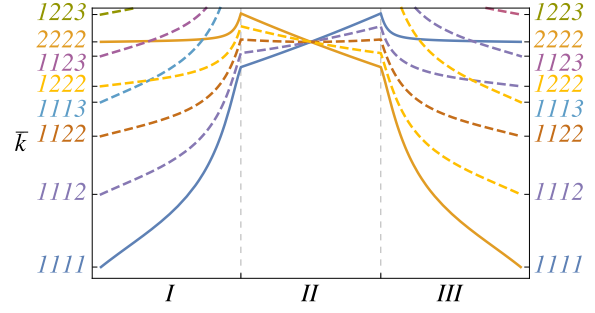


FIG. 5. Parametric evolution of normalized wavenumbers for $N = 4$. Other parameters are the same as in Fig. 3

Still, there may be a tiny avoided crossing whose magnitude can be explained by the standard second-order perturbation theory. We may expect that the diabatic process induces complete population inversion whose final state is $|2^{\otimes 3}\rangle$. Also, even if the interaction strength λ is moderately large, where the topology of the level diagram remains unchanged except that the avoided crossing becomes noticeable, the final state should be $|113\rangle$, whose energy is far larger than the ground state. In this sense, an incomplete population inversion should be realized.

4.3. The population inversion for $N > 2$

We shall prove that the adiabatic cycle C delivers $|1^{\otimes N}\rangle$ to $|2^{\otimes N}\rangle$ for $N > 2$, even in the presence of two-body interparticle interaction. Here, we explain the selection rule for arbitrary $N (> 2)$, and examine each part of the cycle C . For example, $N = 4$ case is shown in Fig. 5.

We explain the selection rule of the two-body interparticle interaction for $N > 2$. Namely, we examine the matrix element $\langle n'_1 n'_2 \dots n'_N | V | n_1 n_2 \dots n_N \rangle$. The matrix element vanishes when the two sets of quantum numbers $(n'_1, n'_2, \dots, n'_N)$ and (n_1, n_2, \dots, n_N) have at least three different elements, i.e., the number of the common quantum numbers is equal to $N - 3$ or less. In other words, non-vanishing matrix element has the following $\langle n'_1 n'_2 n_3 \dots n_N | V | n_1 n_2 n_3 \dots n_N \rangle$ where (n_3, \dots, n_N) are the common quantum numbers.

We examine the first part C_I of C . We assume that the system is initially in the ground state $|1^{\otimes N}(\lambda)\rangle$. According to the selection rule, it is sufficient to examine $|1^{\otimes N-2}\psi, \phi\rangle$, where $|\psi\rangle$ and $|\phi\rangle$ are single particle adiabatic states, e.g. $|2\rangle$. Now, we examine whether the eigenenergies of these states are degenerate. This is equivalent to comparing the eigenenergies corresponding to $|11\rangle$ and $|\psi, \phi\rangle$ of the two particle system. As is seen in Fig. 3, there is no level crossing in C_I . In this sense, there is no effective level crossing with the level $|1^{\otimes N}(\lambda)\rangle$, during C_I .

As for C_{III} , we conclude from a similar argument above, that the energy level corresponding to $|2^{\otimes N}(\lambda)\rangle$ has no effective level crossing.

Next, we examine C_{II} , where the system is in $|R_1^{\otimes N}\rangle$. According to the selection rule, it suffices to examine $|R_1^{\otimes N-2}\psi, \phi\rangle$ with single particle adiabatic states $|\psi\rangle$ and $|\phi\rangle$. To clarify the level crossing, we compare $|R_1 R_1\rangle$ with $|\psi, \phi\rangle$. There are three cases. First, the levels corresponding to $|R_1 R_1\rangle$ and $|R_n, R_{n'}\rangle$ ($(n, n') \neq (1, 1)$) do not occur. Second, the levels corresponding to $|R_1 R_1\rangle$ and $|R_n, L_{n'}\rangle$ exhibit a degeneracy only when $n = 1$ and $n' = 1$, where the corresponding matrix element involves a single-particle tunneling. Third, the levels corresponding to $|R_1 R_1\rangle$ and $|L_n, L_{n'}\rangle$ exhibit a degeneracy only when $n = 1$ and $n' = 1$, where the corresponding matrix element involves two-particle tunneling. Since the matrix elements involving tunneling contribution are exponentially small, the resultant gap should also be small. Hence, the diabatic process should occur even when the speed of the impenetrable wall is moderately slow.

5. Discussion and summary

Here, we argue that the experimental realization of the population inversion suggested in this paper is feasible with the current state of the art. For example, we may utilize the scheme [20] to realize δ -wall with an approximate Gaussian wall.

Another possibility is to use a heavy particle as a wall, whose position may be manipulated by, say, an optical tweezer. The effective interaction between the wall particle and other particle may be tuned by external fields.

We note that the present scheme may offer a way to realize other exotic nonequilibrium states. Let us suppose, for example, the state of bosons is in $|2^{\otimes N}(\lambda)\rangle$, which can be generated from the adiabatic cycle C . After the interparticle interaction λ is adiabatically increased to ∞ , the system arrives the higher excited state of the Tonks-Girardeau system, which may be described by the Lieb-Liniger model with the infinite interparticle interaction strength [21,22]. Similarly, after λ is adiabatically decreased to $-\infty$, the system now arrives at the higher excited state of the super-Tonks-Girardeau system [4]. This state is a much more highly-excited state compared to the super-Tonks-Girardeau state, because the initial state $|2^{\otimes N}(\lambda)\rangle$ is a higher excited state of noninteracting bosons.

We note that the present scheme offers a way to realize the super-Tonks-Girardeau gas in a one-dimensional box. For example, once we obtain $|2^{\otimes N}\rangle$ from $|1^{\otimes N}\rangle$ through the adiabatic cycle C , the system arrives at the super-Tonks-Girardeau gas as the strong attractive interparticle interaction is imposed. This scheme do not require neither the preparation of the Tonks-Girardeau gas [21,22] nor the sudden flip of the interparticle potential [4].

In summary, we have shown that the adiabatic cycle C induces the nearly complete population inversion of the multi-boson system, when the interparticle interaction is not too strong. As pointed out in [8], for a single particle case, the present scheme may be extended to the case of an arbitrary shape of the confinement potential $V(x)$.

Acknowledgements

This research was supported by the Japan Ministry of Education, Culture, Sports, Science and Technology under the Grant number 15K05216.

References

- [1] Berry M.V. Quantal Phase Factors Accompanying Adiabatic Changes. *Proc. Roy. Soc. A*, 1984, **392**, P. 45–57.
- [2] Tanaka A., Miyamoto M. Quasienergy Anholonomy and its Application to Adiabatic Quantum State Manipulation. *Phys. Rev. Lett.*, 2007, **98**, P. 160407.
- [3] Tanaka A., Cheon T. Bloch Vector, Disclination and Exotic Quantum Holonomy. *Phys. Lett. A*, 2015, **379**, P. 1693–1698.
- [4] Haller E., Gustavsson M., et al. Realization of an Excited, Strongly Correlated Quantum Gas Phase. *Science*, 2009, **325**, P. 1224–1227.
- [5] Yonezawa N., Tanaka A., Cheon T. Quantum Holonomy in the Lieb-Liniger Model. *Phys. Rev. A*, 2013, **87**, P. 062113.
- [6] Flügge S. *Practical Quantum Mechanics*, vol. 1. Berlin, Springer-Verlag, 1971.
- [7] Ushveridze A.G. Analytic Properties of Energy Levels in Models with Delta-function Potentials. *J. Phys. A*, 1988, **21**, P. 955–970.
- [8] Kasumie S., Miyamoto M., Tanaka A. Adiabatic Excitation of a Confined Particle in One Dimension with a Variable Infinitely Sharp Wall. *Phys. Rev. A*, 2016, **93**, P. 042105.
- [9] Grynberg G., Aspect A., Fabre C. *Introduction to Quantum Optics*. Cambridge, Cambridge University Press, 2010.
- [10] Astrakharchik G.E., Boronat J., Casulleras J., Giorgini S. Beyond the Tonks-Girardeau Gas: Strongly Correlated Regime in Quasi-One-Dimensional Bose Gases. *Phys. Rev. Lett.*, 2005, **95**, P. 190407.
- [11] Olshanii M. Scattering in the Presence of an External Confinement and a Gas of Impenetrable Bosons. *Phys. Rev. Lett.*, 1998, **81**, P. 938–941.
- [12] Guan X. Critical Phenomena in One Dimension from a Bethe Ansatz Perspective. *Int. J. Mod. Phys. B*, 2014, **28**, P. 1430015.
- [13] Lieb E.H., Liniger W. Exact Analysis of an Interacting Bose Gas. I. The General Solution and the Ground State. *Phys. Rev.*, 1963, **130**, P. 1605–1616.
- [14] Girardeau M. Relationship between Systems of Impenetrable Bosons and Fermions in One Dimension. *J. Math. Phys.*, 1960, **1**, P. 516–523.
- [15] Vitanov N.V., Halfmann T., Shore B.W., Bergmann K. Laser-induced Population Transfer by Adiabatic Passage Techniques. *Annu. Rev. Phys. Chem.*, 2001, **52**, P. 763–809.
- [16] Guérin S., Yatsenko L.P., Jauslin H.R. Dynamical Resonances and the Topology of the Multiphoton Adiabatic Passage. *Phys. Rev. A*, 2001, **63**, P. 031403(R).
- [17] Karkuszewski Z.P., Sacha K., Zakrzewski J. Method for Collective Excitation of a Bose-Einstein Condensate. *Phys. Rev. A*, 2001, **63**, P. 061601.
- [18] Damski B., Karkuszewski Z.P., Sacha K., Zakrzewski J. Simple Method for Excitation of a Bose-Einstein Condensate. *Phys. Rev. A*, 2002, **65**, P. 013604.
- [19] Karkuszewski Z.P., Sacha K., Smerzi A. Mean Field Loops versus Quantum Anti-crossing Nets in Trapped Bose-Einstein Condensates. *Eur. Phys. J. D*, 2002, **21**, P. 251–254.
- [20] Meyrath T.P., Schreck F., et al. Bose-Einstein Condensate in a Box. *Phys. Rev. A*, 2005, **71**, P. 041604(R).
- [21] Paredes B., Widera A., et al. Tonks-Girardeau Gas of Ultracold Atoms in an Optical Lattice. *Nature*, 2004, **499**, P. 277–281.
- [22] Kinoshita T., Wenger T., Weiss D.S. Observation of a One-Dimensional Tonks-Girardeau Gas. *Science*, 2004, **305**, P. 1125–1128.

Crystalline structure and properties of diamond-like materials

E. A. Belenkov¹, M. M. Brzhezinskaya², V. A. Greshnyakov¹

¹Chelyabinsk State University, Bratiev Kashirinykh, 129, Chelyabinsk, 454001, Russia

²Helmholtz-Zentrum Berlin für Materialien und Energie,
Albert-Einstein-Strasse, 15, Berlin, 12489, Germany

belenkov@csu.ru, maria.brzhezinskaya@helmholtz-berlin.de, greshnyakov@csu.ru

PACS 61.50.Ah, 81.05.ug

DOI 10.17586/2220-8054-2017-8-1-127-136

Using density functional theory, the structures and properties of carbon diamond-like phases, all of whose atoms occupy equivalent crystallographic positions, were studied. Structures of these phases were obtained by linking or superposing of carbon clusters. It was found that thirteen such phases can exist. The calculated structural characteristics and properties (density, cohesive energy, bandgap, bulk modulus, hardness, and x-ray diffraction pattern) of the diamond-like phases under study differ significantly from respective parameters of cubic diamond.

Keywords: Diamond crystal, diamond-like carbon, fullerenes, modeling.

Received: 18 September 2016

Revised: 21 November 2016

1. Introduction

Fullerene is a nano-allotropic carbon form consisting of 3-coordinated atoms [1–3] whose structure complies with the Euler’s rule for convex polyhedrons. The fullerene surface is formed by carbon atoms located in the pentagon and hexagon vertices. Fullerenes can be practically used in medicine and nanophotonics, as well as in producing adsorbers, abrasive agents and construction materials [4,5]. Highly strong construction materials may be obtained by bulk compression of fullerene condensates (fullerites). Pioneering work in this field was performed by several research groups [6–9]. When pressure is about 1 GPa and temperature is 200°C, some atoms of fullerite initially consisting only of tri-coordinated carbon atoms begin transforming to the tetra-coordinated state [10]. This gives rise to inter-fullerene covalent bonds and initiates formation of a hybrid structure consisting of tri- and tetra-coordinated atoms. The increase in pressure results in an increase in the fraction of tetra-coordinated atoms; thus, when pressure exceeds 17 GPa, almost all the atoms transfer to the tetra-coordinated state, and phases of diamond-like structures arise [9, 11–13]. Theoretical study of diamond-like phases that can be obtained from fullerenes and carbon clusters was performed in a number of works [14–18]. Theoretical analyses have shown the possibility of existence of six phases of this type: supercubane and tetrahedral diamond [14], “simple cubic fullerite” C₂₄ [15], T-carbon [16], carbon sodalite [17], and face-centered cubic C₁₂ phase (fcc-C₁₂) [18]. Additional investigations should be performed to ascertain if other diamond-like phases can be obtained from carbon clusters. A schematic diagram for deriving diamond-like phases from various precursors was proposed in [19]. Earlier, this scheme was used to study diamond-like phases of the L-, T- and S-groups obtained from graphene layers, carbon nanotubes, and three dimensionally (3D) covalently bonded graphites, respectively [20,21]. This paper presents calculations for the structures and properties of thirteen carbon diamond-like phases with crystallographically equivalent atomic positions simulated by either linking or superposing the last precursor group, namely, carbon clusters.

2. Calculation methods

The diamond-like carbon phases were obtained from carbon clusters consisting of tri-coordinated atoms via the technique described in [19]. Diamond-like phases arising from cluster nanoprecursors of the [0D_c,3] structural group are referred to as C-phases.

Since in this work we studied diamond-like phases with crystallographically equivalent atom positions, clusters with equivalent atom positions were considered as possible precursors for their formation. Such clusters are carbon molecules with carbon skeletons shaped as regular and semi-regular polyhedrons and prisms [19]. The number of regular and semi-regular clusters is limited to three and seven, respectively, while the number of prismatic clusters is infinite. Further decrease in the number of clusters is because any three dimensionally ordered structure of the diamond-like phase can have only 2-, 3-, 4- and 6-fold symmetry axes. Due to this restriction, the following clusters cannot be used as precursors: all 53m semiregular clusters (C₂₀, two polymorphs of C₆₀, and C₁₂₀) and prismatic clusters except for C₆, C₁₂, C₁₆, and C₂₄. In the two last prismatic clusters (C₁₆ and C₂₄), 8- and

12-fold symmetry axes (respectively) may degenerate into the 4- and 6-fold axes in case of changes in lengths of a half of the prism base bonds. Fig. 1 presents carbon clusters used to construct diamond-like phases.

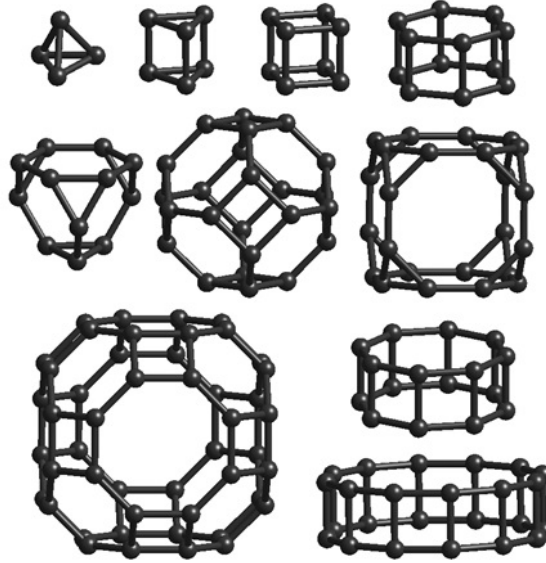


FIG. 1. Fullerene-like clusters

The primary mechanism for modeling C-phase structures is cluster linking that leads to formation of bonds between pairs or groups of atoms of neighboring clusters. Phases formed as a result of cluster linking are referred to as CA-phases [22]. The other method for obtaining diamond-like C-phases consists of superposing equivalent faces of neighboring clusters with subsequent removal of a half of combined atoms. The neighboring clusters may be combined by either vertices, or edges, or faces. In cases where the edges or vertices are combined, the atom coordination number will be five or six, respectively. The atom coordination number in diamond-like phases should be four; this number occurs only when cluster faces are combined. To designate C-phases obtained by superposing carbon clusters, symbols “CB” are used.

To create 3D crystalline structures of diamond-like phases, each cluster should be linked or superposed with minimum three nearest clusters so as to form a structural motif similar to uninodal 3D lattices of the $[3D_c, 3]$ structural group [19]. The cluster coordination number corresponding to close packing may be a maximum of twelve. However, not every type of 3D cluster packing can be used to form C-phases with equivalent atom positions. The possibility of constructing diamond-like phases is restricted by the number and shape of carbon cluster faces. Table 1 presents the results of analyzing all possible coordination numbers of clusters from which diamond-like phases may be derived.

Geometrical optimization of diamond-like phase crystalline structures was performed by using the density functional theory (DFT) method [23] realized in program code Quantum Espresso [24]. Energetic characteristics and densities of the C-phase electronic states were calculated in the Generalized Gradient Approximation (GGA) and Local Density Approximation (LDA) using the B3LYP [25] and Perdew-Zunger [26] exchange-correlation energy functionals respectively. The ion core effect was accounted for via the norm-conserving pseudopotentials. Calculation was performed by using Brillouin-zone k-point grids $12 \times 12 \times 12$ calculated by the Monkhorst-Pack method [27]; the cut-off energy was 60 Rydberg.

Bulk moduli of the diamond-like phases were determined by the method presented in [28]. Atomic volumes and total energies necessary for calculating the bulk moduli were evaluated by the DFT-GGA method at the relative phase volume variation of up to 3.5 %. The phase hardness was calculated by the Li’s method [29]. C-phase powder x-ray diffraction (XRD) patterns were simulated via the standard technique described in [30] assuming that $\lambda_{Cu-\alpha} = 1.5405 \text{ \AA}$ and using the unit cell parameters and atom coordinates calculated by the DFT-LDA method.

3. Results and Discussion

Theoretical analysis performed in the scope of this work showed the possibility of creating fifteen different diamond-like structures from carbon clusters with equivalent atom positions. Fourteen of these structures can be formed by cluster linking, while the remaining structure can be created by cluster superposition. Geometric

TABLE 1. Structural characteristics and coordinations of fullerene-like clusters necessary for obtaining the diamond-like phases

| Cluster | Ring parameter | Point group | Coordination number | |
|-----------------|--|-------------|---------------------|---------------|
| | | | Linking | Superposition |
| C ₄ | 3 ³ | $\bar{4}3m$ | 4 | – |
| C ₆ | 3 ¹ 4 ² | $\bar{6}m2$ | 3, 6 | – |
| C ₈ | 4 ³ | $m\bar{3}m$ | 4, 8 | – |
| C ₁₂ | 4 ² 6 ¹ | $6/mmm$ | 3, 6, 12 | 3 |
| C ₁₂ | 3 ¹ 6 ² | $\bar{4}3m$ | 4, 6, 12 | 4 |
| C ₁₆ | 4 ² 8 ¹ | $8/mmm$ | 4 | 4 |
| C ₂₄ | 4 ¹ 6 ² | $m\bar{3}m$ | 4, 6, 8, 12 | 4, 6 |
| C ₂₄ | 3 ¹ 8 ² | $m\bar{3}m$ | 3, 6, 8, 12 | 3, 8 |
| C ₂₄ | 4 ² 12 ¹ | $12/mmm$ | 6, 12 | 6 |
| C ₄₈ | 4 ¹ 6 ¹ 8 ¹ | $m\bar{3}m$ | 6, 8, 12 | 6, 8, 12 |

optimization of those structures by the DFT method proved the possible stable existence of thirteen diamond-like C-phases whose structures are shown in Fig. 2. Twelve CA-phases (Fig. 2(a-l)) were obtained by linking together carbon clusters depicted in Fig. 1. Clusters corresponding to each phase are presented in Table 2. Only one phase, i.e., CB, was formed by cluster superposition (Table 2). The symmetry of the final phases' crystal lattices did not change in the course of geometrical optimization of initial structures obtained from linked clusters. In the diamond-like phases, the shape of cluster-like structural units remained similar to that of initial clusters. Two C-phases appeared to be unstable: a highly symmetrical (I432) structure formed by linked C₂₄ clusters in the bcc packing and a chiral (P6₂22) structure consisting of polymerized tetrahedral C₄ clusters located in the phase SA2 lattice sites [26]. In the process of DFT optimization, lattice destruction of these phases was observed.

For thirteen C-phases, ring parameters (Wells' parameters), space groups of symmetry, unit cell parameters (a, c, and Z), and deformation parameters (Def and Str) were determined (Table 2). Analyzing the ring parameters of the diamond-like phases, we have found out that C-phase structures inevitably inherit three covalent bond rings that are characteristic of the clusters-precursors (see also Table 1). Three-membered rings were observed in four phases, four-membered rings – in eleven phases, 6-membered rings – in eight phases, 8-membered rings – in nine phases, and twelve-membered rings were observed in the structures of two C-phases. The C-phase unit cells belong to the following syngonies: cubic (CA1, CA3, CA4, CA6–CA9, CA12, CB), hexagonal (CA2, CA11), tetragonal (CA5), and trigonal (CA10) (see Table 2). Calculated unit-cell parameters agree rather well with the experimental parameters for cubic diamond [2], hexagonal diamond (lonsdaleite) [31], C₈ [32], and simple cubic diamond polymorph [33].

Crystalline structure distortion of the diamond-like phases relative to the cubic diamond structure (LA1) is characterized by parameters Def [20] and Str [21]. The C-phase deformation parameter Def accounting for the deviation of the interatomic bond angles of a certain structure from the diamond angle of 109.47° varies from 81.1 (CA6) to 254° (CA1) (Table 2). The C-phase stress parameter Str characterizing deviations of interatomic bond lengths from the diamond bond length ranges from 0.02 (CA6) to 0.25 Å (CA1) for the DFT-GGA method and from 0.01 (CA6) to 0.23 Å (CA1) for the DFT-LDA method (Table 2).

The diamond-like phase densities were determined by using calculated equilibrium parameters of unit cells at zero pressure (Table 3). All the C-phase densities were shown to be lower than the diamond one from 18 to 65% for the CA6 and CA12 phases, respectively.

In addition, cohesive energies (E_{coh}) were determined for the C-phases (their values are listed in Table 3). The cubic diamond (LA1) cohesive energies calculated by the GGA and LDA methods proved to exceed experimental values [34] by 0.49 and 1.59 eV/atom, respectively. Cohesive energies of the diamond-like C-phases proved to be lower than that of diamond by a value ranging from 5.3 (CA6) to 19.2 % (CA12). Phases CA3, CA6, and CB are the most stable among all the C-phases since their cohesive energies are maximal. A correlation between the deformation parameters and the cohesive energy is observed: E_{coh} decreases linearly with increasing a combination of Str and Def (Fig. 3). The dependence presented in Fig. 3 is common for the diamond-like C-phases and diamond-like phases of the L-, T- and S-types previously studied [20–22]. As another evidence of stability of not-yet synthesized carbon C-phases, one can consider the fact that they contain structural units existing in

TABLE 2. Precursors and structural characteristics of diamond-like C-phases based on the GGA and LDA calculations (LDA calculations are given in brackets)

| Phase | Precursor | Ring parameter | Space group | a , Å | c , Å | Z , at. | Def , ° | Str , Å |
|-------------------|-------------------------------|-------------------|--------------|--------------------------|------------------|-----------|------------------|-----------------|
| c -diam. (LA1) | L_6 $p6mm$ | 6^6 | $Fd\bar{3}m$ | 3.597 (3.557) | 3.597 (3.557) | 8 | 0.0 | 0.00 |
| experiment | | | | 3.567^a | 3.567 | | – | – |
| h -diam. (LA2) | L_6 $p6mm$ | 6^6 | $P6_3/mmc$ | 2.528 (2.499) | 4.203 (4.157) | 4 | 1.8 (2.6) | 0.04 (0.03) |
| experiment | | | | 2.52^a | 4.14 | | – | – |
| C_8 (LA4) | L_6 $p6mm$ | 6^6 | $Ia\bar{3}$ | 4.504 (4.448) | 4.504 (4.448) | 16 | 44.99 (46.03) | 0.34 (0.313) |
| experiment | | | | 4.279^a | 4.279 | | – | – |
| CA1 | $C_4(3^3)$ | $3^3 12^3$ | $Fd\bar{3}m$ | 7.588 (7.516) | 7.588 (7.516) | 32 | 254 (254) | 0.25 (0.23) |
| CA2 | C_6 ($3^1 4^2$) | $3^1 4^2 8^3$ | $P6_3/mmc$ | 5.015 (4.949) | 5.062 (5.031) | 12 | 153 (152) | 0.13 (0.12) |
| CA3 | $C_8(4^3)$ | $4^3 8^3$ | $Im\bar{3}m$ | 4.895 (4.851) | 4.895 (4.851) | 16 | 106 (106) | 0.19 (0.21) |
| CA4 | C_{24} ($4^1 6^2$) | $4^3 6^2 8^1$ | $Pm\bar{3}m$ | 5.946 (5.891) | 5.946 (5.891) | 24 | 105 (105) | 0.20 (0.21) |
| experiment | | | | 5.545^a | 5.545 | | – | – |
| CA5 | C_{16} ($4^2 8^1$) | $4^3 8^3$ | $I4/mmm$ | 7.185 (7.124) | 4.802 (4.730) | 32 | 114 (114) | 0.13 (0.13) |
| CA6 | C_{24} ($4^1 6^2$) | $4^2 6^4$ | $Im\bar{3}m$ | 4.393 (4.352) | 4.393 (4.352) | 12 | 81.1 (81.1) | 0.02 (0.01) |
| CA7 | C_{48} ($4^1 6^1 8^1$) | $4^3 6^1 8^2$ | $Im\bar{3}m$ | 7.552 (7.477) | 7.552 (7.477) | 48 | 120 (120) | 0.09 (0.09) |
| CA8 | C_{48} ($4^1 6^1 8^1$) | $4^3 6^1 8^2$ | $Im\bar{3}m$ | 9.319 (9.228) | 9.319 (9.228) | 96 | 109 (109) | 0.12 (0.13) |
| CA9 | C_{24} ($4^1 6^2$) | $4^3 6^2 12^1$ | $Fd\bar{3}m$ | 12.44 (12.32) | 12.44 (12.32) | 192 | 114 (114) | 0.11 (0.12) |
| CA10 | C_{12} ($4^2 6^1$) | $4^3 6^1 8^2$ | $R\bar{3}m$ | 6.843 (6.783) | 7.371 (7.262) | 36 | 109 (109) | 0.18 (0.18) |
| CA11 | C_{12} ($4^2 6^1$) | $4^3 6^1 8^2$ | $P6_3/mmc$ | 6.831 (6.779) | 4.966 (4.890) | 24 | 110 (110) | 0.15 (0.15) |
| CA12 | $C_4(3^3)$ | $3^3 8^1 12^2$ | $Im\bar{3}m$ | 9.249 (9.157) | 9.249 (9.157) | 48 | 252 (252) | 0.23 (0.22) |
| CB | C_{48} ($4^1 6^1 8^1$) | $3^1 4^1 6^2 8^2$ | $Fm\bar{3}m$ | 9.513 (9.420) | 9.513 (9.420) | 96 | 141 (141) | 0.13 (0.12) |

^aRef. [2]; ^bRef. [31]; ^cRef. [32]; ^dRef. [33]

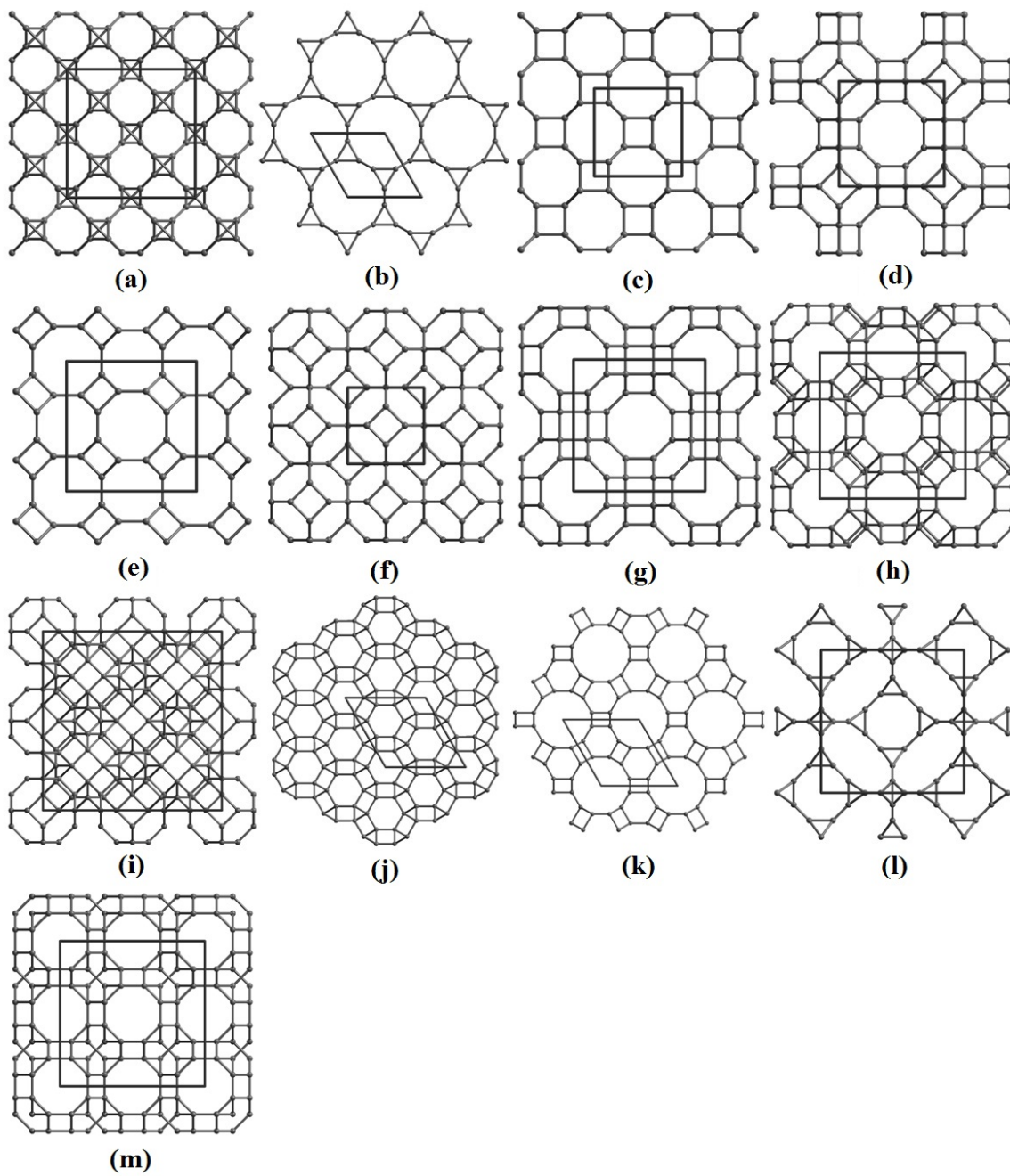


FIG. 2. The diamond-like phase structure projection onto the (001)-plane: (a) CA1; (b) CA2; (c) CA3; (d) CA4; (e) CA5; (f) CA6; (g) CA7; (h) CA8; (i) CA9; (j) CA10; (k) CA11; (l) CA12; (m) CB

TABLE 3. Density, cohesive energy (E_{coh}), bandgap (E_g), bulk modulus (B_0) and hardness (H) of diamond-like C-phases calculated by the GGA and LDA methods (LDA calculations are given in brackets)

| Phase | Density, g/cm ³ | E_{coh} , eV/atom | E_g , eV | B_0 , GPa | H , GPa |
|----------------|----------------------------|-------------------------|-------------------------|------------------------|-----------------------|
| c-diam. (exp.) | 3.517^a | 7.37^b | 5.48^b | 443^b | 90^c |
| LA1 | 3.428 (3.546) | 7.86 (8.96) | 5.44 (4.61) | 445 | 86.6 (90.8) |
| LA2 | 3.429 (3.549) | 7.83 (8.93) | 5.03 (3.64) | 445 | 86.5 (90.7) |
| LA4 | 3.492 (3.627) | 7.11 (8.22) | 2.70 (2.12) | 410 | 86.0 (90.5) |
| CA1 | 1.461 (1.503) | 6.43 (7.32) | 2.41 (1.98) | 177 | 36.5 (38.1) |
| CA2 | 2.171 (2.242) | 6.92 (7.87) | 1.90 (1.55) | 250 | 54.4 (56.9) |
| CA3 | 2.720 (2.795) | 7.15 (8.15) | 3.95 (3.06) | 346 | 67.6 (70.2) |
| CA4 | 2.276 (2.342) | 7.06 (8.04) | 2.91 (2.30) | 285 | 55.9 (58.2) |
| CA5 | 2.575 (2.658) | 6.97 (7.97) | 2.66 (1.92) | 316 | 63.8 (66.7) |
| CA6 | 2.824 (2.904) | 7.44 (8.46) | 3.96 (3.18) | 351 | 70.9 (73.8) |
| CA7 | 2.223 (2.290) | 6.86 (7.84) | 3.32 (2.68) | 270 | 54.6 (56.9) |
| CA8 | 2.366 (2.436) | 6.96 (7.95) | 3.11 (2.50) | 275 | 58.3 (60.7) |
| CA9 | 1.987 (2.048) | 6.82 (7.79) | 3.69 (3.03) | 239 | 48.3 (50.4) |
| CA10 | 2.402 (2.482) | 7.02 (8.00) | 4.37 (3.56) | 273 | 59.3 (62.0) |
| CA11 | 2.386 (2.459) | 6.98 (7.97) | 4.18 (3.35) | 280 | 58.8 (61.4) |
| CA12 | 1.210 (1.247) | 6.35 (7.24) | 2.14 (1.72) | 141 | 29.6 (30.9) |
| CB | 2.224 (2.290) | 7.16 (8.14) | 3.34 (2.70) | 278 | 56.3 (58.6) |

^aRef. [2]; ^bRef. [34]; ^cRef. [35]

synthesized saturated hydrocarbons. These phases are: (i) CA1 whose structure is based on fragments like the carbon tetrahedral skeleton of the tetrahedrane molecule [36]; (ii) CA2 containing carbon skeleton fragments similar to the carbon skeleton of experimentally obtained prismane [37]; (iii) CA3 and CA4 whose structural elements look like the cubane molecule carbon skeleton [38]; (iv) CA6 consisting of the four-membered carbon rings.

Figure 4 presents calculated electronic densities of states (DOS) of the cubic diamond and diamond-like phases derived from carbon clusters. From the DOS patterns, the bandgaps (E_g) of the phases under study were obtained (Table 3). The diamond bandgap calculated by the GGA and LDA methods differ from the experimental value [34] by 0.04 and 0.87 eV, respectively. Calculations have shown that the diamond-like phase bandgaps are narrower than that of LA1 by values varying from 20 (CA10) to 66 % (CA2), i.e., C-phases are either semiconductors or insulators. Semiconductor properties may be exhibited by carbon materials based on the CA2 and CA12 phases whose structures are formed by great numbers of covalently bonded prismatic or tetrahedral clusters, respectively. Other C-phases have wider bandgaps typical for insulators. We have determined that the bandgap decreases with increasing deformation parameter Str.

To assess the mechanical characteristics of the diamond-like phases, bulk moduli (at high compression: $0.965 < V/V_0 < 1$) and Knoop hardness (see Table 3) were calculated. Calculations of bulk modulus B_0 and hardness H of the cubic diamond fit well the measurements [34,35]. The bulk moduli of all the C-phases are below the LA1 B_0 by 21–68 %. Phases CA3, CA5, and CA6 are expected to be the least compressible among the C-phases since their bulk moduli are comparable with that of titanium nitride [39]. A linear decrease in B_0 is observed when parameter Def increases. Theoretical hardness of the C-phases is also lower than the diamond hardness by 18 to 66 %. The densest phases CA3 and CA6 should exhibit high strength characteristics comparable with those of boron nitride [40]. Theoretical hardness of other C-phases is higher than that of silicon carbide or almost the same [40].

XRD patterns of the diamond-like phases were calculated based on structural data obtained by the LDA method; this approximation was chosen since it provides the best fit between the calculated and measured parameters of the cubic diamond and lonsdaleite unit cells (see Table 2). The obtained C-phase XRD patterns were compared with the experimental XRD patterns of cubic diamond [41], lonsdaleite [31], cubic diamond polymorph [33], hexagonal (2H) graphite [42], and also with those of fcc C₆₀ [43] and hexagonal close-packed (hcp) C₇₀ [44];

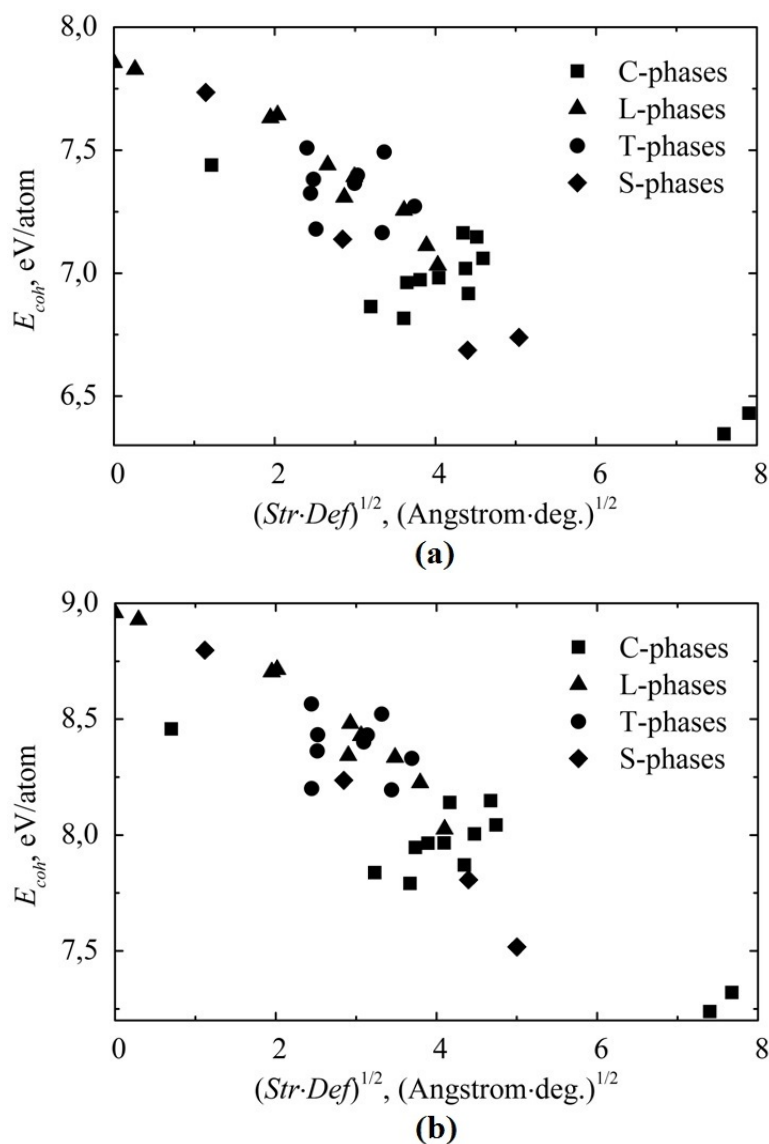


FIG. 3. Dependences of the cohesive energy (E_{coh}) on the deformation parameters (Str and Def), obtained by the DFT-GGA (a) and DFT-LDA (b) methods

three main diffraction peaks are given for each in Table 4. The comparison has shown that XRD patterns of all the C-phases differ significantly from those of diamond, lonsdaleite, and cubic diamond polymorph. XRD patterns of theoretically studied diamond-like phases are comparable with those of carbon compounds consisting of 3-coordinated atoms. For instance, positions of the CA3-phase 100 % maximum and CA10-phase 9.7 % maximum have been shown to be close to the main 002-maximum of graphite ($\Delta d \sim 0.05$ Å). The most intense maxima of phases CA1 and CA2 are located close to the 70 %-maximum 311 of fullerite C_{60} ($\Delta d \sim 0.05$ Å). In the case of the CA7 diamond-like phase, the 100 % maximum almost coincides with the main 110 peak of fullerite C_{70} ($\Delta d = 0.01$ Å). In addition, the 79 % maximum 112 of fullerite C_{70} may be overlapped by the 100 % maxima of phases CA8 and CA10 ($\Delta d \sim 0.07$ Å). The main diffraction maxima of phases CA1, CA2, CA4, CA7–CA12, and CB are within the diffraction angle range (2θ) of 12.4 to 20.6 °, which makes much easier to identify these phases. The most intense peaks of diamond-like phases CA3, CA5, and CA6 are rather close (25.0–29.0 °) to the 100 % maximum of hexagonal graphite; however, it may be possible to identify them by secondary diffraction peaks.

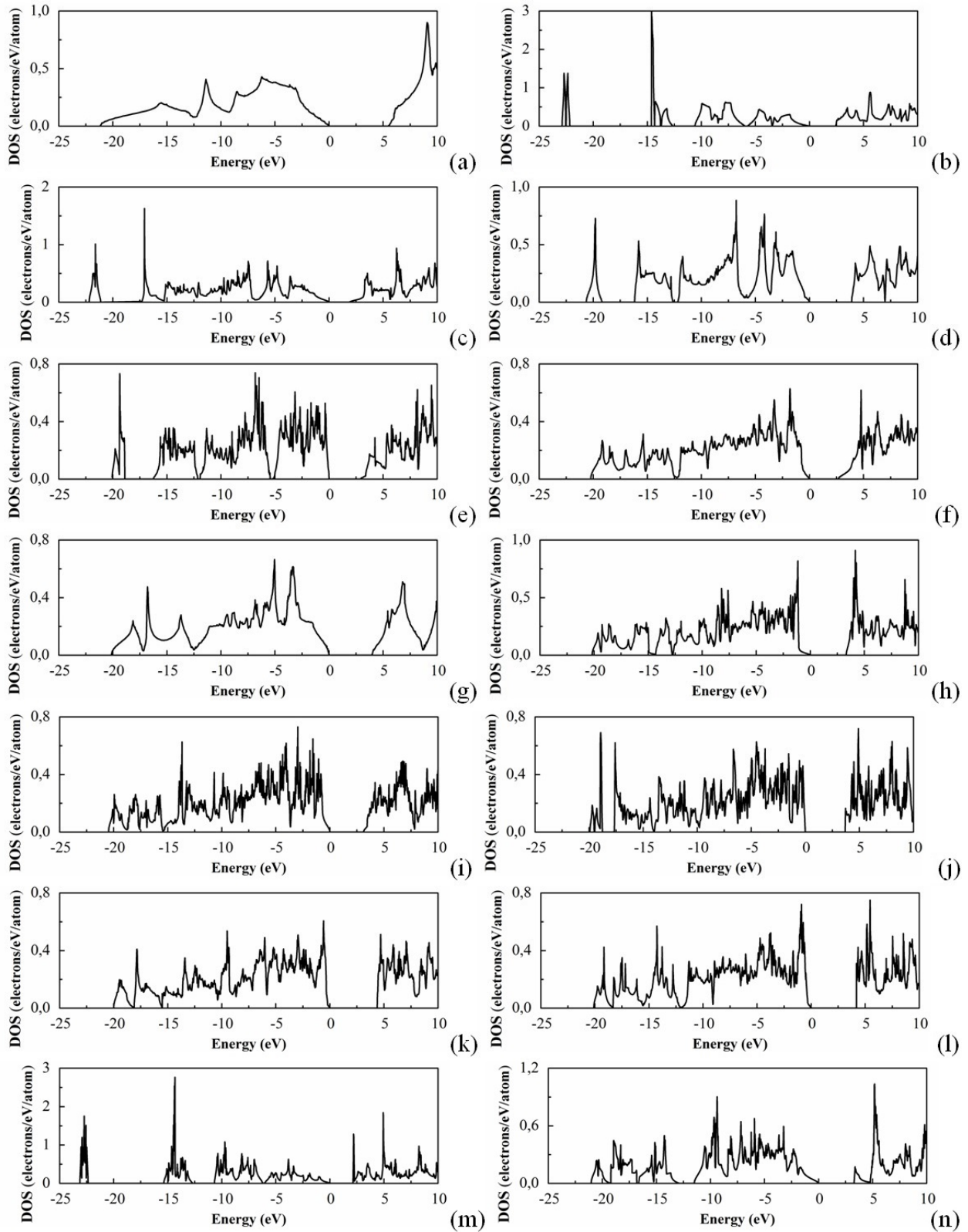


FIG. 4. Electronic density of states of diamond-like phases (the maximum energy of valence band electrons is assumed to be zero): (a) LA1; (b) CA1; (c) CA2; (d) CA3; (e) CA4; (f) CA5; (g) CA6; (h) CA7; (i) CA8; (j) CA9; (k) CA10; (l) CA11; (m) CA12; (n) CB

TABLE 4. The most intense x-ray diffraction maxima of synthesized carbon compounds and theoretically studied diamond-like phases (d and I are the interplanar distance and relative intensity of the diffraction peak, respectively)

| Phase | $d_1, \text{Å}$ | $I_1, \%$ | $d_2, \text{Å}$ | $I_2, \%$ | $d_3, \text{Å}$ | $I_3, \%$ |
|---|-----------------|-----------|-----------------|-----------|-----------------|-----------|
| diamond ^a | 2.060 | 100 | 1.261 | 27 | 1.0754 | 16 |
| lonsdaleite ^b | 2.19 | 100 | 2.06 | 100 | 1.26 | 75 |
| cubic phase ^c | 2.770 | 100 | 2.467 | 100 | 3.208 | 50 |
| 2H graphite ^d | 3.376 | 100 | 2.039 | 6 | 1.6811 | 4 |
| <i>fcc</i> C ₆₀ ^e | 8.160 | 100 | 5.007 | 92 | 4.272 | 70 |
| <i>hcp</i> C ₇₀ ^f | 5.294 | 100 | 4.510 | 79 | 8.630 | 63 |
| CA1 | 4.339 | 100 | 2.657 | 8.9 | 2.170 | 3.5 |
| CA2 | 4.304 | 100 | 3.270 | 33.2 | 2.152 | 8.0 |
| CA3 | 3.430 | 100 | 2.426 | 33.8 | 1.534 | 23.3 |
| CA4 | 5.891 | 100 | 4.165 | 28.9 | 3.401 | 14.1 |
| CA5 | 3.562 | 100 | 3.941 | 63.3 | 2.643 | 31.0 |
| CA6 | 3.077 | 100 | 1.777 | 19.1 | 1.256 | 12.4 |
| CA7 | 5.287 | 100 | 3.052 | 19.4 | 3.739 | 7.6 |
| CA8 | 4.614 | 100 | 6.526 | 54.5 | 2.918 | 9.7 |
| CA9 | 7.113 | 100 | 4.356 | 5.1 | 3.715 | 3.5 |
| CA10 | 4.548 | 100 | 3.393 | 9.7 | 2.122 | 3.6 |
| CA11 | 5.871 | 100 | 3.758 | 27.4 | 3.390 | 13.9 |
| CA12 | 6.475 | 100 | 3.738 | 13.9 | 4.579 | 7.5 |
| CB | 4.710 | 100 | 5.439 | 27.9 | 2.840 | 14.4 |

^aRef. [41]; ^bRef. [31]; ^cRef. [33]; ^dRef. [42]; ^eRef. [43]; ^fRef. [44]

4. Conclusions

In this paper, we have theoretically calculated structures and properties of carbon diamond-like phases derived from carbon clusters. Crystalline structures of twelve C-phases were modeled by cluster linking. The structure of one of the phases (CB) was formed by cluster superposition. Based on the DFT-GGA and DFT-LDA calculations, various structural characteristics, densities, cohesive energies, bandgaps, bulk moduli, and hardness have been determined for the C-phases. To make possible experimental identification of diamond-like phases, powder XRD patterns were simulated. We also revealed a correlation between the structural parameters and properties of the diamond-like phases derived from carbon clusters, namely: density, cohesive energy, bulk modulus and bandgap decrease with increasing deformation parameters characterizing the phase structure stress with respect to the cubic diamond.

Acknowledgements

The reported study was funded by RFBR according to the research project No. 16-33-00030 mol.a.

References

- [1] Smalley R.E. Discovering the fullerenes (Nobel lecture). *Angewandte Chemie International Edition in English*, 1997, **36** (15), P. 1595–1601.
- [2] Pierson H.O. *Handbook of carbon, graphite, diamond, and fullerenes: properties, processing, and application*. Noyes, Park Ridge, New Jersey, 1993, 402 p.
- [3] Dresselhaus M.S., Dresselhaus G., Eklund P.C. *Science of fullerenes and carbon nanotubes*. XVIII, Academic Press, San Diego, 1996, 965 p.
- [4] Sheka E. *Fullerenes: nanochemistry, nanomagnetism, nanomedicine, nanophotonics*. CRC Press, Taylor & Francis Group, Boca Raton, 2011, 312 p.
- [5] Osawa E. *Perspectives of fullerene nanotechnology*. Kluwer Academic Pub., Dordrecht-Boston-London, 2002, 386 p.
- [6] Nunez-Regueiro M., Monceau P., Rassat A., Bernier P., Zahab A. Absence of a metallic phase at high pressure in C₆₀. *Nature*, 1991, **354**, P. 289–291.

- [7] Duclos S.J., Brister K., Haddon R.C., Kortan A.R., Thiel F.A. Effects of pressure and stress on C₆₀ fullerite to 20 GPa. *Nature*, 1991, **351**, P. 380–382.
- [8] Yoo C.S., Nellis W.J. Phase transformations in carbon fullerenes at high shock pressures. *Science*, 1991, **254**, P. 1489–1491.
- [9] Moshary F., Chen N.H., Silvera I.F., Brown C.A., Dorn H.C., de Vries M.S., Bethune D.S. Gap reduction and the collapse of solid C₆₀ to a new phase of carbon under pressure. *Physical Review Letters*, 1992, **69**, P. 466–469.
- [10] Bashkin I.O., Rashchupkin V.I., Gurov A.F., Moravsky A.P., Rybchenko O.G., Kobelev N.P. A new phase transition in the T-P diagram of C₆₀ fullerite. *Journal of Physics: Condensed Matter*, 1994, **6**, P. 7491–7498.
- [11] Nunez-Regueiro M., Monceau P., Hodeau J.-L. Crushing C₆₀ to diamond at room temperature. *Nature*, 1992, **355**, P. 237–239.
- [12] Hodeau J.-L., Tonnerre J.M., Bouchet-Fabre B., Nunez-Regueiro M., Capponi J.J., Perroux M. High-pressure transformations of C₆₀ to diamond and sp³ phases at room temperature and to sp² phases at high temperature. *Physical Review B*, 1994, **50**, P. 10311–10314.
- [13] Hirai H., Kondo K.-I., Ohwada T. Quenching a transition of C₆₀ fullerene to diamond under shock compression. *Carbon*, 1993, **31**(7), P. 1095–1098.
- [14] Burdett J.K., Lee S. The moments method and elemental structures. *Journal of the American Chemical Society*, 1985, **107**, P. 3063–3082.
- [15] Pokropivny V.V., Pokropivny A.V. Structure of “cubic graphite”: simple cubic fullerite C₂₄. *Physics of the Solid State*, 2004, **46**(2), P. 392–394.
- [16] Chen X.-Q., Niu H., Franchini C., Li D., Li Y. Hardness of T-carbon: density functional theory calculations. *Physical Review B*, 2011, **84**, P. 121405(R).
- [17] Pokropivny A., Volz S. “C₈ phase”: supercubane, tetrahedral, BC-8 or carbon sodalite? *Physica Status Solidi B*, 2012, **249**(9), P. 1704–1708.
- [18] Hu M., Tian F., Zhao Z., Huang Q., Xu Bo, Wang Li-M., Wang H.-T., Tian Y., He J. Exotic cubic carbon allotropes. *The Journal of Physical Chemistry C*, 2012, **116**, P. 24233–24238.
- [19] Belenkov E.A., Greshnyakov V.A. Classification schemes of carbon phases and nanostructures. *New Carbon Materials*, 2013, **28**(4), P. 273–283.
- [20] Belenkov E.A., Brzhezinskaya M.M., Greshnyakov V.A. Novel carbon diamond-like phases LA5, LA7 and LA8. *Diamond and Related Materials*, 2014, **50**, P. 9–14.
- [21] Belenkov E.A., Greshnyakov V.A. Structures and properties of diamond-like phases derived from carbon nanotubes and three-dimensional graphites. *Journal of Materials Science*, 2015, **50**(23), P. 7627–7635.
- [22] Belenkov E.A., Greshnyakov V.A. New structural modifications of diamond: LA9, LA10, and CA12. *Journal of Experimental and Theoretical Physics*, 2014, **119**(1), P. 101–106.
- [23] Hohenberg P., Kohn W. Inhomogeneous electron gas. *Physical Review*, 1964, **136**(3B), P. 864–871.
- [24] Giannozzi P., Baroni S., Bonini N., Calandra M., Car R., Cavazzoni C., Ceresoli D., Chiarotti G.L., Cococcioni M., Dabo I., Corso A.D., de Gironcoli S., Fabris S., Fratesi G., Gebauer R., Gerstmann U., Gougousis C., Kokalj A., Lazzeri M., Martin-Samos L., et al. QUANTUM ESPRESSO: a modular and open-source software project for quantum simulations of materials. *Journal of Physics: Condensed Matter*, 2009, **21**(39), P. 395502.
- [25] Becke A.D., Density-functional thermochemistry. III. The role of exact exchange. *The Journal of Chemical Physics*, 1993, **98**, P. 5648–5652.
- [26] Perdew J.P., Zunger A. Self-interaction correction to density-functional approximations for many-electron systems. *Physical Review B*, 1981, **23**(10), P. 5048–5079.
- [27] Monkhorst H.J., Pack J.D. Special points for Brillouin-zone integrations. *Physical Review B*, 1976, **13**(12), P. 5188–5192.
- [28] Greshnyakov V.A., Belenkov E.A. Technique for calculating the bulk modulus. *Russian Physics Journal*, 2014, **57**(6), P. 731–737.
- [29] Li K., Wang X., Zhang F., Xue D. Electronegativity identification of novel superhard materials. *Physical Review Letters*, 2008, **100**, P. 235504.
- [30] Guinier A. *Theorie et technique de la radiocristallographie*. 3-rd ed., A. Dunod, Paris, 1964, 740 p.
- [31] Bundy F.P., Kasper J.S. Hexagonal diamond – a new form of carbon. *The Journal of Chemical Physics*, 1967, **46**(9), P. 3437–3446.
- [32] Matyushenko N.N., Strel'nitskii V.E., Gusev V.A. A dense new version of crystalline carbon C₈. *Journal of Experimental and Theoretical Physics Letters*, 1979, **30**(4), P. 199–202.
- [33] Aust R.B., Drickamer H.G. Carbon: a new crystalline phase. *Science*, 1963, **140**(3568), P. 817–819.
- [34] Kittel C. *Introduction to solid states physics*. 7-th ed., Wiley, New York, 1996, 673 p.
- [35] Brookes C.A., Brookes E.J. Diamond in perspective: a review of mechanical properties of natural diamond. *Diamond and Related Materials*, 1991, **1**, P. 13–17.
- [36] Maier G., Pfriem S., Schafer U., Matusch R. Tetra-tert-butyltetrahedrane. *Angewandte Chemie International Edition in English*, 1978, **17**(7), P. 520–521.
- [37] Katz T.J., Acton N. Synthesis of prismane. *Journal of the American Chemical Society*, 1973, **95**(8), P. 2738–2739.
- [38] Eaton P.E., Cole T.W. Jr. The cubane system. *Journal of the American Chemical Society*, 1964, **86**, P. 962–964.
- [39] Chen H., Peng F., Mao Ho-K., Shen G., Liermann H.-P., Li Z., Shu J. Strength and elastic moduli of TiN from radial x-ray diffraction under nonhydrostatic compression up to 45 GPa. *Journal of Applied Physics*, 2010, **107**, P. 113503.
- [40] Chen X.-Q., Niu H., Li D., Li Y. Modeling hardness of polycrystalline materials and bulk metallic glasses. *Intermetallics*, 2011, **19**, P. 1275–1281.
- [41] Powder Diffraction File Number 6-675. Inorganic Crystal Structure Database. FIZ Karlsruhe, Leibniz-Institut für Informationsinfrastruktur GmbH.
- [42] Powder Diffraction File Number 41-1487. Inorganic Crystal Structure Database. FIZ Karlsruhe, Leibniz-Institut für Informationsinfrastruktur GmbH.
- [43] Powder Diffraction File Number 44-558. Inorganic Crystal Structure Database. FIZ Karlsruhe, Leibniz-Institut für Informationsinfrastruktur GmbH.
- [44] Powder Diffraction File Number 48-1206. Inorganic Crystal Structure Database. FIZ Karlsruhe, Leibniz-Institut für Informationsinfrastruktur GmbH.

The polymer composites' morphological structure simulation

S. A. Drozdov, V. G. Nazarov, S. A. Nozdrachev, Yu. V. Rudyak, G. O. Rytikov

Moscow Polytechnic University, Pryanishnikova st., 2A, Moscow, 127550, Russia

sergcuxi@rambler.ru

PACS 68.55.Nq

DOI 10.17586/2220-8054-2017-8-1-137-145

The digital two-dimensional Fourier decomposition of surface scanning electron microscopy (SEM) micrographs is used to detect the regular morphological structures on a polymer composite surface. Analyzing the SEM images of fluorinated and sulfonated low density polyethylene (LDPE), we identify and specify both regular and irregular submicron surface structures. The possibility of similar information processing techniques generalization for the morphological simulating of modified polymers bulk structures is discussed.

Keywords: Surface and bulk modification of polymers, gas-phase fluorination and sulfonation, surface structure, image processing and analysis, scanning electron microscopy.

Received: 20 July 2016

Revised: 28 November 2016

1. Introduction

The polymer composite material is a solid two- or multicomponent system based on polymeric matrix with some fillers and/or ingredients located in a volume or on the surface [1]. The main advantages of such materials include a significant improvement in some physicochemical and mechanical properties compared to the properties of merging the composite material's individual components. The considerable enhancement of the mechanical (deformation, elastic and endurance), thermo- and electrical properties, as well as wettability, permeability, radiation resistance and other properties of polymer composite materials was noted and investigated [2–7].

Recently, additive manufacturing technology for polymer composite synthesis has spread. Some characteristics of polymer matrix surface layers are changed under the chemical, mechanical, thermal or complex influences in the “surface modification” case. The “bulk modification” of polymer matrix is implemented as the formation of inclusions, cracking, chemical heterogeneities, etc. and used mostly at the stage of polymerization. However, additive technologies in the “bulk modification” case are also applicable [8–17].

The influence of the surface and bulk morphology of a composite on its' chemical, mechanical, thermal and other properties has been repeatedly noted [18–25]. Great attention was not only paid to the chemical composition of the polymer matrix, modifiers and intensity of interfacial interaction, but also to the morphological structure of the surfaces and volumes of the objects under consideration when describing the properties of polymer composite materials [9, 16, 21]. The role of surface and bulk morphology was mainly observed at the qualitative level and was followed by a demonstration of images received by means of electronic, optical near-field, atomic force and other special microscopy [18, 25, 28–30].

Mathematical function of the profile cross sections of the considered sample [2], some collective integrated generalized characteristics (waviness, roughness, etc) [31, 32] or the empirical distributions on any parameters [25, 33, 34] were used for the qualitative description of regular structures' shapes. However, the applied methods revealing the localization of inhomogeneities and techniques to construct the corresponding empirical distributions in the reviewed articles were not published.

The present work is devoted to the development of an approach for the description of topographic and stereometric properties of polymer composites obtained in various ways. It is anticipated that the approach will allow comparison of the morphological structure of the materials and, to some extent, to analyze the relationships between individual physicochemical properties and characteristics of the detected structures. The task of building the integrated structural-functional models of developed polymer composites is very important, because experiments to develop new polymer composite materials which possess a set of defined physicochemical properties are often quite expensive and quite complex technically.

2. The experimental data

Some different polymer composites had their physical properties investigated (e.g. wettability, permeability, strength, etc.) and their surfaces were subjected to imaging [35–38].

The images of surfaces of polymer composites made on the basis of low density polyethylene (LDPE) resulting from ~ 30 minutes sulfonation and ~ 15 minutes fluorination are presented in Fig. 1a and Fig. 1b, respectively.

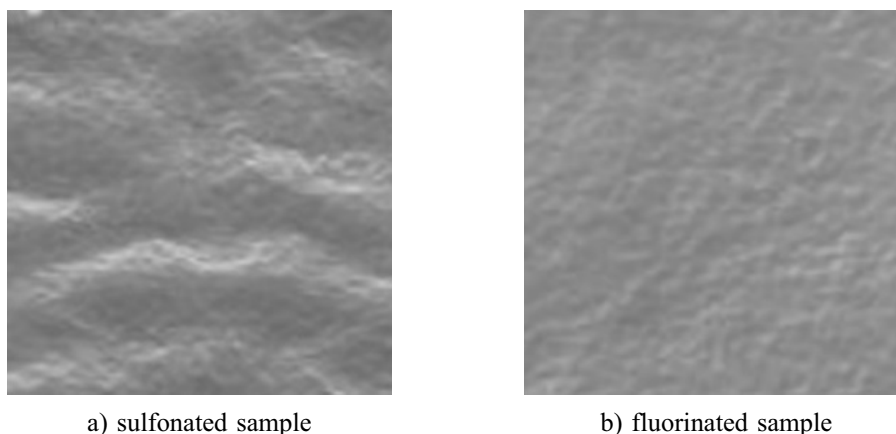


FIG. 1. SEM-micrographs of the samples' surfaces for the a) sulfonated and b) fluorinated samples

The images were reduced to the same scale for standardization of the data processing procedures. Further digital processing was subjected to square sub images of 128 by 128 pixels. The typical pixel size for the presented images was $\sim 0.04 \mu\text{m}$. Digital images of the surfaces of the samples are characterized by horizontal and vertical resolution. The horizontal resolution here is the number of pixels per unit length (e.g., 300 dpi is 300 pixels per inch). Vertical resolution here means the maximum number available in the used encoding format of image gradation values of pixels' brightness (luminance for displays or optical density for printing stamps). The vertical resolution of represented images is 8 bits, which corresponds to 256 possible levels of pixel brightness (from 0 ("black") to 255 ("white") with increment of 1). And "unit" change of pixel's brightness corresponds to ~ 2 nm changing of the local relief height.

The traditional way of quantitatively describing the surface structures is the construction of empirical probability distributions on any parameters (see, for example, [18, 25, 38]). The empirical distributions of the observed non-periodic structures from the amounts of pixels forming them were built taking into account features of digital image presentation formats. "The observed non-periodic structure" here refers to a region of the image, bounded by the closed contour formed by pixels of the same brightness. Such distributions actually coincide with the distributions of the probability of observing a heterogeneous surface structure depending on the square of the projection of this structure on a horizontal plane. This method can be applied when the observed surface features are few, and they are obviously non-periodic [39].

The empirical distributions histograms of quantities of the "observed" structures for the sulfonated and for the fluorinated polymeric samples are presented in Fig. 2a and Fig. 2b respectively.

It is clearly seen that the sulfonated (a) and the fluorinated (b) polymer matrices are characterized by significantly different empirical distributions of their images' pixels' brightness. The empirical distribution of submicron objects for the fluorinated sample is much narrower than for the sulfonated one. The observed fractions of "convex" and "concave" objects are significantly different in case (a) and approximately the same in case (b). This is due to the fact that the sulfonation generates micro-sized cavities on the surface of experimental samples and the fluorination contributes to the increase in its average roughness [37, 38].

3. The surface morphological structures simulating

3.1. Concept

It is obvious that the above method of quantitatively describing the composite surface features does not allow one to restore the morphological structure of the sample surface, and requires considerable effort to ensure the possibility of comparison of results obtained by different research groups (e.g. selection of base level and cutoff level [39] are not standardized and implemented by researchers arbitrarily). We believe that the leading candidate for a unified way of constructing morphological patterns of the sample surfaces is their representation in the form

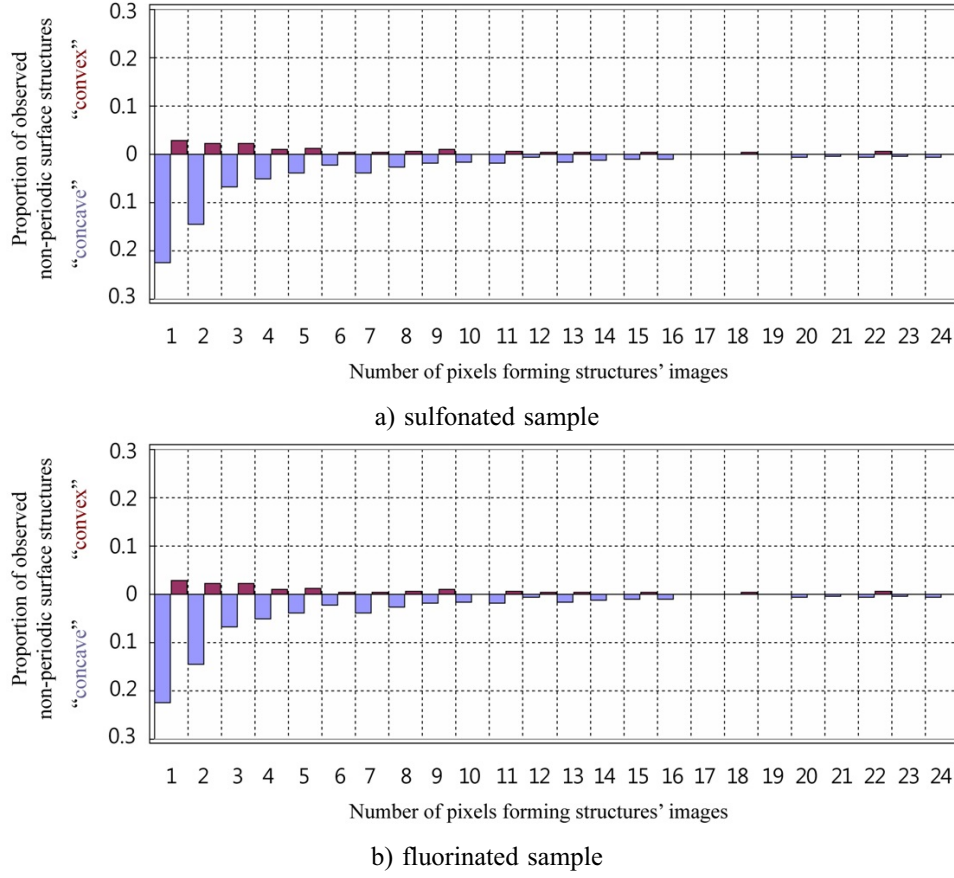


FIG. 2. The empirical distributions of the “observed” structures for the a) sulfonated and b) fluorinated samples

of a linear combination of any known two-dimensional orthogonal functions forming a basis. As an example, we have used the two-dimensional Fourier decomposition of digital images of the corresponding samples.

The well-known relations were applied for the two-dimensional Fourier decomposition:

$$\begin{aligned}
 f(x, y) &= \sum_{k,l=0}^{\infty} \sum_{j=1,2,3,4} a_{jkl} \cdot \varphi_{jkl}(x, y), \\
 \varphi_{jkl}(x, y) &= \begin{cases} \sin \\ \cos \end{cases} \left\{ \frac{k \cdot 2\pi x}{L_x} \right\} \begin{cases} \sin \\ \cos \end{cases} \left\{ \frac{l \cdot 2\pi y}{L_y} \right\}, \\
 a_{jkl} &= \frac{2^\lambda}{L_x L_y} \int_0^{L_x} \int_0^{L_y} f(x, y) \cdot \varphi_{jkl}(x, y) dx dy,
 \end{aligned} \tag{1}$$

where L_x, L_y – the spatial periods “along” two arbitrary orthogonal axes of the coordinate system of sample; k, l – the indexes of the corresponding harmonics, and carried out the necessary numerical integration; j – enumerates all possible combinations of sine and cosine and:

$$\lambda = \begin{cases} 0; & k = l = 0, \\ 1; & k = 0, l \neq 0 \text{ or } k \neq 0, l = 0, \\ 2; & k \neq 0 \text{ and } l \neq 0. \end{cases}$$

In this way, a one-to-one correspondence can be established between any flat image $f(x, y)$ and its two-dimensional spatial spectrum, where the two-dimensional Fourier amplitudes $A_{kl} = \sqrt{\sum_{j=1}^4 a_{jkl}^2}$ are the discrete functions of k, l indexes.

3.2. Implementation

It is readily obvious that matching the real digital image to the set of the decomposition's amplitudes requires one to make a number of assumptions and approximations:

- 1) Summarizing in (1) cannot be carried out in an infinitely large number of terms;
- 2) Integration in (1) is carried out by numerical methods, i.e. approximately.

Actually, used methods of numerical integration indicate the minimum number of sequence values that are necessary for numerical calculations of varying amplitude decay with reasonable accuracy. We considered the simplest methods (Simpson's and trapezium rule) of numerical integration. The relative error of numerical integration for some simple model functions (represented by 5 points per period) amounted to $\sim 5\%$. And for 7 points per period, the relative error amounted to $\sim 0.5\%$, which is less than the "instrument" relative error $\sim 0.7\%$ estimated as the reciprocal average value of pixels' brightness.

Thus, we were limited to 8 points representation of the spatial period "with a reserve". This is more restrictive than what is prescribed by the Kotelnikov theorem, but it provides a guaranteed accuracy of numerical integration and greatly improves the speed of calculations. Thus, the maximum spatial frequency of the "calculated" harmonics was defined as $2\pi \cdot 8/L$, which corresponds to the maximum index values $k_{\max} = l_{\max} = L/8$. Therefore, if the spatial period is selected as 128 units (as in the example), the summarizing should be carried out for 16 two-dimensional harmonics.

In our case, the spatial reference periods are characterized by geometric sizes of the selected subareas and match ($L_x = L_y = 128$). The calculated "top-left realization" spectra of two-dimensional surfaces images of the fluorinated and sulfonated samples are presented in Fig. 3.

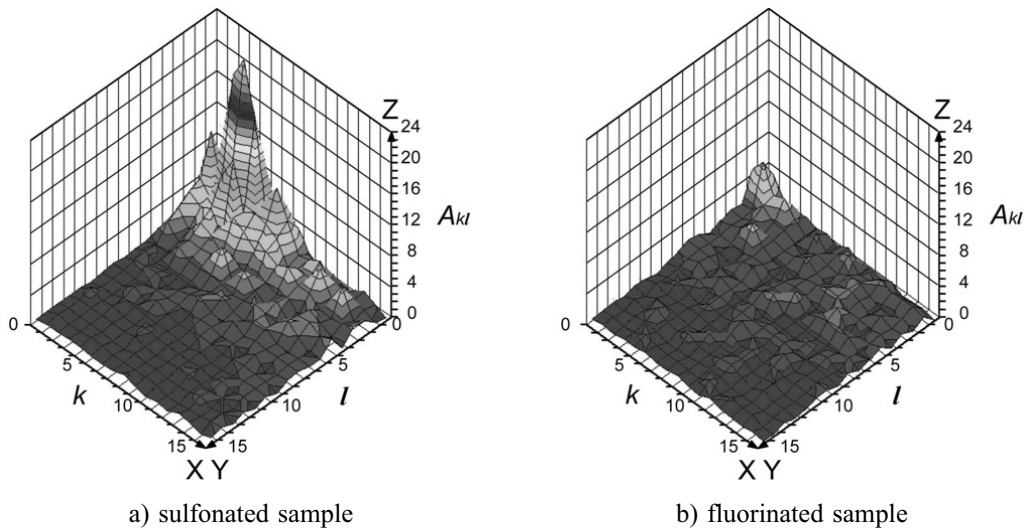


FIG. 3. The particular morphological spectra for the: a) sulfonated and b) fluorinated samples

The representation of the surface in the form of an expansion for any system of periodic (or quasiperiodic) of orthogonal functions leads to the following interpretation of the notion "regular surface structure": each amplitude of a certain basis function corresponds to one of a two-dimensional periodic lattice with two spatial periods. Then, the total number of observed regular structures is determined by the geometric size and horizontal resolution of the analyzed images. This means that at a given resolution the fixed geometric size of the image sample is mapped to a finite set of two-dimensional periodic lattices. Moreover, the smaller the geometric dimensions of the sample, the smaller the number of two-dimensional periodic lattices can be identified through analysis of the image.

To reduce the degree of dependence of the result from the geometric dimensions and resolution of the analyzed images, it is necessary to apply the classical methodology of mathematical statistics, i.e., to solve the problem of statistical reliability of the obtained results.

3.3. Identification

Scanning the whole image with a sub-region of 128 by 128 pixels we got the set of particular morphological spectra (see Fig. 3). There were calculated the average values (Fig. 4), the standard deviations and the t-statistics for each of received 2D-Fourier amplitudes.

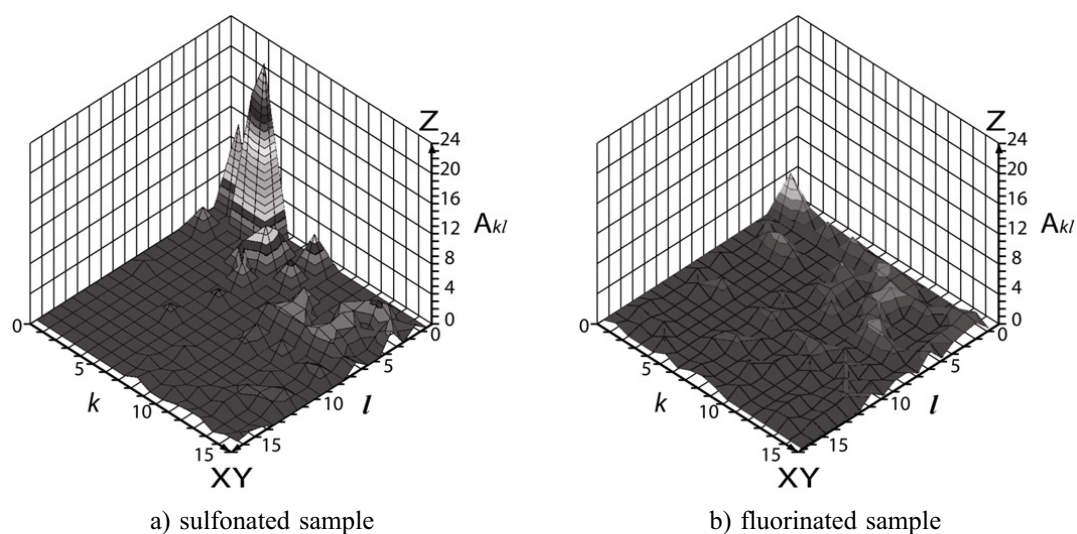


FIG. 4. The average morphological spectra for the: a) sulfonated and b) fluorinated sample

The set of the calculated amplitudes was divided into the statistically significant and statistically insignificant components using Student's *t*-test. The amplitude is statistically significant if its empirical *t*-statistics exceed the critical value dictated by the Student's distribution. The parameters of Student's distribution are "the error probability" and "the number of degrees of freedom". "The error probability" means the probability of rejecting the null hypothesis about the statistical significance of the estimated factor when using bilateral Student's distribution. "The number of degrees of freedom" is defined as the difference between the number of experimental observations and the number of coupling equations.

According to our concept, the statistically significant amplitudes form a model of the morphological spectrum of the surface, and the statistically insignificant ones – the model of morphological noise. We aim to use the statistically significant "average" Fourier amplitudes for quantitative comparison of surface morphologies (and, in the future, of the bulks) of experimental samples (for example, when studying the dependence of the surface micro relief from the duration and the nature of the processing chemicals).

The task of identifying the surface structures and the task of digital modeling/restoring ones (under the "average" morphological spectrum) are characterized by different values of "the error probability" in Student's criteria. It is necessary to choose the minimum (acceptable for the researcher) value of "the error probability" α (e.g., 0.0001, 0.05 etc.) for a reliable identification of the most significant structures. The structures of morphological spectra of sulfonated and fluorinated samples (in cases of the relevant two-dimensional lattices' identification "reliabilities", $(1 - \alpha)$, are 0.9999 and 0.95 respectively) are shown in Fig. 5 schematically.

Obviously, the more reliable the obtained (Fig. 4) amplitudes are, the smaller number of them involves 2D-Fourier morphological spectrum (Fig. 5a) and Fig. 5b. We believe that such surface properties as, for example, wettability determined by small number of statistically significant two-dimensional periodic lattices which form the "effective" microrelief. But when reconstructing (and simulating) the surface (see section 3D), a greater number of amplitudes (Fig. 5c) and (Fig. 5d) with a smaller (but adequate) statistical significance (probability of error ~ 0.05) provide higher quality for matching the models with the images of the experimental samples' surfaces.

3.4. Simulation

The additional information about the Fourier spectra harmonics phases (along with Fourier spectra harmonics amplitudes) is necessary for realistic simulation of the samples' surfaces. This information is contained in a_{jkl} values used to calculate each amplitude A_{kl} . Thus, the "phase" information for all statistically significant harmonics was taken into account when restoring of the surface under the average spectrum and statistically insignificant harmonics were ignored.

In this case, a measure of model quality is the correlation coefficient (or coefficient of determination) between the digital images of the original and the model images. Therefore, the error probability when using the Student's criterion should be selected from the range of researcher-acceptable values (for example, not more than 0.05), but with the need to maximize the value of the correlation coefficient. Otherwise, the excessive demands for statistical

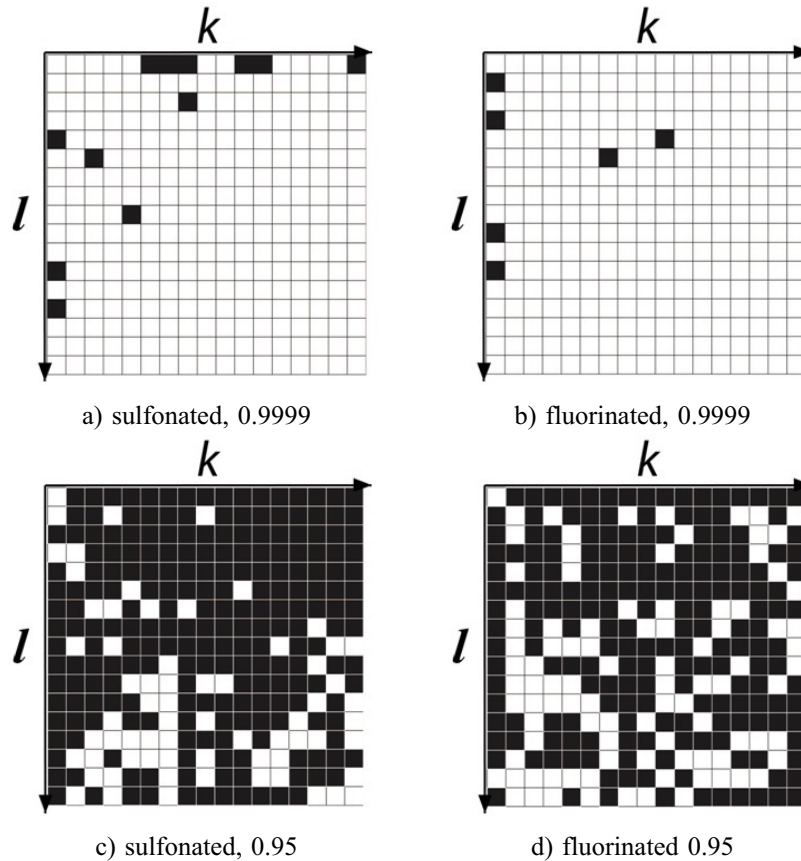


FIG. 5. The morphological spectra's structure for the sulfonated (left) and fluorinated (right) samples with 0.9999 (top) and 0.95 (bottom) reliabilities

significance of the identified surface structures hamper the maintenance of an acceptable quality reconstruction (or modeling) of samples' surfaces under the average morphological spectrum.

The two-dimensional digital relief maps of samples' surfaces and their morphological models are shown in Fig. 6.

When comparing digital originals and morphological models (the error probability 0.05) of images of the fluorinated and sulfonated experimental samples surfaces, the correlation coefficient was estimated to be ~ 0.83 and ~ 0.92 , respectively, indicating acceptable quality of the obtained models and the adequacy of this method for solving problems of the polymeric composites surfaces' characterization.

The results of the surfaces' image reconstruction under the average two-dimensional Fourier spectra with 0.9999 and 0.95 harmonics reliabilities are represented in the table (reliability defines as $(1-\alpha)$, where α – "Student's" error probability).

TABLE 1. The surfaces' images restoring quality

| The reliability | The sulfonated sample | | The fluorinated sample | |
|---|-----------------------|------|------------------------|------|
| | 0.9999 | 0.95 | 0.9999 | 0.95 |
| The number of significant amplitudes, units | 67 | 244 | 96 | 250 |
| The proportion of significant amplitudes, % | 26 | 95 | 37.5 | 98 |
| The correlation coefficient, units | 0.67 | 0.86 | 0.52 | 0.8 |

In the 0.9999 reliability case for the sulfonated sample, there are 67 statistically significant amplitudes (i.e. ~ 26 % of the total number; see Fig. 5). In the 0.95 reliability case for the sulfonated sample there are 244 statistically significant amplitudes (~ 95 % from total number). The rest of the two-dimensional Fourier spectrum amplitudes form the "morphological noise". The correlation coefficients for the pixels' brightness "between the

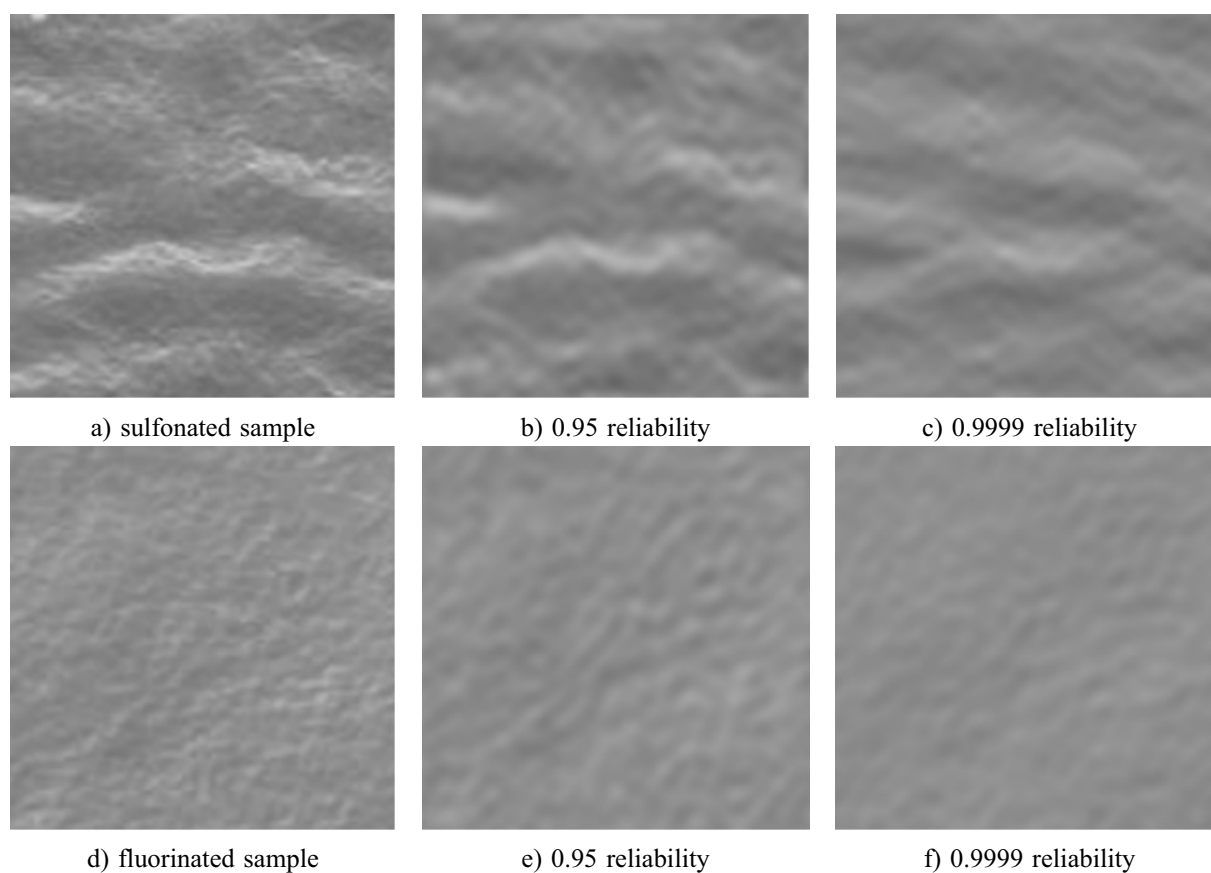


FIG. 6. The two-dimensional digital relief maps of the sulfonated and fluorinated samples surfaces and their reconstructions with different reliability values

samples and the models" are ~ 0.67 and ~ 0.86 for 0.9999 and 0.95 reliability cases respectively. Similarly, for the fluorinated sample: the 0.9999 reliability corresponds to 96 (37.5 %) significant amplitudes, the 0.95 reliability – to 250 (98 %) significant amplitudes, and provides 0.52 and 0.8 correlation coefficient values respectively.

Thus, the greater reliability in morphological spectrum amplitudes identification is required by the researcher, the smaller number of the periodic lattices (forming the surface relief) will be identified and the worse quality of surface restoring will be achieved. Conversely, the greater the quality of correspondence between reconstructed and initial images is required, the less the accuracy in the morphological spectrum identification it's necessary to settle for.

4. The volume morphological structure modeling (concept)

It is proposed to use a technique similar to that described above for the simulation of the volume morphological structure of the modified polymer. Since the volumetric modification is the formation of submicron pores, cavities, inclusions and impurities (chemically homogeneous or chemically heterogeneous with respect to the original polymer matrix), it is necessary to identify three-dimensional regular structure (three-dimensional periodic lattices) the superposition of which would form the corresponding volumetric heterogeneity.

Three-dimensional Fourier decomposition is determined by:

$$\rho(x, y, z) = \sum_{k,l,m=0}^{\infty} \sum_{j=1,\dots,8} a_{jklm} \cdot \varphi_{jklm}(x, y, z),$$

$$\varphi_{jklm}(x, y, z) = \begin{cases} \sin \\ \cos \end{cases} \left\{ \frac{k \cdot 2\pi x}{L_x} \right\} \begin{cases} \sin \\ \cos \end{cases} \left\{ \frac{l \cdot 2\pi y}{L_y} \right\} \begin{cases} \sin \\ \cos \end{cases} \left\{ \frac{m \cdot 2\pi z}{L_z} \right\}, \quad (2)$$

$$a_{jklm} = \frac{2^\lambda}{L_x L_y L_z} \int_0^{L_x} \int_0^{L_y} \int_0^{L_z} \rho(x, y, z) \cdot \varphi_{jklm}(x, y, z) \, dx dy dz.$$

Here, L_x , L_y , L_z – the spatial periods “along” three arbitrary orthogonal axes of the coordinate system of sample; k , l , m – the indices of the corresponding harmonics, and

$$\lambda = \begin{cases} 0; & k = l = m = 0, \\ 1; & k = l = 0, m \neq 0 \text{ or } k = m = 0, l \neq 0 \text{ or } l = m = 0, k \neq 0, \\ 2; & k = 0, l \neq 0, m \neq 0 \text{ or } k \neq 0, l = 0, m \neq 0 \text{ or } k \neq 0, l \neq 0, m = 0, \\ 3; & k \neq 0, l \neq 0, m \neq 0. \end{cases}$$

Thus, any empirical three-dimensional distribution of density of matter $\rho(x, y, z)$ can be mapped to morphological range $A_{klm} = \sqrt{\sum_{j=1}^8 a_{jklm}^2}$, allowing you to visualize the morphological model in the form of modulation of optical density, using the color space or in the form of animation. We consider the possibility of practical implementation of these methods for visualizing morphological patterns of volumetric modified polymers as an important task for further research.

5. Conclusion

This paper discusses ways to identify morphological structures on the surfaces and in the volumes of polymer composites. Examples of surface-modified polymers obtained by gas-phase sulfonation and fluorination were considered. A number of regular surface structures were revealed when processing was obtained by means of scanning electron microscopy images of samples' surfaces with two-dimensional Fourier analysis. A method based on three-dimensional Fourier analysis of the distribution of density fluctuations of matter for the identification and specification of the regular submicron structures in polymeric composites volumes was offered.

Acknowledgements

The work was performed with financial support from the RFBR grant 16-03-00540. The authors express their deep appreciation to the referee and the editor for helpful and significant suggestions and tips.

References

- [1] Kerber M.L., Vinogradov V.M., Golovkin G.S., et al. *Polymer composite materials: structure, properties, technology*. SPb.: Profession, 2008. (RUS)
- [2] Myakin S.V., Sychev M.M., Zahradnicek A.L., Vasilyev V.I., Sosnov E.A., Kolovangina E.S. Investigation of radiation resistance of polyimide films under the influence of high doses of accelerated electrons. *Bulletin of St. Petersburg state technological Institute (technical University)*, 2012, **14**, P. 36–40. (RUS)
- [3] Sevast'yanov V.I., Nemets E.A., Stolyarov V.P., Baranov V.A., Bozhko N.N., Nazarov V.G. Comparative study of the influence of polyethylene film surface modification on interaction with blood components. *Inorganic Materials: Applied Research*, 2011, **2** (2), P. 46–152.
- [4] Chung J.Y., Stafford C.M. and Youngblood J.P. Anisotropic wetting on tunable micro-wrinkled surfaces. *Soft Matter*, 2007, **3** (9), P. 1163–1169.
- [5] Pertsov A.V., Soboleva O.A., Protsenko P.V. and Nazarov V.G. Selective wetting in a hydrocarbon liquid-perfluorocarbon liquid-solid system. *Colloid Journal*, 2008, **70** (6), P. 759–762.
- [6] Nazarov V.G., Stolyarov V.P., Volynskii A.L., Yarysheva L.M., Bakeev N.F. Transformation of the modified layer of fluorinated polyolefins under stretching. *Polymer Science. Series A*, 2012, **54** (9), P. 679–683.
- [7] Arzhakova O.V., Dolgova A.A., Yarysheva L.M., Volynskii A.L. and Bakeev N.F. Development of a Stable Open-Porous Structure in the Solvent-Crazed High-Density Polyethylene. *Inorganic Materials: Applied Research*, 2011, **2** (5), P. 493–498.
- [8] Nazarov V.G. Multiple surface structures in polyolefins formed by modification methods. *Journal of Applied Polymer Science*, 2005, **95** (5), P. 1198–1208.
- [9] Volynsky A.L., Kecekjan A.S., Bakeev N.F. Polymer-polymer systems “rigid coating on a compliant base”. *Polimer Science. Series A*, 2003, **45** (7), P. 1130. (RUS)

- [10] Goikhman M.Ya., Subbotina L.I., Romashkova K.A., Smirnov N.N., Ershov Y.A., Gofman I.V., Lukoshkin V.A., Yakimansky A.V., Kudryavtsev V.V. Synthesis and properties of copolymers of glycidyl methacrylate with side chromophore groups. *Polimer Science. Series A*, 2007, **49** (7), P. 1170–1180. (RUS)
- [11] Belomoina N.M., Rusanov A.L. Modified polymers and materials on their basis. *Polimer Science. Series A*, 2007, **49** (7), P. 1426–1447. (RUS)
- [12] Badamshina E.R., Gafurova M.P. Modification of properties of polymers by doping with fullerene C₆₀. *Polymer Science. Series A*, 2008, **50** (8), P. 1572–1584. (RUS)
- [13] Valuev I.L., Valuev L.I., Obydenova V. I., Sytov G.A., Vanchugov L.V. Modified polyurethanes: a new type thromboresistant polymers. *Polymer Science. Series A*, 2010, **52** (8), P. 1432–1435. (RUS)
- [14] Panin S.V., Kornienko L.A., Puvadin T., Sergeev V. P., Ivanova L.R., Shilko S.V. The modification of ultra-high molecular weight polyethylene with high-energy surface treatment methods. *Advanced materials*, 2011, **13**, P. 376–383. (RUS)
- [15] Hodyrevskaya Y.I., Tverdokhlebov S.I., Kudryavtseva Y.A. Plasma-chemical modification of polymer materials for cardiovascular surgery to control the degree of wettability. *Bulletin of the Tomsk Polytechnic University. Mathematics and mechanics. Physics*, 2014, **325** (2), P. 158–165. (RUS)
- [16] Nazarov V.G. Structure and composition of the surface layer in polymers modified by elemental fluorine. *Journal of Applied Polymer Science*, 2005, **95** (4), P. 897–902.
- [17] Nazarov V.G., Kondratov A.P., Stolyarov V.P., Evlampieva L.A., Baranov V.A., Gagarin M.V. Morphology of the surface layer of polymers modified by fluorine gas. *Polymer Science. Series A*, 2006, **48** (11), P. 1976–1985. (RUS)
- [18] Krisilova E.V., Eliseeva T.V., Grechkina M.V. The analysis of the structure of the surface sulfocationites perfluorinated membranes in hydrogen and lysine forms by atomic force microscopy. *Sorption and chromatographic processes*, 2010, **10**(1), P. 103–107. (RUS)
- [19] Safronova T.V., Putlyaev V.I. Medical inorganic materials science in Russia: the calcium-phosphate materials. *Nanosystems: physics, chemistry, mathematics*, 2013, **4** (1), P. 24–47. (RUS)
- [20] Kurylenko K.A., Brylev O.A., Filippov T.V., Baranchikov A.E., Shlyakhtin O.A. Cryogenically synthesis of cathode materials based on LiNi_{0.4}Mn_{0.40}O₂ for Li-ion batteries. *Nanosystems: physics, chemistry, mathematics*, 2013, **4** (1), P. 105–112. (RUS)
- [21] Shipovskaya A.B., Rudenko D.A., Fomina V.I. and Ostrovsky N.V. Structure and Properties of Chitosan-Based Films for Biomedical Purposes. *European Journal of Natural History*, 2012, **6**, P. 7–12.
- [22] Volynskii A.L., Panchuk D.A., Bolshakova A.V., Yarysheva L.M., Bazhenov S.L., Yablokov M.Y., Gilman A.B. and Bakeev N.F. The structure and properties of thin aluminum coatings. *Thin Solid Films*, 2013, **536**, P. 179–186.
- [23] Volynskii A.L., Yarysheva L.M., Bagrov D.V., Rukhlya E.G., Yarysheva A.Y., Bakeev N.F., Nazarov V.G., Stolyarov V.P. and Tsypysheva S.V. Evaluation of the deformation strength properties of a fluorinated polymer layer on the surface of poly(ethylene terephthalate) films. *Doklady Physical Chemistry*, 2012, **442** (1), P. 5–7.
- [24] Sotskaya N.V., Dolgikh O.V., Kashkarov V.M., Lenshin A.S., Kotlyarova E. A., Makarov S.V. Physico-chemical properties of surfaces modified with nanoparticles of metals. *Sorption and chromatographic processes*, 2009, **9** (5), P. 643–652. (RUS)
- [25] Vernigorov K.B., Alentiev A., Meshkov I.B., Muzafarov A.M., Voronina E.N., Novikov L.S., Chernik V.N. Improving the sustainability of the thermoplastic polyimide exposure to atomic oxygen by modification of the hyperbranched polyethoxysiloxanes. *Advanced materials*, 2011, **4**, P. 10–17. (RUS)
- [26] Prudnikov A.M., Linnik A.I., Shalaev R.V., Rumyantsev V.V., Kucherik A.O., Alodjants A.P., Arakelian S.M. The features of formation and modification of nanostructured films of carbon nitride. *Nanosystems: physics, chemistry, mathematics*, 2012, **3** (6), P. 134–145. (RUS)
- [27] Balakhonov S.V., Luchinkin D.S., Efremova M.V., Churagulov B.R., Tretyakov Yu.D. The synthesis and physics-chemical properties of lithium-doped nanowhiskers on the basis of oxides of vanadium. *Nanosystems: physics, chemistry, mathematics*, 2011, **2** (3), P. 102–112. (RUS)
- [28] Goerg H. Michler. *Electron Microscopy of Polymers*. Springer Laboratory, 2008.
- [29] Evdokimov P.V., Putlyaev V.I., Merzlov D.A., Shatalova T.B., Safronova T.V., Klimashin E.S., Churagulov B.R. The polymorphisms of Ca₃(PO₄)₂. *Nanosystems: physics, chemistry, mathematics*, 2013, **4** (1), P. 48–53. (RUS)
- [30] Sarychev A.S., Parshina E.Yu., Bayzhumanov A.A., Semenova A.A., Gudilin E.A., Maksimov G.V. The influence of silver hydrosols on structural integrity of erythrocytes. *Nanosystems: physics, chemistry, mathematics*, 2013, **4** (1), P. 66–71. (RUS)
- [31] Manakina D.S., Tcherdyntsev V.V., Ludikova A.A. The investigation of the structure and roughness of the hydrophobic composite coatings on the basis of polysulfone. *Modern problems of science and education*, 2012, **5**, P. 126. (RUS)
- [32] Senatov F.S., Maksimkin V.A., Yergin K.S. The investigation of structure of coatings based on polyster by scanning electron microscopy and optical profilometry. *Modern problems of science and education*, 2012, **5**, P. 129. (RUS)
- [33] Arzhakova O.V., Dolgova A.A., Yarysheva L.M., Volinsky A.L., Bakeev N.F. The creation of a stable open-pored structure in the high-density polyethylene deformed in liquid media by the mechanism of crazing. *Advanced materials*, 2011, **1**, P. 39–46.
- [34] Yanovsky Yu.G., Nikitina E.A., Karnet Yu.N., Valiev H.H., Yumashev O.V., Semenov N.A. Quantum-mechanical description of adhesive interactions and experimental studies of the processes of aggregation of carbon-silicate nanoparticles-reinforcing fillers of polymer composites. *Physical Mesomechanics*, 2013, **16** (4), P. 85–96. (RUS)
- [35] Nazarov V.G., Sevast'Yanov V.I., Stolyarov V.P., Evlampieva L.A., Baranov V.A., Gagarin M.V. Simulation of the development of the mosaic surface structures in polyethylene. *Polymer Science. Series B*, 2009, **51** (9–10), P. 367–376.
- [36] Nazarov V.G., Stolyarov V.P., Evlampieva L.A., Baranov V.A., Gagarin M.V. Simulation of sulfonation and structure of surface layer in polyethylene. *Polymer Science. Series A*, 2009, **51** (3), P. 340–349.
- [37] Nazarov V.G., Stolyarov V.P., Molchanov S.P., Yurasik G.A., Artemenko M.N. Heterogeneous fluorine-containing surface macro-, micro- and nanostructures in polymer films and their applications. *Polymer Science. Series A*, 2013, **55** (11), P. 652–665.
- [38] Nazarov V.G., Stolyarov V.P., Novikov M.S., Mikhaleva L.A., Bablyuk E.B., Benda A.F. The influence of fluorination on surface characteristics of polymeric materials. *Bulletin of Higher Educational Institutions. Problems of printing and publishing industries*, 2011, **2**, P. 118–127. (RUS)
- [39] Kopachev E.S., Nozdrachev S.A., Petrushin V.N., Rudyak Yu.V., Rytikov G.O., Nazarov V.G. A complex technique of surface image characterization for polymer composites. *Physical mesomechanics*, 2015, **18** (6), P. 98–110. (RUS)



NANOSYSTEMS:

PHYSICS, CHEMISTRY, MATHEMATICS

INFORMATION FOR AUTHORS

The journal publishes research articles and reviews, and also short scientific papers (letters) which are unpublished and have not been accepted for publication in other magazines. Articles should be submitted in English. All articles are reviewed, then if necessary come back to the author to completion.

The journal is indexed in Web of Science Core Collection (Emerging Sources Citation Index), Chemical Abstract Service of the American Chemical Society, Zentralblatt MATH and in Russian Scientific Citation Index.

Author should submit the following materials:

1. Article file in English, containing article title, the initials and the surname of the authors, Institute (University), postal address, the electronic address, the summary, keywords, MSC or PACS index, article text, the list of references.
2. Files with illustrations, files with tables.
3. The covering letter in English containing the article information (article name, MSC or PACS index, keywords, the summary, the literature) and about all authors (the surname, names, the full name of places of work, the mailing address with the postal code, contact phone number with a city code, the electronic address).
4. The expert judgement on possibility of publication of the article in open press (for authors from Russia).

Authors can submit a paper and the corresponding files to the following addresses: nanojournal.ifmo@gmail.com, popov1955@gmail.com.

Text requirements

Articles should be prepared with using of text editors MS Word or LaTeX (preferable). It is necessary to submit source file (LaTeX) and a pdf copy. In the name of files the English alphabet is used. The recommended size of short communications (letters) is 4-6 pages, research articles– 6-15 pages, reviews – 30 pages.

Recommendations for text in MS Word:

Formulas should be written using Math Type. Figures and tables with captions should be inserted in the text. Additionally, authors present separate files for all figures and Word files of tables.

Recommendations for text in LaTeX:

Please, use standard LaTeX without macros and additional style files. The list of references should be included in the main LaTeX file. Source LaTeX file of the paper with the corresponding pdf file and files of figures should be submitted.

References in the article text are given in square brackets. The list of references should be prepared in accordance with the following samples:

- [1] Surname N. *Book Title*. Nauka Publishing House, Saint Petersburg, 2000, 281 pp.
- [2] Surname N., Surname N. Paper title. *Journal Name*, 2010, **1** (5), P. 17-23.
- [3] Surname N., Surname N. Lecture title. In: Abstracts/Proceedings of the Conference, Place and Date, 2000, P. 17-23.
- [4] Surname N., Surname N. Paper title, 2000, URL: <http://books.ifmo.ru/ntv>.
- [5] Surname N., Surname N. Patent Name. Patent No. 11111, 2010, Bul. No. 33, 5 pp.
- [6] Surname N., Surname N. Thesis Title. Thesis for full doctor degree in math. and physics, Saint Petersburg, 2000, 105 pp.

Requirements to illustrations

Illustrations should be submitted as separate black-and-white files. Formats of files – jpeg, eps, tiff.



NANOSYSTEMS:

PHYSICS, CHEMISTRY, MATHEMATICS

Журнал зарегистрирован

Федеральной службой по надзору в сфере связи, информационных технологий и массовых коммуникаций

(свидетельство ПИ № ФС 77 - 49048 от 22.03.2012 г.)

ISSN 2220-8054

Учредитель: федеральное государственное автономное образовательное учреждение высшего образования

«Санкт-Петербургский национальный исследовательский университет информационных технологий, механики и оптики»

Издатель: федеральное государственное автономное образовательное учреждение высшего образования

«Санкт-Петербургский национальный исследовательский университет информационных технологий, механики и оптики»

Отпечатано в Учреждении «Университетские телекоммуникации»

Адрес: 197101, Санкт-Петербург, Кронверкский пр., 49

Подписка на журнал НФХМ

На второе полугодие 2017 года подписка осуществляется через

ОАО Агентство «Роспечать»

Подписной индекс 57385 в каталоге «Издания органов научно-технической информации»